

Inter-University Centre for Astronomy and Astrophysics Post-Bag 4, Ganeshkhind,
Pune 411007 MH, India

Exploring the Impact of Wave Effects in the Lensing of Gravitational Waves from Chirping Binaries

Candidate: Anuj Mishra

Supervisor: Prof. Gulab Dewangan

Co-Supervisor: Prof. Sukanta Bose and Dr. Anupreeta More

A thesis to be presented for the degree of

Doctor of Philosophy

to

Jawaharlal Nehru University, New Delhi, India



Declaration from Candidate

I hereby declare that the material present in this thesis is based on work done at the Inter-University Centre for Astronomy and Astrophysics, Pune. This thesis is original and has not been submitted previously for any academic cause. The work of other researchers utilized by us has been properly cited.

Anuj Mishra

Inter-University Centre for Astronomy and Astrophysics, Pune, MH - 411007

Signature:  _____

Date: 15/11/2023

Declaration from Supervisor

This is to certify that this thesis titled 'Exploring the Impact of Wave Effects in the Lensing of Gravitational Waves from Chirping Binaries' is based on work done by Mr. Anuj Mishra at the Inter-University Centre for Astronomy and Astrophysics, Pune, under my supervision. To the best of my knowledge, this thesis is original and has not been submitted previously for any academic cause.

Supervisor: Prof. Gulab Dewangan

Inter-University Centre for Astronomy and Astrophysics, Pune, MH - 411007

Signature: 

Date: 16/11/2023



Declaration from the Head of the Institute

This is to certify that this thesis titled 'Exploring the Impact of Wave Effects in the Lensing of Gravitational Waves from Chirping Binaries' is based on work done by Mr. Anuj Mishra at the Inter-University Centre for Astronomy and Astrophysics, Pune. To the best of my knowledge, this thesis is original and has not been submitted previously for any academic cause.

Prof. R. Srianand

Director (Officiating)

Inter-University Centre for Astronomy and Astrophysics, Pune, MH - 411007

Signature: 

Date: 16/11/23



Acknowledgments

I extend my heartfelt gratitude to my supervisor, Prof. Sukanta Bose, and co-supervisor, Dr. Anupreeta More, for giving me the opportunity to work on this interesting and relevant topic. Their mentorship has not only allowed me to contribute to this field but has also played a pivotal role in my growth as a scientist. It has been an exciting journey, from crawling to running to tumbling and falling down to standing again, having a life of its own.

While keeping this acknowledgement brief, I must mention a few names who inspired me to pursue (astro)physics. It all started when I got hold of the book 'A Brief History of Time' by Prof. Stephen Hawking when I was in seventh grade. Although I couldn't understand much, which is obvious, I did grasp some basic ideas that really made me think and, more importantly, introduced me to the scientific method of reasoning. I also want to express my gratitude to Prof. Thanu Padmanabhan (affectionately known as Paddy) and Prof. V. Balakrishnan for their immense contribution to pedagogy through their books and lectures. Their invaluable insights will benefit generations to come and have greatly helped me in my own learning journey.

I am grateful to Prof. Subenoy Chakraborty for his instrumental role in kick-starting my career in scientific writing. He offered me guidance when no one else did, and together, we authored my first paper on General Relativity. His unwavering support has been crucial for my journey and has contributed significantly to where I am today. I would also like to express my sincere thanks to my collaborators, Dr. Apratim Ganguly, Dr. Ashish K. Meena, Dr. Nathan K. Johnson-McDaniel, and Dr. N.V. Krishnendu, who played a crucial role in expanding my horizons and moulding me into a more meticulous researcher along the way.

Special thanks to my family, who always encouraged me to pursue whatever I wanted and for being very understanding and present whenever I needed them. Additionally, I extend my thanks to ancient Indian wisdom, particularly in terms of yoga and the philosophy of Upanishads (Vedanta), which kept me sane (well, for the most part of it!) and inspired me to work for the sake of working.

Lastly, I extend my gratitude to my colleagues here at IUCAA, especially Bhaskar, Bikram, Kanchan, Samanwaya, Tathagata, Supravo, and Vishal (in alphabetical order), with whom I had a great time interacting. I am also thankful to my (unofficial) students, Anirudh, Nishkal and Sreelakshmi, for providing me valuable mentoring experience. Additionally, I express my gratitude to my other longtime friends: Ankit, Aritra, Deepak, Gaurav, Junaid, Koustav, Sandeep and Tushar for so many things that are hard to list here. Special thanks also to my piano teacher, Mrs. Sonam Lodhi, for keeping my journey enjoyable and for bringing out the best in me.

Dedicated to all the giants on whose shoulders I stood; all the stars who die to make us
and this research field alive; and all the teachers who light our path.

उत्तिष्ठत जाग्रत
प्राप्य वरान्निबोधत ।
क्षुरस्य धारा निशिता दुरत्यया
दुर्ग पथस्तत्कवयो वदन्ति ॥ १४ ॥

Arise! Awake! Approach the great and learn. Like the sharp edge of a razor is that path, so the wise say-hard to tread and difficult to cross.

- Katha Upanishad 1.3.14

Abstract

With increasing sensitivities of current ground-based gravitational wave (GW) detectors, the prospects of detecting gravitationally lensed GW signals are poised to improve in the coming years. While the lensing of GWs shares similarities with electromagnetic waves, their observed effects can exhibit striking differences. This thesis delves into the impact of wave-optics effects in gravitational lensing of GWs originating from compact binary coalescence.

When a GW encounters compact objects, such as stars, stellar remnants, or possible compact dark matter objects like primordial black holes, it can lead to the emergence of wave-optics effects. These effects result in frequency-dependent modulations of the signal, which we refer to as 'microlensing.' In such cases, the geometrical optics approximation breaks down, necessitating the consideration of the wave nature of propagation. Consequently, these frequency-dependent modulations influence the GW strain, potentially introducing biases if these lensing effects are not accounted for. This leads to natural questions: When do these modulations become significant? What parameters can they affect? How do these microlenses behave when embedded in a strong lens? What is their impact on the physics extracted from GW signals? Can they influence other GW analyses, such as tests of general relativity (GR)? What are the prospects for their detection, and what challenges are associated with such model comparison studies, and more?

In this thesis, I aim to answer these questions, with some of them being investigated for the first time in the literature. I begin by demonstrating how microlensed signals affect the detectability of GW signals from the perspective of standard matched-filter searches. I find that while typical unlensed searches can significantly decrease the true SNR by over 30%, the presence of isolated microlenses consistently amplifies the GW signals they lens, thereby extending the detection horizon to potentially distant sources, reaching as far as redshifts $z \sim 10$. I also discuss the consequences of neglecting microlensing effects when inferring source properties. The phase modulations can significantly bias intrinsic parameters, with in-plane spin components (precession) being the most affected. Similarly, amplitude modulations often lead to the underestimation of luminosity distance, by up to a factor of 10 in extreme cases. Study of a population of microlensed signals

due to an isolated point lens primarily reveals: (i) using unlensed templates during the search causes fractional loss (20% to 30%) of potentially identifiable microlensed signals; (ii) Bayes factor analysis of the population indicates that certain region in $M_{Lz} - y$ parameter space have a higher probability of being detected and accurately identified as microlensed. Importantly, the microlens parameters for the most compelling candidate in the third GW transient catalogue (GWTC-3), GW200208_130117, fall within a 1-sigma range of the aforementioned high-probability region, favouring the microlensing hypothesis. Furthermore, I explore more realistic scenarios involving microlensing, where a microlens or a population of stellar-mass microlenses is embedded in a strong gravitational lens. I demonstrate how the presence of a strong lens can amplify microlensing effects, effectively increasing the effective mass of microlenses. Consequently, I examine the impact of the microlens population within lensing galaxies on strongly lensed GWs. I find that microlensing atop strong lensing can lead to substantial biases as the strong lensing magnification (μ) increases, with mismatch values exceeding 5% for $|\mu| > 100$. Furthermore, the presence of these microlensing features can also influence strong lensing searches, potentially resulting in orders of magnitude drops in Bayes factors, measuring the strength of the strong lensing hypothesis versus the unlensed hypothesis, especially in extreme cases. Additionally, I investigate how microlensing effects can bias tests of GR, with a confidence level even exceeding 5σ . I show how deviations from GR correlate with pronounced interference effects and also discuss how one can identify such biases to avoid (erroneous) claims of deviations from GR.

Lastly, I discuss how microlensing searches can be biased due to the presence of other atypical physical effects, specifically, the presence of non-zero eccentricity in the signal. I demonstrate the bias in microlensing searches and show that it monotonically increases with increasing eccentricity, the duration of the signal (low mass binaries), and the signal-to-noise ratio (SNR) of the signal. Furthermore, I demonstrate that the degeneracy between microlensing and eccentricity can be broken, and the biases in microlensing searches can be resolved by including eccentricity in the recovery process while doing parameter estimation.

List of publications

Included in thesis

Publications as leading author

For each of the following manuscripts, I contributed to the drafting of the entire text, the production of all figures and tables, the production of all results, the implementation and development of all computational methods.

1. **Anuj Mishra**, Ashish K. Meena, Anupreeta More, Sukanta Bose, and Jasjeet Singh Bagla. "Gravitational lensing of gravitational waves: effect of microlens population in lensing galaxies." *Monthly Notices of the Royal Astronomical Society*, 508(4), 4869-4886, 2021. [arXiv:2102.03946](https://arxiv.org/abs/2102.03946)
2. **Anuj Mishra**, Ashish K. Meena, Anupreeta More, and Sukanta Bose. "Exploring the Impact of Microlensing on Gravitational Wave Signals: Biases, Population Characteristics, and Prospects for Detection." *Monthly Notices of the Royal Astronomical Society*, Accepted manuscript. DOI: [10.1093/mnras/stae836](https://doi.org/10.1093/mnras/stae836). [arXiv:2306.11479](https://arxiv.org/abs/2306.11479)
3. **Anuj Mishra**, N.V. Krishnendu, and Apratim Ganguly. "Unveiling Microlensing Biases in Testing General Relativity with Gravitational Waves." Under review in *Physical Review D*. [arXiv:2311.08446](https://arxiv.org/abs/2311.08446)
4. **Anuj Mishra** and Apratim Ganguly. "Unraveling the Connection: Eccentric Binary Black Holes and Microlensed Signals." (In Preparation). Available at: <https://dcc.ligo.org/P2300206>
5. **Anuj Mishra**. "Introducing GWMAT: Gravitational Wave Microlensing Analysis Tools." (In Preparation)

Publications as the second author

1. Ashish K. Meena, **Anuj Mishra**, Anupreeta More, Sukanta Bose, and Jasjeet Singh Bagla. "Gravitational lensing of gravitational waves: Probability of microlensing in galaxy-scale lens population." *Monthly Notices of the Royal Astronomical Society* 517, no. 1 (2022): 872-884. [arXiv:2205.05409](https://arxiv.org/abs/2205.05409)
Contributions: provided the foundational code for computing amplification factor, and the code for modifying waveforms and match computations for cross verification; generated data for Fig. 8; assisted with text editing.

Other publications

Publications with substantial contributions that are not included in the thesis.

1. Justin Janquart et al. "Follow-up analyses to the O3 LIGO-Virgo-KAGRA lensing searches." <https://arxiv.org/abs/2306.03827>
2. Abbott et al. "Search for gravitational-lensing signatures in the full third observing run of the LIGO-Virgo network." <https://arxiv.org/abs/2304.08393>
3. **Anuj Mishra**, and Subenoy Chakraborty. "On the trajectories of null and timelike geodesics in different wormhole geometries." *The European Physical Journal C* 78 (2018): 1-16. <https://arxiv.org/abs/1710.06791>

Contents

List of publications	xvii
List of Figures	xxiii
List of Tables	xxxv
1 Introduction	1
2 Methodology	5
2.1 Basic Theory of Gravitational Lensing	5
2.2 Wave-Optics Effects in Gravitational Lensing	7
2.2.1 Microlensing due to an isolated point-lens	8
2.3 Gravitational Wave Data Analysis	12
2.3.1 Microlensed Waveforms	13
2.3.2 Matched-filtering Techniques	14
2.3.3 Simulated Injections	16
2.3.4 Bayesian Inference	16
2.3.5 Fisher Information formalism	20
3 Effect on Inferred Parameters	22
3.1 Introduction	23

CONTENTS

3.2	Effect of microlensing on the detection of GWs: Matched-filtering Analysis	24
3.3	Effect of microlensing on parameter estimation of GWs: Bayesian Analysis	28
3.4	Study of a population of Microlensed Signals	37
3.5	Model Comparison: Unlensed vs. Microlensed hypothesis	40
3.6	Statistical Uncertainties in the measurement of lensing parameters using Fisher Analysis	49
3.7	Discussion and Conclusion	51
4	Beyond isolated point lens model: Complex configurations of microlensing	55
4.1	Numerical Computation of the Amplification Factor	55
4.1.1	Formalism	56
4.1.2	Testing Numerical Code: Isolated Point lens	58
4.1.3	Testing Numerical Code: Type-I (Minima) Macroimages	60
4.1.4	Testing Numerical Code: Type-II (Saddle) Macroimages	61
4.2	Single Microlens Embedded in a Macrolens	63
4.3	Effect of microlens population present in lensing galaxies on strongly lensed GWs	66
4.3.1	Methodology	66
4.3.2	Studying effect of microlens population on type-I and type-II macroim- ages	70
4.3.3	High density systems	74
4.4	Effect of microlens population on the signatures of strong lensing	75
4.5	Conclusions	79
5	Microlensing meets Tests of General Relativity	81
5.1	Introduction	82
5.2	Basics	84
5.2.1	Tests of General Relativity (TGR)	84

CONTENTS

5.2.2	GW data analysis and Parameter Estimation Setup	87
5.2.3	Comparative Analysis of Fitting Factor and Time-Delay Trends in the Microlensing Parameter Space	89
5.3	Results and Discussions	91
5.3.1	GW150914-like Microlensed Injections	91
5.3.2	Population of Microlensed Injections	97
5.3.3	Normality Test of Posterior Samples	101
5.3.4	Investigating the correspondence between f_{ML} and f_{GW} : A closer perspective	103
5.4	Conclusion	105
6	Eccentricity vs Microlensing	108
6.1	Introduction	109
6.2	Results	110
6.2.1	Numerical Relativity Injections	110
6.2.2	Population Study	112
6.2.3	Eccentric BBH Injection Study using TEOBResumS	116
6.3	Conclusion	120
7	Conclusion and Future Directions	123
	References	126
A	Wave-optics effects in Gravitational Lensing of Gravitational Waves: Technical derivations and assumptions	140
A.1	Lensing Amplification Factor derivation	140
A.1.1	Basic Equations	140
A.1.2	Kirchhoff's Diffraction Integral	141
A.1.3	Diffraction by a microlensing compact object	143

CONTENTS

A.1.4	Lensing Amplification Factor	146
A.2	Lensing Time Delay Derivation	147
A.2.1	Geometric Time Delay	147
A.2.2	Gravitational Time Delay (Shapiro Delay)	148
A.2.3	Total lensing time delay	150

List of Figures

2.1	Illustration of the lensing configuration in the thin lens approximation. The lensing configuration is described by the source displacement from the line-of-sight η , the angular diameter distance from the observer to the source D_s , to the lens D_d and from lens to the source D_{ds} and by the relative position of the image in the image plane ξ . [Credit: Adapted from Pagano et al. (2020)]	6
2.2	Contour plot of the characteristic frequency, f_{ML} , indicating the onset of significant microlensing effects for varying point lens parameters M_{Lz} and y within the LIGO–Virgo sensitivity band (10 - 10^3 Hz). Contours at 10 and 10^3 Hz denote the rough transition regions, dividing the parameter space into three zones: (i) <i>Long-wavelength regime (left-panel)</i> , where GW frequency f_{GW} is significantly lesser than f_{ML} , i.e., $f_{GW} \ll f_{ML}$, resulting in minimal interaction; (ii) <i>Wave dominated zone (middle-panel)</i> : region where $f_{GW} \sim f_{ML}$, leading to significant interference effects on GWs. (iii) <i>Geometrical-optics regime (right panel)</i> : region where $f_{GW} \gg f_{ML}$. This region is inclusive of milli-lensing and strong-lensing scenarios.	10
2.3	Illustration of the nature of microlensing modulations in the three regimes. The absolute part of the amplification factor, $ F(f) $, is plotted against frequency (black lines). Microlens parameters are fixed at $y = 0.3$ and $M_{Lz}/M_{\odot} \in \{10, 10^3, 10^5\}$, arranged from left to right. The blue-shaded region represents the sensitivity band of current ground-based detectors, approximately $10 - 100$ Hz, for reference. The red vertical line indicates the characteristic frequency for the onset of significant microlensing effects, f_{ML} . The panels are divided based on whether $f_{ML} > 1000$ Hz (<i>left panel</i> , long-wavelength regime), $f_{ML} \in (10 - 1000)$ Hz (<i>middle panel</i> , wave-dominated zone), or $f_{ML} < 10$ Hz (<i>right panel</i> , geometrical optics regime).	11

LIST OF FIGURES

- 3.1 Effect of microlensing on GW WFs for different microlensing and CBC parameters. The top panel shows match values between the unlensed and the corresponding microlensed WFs, whereas the bottom panel show FF values (or, the maximum match) for the microlensed WFs when recovering with the unlensed WFs corresponding to the 4D aligned-spin template WFs modelled by parameters $\{\mathcal{M}_c, q, \chi_{1z}, \chi_{2z}\}$. The analysis has been done for: (i) varying redshifted lens mass (M_{Lz}) and impact parameter (y) for a fixed binary mass of $M_{\text{tot}} = 60 M_{\odot}$ and mass ratio $q = 1$ (*left panel*), (ii) M_{tot} vs. y parameter space for fixed $(M_{Lz}, q) = (100 M_{\odot}, 1)$ (*middle panel*), (iii) q vs. y parameter space for fixed $(M_{Lz}, M_{\text{tot}}) = (100 M_{\odot}, 60 M_{\odot})$ (*right panel*). The injected spins are kept zero. 25
- 3.2 The figure depicts the variation in the optimal SNR in the no-lens versus microlens cases. The variation is shown as a function of point-lens mass (M_{Lz} ; left panel), binary mass (M_{tot} ; middle panel), and mass-ratio (q ; right panel). The presence of an isolated microlens always increases the SNR relative to the no lensing case. 26
- 3.3 Correlations between the parameters of microlensed WFs. The injected WFs correspond to a BBH with a total binary mass of $M_{\text{tot}} = 60 M_{\odot}$, mass-ratio $q = 1$, and having observed network SNR of ~ 50 . Among the microlens parameters, the redshifted lens mass is fixed to $M_{Lz} = 100 M_{\odot}$ and the impact parameter increases from left to right as $y \in \{0.05, 0.1, 0.5, 1.0, \gg 1\}$ (also indicated at the top of each column). *Top*: correlations when the recovery model corresponds to 17D microlensed WFs. *Bottom*: correlations when the recovery model is the usual 15D unlensed BBH WFs. 29

LIST OF FIGURES

- 3.4 Bias in the inferred intrinsic source parameters of a microlensed signal when recovered using the usual unlensed WF model, characterised by 15 parameters. Each column represents the bias in a specific parameter, indicated at the top, while different rows correspond to different source binaries, indicated on the right side of each row. The intrinsic parameters are represented by the detected chirp mass (\mathcal{M}_{det}), symmetric mass-ratio (η), projected effective spin (χ_{eff}), and precession effective spin (χ_{p}). The source parameters correspond to equal mass binaries with a mass ratio of $q = 1$ and a total mass of $M_{\text{tot}}/M_{\odot} \in \{20, 60, 100, 200\}$. Each subplot shows the bias in the microlensing parameter space of the redshifted lens mass, denoted as $M_{\text{Lz}}/M_{\odot} \in \{1\text{e}1, 5\text{e}1, 1\text{e}2, 5\text{e}2, 1\text{e}3, 5\text{e}3, 1\text{e}4, 5\text{e}4, 1\text{e}5\}$, and the impact parameter values denoted as $y \in \{0.01, 0.05, 0.1, 0.5, 1.0, 3.0, 5.0\}$. Each circular marker in the plot has two halves: the left half represents the relative percentage error (absolute error for χ_{eff} and χ_{p}) between the median values of the microlensed and unlensed recoveries, while the right half represents the two-sample Kolmogorov-Smirnov (KS) Statistic value between the 1D marginalised posteriors of the microlensed and unlensed recoveries (in percentage). We further ignore points in the parameter space corresponding to a time-delay between microimages greater than the signal duration, indicating cases where strong lensing is observed (empty region in the top-right corner of each subplot). 31
- 3.5 Same as Fig. 3.4, but for extrinsic parameters. The extrinsic parameters are represented by the luminosity distance (d_{L}), inclination (θ_{JN}), sky location (RA and Dec; α and δ), polarization angle (Ψ), and coalescence phase (ϕ). The trigger time t_{c} is not shown as it is well recovered throughout the parameter space. 32
- 3.6 1D marginalised posterior distributions for the recoveries of $\{\mathcal{M}_{\text{det}}, q, a_1\}$ of the $60M_{\odot}$ binary system shown in Fig. 3.4 and 3.5. The dashed red line represents the injected value 35

LIST OF FIGURES

- 3.7 Variation in the correlation values between the 15 parameters of a BBH system due to microlensing effects. The studied BBH and lens system corresponds to the $60 M_{\odot}$ binary shown in Figures 3.4 and 3.5. *Left:* The variation is displayed for each parameter pair, resulting in a total of 120 possible pairs represented as individual lines. These lines illustrate the correlation values as a function of the time-delay between micro-images, determined by the microlens parameters in the grid shown in Fig. 3.4 and 3.5. Each line is associated with 63 data points, represented as dots, indicating the specific time-delay values used to construct the line. *Right:* Same as the left panel but explicitly showing the correlations for four pairs as written in the legend. Moreover, the lines originate from $\tau_d = 0$, showcasing the unlensed case. 37
- 3.8 Population study of microlensed BBH signals for the joint network of LIGO–Virgo detectors assuming the targeted O4 sensitivities. *Top:* Distribution of population is shown in the microlensing parameter space of M_{Lz} and y (left), and for y vs. z_S (right), where M_{Lz} , y and z_S denote the redshifted lens mass, impact parameter and source redshift, respectively. The colour bar represents the observed network optimal SNR. *Bottom:* Comparison of probability density functions (PDFs) between the ones that were used while generating the population (black coloured curves), and the ones inferred from the observed population themselves (red coloured curves). The PDF comparison is shown for three parameters, y (left), M_{Lz} (middle) and z_S (right). 39
- 3.9 The figure shows log Bayes factor values, $\log_{10} \mathcal{B}_{UL}^{ML}$, for the evidence for microlensed hypothesis (\mathcal{H}_{ML}) over unlensed hypothesis for varying network SNR, $\rho_{opt}^{net} \in \{8, 13, 20, 32, 50\}$, redshifted lens mass, $M_{Lz} \in \{5, 20, 35, 50, 100\} M_{\odot}$, and impact parameter values, $y \in \{0.1, 1.0\}$ 41

LIST OF FIGURES

- 3.10 Bayes factor study for the microlensed population estimated using the FF and the SNR (ρ), i.e., $\ln \mathcal{B}_{\text{UL}}^{\text{ML}} \approx (1 - FF^2)\rho^2/2$. *Top row:* FF values and the Bayes factor values for the evidence of microlensing over the unlensed hypothesis ($\log_{10} \mathcal{B}_{\text{UL}}^{\text{ML}}$) are shown in the microlens parameter space of the observed population. *Bottom row:* The probability density functions (PDFs) for the microlens parameters are shown for four cases: (i) our prior assumption, (ii) the detected population (selection bias), (iii) the population that is detected and also correctly identified as being microlensed assuming a threshold of $\log_{10} \mathcal{B}_{\text{UL}}^{\text{ML}} > 3 \log_{10}(e)$, and (iv) same as (iii) but with a higher threshold of $\log_{10} \mathcal{B}_{\text{UL}}^{\text{ML}} > 9 \log_{10}(e)$. These threshold values are chosen to investigate various confidence levels in a microlensed event detection while also taking into account the uncertainties related to using the approximation for $\mathcal{B}_{\text{UL}}^{\text{ML}}$ 42
- 3.11 Same as Fig. 3.9, but with added theoretical estimates (cross marks) using Eq. 2.33 for comparison. For nested sampling, the dashed black and red lines have a similar meaning as in Fig. 3.9, representing the threshold values for positive and strong evidence for microlensing, respectively. For the theoretical estimate, these values are depicted using dashed and solid red lines, respectively. 43
- 3.12 The corner plots depict the probable region in the microlensing parameter space for a point lens that can be detected and identified as a microlensed event in the joint network of LIGO–Virgo detectors, assuming the targeted O4 sensitivities. The Bayes factor values of the population and the probability density functions (PDFs) of the microlens parameters are explicitly shown in Fig. 3.10. The panels on the *left* and *right* use different threshold values for $\log_{10} \mathcal{B}_{\text{UL}}^{\text{ML}}$, which is estimated using the expression $\ln \mathcal{B}_{\text{UL}}^{\text{ML}} \approx (1 - FF^2)\rho^2/2$. These threshold values are chosen to explore different confidence levels for claiming a microlensed event detection while also considering the uncertainties associated with this approximation. The contour plot in the 2D space and the red lines in the 1D distributions represent credible regions with quantile values of 16%, 50%, and 84%. 45
- 3.13 Comparison between the $1-\sigma$ regions of the posteriors for the microlensed parameters of event GW200208_130117 (highlighted in red) and the predicted $1-\sigma$ region of the low-confidence microlensed population derived from our population study (highlighted in blue). Additionally, the $1-\sigma$ contour for the predicted high-confidence microlensed population is shown for reference (marked with a black dotted line). 48

LIST OF FIGURES

3.14	<p>Statistical $1\text{-}\sigma$ relative uncertainties in the measurement of the redshifted lens mass $\Delta M_{Lz}/M_{Lz}$ (top panel) and impact parameter $\Delta y/y$ (bottom panel) in the (M_{Lz}, y) plane for a point lens. The white and blue lines correspond to 10% and 100% relative errors. In the white regions, the relative errors are larger than 100%. The system comprises GW150914-like signals with added microlensing effects. The SNR is kept fixed to 50 in the detector network of Hanford, Livingston and Virgo using projected O4 sensitivities.</p>	49
3.15	<p>Comparison of the relative $1\text{-}\sigma$ uncertainties in the (log) redshifted lens mass $\log_{10} M_{Lz}$ and y. The relative uncertainties in the measurement of $\log_{10} M_{Lz}$ are almost always less than that in y.</p>	50
4.1	<p>Test of numerical code shown for an isolated point lens of $100 M_{\odot}$ at $z_d = 0.5$ for a source at $z_s = 2$. The analysis is done for four different values of the impact parameter $y = \beta/\theta_0 = \{0.01, 0.1, 0.3, 1.0\}$. <i>Left:</i> The curves show numerically computed $\tilde{F}(t)$ normalised by a factor of 2π so that its value approaches unity in the no-lens limit (large time delays). <i>Middle and Right:</i> The curves show the comparison between the analytical and the numerically computed frequency-dependent amplification factor $F(f) = F e^{i\theta_F}$. The solid coloured curves have been numerically obtained from the $\tilde{F}(t)$ curves using Eq. 4.3, whereas the dotted black curves denote analytical results (see Eq. 2.8).</p>	58
4.2	<p>Test of numerical code shown for a point mass microlens of $100 M_{\odot}$ at $z_d = 0.5$ in the presence of shear. The source is kept at $z_s = 2$ and the source position is fixed to $(y_1, y_2) = 0.4(\cos(\pi/8), \sin(\pi/8))$. The analysis is done for three different values of the shear $\gamma = \{-0.2, -0.5, -0.8\}$. <i>Left:</i> The curves show numerically computed $\tilde{F}(t)$ (using Eq. 4.4) normalised by a factor of 2π, which ensures that they approach their no-microlens (strong lensing) limit, $\sqrt{\mu} = (1 - \gamma^2)^{-1/2}$, at large time-delay values. <i>Middle and Right:</i> The curves show the comparison between the numerical and the direct evaluation methods for computing the frequency-dependent amplification factor $F(f) = F e^{i\theta_F}$. The solid coloured curves have been numerically obtained from the $\tilde{F}(t)$ curves using Eq. 4.3, while the dotted black curves are obtained via direct (numerical) integration of Eq. 2.5.</p>	60

- 4.3 Test of our numerical code for the case of microlensing of a saddle point macroimage of a source at $z_s = 2$. The analysis is shown for two cases, with and without the presence of a $100 M_\odot$ microlens at $z_d = 0.5$. *Left:* The curves show numerically computed $\tilde{F}(t)$ obtained using Eq. 4.4. The presence of microlens, in this case, leads to a four-microimage configuration (see orange curve in the inset of the leftmost panel). *Middle and Right:* The curves show the comparison between the numerical and the analytical computation of $F(f) = |F|e^{i\theta_F}$ in the geometrical optics limit ($ft_d \gg 1$). The solid coloured curves have been numerically obtained from the $\tilde{F}(t)$ curves using Eq. 4.3, while the dotted black curves are obtained using Eq. 2.7. For the no microlens case, the geometric optics limit is equivalent to the strong lens limit ($ft_d \ll 1$), while in general, the geometrical optics limit is reached at high frequencies $\gtrsim 10^4$ Hz where the $F(f)$ and $F(f)|_{\text{geo}}$ match (see dotted black and orange curves). 62
- 4.4 Illustration of how microlensing can vary with varying convergence (κ), shear (γ), and the direction of shear (ϕ) by numerically computing the amplification factor $F(f)$ for the time-delay function given in Eq. 4.8. We fix the parameters $\{M_{Lz} = 150 M_\odot, y = 1\}$, where we set the redshifts as $\{z_d = 0.5, z_s = 2.0\}$, for all the three cases, and vary the rest three in the three subplots. *Top panel:* variation of $F(f)$ with κ , where we fix the other two parameters as $\{\gamma = 0, \phi = \pi/2\}$, and vary $\kappa \in \{0.0, 0.1, 0.2, 0.3, 0.4, 0.5, 0.6, 0.7, 0.8, 0.9\}$. *Middle panel:* variation of $F(f)$ with the angle ϕ between the shear direction and the source relative to the lens. Here, we fix $\{\kappa = \gamma = 0.3\}$. *Bottom panel:* variation of $F(f)$ with shear value γ with a focus on quadruply-imaged systems. Here, we set $\kappa = 0$ and set $\phi = \pi/2$ 64
- 4.5 Distribution of images formed in quad lens systems in the parameter space of macro-magnification ($|\mu|$) and microlens density (Σ). The black, yellow, red, and blue points represent the image-1 (minima), image-2 (minima), image-3 (saddle points) and image-4 (saddle points), which are ordered according to their time delay values relative to the image-1. The histograms at the top and on the right represent probability density functions for the magnifications $p(|\mu|)$ and microlens density $p(\Sigma_\bullet)$, respectively, for all four images combined. The quad-lensed systems are obtained from a realistically generated mock sample from More & More (2022) assuming projected O4 detector sensitivity. 69

LIST OF FIGURES

- 4.6 Effect of microlens population on the minima type macroimages. The analysis is done for five pairs of the macro amplification and the surface microlens density values as denoted by $(\sqrt{\mu}, \Sigma_{\bullet})_m$ in the left-most panels. These values are drawn from our SIE model (see Table 4.1). *Left:* Normalised $\tilde{F}(t)$ curves, computed numerically using Eq. 4.4. *Middle and Right:* The corresponding amplification factor $F(f) = |F|e^{i\theta_F}$. Each row shows the analysis for all 36 realisations (coloured differently). 72
- 4.7 Same as Fig. 4.6 but for the saddle point macroimages. The analysis is done for two pairs of the macro amplification and the surface microlens density values as denoted by $(\sqrt{\mu}, \Sigma_{\bullet})_s$ in the left-most panels. These values are drawn from our SIE model (see Table 4.1). 73
- 4.8 Microlensing effects observed in the saddle points of image-4 in high-density regions. The absolute part of the amplification factor $F(f)$ is shown as a function of frequency for four different combinations of $\{|\mu|, \Sigma_{\bullet}\}$ (corresponding to maroon stars in Figure 1 of Meena et al. (2022)). There are 50 realizations for each of the four cases, and their respective macro-magnifications and microlens densities are given in the legend. The amplitude of the distortions due to microlensing is negligible despite the high microlens densities owing to the low macro-magnification of these images. 75
- 4.9 Effect of microlensing on strongly lensed GW signals due to a population of microlenses. *Left panel:* The comparison between the Bayes factors in favour of lensing using the posterior overlap analysis is shown for two quadruple-lensed systems (*top* and *bottom* rows), indicating both the strongly lensed systems ("SL only"; represented using black circled markers) and the systems further undergoing microlensing ("SL+ML"; represented using star-shaped red markers). *Middle and Right panels:* A realisation of the (micro-)lensing amplification factor $F(f)$ is displayed for the four macroimages, resulting due to the presence of microlens population in the vicinity of the macroimages. 77

4.10 Effect of microlensing due to a population of microlenses on strongly lensed GW signals. The panels display 1D marginalised posterior distributions for a set of parameters, as labelled on the x -axis, for two systems (along the row). These parameters were utilised to compute the posterior overlap, with the exception that we have condensed the spin parameters to $\{\chi_{\text{eff}}, \chi_p\}$ instead of $\{a_1, a_2, \theta_1, \theta_2\}$ for the ease of representation here. The differently coloured curves correspond to posteriors associated with different images, as shown in Figure 4.9. The dotted curves represent cases with only strong lensing, while the solid curves depict recoveries for signals that undergo both strong lensing and microlensing. The dashed black vertical lines represent the injected values. 78

5.1 Similar to Fig. 2.2 but with added FF contours, illustrating the contrast in trends between the variations of f_{ML} and the FF values when microlensed signals are recovered using unlensed templates. f_{ML} indicates the onset of significant microlensing effects (see Eq. 2.12), whereas FF is related to the Bayes Factor in favour of microlensing against the unlensed hypothesis (see Eq. 2.33). The analysis is conducted within the parameter space relevant to isolated point lenses, focusing on the current-generation ground-based detectors. The f_{ML} values are shown in *Blue - Green colorbar*. Contours at 10 and 1000 Hz denote the rough transition regions, dividing the parameter space into three zones. (i) Long-Wavelength Regime where the GW frequency (f_{GW}) is significantly lower than f_{ML} , meaning $f_{\text{GW}} \ll f_{\text{ML}}$, resulting in minimal interaction between GWs and the microlens, as seen from the light green colored region of the figure. (ii) Wave Dominated Zone: This is the region where $f_{\text{GW}} \sim f_{\text{ML}}$, leading to substantial interference effects on GWs, depicted with light blue color. (iii) Geometrical-Optics Regime: The right-most region in the figure is shown with light coral colour where $f_{\text{GW}} \gg f_{\text{ML}}$. This region is inclusive of milli-lensing and strong-lensing scenarios. *Blue - Green colorbar* represent FF contours where the parameters of the source binary are kept fixed to a non-spinning equal mass binary having $60 M_{\odot}$. For each microlensed WF, the FF values are computed by maximizing its match with the unlensed WFs within the parameter space of component masses and aligned spins. 90

5.2 IMR consistency test results for GW150914-like microlensed injections, highlighting deviations from GR (Q_{GR}), alongside the microlensing Bayes factor ($\log_{10} \mathcal{B}_{\text{UL}}^{\text{ML}}$) for reference. 92

LIST OF FIGURES

5.3	Bias in the parametrised test of GR in GW150914-like microlensed injections for four deviation parameters $\{\delta\chi_0, \delta\chi_4, \delta\alpha_2, \delta\beta_2\}$. Each of the four panels displays the Gaussian sigma values at which GR is excluded (σ_{GR}) in one of the four parametrized parameters, as indicated in the colorbar, within the $\log_{10} M_{\text{Lz}} - y$ parameter space. The larger the magnitude of σ_{GR} , the greater the significance of deviations from GR. For better visualization, we mark the cases with significant deviations ($\sigma_{\text{GR}} > 1$) using a diamond marker instead of the circular markers.	95
5.4	Similar to Fig. 5.3, but with $M_{\text{Lz}} - y$ parameter space suppressed into a one-dimensional representation using f_{ML} (see Eq. 2.12). The figure highlights three scenarios: the long-wavelength regime, the wave-dominated zone, and the geometrical optics regime. The colormap represents $\log_{10} \mathcal{B}_{\text{UL}}^{\text{ML}}$ values for each injection. Transparent markers with black edges indicate cases where $\log_{10} \mathcal{B}_{\text{UL}}^{\text{ML}} < 0$. Dotted-red lines indicate the 1σ and 3σ significance of deviations. Diamond markers indicate significant deviations ($\sigma_{\text{GR}} > 1$), and cases meeting $\log_{10} \mathcal{B}_{\text{UL}}^{\text{ML}} < 1$ (indicating stealth bias) have an added red cross.	96
5.5	Illustration of correlation between \mathcal{Q}_{GR} and $\Delta\mathfrak{M}_{\text{MR}}^{\text{I}}$	98
5.6	IMRCT results for a population of simulated microlensed signals using $\Delta\mathfrak{M}_{\text{MR}}^{\text{I}}$ (Eq. 5.6) as a proxy to quantify deviations in IMRCT. <i>Top panel:</i> Depicts $\Delta\mathfrak{M}_{\text{MR}}^{\text{I}}$ in the $\log_{10} M_{\text{Lz}} - y$ parameter space. Marker colour and size represent the strength of $\Delta\mathfrak{M}_{\text{MR}}^{\text{I}}$. <i>Bottom panel:</i> Depicts $\Delta\mathfrak{M}_{\text{MR}}^{\text{I}}$ as a function of f_{ML} . The colorbar represents Bayes factor values $\ln \mathcal{B}_{\text{UL}}^{\text{ML}}$ estimated using Eq. 2.33.	99
5.7	Same as Fig. 5.3, but for a population of microlensed injections as studied in Sect. 5.3.2.	100
5.8	Same as Fig. 5.4, but for a population of microlensed injections as studied in Sect. 5.3.2.	101
5.9	Shapiro-Wilk normality test for the posterior samples of $\{\delta\hat{\chi}_0, \delta\hat{\chi}_4, \delta\hat{\alpha}_2, \delta\hat{\beta}_2\}$ in our injections. The colorbar shows the corresponding SNR of the events. <i>Left-panel:</i> Shapiro-Wilk test statistic for samples obtained for GW150914-like injections in Sect. 5.3.1 (see also Figs. 5.3 and 5.4). <i>Right-panel:</i> Shapiro-Wilk test statistic for the samples obtained for the study of the microlensed population in Sect. 5.3.2 (see also Figs. 5.7 and 5.8).	102

LIST OF FIGURES

5.10 Gaussian fits to the distribution of σ_{GR} for the microlensed population injections plotted against the variable $x \in \{f_{\text{ML}}/f_{\text{low}}, f_{\text{ML}}/f_{\text{avg}}, f_{\text{ML}}/f_{\text{ISCO}}, f_{\text{ML}}/f_{\text{RD}}\}$ for all the deviation parameters $\{\delta\hat{\chi}_0, \delta\hat{\chi}_4, \delta\hat{\alpha}_2, \delta\hat{\beta}_2\}$ (indicated on top of each panel). A dashed-black line is included at $x = 1$ for reference, representing the characteristic frequency of GW f_{GW}^c which when comparable to f_{ML} gives rise to wave effects. 103

5.11 The distribution of σ_{GR} is analyzed in the context of some selected values of x for different deviation parameters. *Leftmost two panels:* $x = f_{\text{ML}}/f_{\text{avg}}$ is considered with deviation parameters $\{\delta\hat{\chi}_0, \delta\hat{\chi}_4\}$. *Rightmost two panels:* For parameters $\{\delta\hat{\alpha}_2, \delta\hat{\beta}_2\}$, we choose $x = f_{\text{ML}}/f_{\text{ISCO}}$. A dashed-red line at $x = 1$ is included for reference. 104

6.1 Recovered 1D marginalized posterior densities for the microlens parameters M_{Lz} and y for NR injections corresponding to (a) quasi-circular and (b) eccentric signals. The source binary considered is a non-spinning BBH with $\{M_{\text{tot}}/M_{\odot}, q\} = \{80, 1\}$ (see Table 6.1). 111

6.2 Illustration of the preference for microlensed templates over unlensed templates in the recovery of a population of eccentric signals (Sect. 6.2.2). The Bayes factors of microlensed vs. unlensed hypotheses, $\ln \mathcal{B}_{\text{UL}}^{\text{ML}}$, are shown in the parameter space of eccentricity and mass ratio. These values have been computed using Eq. 2.33, as indicated in the colorbar label. Both color and size of the markers are associated with the deviation of Bayes factors from zero, with red indicating a preference for unlensed templates over microlensed templates, while blue signifies the opposite preference. 113

6.3 Variation in the Bayes factors of microlensed vs. unlensed hypotheses, $\ln \mathcal{B}_{\text{UL}}^{\text{ML}}$, with the binary mass, M_{tot} , for our population of eccentric signals (Sect. 6.2.2). The colorbar represents eccentricity. 114

6.4 Bias in microlensing searches due to the presence of eccentricity. The variation in the Bayes factors of (quasi-circular, or QC) microlensed vs. QC unlensed hypotheses, $\ln \mathcal{B}^{\text{QCM}}_{\text{QCUL}}$, is shown a function of eccentricity (e), binary mass (M_{tot}), and mass-ratio (q). The Bayes factors are computed using the WF approximant IMRPhenomXPHM, which is a fully processing WF model utilizing all 15 parameters in the model for a typical quasi-circular BBH system. 115

6.5 Same as Fig. 6.4, but utilizing the WF approximant TEOBResumS, where we keep eccentricity at zero in the recovery. This makes it an 11D model for a quasi-circular aligned-spin BBH system. 116

LIST OF FIGURES

6.6 Recovered 1D marginalized posterior densities for the microlens parameters M_{Lz} and y for TEOBResumS injections corresponding to a non-spinning equal mass BBH of $30 M_{\odot}$ for (a) $e = 0$, (b) $e = 0.3$, and (c) $e = 0.4$ 117

6.7 Breaking the degeneracy between eccentricity and microlensing and resolving bias in microlensing searches by incorporating eccentricity as a parameter in the recovery process using TEOBResumS WF model. The Bayes factor $\log_{10} \mathcal{B}_{\text{QCML}}^{\text{EccUL}}$ represents the evidence in favor of eccentricity vs. microlensing. 118

A.1 A depiction of the surface of integration. 142

A.2 Illustration of the volume V inside the dashed line. The boundary of this region consists of two parts: S_1 lies close to the lens plane but excludes it, while S_2 constitutes the surface of a sphere with a radius R , centered at the observer. \mathbf{n} is the normal vector to the lens plane. [Figure adapted from Takahashi & Nakamura (2003)]. 144

A.3 Excess path length giving rise to the geometric time delay. The line segment SO denotes the path that a GW signal would traverse if unaffected by lensing. In the presence of the lens, the signal deviates from this path and follows STO 149

List of Tables

3.1	Effect of using unlensed templates during the search for microlensed signals. Below, "Total" refers to all the events; "ML" ("UL") refers to the case when microlensed (unlensed) templates are employed for search; N_1 depicts the total number of events with $\log_{10} \mathcal{B}_{\text{UL}}^{\text{ML}} > 3 \log_{10}(e)$, indicating events with mostly positive evidence in favour of microlensing; N_2 depicts the total number of events with $\log_{10} \mathcal{B}_{\text{UL}}^{\text{ML}} > 9 \log_{10}(e)$, indicating events with strong evidence in favour of microlensing. Here we estimate $\log_{10} \mathcal{B}_{\text{UL}}^{\text{ML}}$ using Eq. 2.33. $\epsilon_{\text{UL}}^{\text{ML}}$ denotes the fractional loss of microlensed signals when unlensed templates are used during the search, as defined in Eq. 3.6.	46
4.1	Lens parameter values for minima and saddle points used in simulations. The (κ, γ) are the local convergence and shear values due to the (smooth) macrolens mass distribution. The κ_* is the local convergence due to the mass in compact objects. The μ represents macro–magnification, and Σ_\bullet represents the surface microlens density.	71
4.2	Lens system information, with the lens and source redshifts denoted by z_L and z_S , respectively, are listed here. The macro (μ_{macro}) and smooth (μ_{smooth}) magnifications, the microlens density (Σ_\odot), and the network optimal SNR for both the SL-only case, $\rho_{\text{opt}}^{\text{net}}(h_{\text{SL}})$, and the SL+ML case, $\rho_{\text{opt}}^{\text{net}}(h_{\text{SL+ML}})$, of our chosen GW150914-like source are also tabulated.	73
6.1	Model comparison analysis between the unlensed (UL) and the microlensed (ML) hypotheses for numerical relativity injections corresponding to quasi-circular (or non-eccentric) and eccentric signals. The source binary considered is a non-spinning BBH with a total mass of $M_{\text{tot}} = 80 M_\odot$ and mass ratio $q \in \{1, 2, 3\}$	110

Abbreviations

BH Black Hole

BBH Binary Black Hole

BNS Binary Neutron Star

FF Fitting Factor

GL Gravitational Lens(ing)

GW Gravitational Wave

KAGRA The Kamioka Gravitational Wave Detector

LIGO The Laser Interferometer Gravitational-Wave Observatory

LVK LIGO-Virgo-KAGRA

ML Micro Lens(ing)

NS Neutron Star

GR General Relativity

PSD Power Spectral Density

SNR Signal-to-Noise Ratio

SL Strong Lens(ing)

TGR Tests of General Relativity

WF Waveform

NR Numerical Relativity

Chapter 1

Where two novel predictions of General Relativity meet - Gravitational Lensing of Gravitational Waves

It has been more than a century since Albert Einstein formulated the General Theory of Relativity (GR), one of the most beautiful and accurate theories in all of physics (Einstein 1916). Since its inception, GR has revolutionized our understanding of the universe and has consistently passed the most precise experimental and observational tests with flying colors (Will 2006; Asmodelle 2017). In this thesis, we explore the interplay of some of its major predictions, which are now individually established fields of research, including the existence of black holes (BHs), gravitational lensing (GL), gravitational waves (GWs), and the Shapiro time delay. Elaboratively, we study the prospective scenario of GWs originating from binary black hole (BBH) systems and getting gravitationally lensed due to intervening matter, potentially affected by additional perturbations from compact objects, which can influence the Fermat potential and consequently the Shapiro time delay.

GL is a phenomenon that arises from the interaction between mass inhomogeneities along the line of sight and the propagation of radiation (Einstein, Albert 1936; Zwicky 1937). From a mathematical point of view, the theory of GL is the theory of lightlike geodesics in a Lorentzian manifold, which encodes the information of the gravitational field in spacetime (Perlick 2010). Ever since the initial confirmation of predictions of GL in 1919 through observations of deflection and the subsequent discovery of multiple images in 1979, as seen in the double quasar Q0957+561, GL has played a pivotal role in validating GR, mapping dark matter distributions, measurement of Hubble constant, detection of exoplanets, etc. While GL has been extensively observed in the context of light (Walsh et al. 1979; Soucail et al. 1988), its manifestation in the realm of GWs has yet to be detected (Hannuksela et al. 2019; Abbott, R. and others 2021; The LIGO Scientific Collaboration et al.

2023a), albeit a few interesting candidates (Dai et al. 2020; Liu et al. 2021; Janquart et al. 2023). The detection of lensing signatures in GWs holds immense significance as they will help to constrain fundamental physics (Mukherjee et al. 2020; Goyal et al. 2021), cosmological parameters (Liao et al. 2017; Jana et al. 2023), measure high-redshift merger rates (Mukherjee et al. 2021), and enhance source localization (Hannuksela et al. 2020).

GWs are ripples in the structure of spacetime, stretching and squeezing space as they travel across the universe. From a mathematical point of view, they are described by the metric tensor perturbations, typically expressed as wave solutions to the linearized Einstein equations in the weak-field limit. The existence of GWs was first established observationally in 1981 through the indirect detection of gravitational radiation in the Hulse-Taylor binary pulsar (Hulse & Taylor 1975; Weisberg et al. 1981). More recently, with the detection of GW150914, a new era of direct detection of GWs started that opened a whole new window to probe the Universe. The ground-based GW detector network currently includes three major observatories: Laser Interferometer Gravitational-wave Observatory (LIGO; Aasi et al. 2015), Virgo (Acernese et al. 2015), and the recently added Kamioka GW Detector (KAGRA; Somiya 2012). GWs observed by current ground-based detectors originate from some of the most violent events in the universe, such as compact binary coalescences. Specifically, we focus on GWs originating from binary black hole systems in this thesis. Direct detection of GW signals allows us to test various theories of gravity (e.g., Abbott, B. P. and others 2016; Abbott et al. 2017a, 2019a, 2021b). Observation of GW signals from BBH mergers lets us probe the properties of BHs in the Universe (e.g., Abbott et al. 2021c) and their possible contribution to the dark matter (e.g., Bird et al. 2016). BNS or BH-NS mergers also emit electromagnetic (EM) signal, in addition to GW signal, which becomes an excellent tool for multi-messenger astrophysics (e.g., Poggiani 2019; Margutti & Chornock 2021). So far, a total of 90 GW signals have been detected by LIGO detector network coming from BBH, BNS and BH-NS mergers in the first three observing runs (Abbott et al. 2019b, 2021a; The LIGO Scientific Collaboration et al. 2024; Abbott et al. 2023). Many more such events are expected to be detected in the future observing run (e.g., Abbott et al. 2018) and with new detectors like LIGO-India (Saleem et al. 2022), Cosmic Explorer (CE; Evans et al. 2021), Deci-hertz Interferometer GW Observatory (DECIGO; Kawamura, Seiji et al. 2021), Einstein Telescope (ET; Maggiore et al. 2020), and Laser Interferometer Space Antenna (LISA; Barausse et al. 2020).

Since GWs couple very weakly with matter, there is no absorption and scattering as they move in space. However, since GWs move along the geodesics, their path can still be altered due to GL if they encounter a matter distribution along their path (e.g., Lawrence 1971; Ohanian 1974). For GW signals in the frequency band of current ground-based detectors, $f \in (10, 10^4)$ Hz, GL by galaxy or galaxy cluster scale lenses can lead to the formation of multiple copies of the GW signal, known as the strong lensing (SL)

regime of GL. These strongly lensed images can be (de-)magnified by different factors and arrive with a certain time delay (t_d) between them, ranging from a few hours to several months (e.g., [Oguri 2018](#); [More & More 2022](#)). In such cases, $ft_d \gg 1$ and we can study GL using the *geometric* optics (or ray-optics) approximation (e.g., [Bernardeau 1999](#)). The extra (de-)magnification introduced by GL can introduce bias in the estimation of source distance and binary component masses (e.g., [Broadhurst et al. 2018](#); [Oguri 2018](#); [Smith et al. 2017](#); [Hannuksela et al. 2019](#); [Broadhurst, Tom et al. 2020](#); [Diego et al. 2021](#)). In addition, strong lensing also introduces a constant phase shift in the lensed GW signal ($e^{-in\pi}$ with $n = 0, 1/2, 1$ for type-I, type-II, type-III lensed images; [Dai & Venumadhav 2017](#)). Interestingly, this phase shift can be a useful aid in the search of type-II lensed GWs ([Dai et al. 2020](#); [Ezquiaga et al. 2021](#); [Vijaykumar et al. 2023](#)). In the context of GWs, strong lensing has been investigated in several works recently (e.g., [Liao et al. 2017](#); [Takahashi 2017](#); [Dai & Venumadhav 2017](#); [Haris et al. 2018](#); [Li et al. 2018](#); [Smith et al. 2017](#); [Broadhurst et al. 2018, 2019](#); [Broadhurst et al. 2020](#); [Shan et al. 2021](#); [Ezquiaga et al. 2021](#); [Cremonese et al. 2021, 2023](#); [Çalışkan et al. 2023b](#); [Shan et al. 2023a](#)). Various searches have also been carried out for signatures of strong lensing in the existing LVK data (e.g., [Hannuksela et al. 2019](#); [Smith et al. 2019](#); [Dai et al. 2020](#); [Liu et al. 2021](#); [Abbott, R. and others 2021](#); [The LIGO Scientific Collaboration et al. 2023a](#); [Janquart et al. 2023](#)). However, none of these searches has provided any indications of the existence of a strongly lensed GW signal.

Since both GWs and EM waves follow null geodesics, the GL theory for the two is the same. However, some remarkable differences arise between the GL of GWs and GL of EM waves because of primarily three reasons: (i) GWs are typically coherent and experience minimal interaction (except gravitationally) with the intervening matter, in contrast to the EM waves observed from astrophysical sources, which often undergo multiple absorption and emission processes. (ii) GW strain measurements include amplitude and phase, preserving phase information, while electromagnetic waves are typically characterized by flux. (iii) ground-based detectors operate at $\sim 10 - 10^4$ Hz, whereas observations in the EM domain are conducted in a much higher frequency range $\sim 10^6 - 10^{20}$ Hz; As a result, wave effects can arise in the lensing of GWs due to intervening compact objects in the mass range $[1, 10^5] M_\odot$ owing to the formation of extra images (microimages) of the signal with time-delay values such that $ft_d \sim 1$ (e.g., [Nakamura & Deguchi 1999](#); [Takahashi & Nakamura 2003](#)). In such cases, these multiple lensed (temporally unresolved) images interfere with each other, giving rise to *wave* effects leading to frequency-dependent modulations in the observed signal (e.g., [Deguchi & Watson 1986](#); [Nakamura 1998](#); [Baraldo et al. 1999](#); [Nakamura & Deguchi 1999](#); [Jung & Shin 2019](#); [Seo et al. 2022](#); [Bulashenko & Ubach 2022](#); [Çalışkan et al. 2023c](#)). In the context of the present thesis, we may also refer to these wave-optics effects as *microlensing*. When inferring source parameters, neglecting these frequency-dependent modulations can lead to a biased inference, impacting more

than just the inferred luminosity distance or chirp mass (e.g., [Mishra et al. 2023b](#); [Meena & Bagla 2020](#); [Diego et al. 2019](#); [Kim & Liu 2023](#)). Recently, this has been studied more robustly in [Mishra et al. \(2023b\)](#) as a part of this thesis. Moreover, we also focus on galaxy or galaxy cluster scale lenses, where instead of isolated microlenses, whole populations (made of stars and stellar remnants like NS and BHs) of microlenses can reside. This can lead to complex frequency-dependent microlensing effects in the already strongly lensed GW signal. As shown in [Diego et al. \(2019\)](#) and [Mishra et al. \(2021\)](#), strong lensing magnification is an important parameter in determining the strength of these microlensing effects. However, we also note that the microlensing effects are expected to be negligible in strongly lensed GW signals lensed by galaxy scale lenses with magnification below ten, as shown in [Meena et al. \(2022\)](#).

Furthermore, in GW data analysis, especially for inferring the source properties correctly, it is crucial to employ an accurate waveform model that encapsulates all the physics contained in the signal. By accuracy, we technically mean when systematic biases due to waveform systematics are less than the statistical uncertainties. Otherwise, as mentioned above, these systematic biases can lead to false conclusions and interpretations. For example, the presence of atypical physical effects, such as eccentricity, overlapping signals, etc., can lead to biases in tests of GR involving GWs ([Hu & Veitch 2023](#); [Bhat et al. 2023](#); [Saini et al. 2022](#); [Narayan et al. 2023](#)) when not accounted for. Similarly, we investigate how ignoring microlensing can also affect tests of GR ([Mishra et al., in prep](#)). Furthermore, confidently detecting a microlensed signal presents its own set of challenges. We will explore how other atypical effects, specifically eccentricity, have the potential to bias microlensing searches if not properly accounted for. In addition to these considerations, noise systematics resulting from non-Gaussianity and non-stationarity can further affect parameter inference and model comparison results.

This thesis is organised as follows: In Chapter 2, we lay the foundation for GW implications by explaining the fundamentals of GL. We also discuss the methodologies that will be relevant in the subsequent chapters. Chapter 3 takes a closer look at the isolated point lens model. We delve into its implications on the detection of GWs, its potential to introduce biases in inferred parameters, and the exploration of population characteristics within microlensed signals. We also assess the prospects for correctly identifying these signals as microlensed. Chapter 4 extends the discussion to more intricate microlensing scenarios, such as a microlens or a population of them embedded in a strong lens (macrolens). In Chapter 5, we venture further into the impact of ignoring microlensing effects on tests of GR. Lastly, in Chapter 6, we examine the challenges of model comparison by illustrating how the presence of atypical physical effects, like eccentricity, can introduce biases in microlensing searches.

Chapter 2

Methodology

2.1 Basic Theory of Gravitational Lensing

In this section, we briefly discuss the basics of GL in geometric (Bernardeau 1999) limits (Takahashi & Nakamura 2003). In the geometric optics limit, the lensing of a source at an angular diameter distance D_s due to the presence of an intervening lens/deflector at an angular diameter distance D_d can be described by the so-called gravitational lens equation (assuming small-angle and thin-lens approximation),

$$\mathbf{y} = \mathbf{x} - \boldsymbol{\alpha}(\mathbf{x}) = \mathbf{x} - \nabla_{\mathbf{x}}\psi(\mathbf{x}), \quad (2.1)$$

where $\mathbf{y} = \boldsymbol{\eta}D_d/(\xi_0D_s) \equiv \boldsymbol{\beta}/\theta_0$ and $\mathbf{x} = \boldsymbol{\xi}/\xi_0 \equiv \boldsymbol{\theta}/\theta_0$ represent the projected unlensed source position and the lensed image position on the lens/image plane (measured with respect to the optical axis), respectively (see Fig. 2.1 for visual illustration). Here $\boldsymbol{\eta} = \boldsymbol{\beta}D_s$ and $\boldsymbol{\xi} = \boldsymbol{\theta}D_d$ represent physical distances on the source and image planes, respectively, while $\boldsymbol{\beta}$ and $\boldsymbol{\theta}$ are their corresponding angular positions on the sky. In order to make the lens equation dimensionless, we have chosen an arbitrary length scale ξ_0 (or angular scale θ_0) such that $\xi_0 \equiv \theta_0D_d$. The lens equation simply describes vector addition and is derived purely from geometry where physics is contained in the deflection term $\boldsymbol{\alpha}(\mathbf{x})$, i.e., in the projected 2D lensing potential $\psi(\mathbf{x})$, which determines the deflection as a function of the impact parameter \mathbf{x} on the lens plane. The nonlinearity brought by the deflection term is what leads to the formation of multiple images of a given source. In the context of GWs, this would lead to multiple detections of the same source, which may be separated in the time domain by order of a few minutes to several years (e.g., see Fig. 13 in Oguri 2018). The magnification factor corresponding to these different lensed macroimages (or, equivalently, events) are given as

$$\mu \equiv |\det \mathbb{A}|^{-1} = [(1 - \kappa)^2 - \gamma^2]^{-1}, \quad (2.2)$$

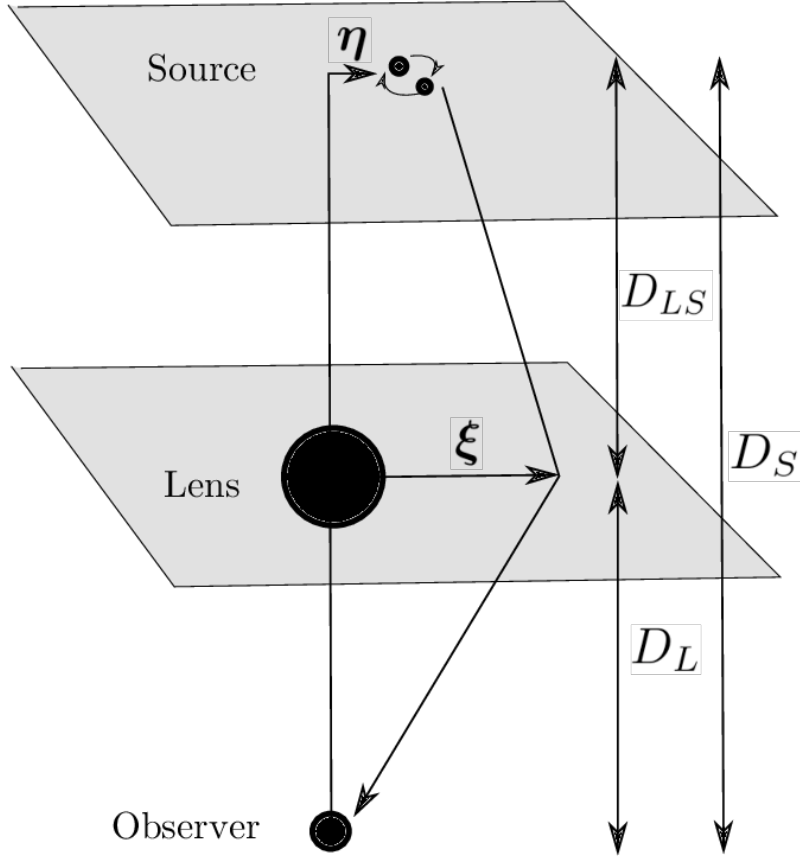


Figure 2.1: Illustration of the lensing configuration in the thin lens approximation. The lensing configuration is described by the source displacement from the line-of-sight η , the angular diameter distance from the observer to the source D_s , to the lens D_d and from lens to the source D_{ds} and by the relative position of the image in the image plane ξ . [Credit: Adapted from Pagano et al. (2020)]

where $\mathbb{A}_{ij} \equiv [\partial y_i / \partial x_j]$ is the Jacobian (matrix) corresponding to the lens equation Eq. 2.1 while κ and γ represent the convergence and shear at the image position, respectively. Both κ and γ are functions of the lens plane coordinate $\mathbf{x} \equiv (x_1, x_2)$.

For a given lensed signal, the corresponding time delay with respect to its unlensed counterpart is given by (see Appendix A.2 for a detailed derivation; Eq. A.50):

$$t_d(\mathbf{x}, \mathbf{y}) = T_s \left[\frac{1}{2} |\mathbf{x} - \mathbf{y}|^2 - \psi(\mathbf{x}) + \phi_m(\mathbf{y}) \right] \equiv T_s \tau_d(\mathbf{x}, \mathbf{y}), \quad (2.3)$$

where $\phi_m(\mathbf{y})$ is a constant independent of lens properties and the factor T_s is the characteristic time delay defined via

$$\frac{T_s}{(1 + z_d)} = \xi_0^2 \frac{D_s}{c D_d D_{ds}} \equiv \frac{2R_{s0}}{c} = \frac{4GM_0}{c^3}. \quad (2.4)$$

Above, z_d is the lens redshift, c is the speed of light, D_{ds} is the angular diameter distance between the source and the lens, and R_{s0} is the Schwarzschild radius corresponding to the mass M_0 . This mass has an Einstein radius ξ_0 if placed on the lens plane. The factor T_s roughly sets the order of the time delay for a given lens system.

2.2 Wave-Optics Effects in Gravitational Lensing

In this section, we provide a brief overview of wave-optics effects in gravitational lensing of GWs. For a more detailed discussion and derivations, readers are encouraged to refer to Appendix A. The formalism of geometrical/ray optics described above is valid as long as the time delay between any two images is sufficiently large compared to the wavelength λ of the signal, i.e., $ft_d \gg 1$, where f is the frequency of the signal. This relation holds in a typical scenario of strong gravitational lensing where different macroimages are formed. GL of GWs due to galaxies or galaxy cluster scale lenses can also be described using the above formalism. However, if the time delay of a lensed signal is of the order of its time period, i.e., when $ft_d \sim 1$ (or, equivalently, $R_{s0} \sim \lambda$), then wave effects are non-negligible, and one has to take diffraction into account. Furthermore, when the source and the deflector are far from the observer, one can use the Huygens-Fresnel principle to analyze the lensing of the incoming plane-wave flux, in which case, every point on the lens plane acts as a secondary source (Huygens point sources), and the amplitude of the signal at each point on the observer plane is the superposition of the signals from these various sources, leading to interference patterns.

For an isolated point mass lens of mass M_L , the above condition ($ft_d \lesssim 1$) translates to, roughly, $M_L \lesssim 10^5 M_\odot (f/\text{Hz})^{-1}$. Therefore, for GWs with frequency in the LIGO band ($10-10^4$ Hz), the mass range where wave effects become significant is $\sim 10-10^4 M_\odot$. This mass range is predominantly responsible for microlensing in the strongly lensed images of a source. In comparison, for electromagnetic (EM) signals with $f \sim 10^6 - 10^{20}$ Hz, the diffraction effects become significant for the mass range $\sim 10^{-15} - 10^{-1} M_\odot$. This is a major difference between the microlensing of EM waves and that of GWs.

In the case of microlensing, one has to consider the corrections arising from wave optics (e.g., Nakamura & Deguchi 1999; Takahashi & Nakamura 2003). If we denote the ratio of the observed lensed and the unlensed GW amplitudes as $F(f, \mathbf{y})$, then the amplification of the lensed signal is given by the diffraction integral (Bernardeau 1999; Goodman 2005) (also see Appendix A.1 for a detailed derivation; Eq. A.33):

$$F(\nu, \mathbf{y}) = \frac{\nu}{i} \int d^2\mathbf{x} \exp[2\pi i \nu \tau_d(\mathbf{x}, \mathbf{y})], \quad (2.5)$$

where

$$\tau_d(\mathbf{x}, \mathbf{y}) = \frac{t_d(\mathbf{x}, \mathbf{y})}{T_s}, \quad \nu \equiv \frac{\xi_0^2 D_s}{D_d D_{ds}} \frac{f}{c} (1 + z_d) = T_s f. \quad (2.6)$$

The definition of dimensionless frequency, ν , and dimensionless time, τ_d , is such that $\nu\tau_d = ft_d$. Since $F(f)$ is a complex-valued function, the total amplification, $|F|$, and phase shift, θ_F , can be obtained through the relation $F(f) = |F|e^{i\theta_F}$. Note that the phase of the lensing amplification factor is determined by the factor ft_d , which sets the threshold for the significance of wave-optics effects. When $ft_d \sim 1$, wave-optics effects become dominant, resulting in frequency-dependent modulations in $F(\omega)$. Conversely, in the geometric optics limit where $ft_d \gg 1$, the phase becomes highly oscillatory, and only the stationary points of t_d contribute to the integral in Eq. 2.5. In that case, wave optics reduces to ray optics and, as a result, the diffraction integral reduces to

$$F(f) \Big|_{\text{geo}} = \sum_j \sqrt{|\mu_j|} \exp(i2\pi ft_{d,j} - i\pi n_j), \quad (2.7)$$

where μ_j and $t_{d,j}$ are, respectively, the magnification factor and the time delay for the j -th image. Also, n_j is the Morse index, with values 0, 1/2, and 1 for stationary points corresponding to minima, saddle points and maxima of the time-delay surface, respectively. As one can see from the above equation, even in the geometric optics limit, gravitational lensing introduces an extra phase, the so-called Morse phase, of $e^{-i\pi/2}$ and $e^{-i\pi}$ in the saddle points and maxima with respect to the minima, respectively (Dai & Venumadhav 2017, Ezquiaga et al. 2021). This phase difference can be used to search for the strongly lensed and multiply imaged GW signals, and to constrain viable lenses (Dai et al. 2020).

2.2.1 Microlensing due to an isolated point-lens

The diffraction integral, Eq. 2.5, can be solved analytically only for some trivial lens models, such as an isolated point-mass lens model (Takahashi & Nakamura 2003). By isolated, we mean the lensing effects are solely due to the point mass in the absence of any appreciable external shear. It has been shown that this model is valid as long as the physical radius of the lens is significantly smaller than the Einstein radius of the lens. In this thesis, the typical Einstein radius of stellar-mass microlenses is $\mathcal{O}(10^{-1})$ pc, which is significantly greater. In the case of an isolated point lens, the lensing potential takes the form $\psi(\mathbf{x}) = \ln|\mathbf{x}|$ (see Sect. A.2.3) and the lensing amplification factor integral in Eq. 2.5

can be solved analytically, resulting in (Takahashi & Nakamura 2003):

$$F(\omega, y) = \exp \left\{ \frac{\pi\omega}{4} + \frac{i\omega}{2} \left[\ln \left(\frac{\omega}{2} \right) - 2\phi_m(y) \right] \right\} \times \Gamma \left(1 - \frac{i\omega}{2} \right) {}_1F_1 \left(\frac{i\omega}{2}, 1; \frac{i\omega y^2}{2} \right), \quad (2.8)$$

where ω represents the dimensionless frequency that depends solely on the redshifted lens mass, M_{Lz} , for a given dimensionful frequency f , expressed as $\omega = 8\pi G M_{Lz} f / c^3$, and $\phi_m(y)$ is a frequency-independent quantity depending only on y , given by $\phi_m(y) = (x_m - y)^2/2 - \ln(x_m)$, where $x_m = (y + \sqrt{y^2 + 4})/2$. ${}_1F_1$ denotes the confluent hypergeometric function, and Γ denotes the gamma function. The scale factor, ξ_0 , has been chosen as equivalent to the Einstein radius of the point mass lens. Therefore, the amplification factor due to an intervening isolated point mass lens can be expressed in terms of only two parameters: the redshifted lens mass (M_{Lz}) and the impact parameter (y).

In the case of the isolated point-mass lens model, the lens equation Eq. 2.1 can also be solved analytically, and the time delay between the two (micro) images is determined only by M_{Lz} and y , given by (Schneider & Weiss 1986; Bernardeau 1999):

$$t_d(M_{Lz}, y) = 4M_{Lz} \left[\frac{y + \sqrt{y^2 + 4}}{2} + \ln \left(\frac{\sqrt{y^2 + 4} + y}{\sqrt{y^2 + 4} - y} \right) \right]. \quad (2.9)$$

By examining how the GW frequency, f_{GW} , compares to the time delay caused by the gravitational lens, t_d , we can categorize $M_{Lz} - y$ space into three distinct regimes (Mishra et al. 2023b; Bondarescu et al. 2023):

- i. *Long-wavelength regime*: In this regime, $f_{GW} \cdot t_d \ll 1$ (or wavelength of GW λ_{GW} is much greater than the Schwarzschild radius of the lens R_{Sch}), leading to only a minimal interaction between the signal and the lens. The amplification factor in this regime can be approximated as (Tambalo et al. 2023):

$$F(\omega, y) \simeq 1 + \frac{\omega}{2} [\pi - i(2 \log(y) - \text{Ei}(i\omega y^2/2))] + \mathcal{O}(\omega^2), \quad (2.10)$$

where $\text{Ei}(z)$ is the exponential integral. Note that, in the leading order, $F(\omega, y) \propto 1 + \omega$. Thus, for $\omega \ll 1$, there is no effect of lensing on signals as $F(\omega, y) = 1$. However, as $f_{GW} \cdot t_d$ approaches unity while still being much less than it, the presence of non-zero ω can lead to a frequency-dependent amplification of the signal. That is why some authors also term this region as the 'amplification' regime (Bondarescu et al. 2023).

- ii. *Wave-dominated zone*: In this zone, $f_{GW} \cdot t_d \sim 1$ (where interference effects will be dominating). This leads to a frequency-dependent modulation of the signal, which, in the case of a point-lens, is governed by Eq. 2.8.

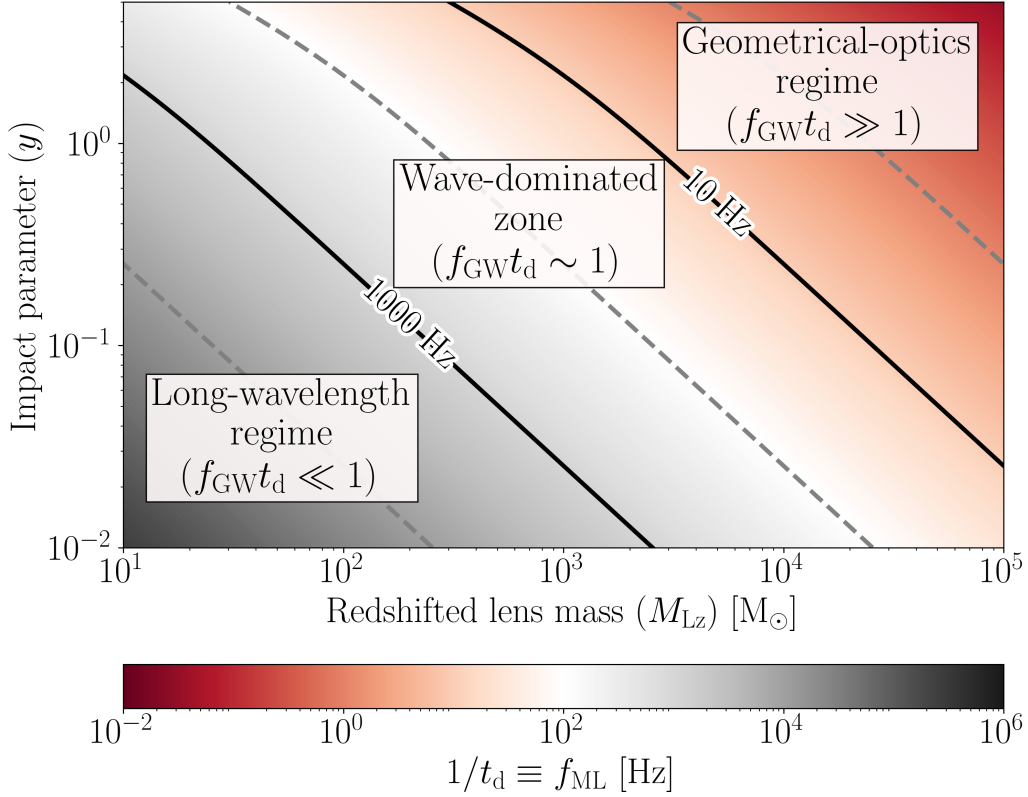


Figure 2.2: Contour plot of the characteristic frequency, f_{ML} , indicating the onset of significant microlensing effects for varying point lens parameters M_{Lz} and y within the LIGO–Virgo sensitivity band (10-10³ Hz). Contours at 10 and 10³ Hz denote the rough transition regions, dividing the parameter space into three zones: (i) *Long-wavelength regime (left-panel)*, where GW frequency f_{GW} is significantly lesser than f_{ML} , i.e., $f_{GW} \ll f_{ML}$, resulting in minimal interaction; (ii) *Wave dominated zone (middle-panel)*: region where $f_{GW} \sim f_{ML}$, leading to significant interference effects on GWs. (iii) *Geometrical-optics regime (right panel)*: region where $f_{GW} \gg f_{ML}$. This region is inclusive of milli-lensing and strong-lensing scenarios.

- iii. *Geometrical Optics regime:* If $f_{GW} \cdot t_d \gg 1$, Eq. 2.7 in the case of an isolated point lens reduces to (Takahashi & Nakamura 2003)

$$F(f) = |\mu_+|^{1/2} - i|\mu_-|^{1/2} e^{i2\pi f t_d}, \quad (2.11)$$

where the magnification of each image is $|\mu_{\pm}| = 1/2 \pm (y^2 + 2)/(2y\sqrt{y^2 + 4})$ and the time delay between the two microimages is given by Eq. 2.9. Physically, Eq. 2.11 implies that in the high-frequency limit, the modifications due to a point lens can be considered as a trivial superposition of two signals which differ only by a constant amplitude, a phase shift of $\pi/2$, and a time-delay value smaller than the chirp time

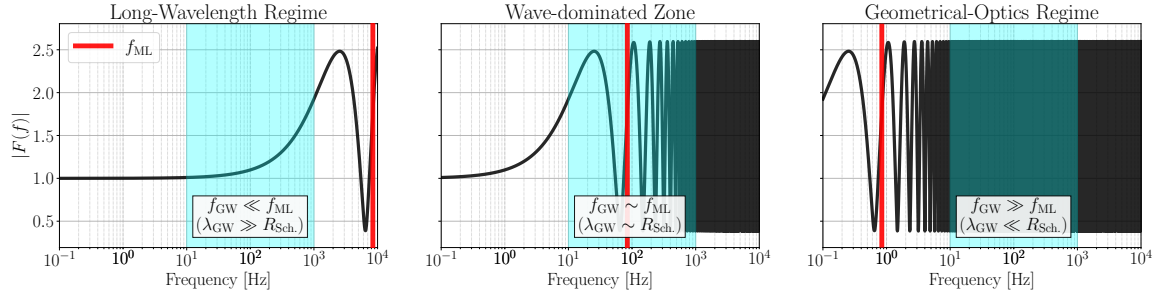


Figure 2.3: Illustration of the nature of microlensing modulations in the three regimes. The absolute part of the amplification factor, $|F(f)|$, is plotted against frequency (black lines). Microlens parameters are fixed at $y = 0.3$ and $M_{Lz}/M_{\odot} \in \{10, 10^3, 10^5\}$, arranged from left to right. The blue-shaded region represents the sensitivity band of current ground-based detectors, approximately 10 – 100 Hz, for reference. The red vertical line indicates the characteristic frequency for the onset of significant microlensing effects, f_{ML} . The panels are divided based on whether $f_{ML} > 1000$ Hz (*left panel*, long-wavelength regime), $f_{ML} \in (10 - 1000)$ Hz (*middle panel*, wave-dominated zone), or $f_{ML} < 10$ Hz (*right panel*, geometrical optics regime).

of the signal¹.

One can explicitly find the characteristic frequency f_{ML} where the wave effects dominate for a given M_{Lz} and y , given by

$$f_{ML}(M_{Lz}, y) \equiv \frac{1}{t_d(M_{Lz}, y)}. \quad (2.12)$$

Considering that current ground-based detectors are primarily sensitive in the band $\sim (10 - 1000)$ Hz, we can illustrate the above regions in the $M_{Lz} - y$ parameter space as shown in Fig. 2.2 (reproduced from (Mishra et al. 2023b)). Here, we roughly demarcate $M_{Lz} - y$ space based on whether $f_{ML} > 1000$ Hz (long-wavelength regime), $f_{ML} \in (10, 1000)$ Hz (wave dominated zone), or $f_{ML} < 10$ Hz (geometrical optics regime). Throughout this thesis, whenever we employ an isolated point lens model in our study, we will primarily focus on the parameter space range depicted in the figure: $M_{Lz}/M_{\odot} \in (10, 10^5)$ and $y \in (0.01, 3)$, unless otherwise stated.

In Fig. 2.3, we illustrate the nature of microlensing modulations in the three regimes. The absolute part of the amplification factor, $|F(f)|$, is plotted against frequency (black lines), where the microlens parameters are fixed at $y = 0.3$ and $M_{Lz}/M_{\odot} \in \{10, 10^3, 10^5\}$,

¹We exclude strong-lensing cases where images are completely separated, requiring the time-delay value to be smaller than the chirp time of the signal.

arranged from left to right. The blue-shaded region represents the sensitivity band of current ground-based detectors, $\sim 10 - 100$ Hz, for reference. In the long-wavelength regime (left panel), we observe solely frequency-dependent amplification, as discussed in relation to Eq. 2.10. Moving to the middle panel, we notice that f_{ML} indeed marks the point where interference effects begin to dominate. This point typically occurs shortly after the first crest and trough of the amplification factor. It is worth pointing out that the characteristic location of f_{ML} (lying between the first two peaks) remains consistent across different lensing parameters. In contrast, the right panel illustrates highly oscillatory modulations that eventually lead to an averaging effect (geometrical optics limit). This behavior eventually results in frequency-independent effects.

2.3 Gravitational Wave Data Analysis

In this thesis, we usually restrict ourselves to GW signals arriving from quasi-circular BBHs and modelled in accordance with GR. The corresponding GW WFs are 15 dimensional, modelled by a set of parameters $\lambda \equiv \{\lambda_{\text{int}}, \lambda_{\text{ext}}\}$, with 8 intrinsic parameters (λ_{int}) that depend only on the properties of the two BHs, and 7 extrinsic parameters (λ_{ext}) that are related to how the source is located and oriented relative to the GW detector (e.g., Husa 2009). The 8 intrinsic parameters comprise the two masses, m_1 and m_2 , and the 6 spin components of the two spin angular momenta, \vec{s}_1 and \vec{s}_2 of the heavier and lighter binary components, respectively. The spin parameters are usually defined in the frame aligned with the total angular momentum \vec{J} , as it remains approximately constant for simple precession cases (Fairhurst et al. 2020). These are - (dimensionless) spin magnitudes, $|\vec{s}_1| = a_1$ and $|\vec{s}_2| = a_2$, the tilt angles between the spin vectors and the orbital angular momentum vector (\vec{L}), $\theta_1 = \arccos(\hat{L} \cdot \hat{s}_1)$ and $\theta_2 = \arccos(\hat{L} \cdot \hat{s}_2)$ (where $\hat{s}_i \equiv \vec{s}_i/|\vec{s}_i|$), the difference between the azimuthal angles of the individual spin vector projections onto the orbital plane, ϕ_{12} , and the azimuthal angle of \vec{L} on its cone about \vec{J} , ϕ_{JL}). The fact that λ_{int} is only 8 dimensional in this case is a consequence of the no-hair theorem, while ignoring electric charge. The rest 7 extrinsic parameters are: 4 spacetime coordinates for the coalescence event (arrival time of the signal as it enters the sensitivity band of the detectors, t_c , luminosity distance to the source, d_L , and two coordinates for specifying its sky location, i.e., right ascension, α , and declination, δ), and 3 Euler angles for the binary's orientation relative to the Earth (inclination, ι , polarisation, ψ , and coalescence phase, ϕ).

A frequency domain GW WF, $\tilde{h}(f)$, for a chirping BBH system can be written in the form:

$$\tilde{h}(f) = A(f; \mathcal{M}, D_{\text{eff}}) e^{-i\Psi(f; \mathcal{M}, \eta, s_1^{\vec{s}_1}, s_2^{\vec{s}_2}) + \phi_o}, \quad (2.13)$$

Here, \mathcal{M} and η represent the chirp mass and the symmetric mass ratio, while $s_{1,2}^{\vec{}}$ denote the binary constituent spin vectors, ϕ_o is a constant phase shift depending upon the coalescence phase ϕ and other extrinsic parameters, while D_{eff} is the effective luminosity distance of the source which is related to the true luminosity distance, d_L , as (Allen et al. 2012):

$$D_{\text{eff}} = d_L \left[F_+^2 \left(\frac{1 + \cos^2 \iota}{2} \right)^2 + F_x^2 \cos^2 \iota \right]^{-1/2} \quad (2.14)$$

where ι is the inclination angle defined in the orbital angular momentum frame between the direction to the observer and the orbital angular momentum axis of the binary system; $F_{+/x} \equiv F_{+/x}(\alpha, \delta, \psi, t_c)$ are the antenna pattern response functions that relate the source orientation to the detector orientation, described by the right ascension and declination of the source, (α, δ) , the trigger time at the detector, t_c , and on the polarisation angle ψ . The induced strain on the detector is then related to the pure polarised components as

$$h = F_+(\alpha, \delta, \psi)h_+ + F_x(\alpha, \delta, \psi)h_x \quad (2.15)$$

Therefore, from Eq. 2.13, the inference of GW phasing is extremely important to study the intrinsic source properties, like their masses and spins, while the extrinsic parameters mainly affect the amplitude of the signal and result in an effective luminosity distance. As already pointed out earlier, since microlensing induces modulations in both the amplitude and phase, Eq. 2.16, it is expected it will affect most of the GW parameters.

2.3.1 Microlensed Waveforms

The lensed GW signal $h_L(t)$ can be obtained from the unlensed signal $h_U(t)$ by using the net lensing amplification factor $F(f; \lambda_L)$ caused by the intervening lens system(s), given as:

$$\tilde{h}_L(f; \{\lambda_U, \lambda_L\}) = F(f; \lambda_L) \cdot \tilde{h}_U(f; \lambda_U), \quad (2.16)$$

where \tilde{h}_L and \tilde{h}_U are the Fourier transforms of the timeseries h_L and h_U , respectively. Here, λ_L denotes the lens-related parameters contributing to the amplification factor, while λ_U represents the parameters of the unlensed GW signal. For an isolated point-mass lens, $\lambda_L \in \{M_{Lz}, y\}$ and the amplification factor $F(f; \lambda_L)$ is given by Eq. 2.8.

Since $F(f; \lambda_L)$ maps frequencies to complex numbers, it causes modulations in both the amplitude and the phase of the signal, thereby affecting the morphology of the WF. As intrinsic parameters are mainly determined from GW phasing, it is highly likely that the intrinsic parameters of a detected microlensed signal will be biased. Similarly, the modulations in the amplitude are likely to affect the extrinsic parameters. Consequently, any analysis disregarding microlensing effects may yield erroneous results. This aspect will be the focus of our investigation in subsequent chapters of this thesis.

2.3.2 Matched-filtering Techniques

The strain amplitude of GW signals is often much smaller than the random noise present in the detectors. However, with the knowledge of physical models describing the dynamics of compact binary mergers and their associated GW WFs, one can employ an optimal filter to devise a very sensitive search methodology to detect such signals, called the *matched-filtering* technique (Sathyaprakash & Dhurandhar 1991). This involves computing correlations between the detector data and millions of WF *templates*, covering the parameter space of possible masses and spins of the binary components, and identifying instances of signal-to-noise ratio (SNR, or ρ) above a certain threshold² (e.g., Usman et al. 2016; Allen et al. 2012).

For detector time-series data $d(t) = h(t) + n(t)$, where $h(t)$ is a GW signal and $n(t)$ is the detector noise, the matched-filter SNR of a WF template $h_{\text{T}}(t, \boldsymbol{\lambda})$ with $d(t)$ is given by

$$\rho = \max_{\{\phi, t\}} \langle d | \hat{h}_{\text{T}} \rangle \equiv \max_{\{\phi, t\}} \frac{\langle d | h_{\text{T}} \rangle}{\sqrt{\langle h_{\text{T}} | h_{\text{T}} \rangle}}, \quad (2.17)$$

where the maximisation is done over phase ϕ and time t , and $\langle \cdot | \cdot \rangle$ is the noise-weighted inner product, called *overlap*, defined as (Usman et al. 2016)³

$$\langle h_1 | h_2 \rangle \equiv 4 \operatorname{Re} \left[\int_{f_{\text{low}}}^{f_{\text{high}}} df \frac{\tilde{h}_1^*(f) \tilde{h}_2(f)}{S_n(f)} \right], \quad (2.18)$$

where $\tilde{h}(f) = \mathcal{F}\{h(t)\}(f) = \int dt h(t) e^{i2\pi ft}$ and $S_n(f)$ is the single-sided PSD of the detector noise. Note that since extrinsic parameters primarily affect the signal by introducing a constant phase shift and amplitude, they need not be incorporated explicitly; they are implicitly accounted for during the phase maximization process⁴. In this thesis, we mostly use the target PSDs for the fourth observing run (O4) of the advanced LIGO and Virgo detectors (Abbott et al. 2018)⁵.

²Current (network) SNR threshold used in the search of GW signals in the LIGO–Virgo collaboration is 8.

³In writing this, we assume that noise is stationary, i.e., $\overline{\tilde{n}(f)^* \tilde{n}(f')} = (1/2) S_n(|f|) \delta(f - f')$.

⁴However, this is not always true. For example, in the presence of higher-order modes, the effect of coalescence phase cannot be absorbed into a constant phase shift.

⁵For LIGO detectors, we used the PSD given in https://dcc.ligo.org/public/0165/T2000012/002/aligo_04high.txt. For Virgo, we used the PSD available at https://dcc.ligo.org/public/0165/T2000012/002/avirgo_04high_NEW.txt.

Without loss of generality, one can also assume the expected value of noise is zero, i.e., $\overline{n(t)} = 0$, in which case the expected value of the SNR of a signal $h(t)$ using a template $h_T(t)$ is given by

$$\bar{\rho} = \max_{\{\phi, t\}} \langle h | \hat{h}_T \rangle = \|h\| \mathfrak{M}(\hat{h}, \hat{h}_T) = \|h\| \cos \theta, \quad (2.19)$$

where we denote the norm as $\|h\| \equiv \sqrt{\langle h | h \rangle}$, and θ is the angle between h and h_T in the Hilbert space of GW signals; the term

$$\mathfrak{M}(\hat{h}, \hat{h}_T) \equiv \max_{\{\phi, t\}} \langle \hat{h} | \hat{h}_T \rangle \quad (2.20)$$

is referred to as *match*⁶, defined as the overlap maximised over time and phase. In the context of GW searches, the function $\mathfrak{M}(\lambda_T) \equiv \langle \hat{h} | \hat{h}_T(\lambda_T) \rangle$ is called the *ambiguity function*, where the vector $\lambda_T \subseteq \lambda$ represents parameters of the template vector and $\lambda_T \in \mathcal{T}$, where \mathcal{T} is the discrete set of parameter grid employed for searching (e.g., [Creighton & Anderson 2011](#); [Droz 1999](#)). From Eq. 2.19, one can see that the optimal value of SNR, ρ_{opt} , is simply $\|h\|$. However, in realistic scenarios, the expected value of the observed matched-filter SNR will be some fraction of the optimal SNR. This fraction is called the (effective) *fitting factor* ([Ajith et al. 2014](#); [Canton & Harry 2017](#)),

$$\text{FF} = \max_{\lambda_T, t, \phi} \mathfrak{M}(\lambda_T) = \frac{\bar{\rho}}{\rho_{\text{opt}}}, \quad (2.21)$$

which is the maximum match obtained among all the templates. The FF value then corresponds to the match with the nearest template to the actual signal (one that subtends the minimum angle to it). The reason why $\text{FF} < 1$ is primarily three folds - (i) parameter grid of the templates are discretely spaced. (ii) limited dimensionality of the template WFs: implying the template signals usually live on a sub-manifold of the actual signal. Hence, the signal can only have a fraction of the projection along that subspace. (iii) incomplete model of the template WFs (or some missing physics): in addition to the previous point, if the true WF contains some physics not incorporated in our template WFs, such as microlensing, eccentricity, non-GR effects, etc., the non-inclusion of these physical effects in the template WFs can further decrease the FF value.

A FF value of x ensures that the maximum fractional loss of possible astrophysical signals is not more than a factor of $(1 - x^3)$, assuming the rate of mergers $R \propto d_L^3$ and that $\rho \propto d_L^{-1}$. The template banks typically used for searching GW signals from compact binary coalescences (CBCs) have a minimum FF threshold of around 97% for WFs within the parameter space, which implies no more than $\sim 10\%$ of possible astrophysical signals are lost due to the discrete nature of the bank.

⁶Unless otherwise noted, the overlap is always maximised over time t , phase ϕ . A natural measure of deviation between any two WFs can also be defined using *mismatch*, $\mathfrak{MM} \equiv 1 - \mathfrak{M}$.

2.3.3 Simulated Injections

To study the effect of microlensing on the inference of GW signals, we consider simulated BBH events, called *injections* (or simulated observations). These injections are done in the detector network of LIGO-Virgo with the projected O4 sensitivity⁷ (Abbott et al. 2018). To avoid noise systematics, i.e., biases due to specific noise realizations, we usually do not include noise in our injections unless otherwise noted (assuming the realisation of Gaussian noise that yields zero noise in the data containing the signal). Put simply, the posteriors obtained in our zero-noise scenario can be viewed as the expected values derived from numerous posteriors resulting from injections in zero-mean Gaussian noise, providing a robust approach for analysing microlensing effects.

To generate injections, whether unlensed or microlensed, we utilize the publicly available package developed by the author, named GWMAT:Gravitational Waves Microlensing Analysis Tools⁸ (Mishra, A., in prep.).

2.3.4 Bayesian Inference

Here, we give a brief overview of the Bayesian inference in GW astronomy. For a more comprehensive discussion, the reader is referred to (Thrane & Talbot 2019; Christensen & Meyer 2022).

Parameter Estimation

In GW astronomy, it is crucial to infer the parameters of a GW signal with precision. We usually adopt Bayesian approach to statistically infer the GW parameters λ , where the primary aim is to construct a posterior distribution

$$p(\lambda|d), \tag{2.22}$$

which is the probability density function for the continuous variable λ given the data d . Since it is a probability density, it satisfies the condition

$$\int_{\mathcal{V}} p(\lambda|d)d\lambda = 1, \tag{2.23}$$

⁷For LIGO detectors, we used the PSD given in https://dcc.ligo.org/public/0165/T2000012/002/aligo_04high.txt. While for Virgo, we used the PSD available at https://dcc.ligo.org/public/0165/T2000012/002/avirgo_04high_NEW.txt.

⁸<https://git.ligo.org/anuj.mishra/gwmat>

where \mathcal{V} denotes the volume of the parameter space under consideration, and $p(\boldsymbol{\lambda}'|d)d\boldsymbol{\lambda}'$ denotes the probability that the true value of $\boldsymbol{\lambda}$ is between $(\boldsymbol{\lambda}', \boldsymbol{\lambda}' + d\boldsymbol{\lambda}')$. Using Bayes theorem, the posterior distribution can be simply written as:

$$p(\boldsymbol{\lambda}|d) = \frac{\mathcal{L}(d|\boldsymbol{\lambda})\pi(\boldsymbol{\lambda})}{\mathcal{Z}} = \frac{\mathcal{L}(d|\boldsymbol{\lambda})\pi(\boldsymbol{\lambda})}{\int_{\mathcal{V}} d\boldsymbol{\lambda}' \mathcal{L}(d|\boldsymbol{\lambda}')\pi(\boldsymbol{\lambda}')} \propto \mathcal{L}(d|\boldsymbol{\lambda})\pi(\boldsymbol{\lambda}). \quad (2.24)$$

Here, $\mathcal{L}(d|\boldsymbol{\lambda})$ is the likelihood function of the data given the parameters $\boldsymbol{\lambda}$, $\pi(\boldsymbol{\lambda})$ is the prior distribution for $\boldsymbol{\lambda}$ (our prior belief), and the denominator \mathcal{Z} is a normalization factor called the *evidence*, or *marginal likelihood*. Note that we use \mathcal{L} to denote the likelihood instead of using p , because it is not a probability density, i.e., $\int d\boldsymbol{\lambda}' \mathcal{L}(d|\boldsymbol{\lambda}') \neq 1$. The likelihood function is something that we choose, and is a description of the measurement. By writing down a likelihood, we implicitly assume a noise model. For GW astronomy, we typically assume a Gaussian-noise model, where the likelihood function takes the form:

$$\mathcal{L}(d|\boldsymbol{\lambda}) = \frac{1}{2\pi\sigma^2} \exp\left(-\frac{1}{2} \frac{\|d - \mu(\boldsymbol{\lambda})\|^2}{\sigma^2}\right). \quad (2.25)$$

Here, $\mu(\boldsymbol{\lambda})$ denotes the template GW WF given parameters $\boldsymbol{\lambda}$, σ is the detector noise, and $\|d - \mu(\boldsymbol{\lambda})\|^2 = \langle d - \mu(\boldsymbol{\lambda}) | d - \mu(\boldsymbol{\lambda}) \rangle$. Note that π with no parentheses and no subscript is the mathematical constant, not a prior distribution. Throughout this work, the prior functions $\pi(\boldsymbol{\lambda})$ utilized are standard functions used by the LVK collaboration in analysing real events. Specifically, for estimating chirp mass and mass-ratio, we adopt a prior that is uniform in component masses. Additionally, angles associated with component spin vectors and all Euler angles are assumed to be uniformly distributed in space, indicating random orientation without preference. The magnitude of the component spin vectors is also assumed to have a uniform prior. Furthermore, the distance prior is uniform in comoving volume.

In this thesis, we conduct parameter estimation (PE) employing the nested sampling algorithm (Skilling 2006), which directly computes evidence and is therefore crucial for model comparison studies. Specifically, we utilize the Dynesty sampler (Speagle 2020) as implemented in the Bilby package (Ashton et al. 2019, 2020) to obtain $p(\boldsymbol{\lambda}|d)$ and \mathcal{Z} for our injections.

Model Comparison

In this section, we discuss how we can compare different models in analysing a given data d . To compare any two models, say \mathcal{H}_A and \mathcal{H}_B , we can use Bayes' theorem to calculate the *odds ratio*, defined as (Deutsch 1999):

$$\mathcal{O}_A^B \equiv \frac{p(\mathcal{H}_B|d)}{p(\mathcal{H}_A|d)} = \frac{p(d|\mathcal{H}_B)}{p(d|\mathcal{H}_A)} \cdot \frac{p(\mathcal{H}_B)}{p(\mathcal{H}_A)}. \quad (2.26)$$

The higher the value of \mathcal{O}_A^B , the stronger is the support in favour of model \mathcal{H}_B over model \mathcal{H}_A . Under the assumption that all models are equally likely a priori ⁹, we set $p(\mathcal{H}_A) = p(\mathcal{H}_B)$ in Eq. 2.26. The odds ratio then reduces to the Bayes factor, which is simply the ratio of the evidences (\mathcal{Z}) of the two models:

$$\begin{aligned} \mathcal{O}_A^B = \mathcal{B}_A^B &\equiv \frac{p(d|\mathcal{H}_B)}{p(d|\mathcal{H}_A)} \\ &= \frac{\int_{\mathcal{V}_{\lambda_{\mathcal{H}_B}}} d\lambda_{\mathcal{H}_B} \mathcal{L}(d|\lambda_{\mathcal{H}_B}) p(\lambda_{\mathcal{H}_B}|\mathcal{H}_B)}{\int_{\mathcal{V}_{\lambda_{\mathcal{H}_A}}} d\lambda_{\mathcal{H}_A} \mathcal{L}(d|\lambda_{\mathcal{H}_A}) p(\lambda_{\mathcal{H}_A}|\mathcal{H}_A)} \equiv \frac{\mathcal{Z}_{\mathcal{H}_B}}{\mathcal{Z}_{\mathcal{H}_A}}, \end{aligned} \quad (2.27)$$

where $\lambda_{\mathcal{H}_A}$ and $\lambda_{\mathcal{H}_B}$ are the model parameters of \mathcal{H}_A and \mathcal{H}_B hypotheses, and $\mathcal{V}_{\lambda_{\mathcal{H}}}$ represents the parameter space volume. It is rather convenient to work with the logarithm of the *Bayes factors*, which can be expressed as:

$$\log_{10} \mathcal{B}_A^B = \log_{10} \mathcal{Z}_{\mathcal{H}_B} - \log_{10} \mathcal{Z}_{\mathcal{H}_A}. \quad (2.28)$$

When $\log_{10} \mathcal{B}_A^B$ is large ($\log_{10} \mathcal{B}_A^B > 1$), we say \mathcal{H}_B is strongly preferred over \mathcal{H}_A . When the value is negative or only slightly positive ($\log \mathcal{B}_A^B \lesssim 0.5$), \mathcal{H}_B is discarded in favour of the \mathcal{H}_A .¹⁰ It is important to note that Bayes Factor inherently embodies Occam's principle of parsimony, which favours less complicated models, i.e., models with fewer parameters are more preferred among similarly performing models. In other words, while a more complicated model will give a better fit and higher likelihood values, the evidence of the model is reduced by the smaller prior mass within the support of the likelihood.

For the search of microlensed signals due to a point-mass lens¹¹, we shall invoke at least three hypotheses: (i) $\mathcal{H}_{\text{noise}}$: the data contains only noise, (ii) \mathcal{H}_{UL} : the data contains an unlensed signal (modelled by the parameters $\lambda_{\mathcal{H}_{\text{UL}}}$) in addition to noise, and (iii) \mathcal{H}_{ML} : data contains a microlensed signal (modelled by the parameters $\lambda_{\mathcal{H}_{\text{ML}}}$) in addition to noise. $\lambda_{\mathcal{H}_{\text{ML}}}$ is described using two additional (microlensing) parameters, M_{Lz} and y , to the unlensed hypothesis, i.e., $\lambda_{\mathcal{H}_{\text{ML}}} \equiv \{\lambda_{\mathcal{H}_{\text{UL}}}, M_{Lz}, y\}$. Thus, in case of BBH signals, $\lambda_{\mathcal{H}_{\text{UL}}} \in \mathbb{R}^{15}$ and $\lambda_{\mathcal{H}_{\text{ML}}} \in \mathbb{R}^{17}$. Using Eq. 2.28, we can compare microlensed vs unlensed

⁹In case of model comparison studies between microlensed and unlensed hypotheses, this assumption makes sense only for the initial set of searches. However, based on such results, an informed prior on models can be used, which should incorporate our belief that the number of microlensed signals is much smaller than the unlensed signals.

¹⁰This interpretation is based on Jeffrey's scale (Deutsch 1999).

¹¹Since analytical solutions for the lensing amplification factor are currently only available for simple systems, such as an isolated point-mass lens, microlensing searches typically rely on this model when searching for microlensed signals

hypothesis as follows:

$$\log_{10} \mathcal{B}_{\text{UL}}^{\text{ML}} = \log_{10} \mathcal{Z}_{\mathcal{H}_{\text{ML}}} - \log_{10} \mathcal{Z}_{\mathcal{H}_{\text{UL}}} = \log_{10} \mathcal{B}_{\text{noise}}^{\text{ML}} - \log_{10} \mathcal{B}_{\text{noise}}^{\text{UL}}, \quad (2.29)$$

One can obtain the values for $\log \mathcal{B}_{\text{noise}}^{\text{UL}}$ and $\log \mathcal{B}_{\text{noise}}^{\text{ML}}$ by running a nested sampler with hypotheses \mathcal{H}_{ML} and \mathcal{H}_{UL} , respectively, using Bilby. The second equality in the above equation stems from the fact that the evidence computation for the "noise model", $\mathcal{Z}_{\text{noise}}$, does not depend upon the WF models being compared but only on the data segment and the assumed estimate of the noise PSD profile of the detectors. Therefore, $\mathcal{Z}_{\text{noise}}$ will result in equivalent values for both \mathcal{H}_{ML} and \mathcal{H}_{UL} models given the same settings for the likelihood evaluation and other sampler settings.

In the high-SNR limit, when most of the posterior volume is confined around a particular value¹², i.e., when the posterior density is highly peaked around the posterior mode, the evidence can be approximated using the Laplace approximation and the resulting Bayes factor can be written as (Cornish et al. 2011; Vallisneri, Michele 2012):

$$\ln \mathcal{B}_A^{\text{B}} \approx \frac{1}{2}(\rho_{\mathcal{H}_B}^2 - \rho_{\mathcal{H}_A}^2) + \ln \mathcal{O}_{\mathcal{H}_A}^{\mathcal{H}_B} \quad (2.30)$$

where $\rho_{\mathcal{H}}$ denotes the recovered SNR under the hypothesis \mathcal{H} , \mathcal{O} represents the Occam's factor defined as the ratio of the posterior volume ΔV to the prior volume V , i.e., $\mathcal{O} \equiv \Delta V/V \propto \sqrt{|F^{-1}|}$, where F is the *Fisher information matrix*. If \mathcal{H}_B is the true model which we recover assuming \mathcal{H}_A , we will be able to recover only a fraction of the true SNR $\rho_{\mathcal{H}_B}$. Using Eq. 2.21, we can write:

$$\rho_{\mathcal{H}_A} = FF \rho_{\mathcal{H}_B}. \quad (2.31)$$

Substituting the above equation into Eq. 2.30, we get

$$\ln \mathcal{B}_A^{\text{B}} \approx \frac{1}{2}(1 - FF^2)\rho_{\mathcal{H}_B}^2 + \ln \mathcal{O}_{\mathcal{H}_A}^{\mathcal{H}_B}. \quad (2.32)$$

If one further ignores the Occam's factor term, we obtain a computationally efficient method for estimating Bayes Factors using only the FF values:

$$\ln \mathcal{B}_A^{\text{B}} \approx \frac{1}{2}(1 - FF^2)\rho_{\mathcal{H}_B}^2. \quad (2.33)$$

This expression proves particularly useful when analysing a population of signals, where conducting parameter estimation would be prohibitively computationally expensive.

¹²which coincides with the true value when the recovery model is the true model describing the signal.

To run parameter estimation with model \mathcal{H}_{ML} assuming isolated-point mass lens for microlensing, we employ a custom frequency domain source model¹³, available through the Python/Cython package GWMAT (Mishra, A., in prep.), which incorporates the two microlensing parameters M_{Lz} and y in addition to the standard 15 BBH parameters. The source model provides an efficient computation of the lensing amplification factor for an isolated-point mass lens, utilizing both Eq. 2.8 and Eq. 2.11. Since the evaluation of hypergeometric function in Eq. 2.8 can be time-consuming, we precompute this part and read the data while doing PE. Meanwhile, the geometric optics part is computed using Cython, giving the power of \mathcal{C} . On average, a microlensed parameter estimation run takes about 40% extra time than an unlensed parameter estimation run. While inferring microlens parameters, we assume a log-uniform prior in M_{Lz} and a linear power-law prior for y , i.e., $p(y) \propto y$. This linear relationship comes from geometry and isotropy (Lai et al. 2018). To wit, the probability of a source having an impact parameter y relative to a microlens will be proportional to the area of a ring of infinitesimal width having radius y , i.e., $p(y)dy = 2\pi y dy$.

2.3.5 Fisher Information formalism

In this section, we briefly discuss the application of Fisher Information Matrix formalism, often referred to as Fisher analysis, to quantify the statistical uncertainties associated with parameter measurements due to correlations with other parameters (Finn 1992; Vallisneri 2008; Borhanian 2021; Antonelli et al. 2021; Mukherjee et al. 2022).

Under the assumption that noise, $n(t) = d(t) - h(t)$, is stationary and Gaussian with zero mean, the (log) likelihood of observing a specific data stream realisation can be written as (see Eq. 2.25):

$$\log \mathcal{L}(D|\boldsymbol{\lambda}) \propto -\frac{1}{2} \langle (D - H(\boldsymbol{\lambda}) | D - H(\boldsymbol{\lambda})) \rangle, \quad (2.34)$$

where D and H are Fourier transforms of d and h , respectively, and $\boldsymbol{\lambda}$ is the parameter vector that determines a particular WF. Next, the formalism exploits the fact that for a sufficiently high SNR, the deviation in strain can be approximated as a linear function of parameter errors around the true value at the leading order, called linear signal approximation (LSA) (Finn 1992). Since the best-fit parameter $\boldsymbol{\lambda}_{\text{best-fit}}$ can be assumed to be a perturbation from the true parameter $\boldsymbol{\lambda}_{\text{true}}$ in the presence of noise, one can write $\boldsymbol{\lambda}_{\text{best-fit}} = \boldsymbol{\lambda}_{\text{true}} + \Delta\boldsymbol{\lambda}$. Thus, using LSA, the WF model in the vicinity of the best-fit

¹³https://git.ligo.org/anuj.mishra/gwmat/-/blob/main/gwmat/bilby_custom_FD_source_models/microlensing_source.py

parameters can be written as

$$h(t; \boldsymbol{\lambda}_{\text{best-fit}}) \approx h(t; \boldsymbol{\lambda}_{\text{true}}) + \partial_i h(t; \boldsymbol{\lambda}_{\text{true}}) \Delta \lambda^i, \quad (2.35)$$

where we make use of the Einstein-summation convention and $\partial_i \equiv \partial/\partial \lambda_i$. The expression is valid for $|\Delta \lambda^i| \ll 1$. Substituting Eq. 2.35 into Eq. 2.34, one obtains

$$-2 \log p(D|\boldsymbol{\lambda}) = (\Delta \lambda^i - \Delta \lambda_{\text{noise}}^i) \Gamma_{ij} (\Delta \lambda^j - \Delta \lambda_{\text{noise}}^j), \quad (2.36)$$

$$\Delta \lambda_{\text{noise}}^i = (\Gamma^{-1})^{ij} \langle \partial_j h | n \rangle \quad (2.37)$$

where Γ_{ij} is the Fisher matrix defined by

$$\Gamma_{ij} = \langle \partial_i h | \partial_j h \rangle. \quad (2.38)$$

Defining the statistic $\widehat{\Delta \lambda}^i = \Delta \lambda_{\text{noise}}^i$, one finds

$$\mathbb{E}[\widehat{\Delta \lambda}^i] = 0, \quad \text{Cov}(\widehat{\Delta \lambda}^i, \widehat{\Delta \lambda}^j) \equiv \Sigma = (\Gamma^{-1})^{ij} + \mathcal{O}(\rho^{-1}). \quad (2.39)$$

The diagonal and off-diagonal elements of the covariance matrix Σ denote the variances and covariances of the parameters, respectively, due to the uncertainty introduced by the detector noise and give 1σ -uncertainty estimates via $\sigma_{\lambda_i} = \sqrt{\Sigma_{ii}}$.

Note that the validity of Fisher analysis demands a high-SNR where LSA is valid. Furthermore, the Fisher matrix needs to be 'well-conditioned' for invertibility, which could even be compromised due to the limited arithmetic precision. See, e.g., the excellent discussion in Ref. [Vallisneri \(2008\)](#) of these issues related to Fisher analysis.

Chapter 3

Exploring the Impact of Microlensing on Gravitational Wave Signals: Biases, Population Characteristics, and Prospects for Detection

In this chapter, we investigate the impact of microlensing on GW signals in the LIGO–Virgo sensitivity band. Microlensing caused by an isolated point lens, with (red-shifted) mass ranging from $M_{Lz} \in (1, 10^5) M_{\odot}$ and impact parameter $y \in (0.01, 5)$, can result in a mismatch exceeding even 30% with their unlensed counterparts. When $y < 1$, it strongly anti-correlates with the luminosity distance, enhancing the detection horizon and SNR. Biases in inferred source parameters are assessed, with in-plane spin components being the most affected intrinsic parameters. The luminosity distance is often underestimated, while sky-localisation and trigger times are mostly well-recovered. A study of a population of microlensed signals due to an isolated point lens primarily reveals: (i) using unlensed templates during the search causes fractional loss (20% to 30%) of potentially identifiable microlensed signals; (ii) the observed distribution of y challenges the notion of its high improbability at low values ($y \lesssim 1$), especially for $y \lesssim 0.1$; (iii) Bayes factor analysis of the population indicates that certain region in $M_{Lz} - y$ parameter space have a higher probability of being detected and accurately identified as microlensed. Notably, the microlens parameters for the most compelling candidate identified in previous microlensing searches, GW200208_130117, fall within a 1-sigma range of the aforementioned higher probability region. Identifying microlensing signatures from $M_{Lz} < 100 M_{\odot}$ remains challenging due to small microlensing effects at typical SNR values. Additionally, we also examined how microlensing from a population of microlenses influences the detection of strong lensing signatures in pairs of GW events, particularly in the *posterior-overlap* analysis.

3.1 Introduction

Since microlensing can introduce complex frequency-dependent features in the observed GW signal, it is important to understand and model these lensing features so that we can properly construct the unlensed GW signal and deduce the properties of the microlens itself. Previous studies (e.g., [Cao et al. 2014](#); [Lai et al. 2018](#); [Christian et al. 2018](#); [Urrutia & Vaskonen 2021](#); [Basak et al. 2022](#); [Bondarescu et al. 2023](#)) have made valuable contributions in studying the microlensing effects caused by isolated point-lenses. However, most of the aforementioned studies examined only a restricted microlens or GW parameter space. For example, the region $y < 0.1$ has not been studied well due to its low improbability. However, as we show below, our findings demonstrate that selection bias during detection amplifies the probability density in this region due to the extended detection horizon for such signals. These results are consistent with previous studies conducted by [Takahashi & Nakamura \(2003\)](#) and more recently by [Bondarescu et al. \(2023\)](#). Moreover, due to the computational expense involved in performing a full parameter estimation run, only a few studies have been conducted in this direction (e.g., [Christian et al. 2018](#); [Abbott, R. and others 2021](#)). Furthermore, some studies only worked primarily in geometrical optics for simplicity. Additionally, most studies lack a comprehensive population-wide study that could provide a broader understanding of the phenomenon and make scientific predictions. These limitations pose challenges to gaining a thorough understanding of the phenomenon. Hence, more detailed studies are required to further improve our understanding of microlensing effects in GW signals.

In our current work, we aim to address these gaps by studying the effect of microlensing in a more exhaustive manner: utilizing tools and techniques such as fitting factor, Bayesian analysis and Fisher-information matrix. We begin by conducting an FF-based study to investigate the detectability of microlensed signals and demonstrate how the non-inclusion of microlensing effects during the search can affect the observed SNR. Furthermore, we examine how the presence of isolated microlenses can enhance the true source SNR. Next, we explore the bias in the parameter estimation of GW source parameters when the true signal is microlensed due to an isolated point lens, but the recovery model assumes the usual unlensed signal without incorporating any microlensing effects. To provide a broader perspective, we perform a population study of microlensed signals, inferring the properties of the population and making predictions about the most likely microlensing parameter space that will be detected and correctly identified as a microlensed signal. Additionally, we investigate the identification of microlensed signals using a Bayes factor study, considering various scenarios such as varying SNR values, lens masses, and impact parameter values. Finally, we discuss the crucial aspect of how microlenses in lensing galaxies can affect strongly lensed signals, thereby influencing the

searches for strongly lensed GW signals. Through these comprehensive analyses, we aim to shed light on the multifaceted nature of microlensing effects and their implications for GW signals.

This chapter is mainly based on the paper [Mishra et al. \(2023b\)](#), and is organised as follows. Inspired by recent searches of microlensing, we focus on the point lens model in Sections 3.2–3.5. In Sect. 3.2, we study the effect of individual microlenses on the detection of GW signals. In Sect. 3.3, we study the bias in the estimation of source parameters of observed microlensed GW signals when recovered using the usual unlensed WF model. In Sect. 3.4, we study the properties of a mock microlensed population. In Sect. 3.5, we study the challenges in identifying microlensing signatures in real data. In Sect. 3.7, we conclude this chapter and discuss its implications. Throughout this chapter, we use $H_0 = 70 \text{ km s}^{-1} \text{ Mpc}^{-1}$, $\Omega_m = 0.3$, and $\Omega_\Lambda = 0.7$ to estimate various cosmological quantities. We focus exclusively on transient GW signals originating from compact binary coalescence (CBCs). All mass-related quantities, including M_{Lz} , are consistently reported in solar mass units (M_\odot).

3.2 Effect of microlensing on the detection of GWs: Matched-filtering Analysis

As discussed in Sect. 2.3.2, there are several reasons why we anticipate $\text{FF} < 1$ (or $\bar{\rho} < \bar{\rho}_{\text{opt}}$) in practical scenarios. In the context of microlensing, our objective is to determine the reduction in SNR resulting from the exclusion of this physical effect in the search process. Motivated by real GW searches, we use 4D aligned-spin template WFs to recover the microlensed WFs, which are modelled by the parameters: chirp mass (\mathcal{M}_c), mass ratio (q), and aligned spin components of the two component masses (χ_{1z} , χ_{2z}). To estimate minimum loss of SNR during the search, we compute the maximum match (Eq. 2.21), or the FF, between the microlensed and the unlensed WFs in the 4D parameters listed above. We use the PyCBC package ([Nitz et al. 2020](#), [Usman et al. 2016](#)) for computing match values (Eq. 2.20), and work with the approximant IMRPhenomPv3 ([Khan et al. 2019](#)) with an f_{low} value of 20 Hz, where f_{low} is the lower frequency cutoff in the evaluation of the overlap (see Eq. 2.18). The PSD used is aLIGOZeroDetHighPower¹, which is comparable to O4 targeted PSDs of LIGO detectors ([Abbott et al. 2018](#))². The FF values have been computed

¹<https://dcc.ligo.org/LIGO-T070247/public>;
<https://dcc.ligo.org/T1800044-v5>.

²<https://dcc.ligo.org/LIGO-T2000012/public>;
<https://dcc.ligo.org/LIGO-T1500293/public>.

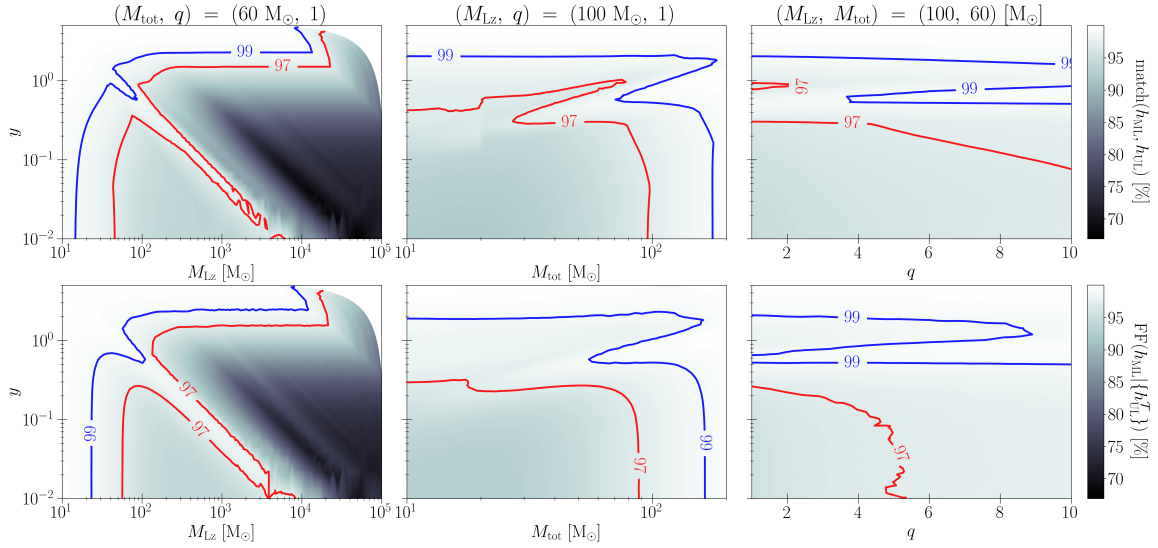


Figure 3.1: Effect of microlensing on GW WFs for different microlensing and CBC parameters. The top panel shows match values between the unlensed and the corresponding microlensed WFs, whereas the bottom panel show FF values (or, the maximum match) for the microlensed WFs when recovering with the unlensed WFs corresponding to the 4D aligned-spin template WFs modelled by parameters $\{\mathcal{M}_c, q, \chi_{1z}, \chi_{2z}\}$. The analysis has been done for: (i) varying redshifted lens mass (M_{Lz}) and impact parameter (y) for a fixed binary mass of $M_{\text{tot}} = 60 M_{\odot}$ and mass ratio $q = 1$ (*left panel*), (ii) M_{tot} vs. y parameter space for fixed $(M_{Lz}, q) = (100 M_{\odot}, 1)$ (*middle panel*), (iii) q vs. y parameter space for fixed $(M_{Lz}, M_{\text{tot}}) = (100 M_{\odot}, 60 M_{\odot})$ (*right panel*). The injected spins are kept zero.

using the Nelder-Mead algorithm as implemented in the 'optimization' module of the Scipy library (Wu et al. 2009). It's important to note that since we employ a maximization algorithm to compute FF, we do not account for any additional reduction in FF due to the discrete placement of templates (point (i) below Eq. 2.21 does not apply in our case).

The results are shown in Fig. 3.1, where we study the effect of microlensing on GW signals for different microlensing and CBC parameters. The top panel shows match values between the unlensed and the corresponding microlensed WFs, quantifying the amount by which a WF changes due to microlensing. The bottom panel shows FF values (or, the maximum match) for the microlensed WFs when recovering with the unlensed WFs corresponding to the 4D aligned-spin template WFs modelled by parameters $\{\mathcal{M}_c, q, \chi_{1z}, \chi_{2z}\}$. As discussed above, this loss can lead to a drop in the detection rate owing to the influence of microlensing on the signals. The analysis has been done for: (i) varying redshifted lens mass (M_{Lz}) and impact parameter (y) for a fixed binary mass

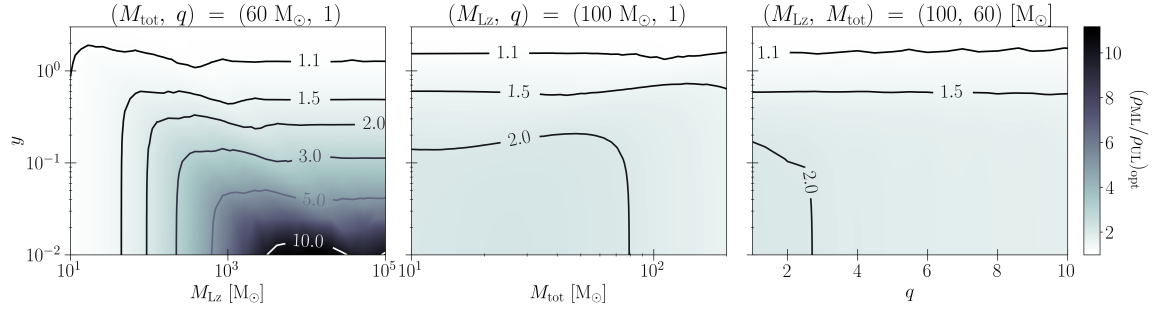


Figure 3.2: The figure depicts the variation in the optimal SNR in the no-lens versus microlens cases. The variation is shown as a function of point-lens mass (M_{Lz} ; left panel), binary mass (M_{tot} ; middle panel), and mass-ratio (q ; right panel). The presence of an isolated microlens always increases the SNR relative to the no lensing case.

of $M_{tot} = 60 M_{\odot}$ and mass ratio $q = 1$, which represents a "golden"³ black-hole binary to which our detectors are sensitive from inspiral to ringdown phase of the coalescence (Hughes & Menou 2005; Nakano et al. 2015; Ghosh et al. 2016) (left panel), (ii) M_{tot} vs. y parameter space for fixed $(M_{Lz}, q) = (100 M_{\odot}, 1)$ (middle panel), (iii) q vs. y parameter space for fixed $(M_{Lz}, M_{tot}) = (100 M_{\odot}, 60 M_{\odot})$ (right panel). The differences between the match and FF values in the top and bottom panels suggest that microlensing of GW signals can lead us to infer biased or inaccurate source parameters.

In the leftmost panel, the ranges of M_{Lz} and y have been kept the same as in Fig. 2.2. The match and FF values are close to 1 for low M_{Lz} and high y , consistent with the unlensed scenario, and decrease almost diagonally as M_{Lz} and $1/y$ are increased. However, we notice both match and FF plots have oscillations across equal time delay contours as shown in Fig. 2.2. Also, the worst match values (or the highest mismatch) come from a region where wave effects are large, i.e., the region depicted between the two contours $f_{ML} = \{10, 100\}$ shown in Fig. 2.2. In the middle panel, the match and FF values are close to 1 for high M_{tot} and y values, and decrease almost diagonally down for low values of M_{tot} and y . The reason we see a high match for higher BBH masses is because the signal length becomes comparable to the time delay between the microimages associated with those lensing parameters. This leads to fewer modulations that can affect the GW signal. It is also worth noting that the match and the FF contours corresponding to a value of 97% (red curves) differ significantly in a region where $y \in \sim (0.1, 1)$ and $M_{tot} \in \sim (20, 60) M_{\odot}$. Similarly, in the rightmost panel, the FF contours corresponding to a value of 97% (red curves) change drastically between the top and the bottom panel. This variation between match and FF values hints towards a strong degeneracy between

³Binaries with total mass $\sim 50 - 200 M_{\odot}$.

microlensing the CBC intrinsic parameters and the microlensing parameters.

Although Fig. 3.1 is important to determine the effect of microlensing on the detection of GWs, it is not sufficient. Since microlensing will also affect the inferred (effective) *luminosity distance*, the horizon distance to a microlensed GW signal will also shift accordingly relative to the unlensed case, and so will the inferred rate of mergers. Therefore, in Fig. 3.2, we show how optimal SNR can vary in the presence of microlens. The leftmost panel shows variation in the microlensing parameter space of M_{Lz} and y , while keeping the binary parameters fixed to $(M_{\text{tot}}, q) = (60 M_{\odot}, 1)$. Same with the middle and the right panels, except we vary M_{tot} and q , respectively, while fixing $M_{Lz} = 100M_{\odot}$. In all the panels, the contours represent the ratio of the optimal SNRs between the case when the microlens is present *vs.* when it is absent, i.e., $\rho_{\text{ML}}/\rho_{\text{UL}}$. This value should tend to unity at higher impact parameter values, consistent with the darker regions at high values of y where microlensing effects are insignificant. In the leftmost panel, we observe a drastic change in the optimal SNR. The SNR in the presence of microlens increases almost monotonically as we increase M_{Lz} and $1/y$, reaching a value of more than 10 times the unlensed SNR in the bottom-right corner of the plot. Even for modest values of microlensing such as $(M_{Lz}, y) = (10, 1)$, we observe a 10% increase in the SNR. In the middle and the right panels, since contour corresponding to the value 1.5 is almost flat, we observe that the change in SNR is not correlated with varying M_{tot} and q for higher values of $y \gtrsim 0.5$. However, for lower values of $y \lesssim 0.5$, we do see a correlation in both panels. SNR tends to increase for lower mass binaries, which is a consequence of longer signal duration, i.e., the integrated effect of microlensing over the signal. Although not visible explicitly, when we examine the variation of the SNR with q , we find oscillatory behaviour of SNR as q increases. This oscillatory behavior is a consequence of amplitude oscillations in $F(f)$. As we fix the microlensing parameters, M_{Lz} and y , and only vary q , the GW frequency at ISCO would decrease monotonically, and so does the strain at maximum strain amplitude. The oscillations in $|F(f)|$ would then translate to oscillations in the optimal SNR as the ISCO frequency varies.

In Fig. 3.1, we observed that although microlensing would further decrease the SNR due to a decrease in FF values, Fig. 3.2 suggests that the SNR itself increases due to the presence of an isolated microlens. Thus, the effect of microlensing on the detection of GWs is non-trivial. These figures suggest that the observed distribution of the microlens population can differ significantly from the expected prior distribution. We study this statistically in more detail in Sect. 3.4.

3.3 Effect of microlensing on parameter estimation of GWs: Bayesian Analysis

In this section, we study the biases caused by the microlensing effects on inferred source parameters. We also investigate the correlations between the recovered parameters when microlensed signals are either recovered with a microlensed WF model or the usual 15D unlensed WF model. We again employ the isolated point lens model for microlensing.

To understand the effect of microlensing on the inferred source parameters, we do a Bayesian analysis by performing a set of parameter estimation runs (Cutler & Flanagan 1994; Husa 2009; Thrane & Talbot 2019; Christensen & Meyer 2022). We inject zero-noised microlensed BBH signals into the three detectors (LIGO Livingston, LIGO Hanford, and Virgo) having PSDs corresponding to the target sensitivities of the upcoming O4 runs (Abbott et al. 2018) (see Sect. 2.3.3 for details). The injected signals are non-spinning with extrinsic parameters corresponding to GW150914, except for the luminosity distance, d_L , which is scaled to obtain a desired SNR. Firstly, we inject and recover a microlensed signal using a microlensed WF model to see the correlation between the 17D parameters, especially between the 15D BBH parameters and the two lensing parameters. Then, to understand the biases in the inferred BBH parameters and their degeneracies with microlensing, we inject a set of microlensed signals and recover using the usual unlensed templates, i.e., assuming no microlensing is present in the signal. Parameter estimation (PE) runs are performed using the publicly available package BILBY-PIPE (Ashton et al. 2020, 2019; Romero-Shaw et al. 2020), keeping all parameters free while recovery. For both the injection and the recovery templates, we use IMRPhenomXPHM (London et al. 2018) WF approximant with $f_{\text{low}} = 20$ Hz as the lower frequency cutoff for the likelihood evaluation. As mentioned previously, we use the Dynesty sampler with the following settings: $\{\text{nlive}=2048, \text{nact}=50\}$, and use $\text{n-parallel}=4$ to combine four independent parallel chains to get the final posterior sample.

In Fig. 3.3, we study correlations between the 17 parameters of a microlensed WF $\lambda_{\text{ML}} \in \{\lambda_{\text{UL}}, M_{\text{Lz}}, y\}$, where λ_{UL} represents the 15 parameters corresponding to an unlensed BBH WF as described in Sect. 2.3. The injected signals are non-spinning equal mass binaries having a total mass of $M_{\text{tot}} = 60 M_{\odot}$ and a network SNR of roughly 50. Among the microlens parameters, the redshifted lens mass is fixed to $M_{\text{Lz}} = 100 M_{\odot}$ and the impact parameter increases from left to right as $y \in \{0.05, 0.1, 0.5, 1.0, \gg 1\}$ (also indicated at the top of each column). The top row shows correlations when the recovery model corresponds to 17D microlensed WFs, while the bottom row depicts correlations when the recovery model is the usual 15D unlensed BBH WFs. The colours depict Pearson correlation coefficients ranging from -1 to 1 , where blue cells represent positive

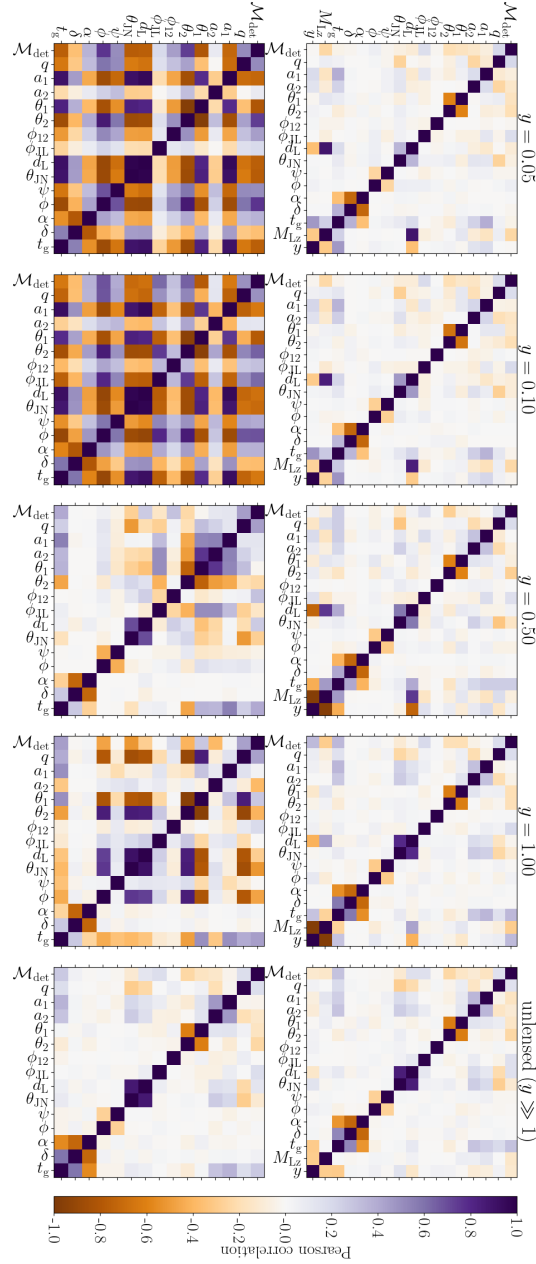


Figure 3.3: Correlations between the parameters of microlensed WFs. The injected WFs correspond to a BBH with a total binary mass of $M_{\text{tot}} = 60 M_{\odot}$, mass-ratio $q = 1$, and having observed network SNR of ~ 50 . Among the microlens parameters, the redshifted lens mass is fixed to $M_{Lz} = 100 M_{\odot}$ and the impact parameter increases from left to right as $y \in \{0.05, 0.1, 0.5, 1.0, \gg 1\}$ (also indicated at the top of each column). *Top:* correlations when the recovery model corresponds to 17D microlensed WFs. *Bottom:* correlations when the recovery model is the usual 15D unlensed BBH WFs.

correlations (> 0) and orange cells represent negative correlations (< 0). The matrix is symmetric by construction. Studying the top row of the figure, we first notice that the correlations of M_{Lz} and y with other parameters are mostly of opposite sign (see, e.g., opposite tonalities in the bottom two rows of each subpanel for almost all the parameters where correlations are significant.). This is expected as the effect of increasing M_{Lz} and decreasing y favours microlensing effects, and vice-versa. *It is worth noting that the luminosity distance d_L shows maximum correlation with the microlensing parameters, which can even exceed $\sim \pm 90\%$.* For lower values of $y < 1$, the anti-correlation can increase significantly. This is because as y decreases, the magnification of micro-images increases even more rapidly, which is compensated by an increase in the effective distance of the binary, thereby showing strong negative correlations. This justifies our earlier result of how optimal SNRs (or distance estimates) get significantly affected due to microlensing, as shown in Fig. 3.2. Next, the (detected) chirp mass \mathcal{M}_{det} ⁴ also shows interesting correlations and can be as high as $\sim \pm 30\%$, while the spin components show only weak correlations with the microlensing parameters. However, even small correlations can have severe effects in the parameter estimation considering the sensitivity of WFs to these parameters. To give an idea, the mismatch between a non-spinning WF, as considered in this exercise, with a WF (i) having a small effective spin $\chi_{\text{eff}} = 0.05$ is $> 5\%$, (ii) having only a slight variation of 1% in the chirp mass is $\sim 3\%$ ⁵. Apart from the luminosity distance d_L and the trigger time⁶, t_c , other extrinsic parameters such as the sky location parameters, right ascension and declination (α, δ), the polarisation angle (ψ), the phase of coalescence (ϕ), and the inclination θ_{JN} show only negligible correlation with microlensing. Another important thing to note is that the two microlensing parameters M_{Lz} and y show a strong negative correlation among themselves, which increases with increasing y from left to right up to $y = 1$, reaching a value $< -95\%$ for $y = 1$. This suggests that the correlation between the two parameters increases in the geometric optics limit. Therefore, while doing the 17D microlens parameter estimation, sampling in these two parameters directly will not be the most efficient choice, and one may resort to different combinations of these two parameters like the relative magnification and the time delay between the micro-images, as used in Liu et al. (2023).

Now focusing on the bottom row of Fig. 3.3, if only the unlensed WF model is used in recovering a microlensed signal, there will be several indirect (yet significant) correla-

⁴We explicitly write "detector frame" here to avoid confusion with the source frame chirp mass, which will be highly biased due to a biased inference of the luminosity distance (or, the redshift).

⁵A mismatch value above 1% is large enough to bias the inferred parameters for an event with SNR $\gtrsim 15$.

⁶Similar behaviour is observed for the 'jitter time' when the time-marginalisation is used.

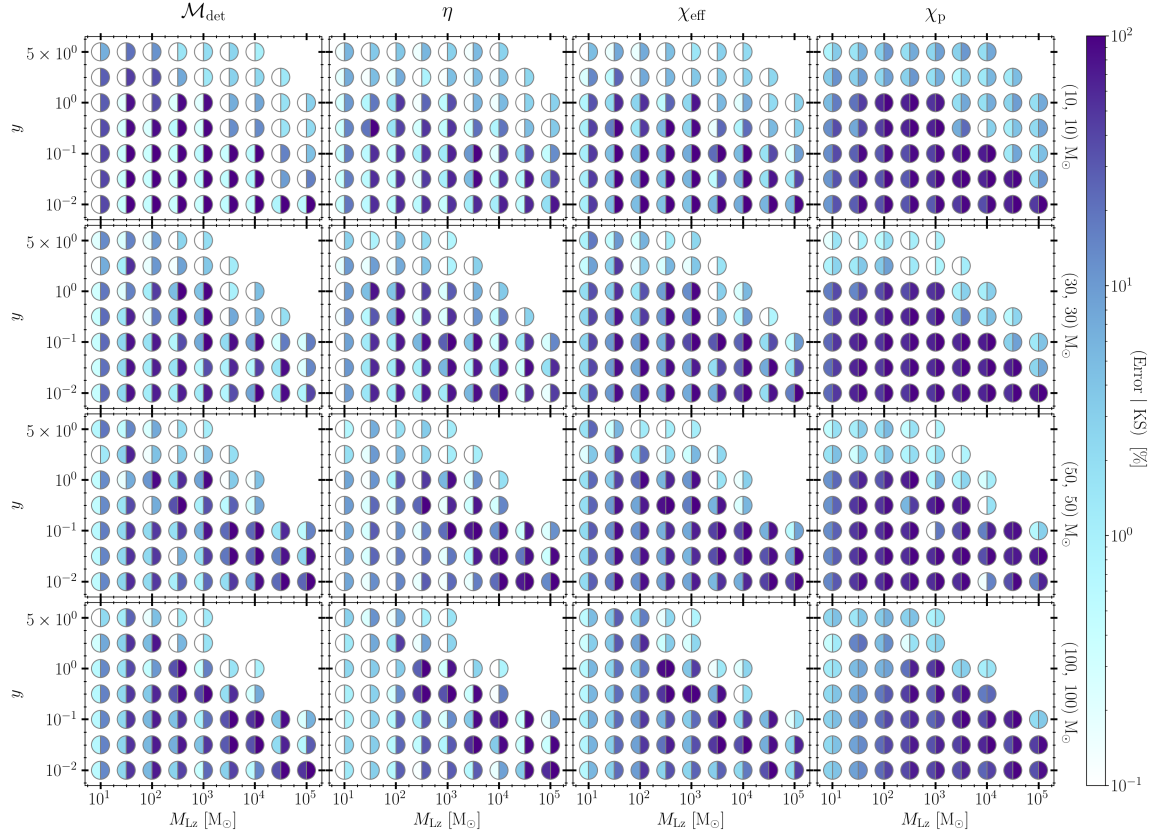


Figure 3.4: Bias in the inferred intrinsic source parameters of a microlensed signal when recovered using the usual unlensed WF model, characterised by 15 parameters. Each column represents the bias in a specific parameter, indicated at the top, while different rows correspond to different source binaries, indicated on the right side of each row. The intrinsic parameters are represented by the detected chirp mass (\mathcal{M}_{det}), symmetric mass-ratio (η), projected effective spin (χ_{eff}), and precession effective spin (χ_{p}). The source parameters correspond to equal mass binaries with a mass ratio of $q = 1$ and a total mass of $M_{\text{tot}}/M_{\odot} \in \{20, 60, 100, 200\}$. Each subplot shows the bias in the microlensing parameter space of the redshifted lens mass, denoted as $M_{Lz}/M_{\odot} \in \{1e1, 5e1, 1e2, 5e2, 1e3, 5e3, 1e4, 5e4, 1e5\}$, and the impact parameter values denoted as $y \in \{0.01, 0.05, 0.1, 0.5, 1.0, 3.0, 5.0\}$. Each circular marker in the plot has two halves: the left half represents the relative percentage error (absolute error for χ_{eff} and χ_{p}) between the median values of the microlensed and unlensed recoveries, while the right half represents the two-sample Kolmogorov-Smirnov (KS) Statistic value between the 1D marginalised posteriors of the microlensed and unlensed recoveries (in percentage). We further ignore points in the parameter space corresponding to a time-delay between microimages greater than the signal duration, indicating cases where strong lensing is observed (empty region in the top-right corner of each subplot).

CHAPTER 3. EFFECT ON INFERRED PARAMETERS

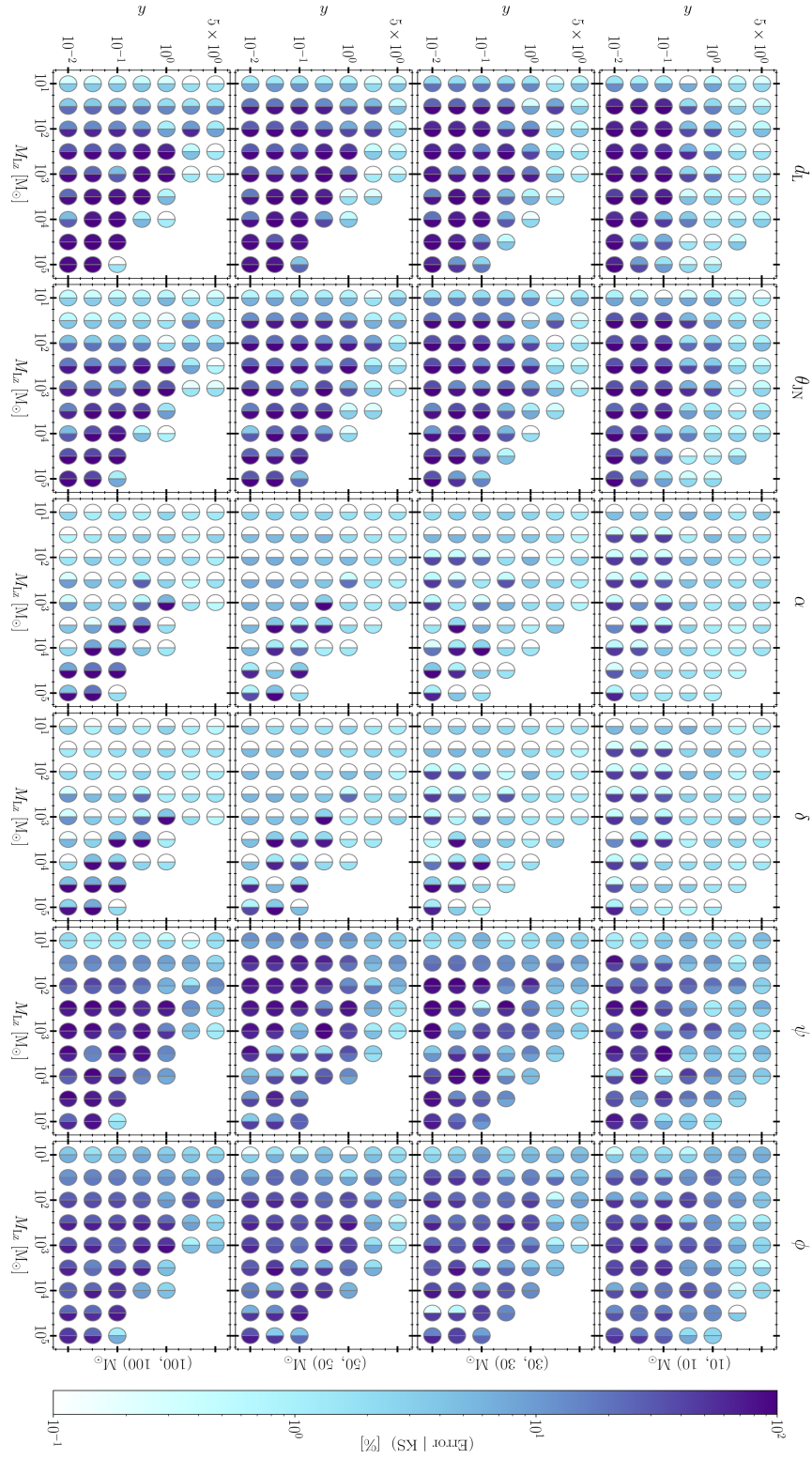


Figure 3.5: Same as Fig. 3.4, but for extrinsic parameters. The extrinsic parameters are represented by the luminosity distance (d_L), inclination (θ_{JN}), sky location (RA and Dec; α and δ), polarization angle (Ψ), and coalescence phase (ϕ). The trigger time t_c is not shown as it is well recovered throughout the parameter space.

tions between the BBH parameters and the microlensing parameters, as parameters that are directly correlated with microlensing parameters will further affect other parameters that are strongly correlated with them, and so on. When this cascade effect is in place, it will drastically affect parameter estimation. Such an effect can be seen for the two leftmost cases $y = \{0.05, 0.10\}$ in the bottom row of Fig. 3.3, where almost all the BBH parameters have become strongly correlated. It is worth noting that these two cases fall in the long-wavelength regime. This behaviour could be a *general characteristic of the bottom-right corner of the long wavelength regime, where microlensing effects are strong but slowly varying.*

As a reference, the rightmost panel show the correlations when the injected WF is unlensed, while the recovery model is either microlensed (top-right panel) or unlensed (bottom-right panel), highlighting the usual correlations present among the BBH parameters. The variation in the correlation coefficient values compared to the unlensed case is clearly visible as we vary the impact parameter. With changing y , the correlations become intertwined in different ways in an attempt to absorb microlensing effects. It is interesting to note that the sign of correlations can also change, i.e., *the correlation between parameters can rotate due to microlensing effects.* For example, the variation in the correlation between \mathcal{M}_{det} and t_c changes from a slightly positive correlation to a strong negative correlation as we decrease the impact parameter y . A similar effect can be observed for spin components which show strong correlations with other parameters and among themselves as we compare the leftmost panel with the other three panels.

In figures 3.4 and 3.5, we show biases in the inferred parameters when the injected microlensed signals are recovered under the assumption of unlensed hypotheses. The injected signals are such that their observed SNR is roughly 50, which is achieved by tweaking the luminosity distance accordingly. Fig. 3.2 then implies that we keep the signals at higher distances as the lens mass increase and the impact parameter decrease. We choose specific grid points to cover the microlensing and source parameter space. For microlensing, we choose the redshifted lens mass values as $M_{Lz}/M_{\odot} \in \{1e1, 5e1, 1e2, 5e2, 1e3, 5e3, 1e4, 5e4, 1e5\}$, and the (possible) impact parameter values as $y \in \{0.01, 0.05, 0.1, 0.5, 1.0, 3.0, 5.0\}$. We further ignore those points in the parameter space that correspond to a time delay between microimages greater than the signal duration, i.e., cases where strong lensing is observed (see the empty region in the top-right corner of each subplot). The source parameters correspond to the equal mass binaries having mass ratio $q = 1$ and total mass $M_{\text{tot}} \in \{20, 60, 100, 200\}$. The x and y axes in each subplot represent varying M_{Lz} and y values, respectively. Each column represents the bias in a specific parameter as indicated at its top, while different rows correspond to different source binaries as indicated on the right side of each row. Each circular marker in the plot has two halves, with the left half representing the relative percentage error between the

median values of the microlensed vs unlensed recoveries, while the right half represents the two-sample Kolmogorov-Smirnov (KS) statistic value between the 1D marginalised posteriors of the microlensed and the unlensed recoveries (in percentage). For parameters χ_{eff} and χ_{p} , the left half represents the percentage absolute error rather than the relative error as their injected values were zero. The KS statistic value for two cumulative distribution functions, $C_1(x)$ and $C_2(x)$, is defined as

$$KS = \max_x |C_1(x) - C_2(x)|, \quad (3.1)$$

which is more sensitive to the change in the distribution itself compared to the change in the median values. So in simple words, the left half indicates the bias in the recovery, while the right half indicates the change in the 1D marginalised posterior distribution, both converted to percentages.

In Fig. 3.4, we show bias in the intrinsic parameters, i.e., in masses and spins of the binaries. The detected chirp mass \mathcal{M}_{det} and symmetric mass-ratio η represent the masses, while the projected effective spin χ_{eff} (Racine 2008; Ng et al. 2018) and precession effective spin χ_{p} (Gerosa et al. 2021; Schmidt et al. 2015) represent the spins of the BBHs. These two-dimensional effective spin quantities, χ_{eff} and χ_{p} , offer a simplified interpretation of the six-dimensional spin parameters. For all the parameters and binary masses (i.e., all the subplots in the figure), we see negligible biases in the recoveries for low M_{Lz} and $1/y$ values as the leftmost and topmost array of markers suggest errors to be $\lesssim 1\%$ in most of the subplots (see the left halves of the markers for the data points having either $M_{\text{Lz}} = 10$ or $y = 5$). This is expected as it corresponds to negligible microlensing effects that are difficult to be detected with the current sensitivities of the ground-based detectors. However, even in this negligibly-lensed regime, the biases in the spin parameters reach $\sim 10\%$ in a few cases, which is a result of bad recoveries of the spin parameters in general, as they appear higher in the post-Newtonian orders. Additionally, the two mass-related parameters, \mathcal{M}_{det} and η , are usually well recovered for $M_{\text{Lz}} \lesssim 100 M_{\odot}$, where we expect a larger number of microlenses.

As suspected in Fig. 2.2 of Sect. 2.1, we indeed observe the biases to increase in the wave zone for all the parameters. This is especially clear if we look at the bottom-most row corresponding to the $(100, 100) M_{\odot}$ binary, where biases seem to be more streamlined and increasing along the diagonal from lower M_{Lz} and $1/y$ values to higher values in each column. As we move up the rows to lower binary masses, this pattern along the diagonal broadens and eventually covers up a large parameter space, even spanning regions in the long-wavelength regime, as we see in the case of $(10, 10) M_{\odot}$ binary. One of the reasons for such broadening of the biases along the diagonal from the wave zone toward the long-wavelength regime is due to the fact that lower mass binaries tend to cover a broader frequency spectrum, i.e., they have a higher power in high frequencies as compared to

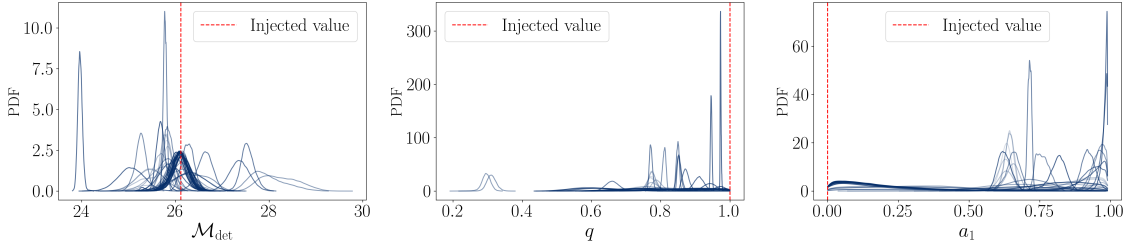


Figure 3.6: 1D marginalised posterior distributions for the recoveries of $\{\mathcal{M}_{\text{det}}, q, a_1\}$ of the $60M_{\odot}$ binary system shown in Fig. 3.4 and 3.5. The dashed red line represents the injected value

heavier binaries. From Fig. 2.2, it is then expected that such a signal with significant contribution from high frequencies will also show bias in the long-wavelength regime, i.e., for lower M_{Lz} and y values.

Of the four parameters, the spin parameters seem to be biased the most, especially the precession effective spin χ_p , as compared to the chirp mass \mathcal{M}_{det} and the symmetric mass-ratio η . This is also true in the usual parameter estimations of the unlensed signals owing to their appearance in the different post-Newtonian orders. Chirp mass and symmetric mass-ratio give the most dominant effect at 0th PN order of GW phasing while χ_{eff} and χ_p appear at 1.5 PN and 2.5 PN orders, respectively (Arun et al. 2005; Schmidt et al. 2015; Isoyama et al. 2020). The recoveries for χ_p exhibit biases across most of the parameter space in each row, particularly in the wave zone, and these biases appear to decrease as we move down the row toward heavier mass binaries. This suggests that the biases in χ_p are correlated with the length of the microlensed signal. It is also worth noting that even for the modest values in our microlensing parameter space, such as $(M_{Lz}, y) \sim (10^2, 1)$, the recovery of χ_p show significant biases. Thus, *the bad recoveries for longer signals indicate that microlensing and spin-precession are degenerate with each other. Therefore, any signal showing signs of precession must also be analysed for the presence of microlensing signatures to break the degeneracy. However, vice-versa may not be true, i.e., it is unlikely that the presence of precession can bias microlensing searches. This is because the unlensed parameter space is always a subset of the microlensed parameter space.*

Similarly, in 3.5, we show the bias in the recoveries of the extrinsic parameters, i.e., luminosity distance (d_L), inclination (θ_{JN}), RA (α), Dec. (δ), polarisation angle (ψ) and coalescence phase ϕ . We do not show the recoveries of trigger time t_c as we do not see any appreciable bias in its recovery. Among all the cases studied here, the absolute errors for t_c never exceeded 5%. We notice that the most affected parameter is the luminosity distance, as it gets directly affected due to the modulations in the amplitude induced by microlensing. On the other hand, the sky position parameters Ra and Dec are among

the best-recovered parameters not affected by microlensing. This is expected since the localization of GW sources is mainly based on the observed time delays between each pair of interferometers. Since microlensing does not affect the observed trigger times, the localisation is not affected except when microlensing effects are extreme.

The KS values (right halves of the markers) show a similar trend as that of errors. It is interesting to note that in most cases, the right half of the circle is darker than the one on the left, indicating that KS values are more sensitive to microlensing effects than the bias in the inferred parameters. This can be seen in Fig. 3.6, where we explicitly show the marginalised 1D posterior distributions for three parameters $\{\mathcal{M}_{\text{det}}, q, a_1\}$ for the case having binary mass $60 M_{\odot}$. In the leftmost panel, one can notice several cases where the distribution shifts because of microlensing effects even when the posterior mode itself hasn't changed much. These cases are examples that result in a high KS-value but a low relative error. In contrast, there are several cases in the middle and the rightmost panels where the recovered distribution is significantly biased and is also well converged (e.g., see well-converged distributions in the rightmost panel for a_1 away from the injected value of 0). Such cases result in a high relative error as well as a high KS-value (markers with both left and right halves coloured as dark blue in Fig. 3.4 and 3.5).

Lastly, in Fig. 3.7, we examine the variation in Pearson correlation values between GW parameters for the $(30, 30) M_{\odot}$ binary discussed earlier (second row in Figures 3.4 and 3.5). The left panel illustrates the correlation values for all possible 120 pair combinations of the 15 parameters (represented by different shades of blue). The x -axis corresponds to the time delay between microimages associated with the microlens parameters considered for that binary. The data points, indicated by circular dots, consist of 54 data points for each of the 120 lines. Additionally, the lines originate from $\tau_d = 0$, representing the unlensed case. The line with a Pearson correlation value of unity indicates the diagonal elements of the correlation matrix, which represents the correlation of a parameter with itself. The purpose of this plot is to demonstrate how correlations can vary based on the microlens parameters. It is evident that correlations can significantly fluctuate depending on the specific microlens parameters. For instance, there is a notable concentration of lines around zero at low time delay values ($\tau_d < 10^{-5}$ s), which becomes sparser at $\tau_d = 10^{-3}$ s. Since it is not possible to follow which line corresponds to which correlation pair, we specifically show the correlations for four pairs in the right panel, as written in the legend.

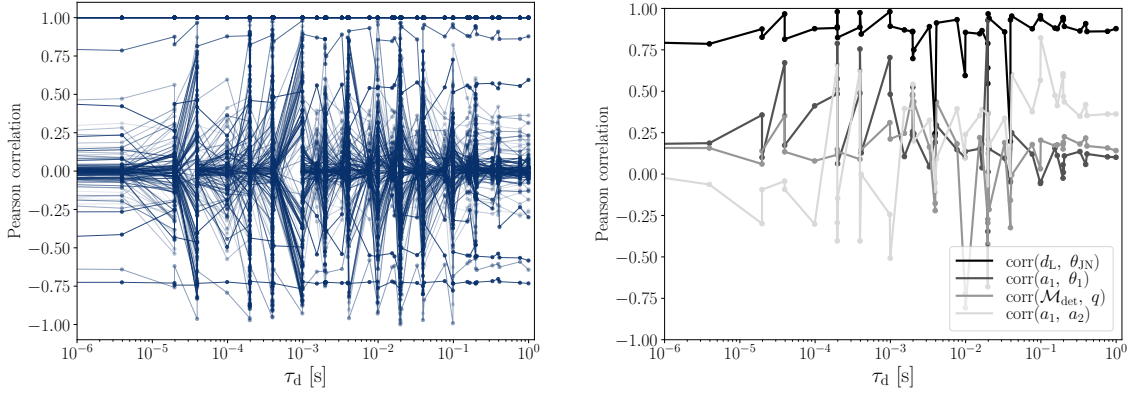


Figure 3.7: Variation in the correlation values between the 15 parameters of a BBH system due to microlensing effects. The studied BBH and lens system corresponds to the $60 M_{\odot}$ binary shown in Figures 3.4 and 3.5. *Left:* The variation is displayed for each parameter pair, resulting in a total of 120 possible pairs represented as individual lines. These lines illustrate the correlation values as a function of the time-delay between micro-images, determined by the microlens parameters in the grid shown in Fig. 3.4 and 3.5. Each line is associated with 63 data points, represented as dots, indicating the specific time-delay values used to construct the line. *Right:* Same as the left panel but explicitly showing the correlations for four pairs as written in the legend. Moreover, the lines originate from $\tau_d = 0$, showcasing the unlensed case.

3.4 Study of a population of Microlensed Signals

In this section and the subsequent section, we investigate a population of microlensed signals. In contrast to the previous sections, where we either fixed certain parameters while varying others or chose a grid to cover the parameter space, in this section, we sample the sources realistically to infer the population-wide distributions of parameters. We will pay particular attention to the microlens parameters, which is the focus of this study. Furthermore, analyzing the population statistics allows us to explore various aspects, such as the effectualness of unlensed WFs in detecting microlensed WFs and the potential parameter space for microlensing detection.

We generate mock GW data of around 2.5×10^4 microlensed BBH signals, where BBH parameters are derived from the population model constructed using the GWTC-3 catalogue (Abbott et al. 2023; The LIGO Scientific Collaboration et al. 2023b). We put an observed network SNR threshold of 8 when using the unlensed templates for recovery, and the detector noise PSDs used correspond to the target O4 sensitivities (Abbott et al. 2018).

The population model basically provides a fit to the distribution of observed parameters, particularly masses, spin magnitudes, spin tilts, and the redshift distribution of the BBH mergers. All other BBH parameters are sampled uniformly from their respective domains. For microlens parameters, we assume a log-uniform prior in M_{Lz} (in units of M_{\odot}) and a power-law prior for y with an index of unity (a linear prior):

$$\begin{aligned} p(M_{Lz}) &\propto \text{LogUniform}(10^1, 10^5), \\ p(y) &\propto y, \quad y \in (0.01, 3.00), \end{aligned} \quad (3.2)$$

where the motivation to use $p(y) \propto y$ comes from geometry and isotropy (Lai et al. 2018). To wit, the probability of a source having an impact parameter y relative to a microlens will be proportional to the area of a ring of infinitesimal width having radius y , i.e., $p(y)dy = 2\pi y dy$. We assume Madau-Dickison profile for the merger rate density in the universe, giving source-redshift density model as (Madau 1997; Fishbach et al. 2018):

$$\begin{aligned} p(z_S) &\propto \frac{dV_c}{dz_S} \frac{1}{1+z_S} \psi(z_S), \\ \text{where } \psi(z_S) &= 0.015 \frac{(1+z_S)^{2.7}}{1 + [(1+z_S)/2.9]^{5.6}}. \end{aligned} \quad (3.3)$$

The source redshift range was set to be $z_S \in (0.001, 10)$, with the lower limit of $z_S \equiv z_{\min} = 0.001 \sim \mathcal{O}(1)$ Mpc corresponding to a value below which merger rate is negligible due to low cosmological volume and star formation rate. The upper limit of $z_S \equiv z_{\max} = 10$ serves as an approximate representation of the maximum distance from which a microlensed signal can be detected using current ground-based detectors. This limit assumes ideal conditions such as low impact parameters, a high lens mass, and a massive binary system as the source. For instance, a system characterized by parameters $(M_{Lz}, y, M_{\text{tot}}, \iota) = (10^4, 10^{-2}, 200, 0)$ exemplifies these ideal conditions.

In Fig. 3.8, we show a mock sample of the detectable microlensed population - its distribution and the inferred properties. The top row shows the network optimal SNR as a function of M_{Lz} and y (left panel), y vs. z_S (middle panel), and M_{Lz} vs. z_S (right panel). Firstly, we note that using only unlensed templates during the search of these microlensed signals, we detected around 91.6% of total signals (using Eq. 2.21) in the parameter space considered here. We observe that most of the detected signals tend to have higher impact parameters, which is expected based on our initial assumption given in Eq. 3.2. However, as predicted in Fig. 3.2 of Sect. 3.2, it is worth noting that we do detect a significant number of events in the range $y \in (0.01, 0.1)$ as well, which is usually considered to be a probabilistically insignificant region. The top-middle panel confirms the hypothesis that these signals with low-impact parameters can indeed arrive from far away regions ($z \gtrsim 2$) as opposed to the current detection horizons for unlensed BBH signals ($z \lesssim 1$). This is a consequence of an increase in their SNR values because of

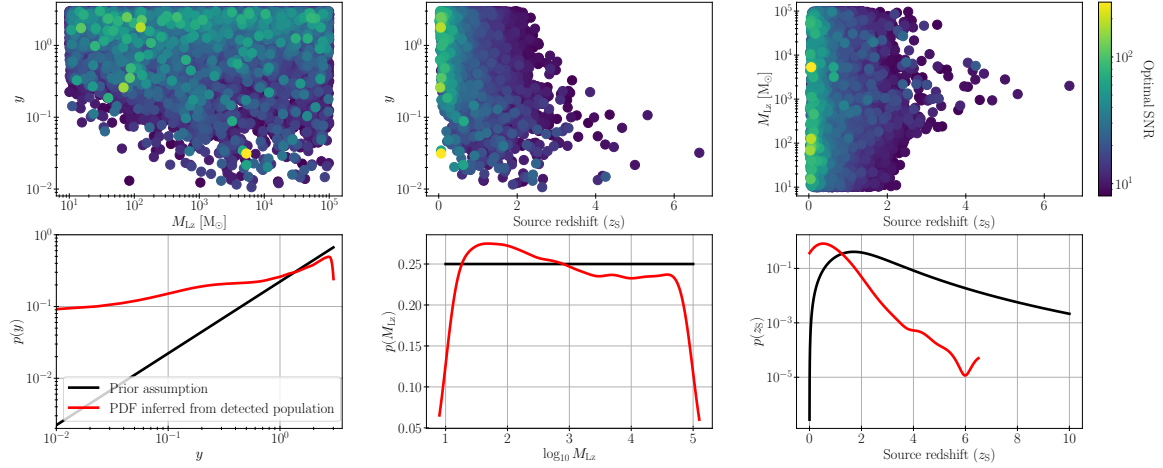


Figure 3.8: Population study of microlensed BBH signals for the joint network of LIGO–Virgo detectors assuming the targeted O4 sensitivities. *Top:* Distribution of population is shown in the microlensing parameter space of M_{Lz} and y (left), and for y vs. z_S (right), where M_{Lz} , y and z_S denote the redshifted lens mass, impact parameter and source redshift, respectively. The colour bar represents the observed network optimal SNR. *Bottom:* Comparison of probability density functions (PDFs) between the ones that were used while generating the population (black coloured curves), and the ones inferred from the observed population themselves (red coloured curves). The PDF comparison is shown for three parameters, y (left), M_{Lz} (middle) and z_S (right).

microlensing, and hence an increase in their detection horizon (see the left-most panel in Fig. 3.2). We also notice that even in the case of population, the behaviour of FF in M_{Lz} and y plane (top-left panel) is similar to the behaviour of FF shown in Fig. 3.1, where we had kept the binary mass fixed.

The bottom row of Fig. 3.8 illustrates the comparison of probability density functions (PDFs). The black curves represent the PDFs used for sampling during the population generation (referred to as the "prior"; see Eq. 3.2), while the red curves represent the PDFs inferred from the detected population itself. The PDF comparison is shown for three parameters, y (left panel) and M_{Lz} (middle panel) and z_S (right panel). We use kernel density estimation (KDE) to obtain the PDFs from the observed data. The comparison of PDFs for the impact parameter, $p(y)$, shows very interesting behaviour. At low values of y ($\lesssim 1$), the observed signals have roughly a flat density profile in y , instead of the linear profile used as the prior (Eq. 3.2; see black curve). The reason for this behaviour can be attributed to the behaviour of magnification due to a point-lens, which is only a function of y , given by

$$\mu_{\pm}(y) = \frac{1}{2} \pm \frac{y^2 + 2}{2y\sqrt{y^2 + 4}}. \quad (3.4)$$

It can be seen that in the limit $y \ll 1$, $\mu_{\pm}(y)$ becomes proportional to $1/y$, which in turn increases the detection horizon, thereby increasing the relative probability density in that region.

On the other hand, the probability density profile for M_{Lz} (bottom-middle panel) is roughly similar to our initial assumption of a Log-uniform distribution with only a slight preference for lower masses compared to heavier masses. This slight preference for lower masses ($\log_{10} M_{Lz} \lesssim 2.5$) is a result of better FF recovery values in that region as shown in the bottom left panel of Fig. 3.1, owing to smaller microlensing effects. If we instead recover with the microlensed templates instead of the unlensed ones, we find $p(M_{Lz})$ to be even more consistent with the Log-Uniform distribution showing no special preference for any mass values. This indicates that the behaviour of FF is indeed the reason behind the slight preference for lower mass values in case of unlensed recoveries. The probability density of the source redshift $p(z_S)$ (bottom-right panel) shows a similar trend as if there were no microlensing (e.g., see Fig. 2 in Fishbach et al. 2018) but with a longer tail reaching much higher values up to $z \sim 5$ as opposed to the current detection horizons for BBH signals ($z \lesssim 1$) (also see The LIGO Scientific Collaboration et al. 2023b).

We showed that the selection bias incurred during detection would significantly affect the properties of the observed population compared to the true microlensed population. However, not all the observed microlensed events will be correctly identified as being microlensed, i.e., having significant evidence for the microlensing hypothesis over the unlensed hypothesis. For example, a low SNR event that has low M_{Lz} and high y values, such as $(M_{Lz}, y) = (10 M_{\odot}, 3)$, would not be correctly identified as being a microlensed event with the current sensitivities of the detectors. Therefore, in order to predict the parameter space which has a higher potential of being detected and also identified as a microlensed event, we should anticipate a further selection bias on the detected events. This involves weighing events according to their microlensing effects, i.e., the events with higher microlensing effects are more probable to be correctly identified as microlensed. In the next section, we investigate this bias and present a combined PDF that incorporates both the detection and identification aspects.

3.5 Model Comparison: Unlensed vs. Microlensed hypothesis

In this section, we study the detectability of microlensing effects and discuss the challenges associated with it. In other words, we do a model comparison study between the unlensed and microlensed hypothesis (see Sect. 2.3.4 for details).

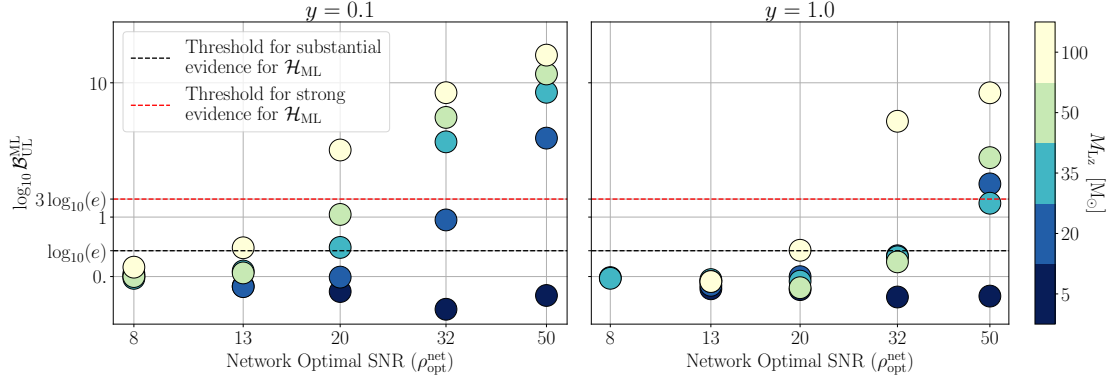


Figure 3.9: The figure shows log Bayes factor values, $\log_{10} \mathcal{B}_{\text{UL}}^{\text{ML}}$, for the evidence for microlensed hypothesis (\mathcal{H}_{ML}) over unlensed hypothesis for varying network SNR, $\rho_{\text{opt}}^{\text{net}} \in \{8, 13, 20, 32, 50\}$, redshifted lens mass, $M_{\text{Lz}} \in \{5, 20, 35, 50, 100\} M_{\odot}$, and impact parameter values, $y \in \{0.1, 1.0\}$.

In Fig. 3.9, we show Bayes factor values, $\log_{10} \mathcal{B}_{\text{UL}}^{\text{ML}}$, for the evidence of microlensed hypothesis over unlensed hypothesis for varying network SNR, $\rho_{\text{opt}}^{\text{net}} \in \{8, 13, 20, 32, 50\}$, redshifted lens mass, $M_{\text{Lz}} \in \{5, 20, 35, 50, 100\}$, and impact parameter values, $y \in \{0.1, 1.0\}$. A low impact parameter value of 0.1 is chosen to foresee results in the case of best-case scenarios while $y = 1$ represents the characteristic value of y . For microlens parameter recoveries, we set priors as $p(M_{\text{Lz}}) \propto \text{LogUniform}(10^{-1}, 10^5)$ and $p(y) \propto y$, $y \in (0.01, 3.00)$. We limit ourselves to only lower microlens masses ($M_{\text{Lz}} \leq 100 M_{\odot}$) because, from an astrophysical standpoint, more massive BH lenses are less probable. The black and red lines correspond to a Bayes factor value of e and e^3 , respectively, and mark the threshold for the positive and strong evidence for microlensing. This threshold has been set following the interpretation of Bayes factors as given in [Kass & Raftery \(1995\)](#), which sets a higher cutoff for the strong evidence as compared to the Jeffrey's scale ([Deutsch 1999](#))⁷. In this and subsequent sections, we will use the terms "positive" and "strong" to characterise the strength of evidence in accordance with the terminology used in the aforementioned references. We can see how SNR exponentially increases the Bayes factor values, especially in the left panel for $y = 0.1$, where microlensing effects are higher than in the right panel. We find that up to an SNR of 13, microlensing effects due to $M_{\text{Lz}} < 100 M_{\odot}$ do not show any interesting Bayes Factor recoveries in favour of microlensing. It is important to note that an SNR of 13 is above the expected average SNR of the detected events (≈ 12 ; see [Schutz \(2011\)](#)), as PDF for the SNR goes as $p(\rho) \propto \rho^{-4}$. Considering the fact that in the real GW data noise will bring in additional complexities,

⁷However, we note that a better approach to interpreting the Bayes factor values would be to do a background injection study.

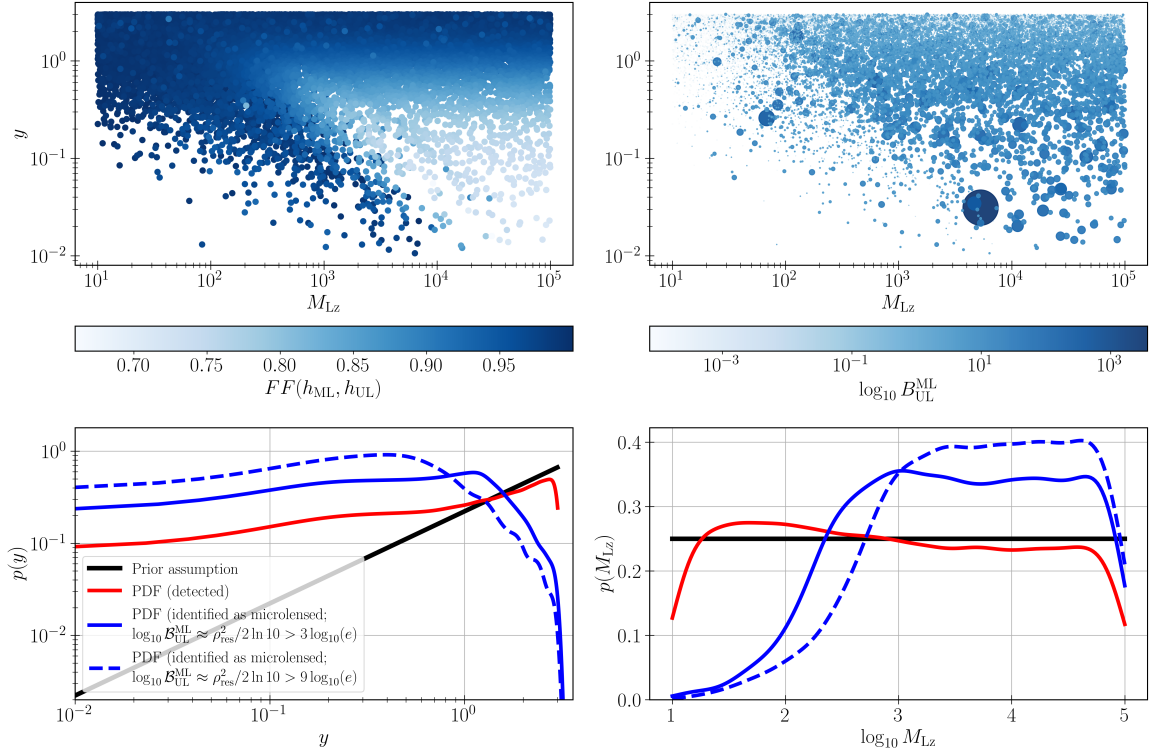


Figure 3.10: Bayes factor study for the microlensed population estimated using the FF and the SNR (ρ), i.e., $\ln \mathcal{B}_{\text{UL}}^{\text{ML}} \approx (1 - FF^2)\rho^2/2$. *Top row:* FF values and the Bayes factor values for the evidence of microlensing over the unlensed hypothesis ($\log_{10} \mathcal{B}_{\text{UL}}^{\text{ML}}$) are shown in the microlens parameter space of the observed population. *Bottom row:* The probability density functions (PDFs) for the microlens parameters are shown for four cases: (i) our prior assumption, (ii) the detected population (selection bias), (iii) the population that is detected and also correctly identified as being microlensed assuming a threshold of $\log_{10} \mathcal{B}_{\text{UL}}^{\text{ML}} > 3 \log_{10}(e)$, and (iv) same as (iii) but with a higher threshold of $\log_{10} \mathcal{B}_{\text{UL}}^{\text{ML}} > 9 \log_{10}(e)$. These threshold values are chosen to investigate various confidence levels in a microlensed event detection while also taking into account the uncertainties related to using the approximation for $\mathcal{B}_{\text{UL}}^{\text{ML}}$.

it seems highly unlikely that we will detect microlensing for $M_{\text{Lz}} < 100 M_{\odot}$ with current sensitivities of the detectors. However, for high SNR events, microlensing effects from even small mass microlenses become detectable, such as $M_{\text{Lz}} \gtrsim 20 M_{\odot}$ for SNR 50.

In the right panel of Fig. 3.9, we notice that for the characteristic value of the impact parameter $y = 1$, the microlensing model is not favoured for $M_{\text{Lz}} < 50 M_{\odot}$ upto an SNR of 32, which further showcases the difficulty of correctly identifying a microlensed event. An important consequence of this is the fact that in dark matter constraint studies using microlensing, one should, in principle, incorporate SNR dependence. That is, the

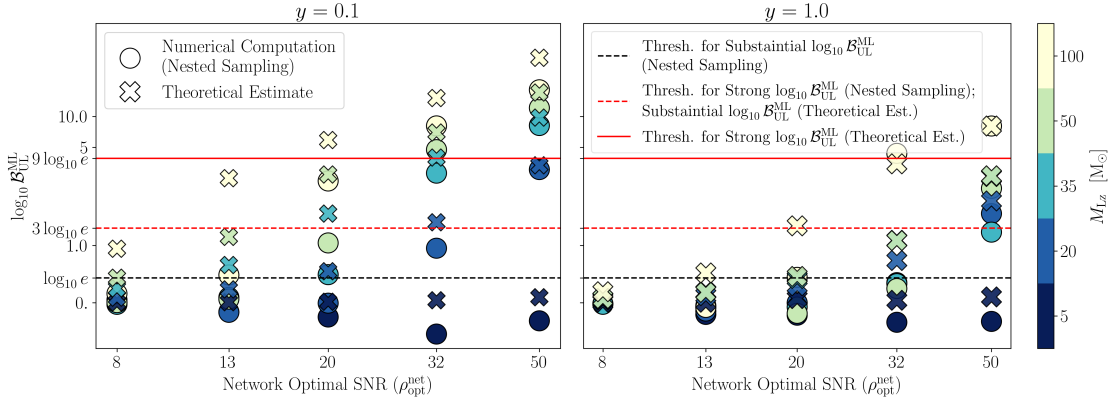


Figure 3.11: Same as Fig. 3.9, but with added theoretical estimates (cross marks) using Eq. 2.33 for comparison. For nested sampling, the dashed black and red lines have a similar meaning as in Fig. 3.9, representing the threshold values for positive and strong evidence for microlensing, respectively. For the theoretical estimate, these values are depicted using dashed and solid red lines, respectively.

microlens parameter space that can be correctly identified to be a microlensed event is SNR dependent. Hence, a non-detection of the microlensed event can only put a constraint on the fraction of dark matter in the parameter space where it is sensitive to detecting those microlensing effects. If such an SNR dependence is not included, it will result in an over-constraint on the dark matter fractions.

The aforementioned observation inspires us to inquire about the microlens parameters that are most likely to be detected and also correctly identified as microlensed. In Fig. 3.8, we presented the distribution of the detected microlensed population. Now in Fig. 3.10, we conduct a more thorough analysis of this population to determine such parameter space where microlensing is most likely to be detected. Although a rigorous approach would require computing Bayes factors for the population using nested sampling algorithms, it will be highly expensive computationally. Therefore, we exploit the expression given in Eq. 2.33 to estimate the Bayes factors. However, a more rigorous study would require estimating Occam's factor as well. As mentioned in 2.3.4, since the Occam's factor term is just the ratio of the posterior to the prior volume, one can estimate it using the (inverse of) Fisher matrix by computing the ratio of the uncertainty in the recovered value of an extra parameter to the prior volume for that parameter. These uncertainties in the parameter roughly scale inversely with the SNR.

Assuming the prior volume to be a unit hypercube of d dimensions, in the case of a true microlensed signal with a sufficient SNR value, the information content in the posteriors would be higher for the microlensing (ML) hypothesis compared to the unlensed

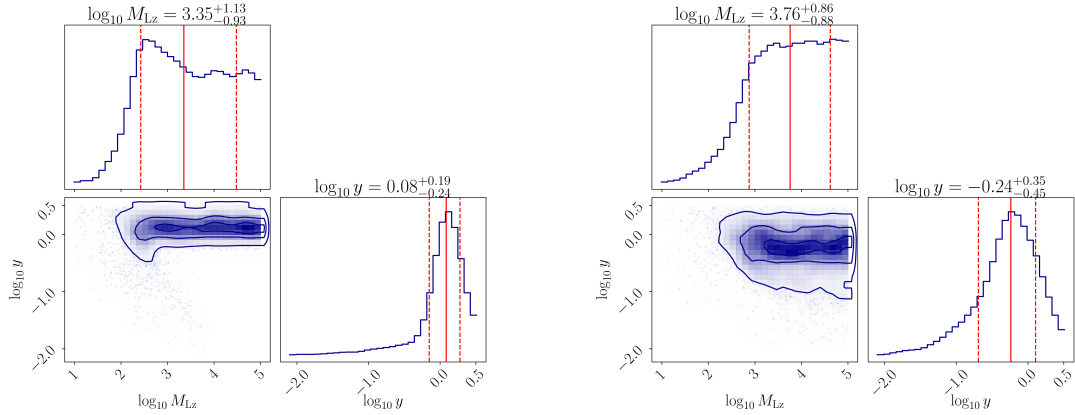
(UL) hypothesis. Consequently, the ratio of the posterior volume to the prior volume would be smaller for the \mathcal{H}_{ML} hypothesis. Thus, the second term in Eq. 2.32 becomes

$$\ln \mathcal{O}_{\text{UL}}^{\text{ML}} \approx \ln \frac{\Delta V_{\text{ML}}}{\Delta V_{\text{UL}}} < 0. \quad (3.5)$$

Since we are neglecting this term, *we conclude that we are mostly over-estimating the Bayes factors when we use Eq. 2.33*. This reasoning is supported by the observations in Fig. 3.11. In this figure, we compare the numerically computed Bayes factors (using nested sampling) displayed in Fig. 3.9 with the theoretically estimated $\mathcal{B}_{\text{UL}}^{\text{ML}}$ values (indicated by cross marks) obtained using Eq. 2.33. We observe that, in almost all cases, our approximation tends to overestimate the true value of $\mathcal{B}_{\text{UL}}^{\text{ML}}$, and its performance improves as the SNR increases. For example, one can see that for SNR values of 32 and 50 in Fig. 3.11, the difference between the numerically computed Bayes factors with that of theoretically estimated ones is quite small compared to what we notice for lower SNR values ($\lesssim 20$).

Our investigation demands that when estimating $\log_{10} \mathcal{B}_{\text{UL}}^{\text{ML}}$ using Eq. 2.33, we employ a higher threshold for positive/strong evidence for microlensing compared to established scales like Kass-Raftery's scale (Kass & Raftery 1995). For our purpose, we choose this threshold heuristically based on our observation in Fig. 3.11. Specifically, we set the threshold values to be three times that of the Kass-Raftery's scale. For positive evidence for microlensing, we consider $\log_{10} \mathcal{B}_{\text{UL}}^{\text{ML}} \in (3 \log_{10}(e), 9 \log_{10}(e))$. For strong evidence, we require $\log_{10} \mathcal{B}_{\text{UL}}^{\text{ML}} > 9 \log_{10}(e)$. By setting these higher thresholds, we aim to ensure that our assessment of positive or strong evidence for microlensing is conservative and accounts for the potential overestimation indicated by our analysis.

We now apply the method described above to analyse the distribution of Bayes factors using FF values, as given by Eq. 2.33, for the population generated in Sect. 3.4. In the top row of Fig. 3.10, we present the FF values and the corresponding Bayes factor values ($\log_{10} \mathcal{B}_{\text{UL}}^{\text{ML}}$) in the microlens parameter space of the observed population. While in the bottom row, the probability density functions (PDF) for the microlensing parameters, M_{Lz} and y , are shown for four cases: (i) our prior assumption (black line), (ii) the detected population (red line; as also shown in the bottom row of Fig. 3.8), (iii) population that is detected and also correctly identified as being microlensed assuming thresholds as discussed above, i.e., $\log_{10} \mathcal{B}_{\text{UL}}^{\text{ML}} > 3 \log_{10}(e)$ (solid blue line; representing threshold for positive evidence for ML), and (iv) a higher threshold of $\log_{10} \mathcal{B}_{\text{UL}}^{\text{ML}} > 9 \log_{10}(e)$ (dashed blue line; representing threshold for strong evidence for ML). Here we employ two distinct threshold values to study how different levels of evidence for microlensing influence the probability density in the lensing parameter space. We observe that the FF values exhibit similar behaviour and range of values as shown in Fig. 3.1, where the source binary was kept fixed. The Bayes factor values also show interesting values in the region where FF values are low (darker and bigger circles), especially the lower end of the *wave zone* as



(a) $\log_{10} \mathcal{B}_{\text{UL}}^{\text{ML}} \in (3 \log_{10}(e), 9 \log_{10}(e))$; Expected microlensed population detectable with low confidence. (b) $\log_{10} \mathcal{B}_{\text{UL}}^{\text{ML}} > 9 \log_{10}(e)$. Expected microlensed population detectable with high confidence.

Figure 3.12: The corner plots depict the probable region in the microlensing parameter space for a point lens that can be detected and identified as a microlensed event in the joint network of LIGO–Virgo detectors, assuming the targeted O4 sensitivities. The Bayes factor values of the population and the probability density functions (PDFs) of the microlens parameters are explicitly shown in Fig. 3.10. The panels on the *left* and *right* use different threshold values for $\log_{10} \mathcal{B}_{\text{UL}}^{\text{ML}}$, which is estimated using the expression $\ln \mathcal{B}_{\text{UL}}^{\text{ML}} \approx (1 - FF^2)\rho^2/2$. These threshold values are chosen to explore different confidence levels for claiming a microlensed event detection while also considering the uncertainties associated with this approximation. The contour plot in the 2D space and the red lines in the 1D distributions represent credible regions with quantile values of 16%, 50%, and 84%.

discussed in 2.2. On the other hand, we do not observe any appreciable $\mathcal{B}_{\text{UL}}^{\text{ML}}$ values for lower M_{Lz} and y values, where the number of detections is also relatively low. When we set a threshold of $3 \log_{10}(e)$ for the recovered $\log_{10} \mathcal{B}_{\text{UL}}^{\text{ML}}$, we find that the distribution of $p(y)$ peaks around $y = 1$, while $p(M_{\text{Lz}})$ peaks at $\log_{10} M_{\text{Lz}} = 3$. Additionally, there is a slight bimodality in the distribution of $p(y)$, with another peak observed at a lower y value around 0.2. This bimodality arises from the fact that although lower y values lead to stronger microlensing effects, their detection probability is lower compared to those with higher y values. When we increase the threshold to $\mathcal{B}_{\text{UL}}^{\text{ML}} > 10$, we find that the bimodal distribution in y converges to a value close to the lower peak at $y \sim 0.3$. Moreover, for $p(M_{\text{Lz}})$, a higher threshold causes the peak to shift towards higher M_{Lz} values, around $M_{\text{Lz}} \sim 4.5$.

In Fig. 3.12, we provide corner plots for the microlens parameters, showcasing the

Table 3.1: Effect of using unlensed templates during the search for microlensed signals. Below, "Total" refers to all the events; "ML" ("UL") refers to the case when microlensed (unlensed) templates are employed for search; N_1 depicts the total number of events with $\log_{10} \mathcal{B}_{\text{UL}}^{\text{ML}} > 3 \log_{10}(e)$, indicating events with mostly positive evidence in favour of microlensing; N_2 depicts the total number of events with $\log_{10} \mathcal{B}_{\text{UL}}^{\text{ML}} > 9 \log_{10}(e)$, indicating events with strong evidence in favour of microlensing. Here we estimate $\log_{10} \mathcal{B}_{\text{UL}}^{\text{ML}}$ using Eq. 2.33. $\epsilon_{\text{UL}}^{\text{ML}}$ denotes the fractional loss of microlensed signals when unlensed templates are used during the search, as defined in Eq. 3.6.

	Total	N_1	N_2	N_1/Total [%]	N_2/Total [%]
ML	25458	8137	3734	32.0	14.7
UL	23318	6481	2653	27.8	11.4
$\epsilon_{\text{UL}}^{\text{ML}}$ [%]	8.4	20.4	29.0	13.1	22.4

distribution of microlensed events that were detected and (potentially) identified as microlensed within our microlensed population. The contour plot in the 2D space and the red lines in the 1D distributions represent credible regions with quantile values of 16%, 50%, and 84%. These correspond to the median with 1σ uncertainty on either side. The left panel of the figure depicts cases where the evidence for the microlensing (ML) hypothesis is positive, specifically when $\log_{10} \mathcal{B}_{\text{UL}}^{\text{ML}} \in (3 \log_{10}(e), 9 \log_{10}(e))$. In simpler terms, the left panel predicts the distribution of microlensed events that would be interesting candidates in the search for microlensed events but may not be definitively confirmed as such. The conclusions drawn from these events would likely remain *inconclusive* due to various systematics that could mimic similar behaviour. Up to an uncertainty of 1-sigma , *the most probable parameters*⁸ *that will show only positive evidence for ML are* $(\log_{10} M_{\text{Lz}}, y) = (3.35_{-0.93}^{+1.13}, 1.21_{-0.51}^{+0.68})$. Meanwhile, the right panel highlights events that would be identified as microlensed with a high degree of confidence, with $\log_{10} \mathcal{B}_{\text{UL}}^{\text{ML}} > 9 \log_{10}(e)$. *The most probable parameters for such confidently detected microlensed events would be* $(\log_{10} M_{\text{Lz}}, y) = (3.76_{-0.88}^{+0.86}, 0.58_{-0.37}^{+0.70})$.

It is interesting to note that among all the super-threshold events detected by LIGO and Virgo detectors so far, the most compelling candidate in the microlensing search was GW200208_130117 during the third observing run ([The LIGO Scientific Collaboration](#)

⁸We note that a lot of reasonable assumptions have gone into making such a prediction. The population is generated assuming an O4-like sensitivity. The Bayes factor estimation is not rigorous and we ignore some other factors such as noise systematics, its degeneracy with other physical effects like eccentricity, etc.

et al. 2023a; Janquart et al. 2023). This event exhibited the highest Bayes factor value for the evidence of microlensing over the unlensed hypothesis, with a value of $\log_{10} \mathcal{B}_{\text{UL}}^{\text{ML}} \sim 0.9$ ⁹. However, the paper concluded the data is inconclusive about the microlensing hypothesis, and it was hinted that the effect could be due to some short-duration noise fluctuations in one of the detectors. The recovered microlens parameter values for the event, with median values and 1-sigma errors, are $(\log_{10} M_{\text{Lz}}, y) = (3.15^{+0.18}_{-0.21}, 1.07^{+0.61}_{-0.32})$. Interestingly, we note that this recovered value is remarkably close to our predicted value of $(\log_{10} M_{\text{Lz}}, y) = (3.35^{+1.13}_{-0.93}, 1.21^{+0.68}_{-0.51})$ (see Fig. 3.13 for the comparison) for events that would only positively support the microlensed hypothesis. Hence, based on our population study, there is suggestive evidence in favour of the microlensing hypothesis for the event GW200208_130117. However, it is important to acknowledge that this study is not rigorous enough to claim lensing with certainty, and therefore, the ultimate nature of this event remains inconclusive.

Furthermore, in Table 3.1, we present the derived statistics from our population, particularly focusing on the fractional loss of signals caused by employing unlensed templates during the search for microlensed signals. The fractional loss, $\epsilon_{\text{UL}}^{\text{ML}}$, is defined as:

$$\epsilon_{\text{UL}}^{\text{ML}} \equiv 1 - \frac{n(\text{UL})}{n(\text{ML})}, \quad (3.6)$$

where $n(\text{UL})$ and $n(\text{ML})$ represent the number of events quoted in the row labelled as 'UL' and 'ML', respectively. These labels indicate scenarios where unlensed templates and microlensed templates are used to recover the signals, respectively. Within the parameter space of $M_{\text{Lz}} \in (10, 10^5)$ and $y \in (0.01, 3.00)$, we observe an approximate loss of 8% for the microlensed signals (refer to the first column, third row). However, this fraction is dependent on our chosen parameter space and does not fully capture the impact on potentially identifiable signals. Therefore, we further estimate the fractional loss for events that satisfy specific conditions: (i) $\log_{10} \mathcal{B}_{\text{UL}}^{\text{ML}} > 3 \log_{10}(e)$ (referred to as N_1 ; column 2), and (ii) $\log_{10} \mathcal{B}_{\text{UL}}^{\text{ML}} > 9 \log_{10}(e)$ (referred to as N_2 ; column 3). We find that the fractional loss of events in case (i) is $\sim 20\%$, while for case (ii) it increases to about 29%. It is expected that the fractional loss would increase with higher threshold values on Bayes factors, as the greater the microlensing effects, the more significant the loss in their SNR during the search process. Moreover, considering that real searches utilize template banks that discretely cover the parameter space, typically constructed with a maximum loss threshold of 3%, there is an additional loss of such microlensed signals during the search process. Specifically, for case (i) and case (ii), we find that the total fractional losses can reach up to 27% and 35%, respectively. *This observation suggests that neglecting the loss of microlensed*

⁹This value differs from the quoted value of 0.8 in The LIGO Scientific Collaboration et al. (2023a) as it has been recomputed by the authors using the GWMAT framework (Mishra, A., in prep.).

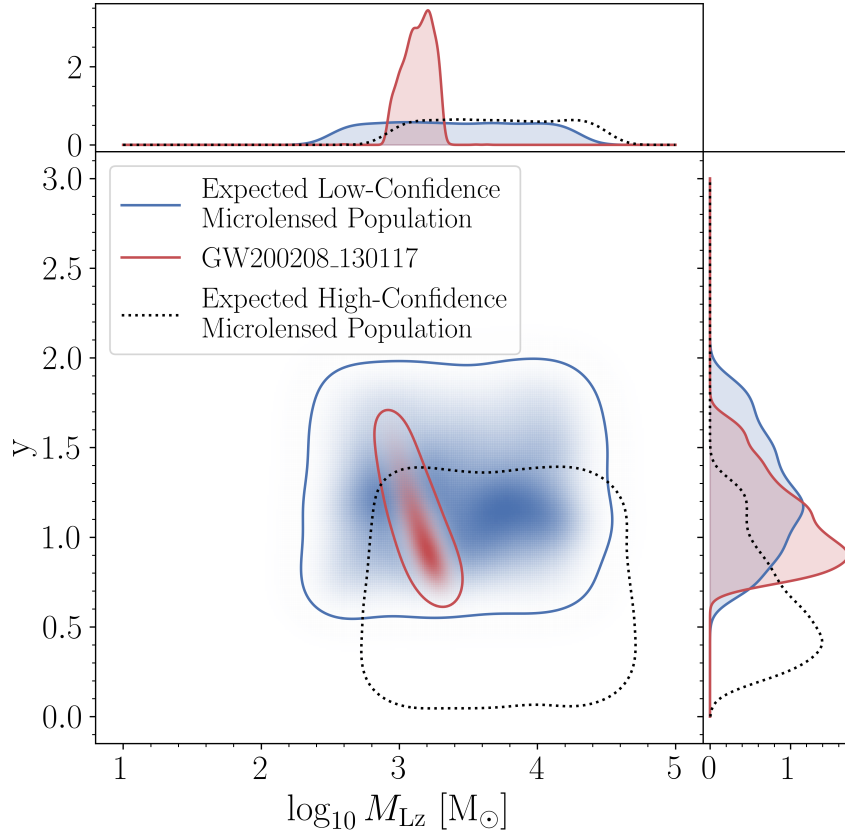


Figure 3.13: Comparison between the $1 - \sigma$ regions of the posteriors for the microlensed parameters of event GW200208_130117 (highlighted in red) and the predicted $1 - \sigma$ region of the low-confidence microlensed population derived from our population study (highlighted in blue). Additionally, the $1 - \sigma$ contour for the predicted high-confidence microlensed population is shown for reference (marked with a black dotted line).

signals during the search process (e.g., [Basak et al. 2022](#)) may impose an over-constraint on the fraction of compact dark matter based on the non-detection of microlensed GW signals.

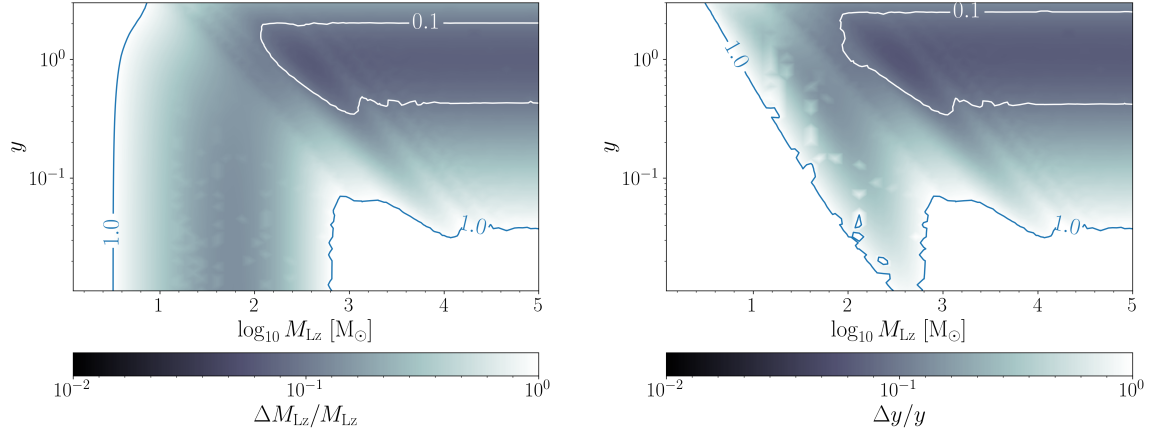


Figure 3.14: Statistical $1\text{-}\sigma$ relative uncertainties in the measurement of the redshifted lens mass $\Delta M_{Lz}/M_{Lz}$ (top panel) and impact parameter $\Delta y/y$ (bottom panel) in the (M_{Lz}, y) plane for a point lens. The white and blue lines correspond to 10% and 100% relative errors. In the white regions, the relative errors are larger than 100%. The system comprises GW150914-like signals with added microlensing effects. The SNR is kept fixed to 50 in the detector network of Hanford, Livingston and Virgo using projected O4 sensitivities.

3.6 Statistical Uncertainties in the measurement of lensing parameters using Fisher Analysis

In this section, we will estimate the statistical uncertainties in the inference of lensing parameters of a point-lens, namely the redshifted lens mass M_{Lz} and the impact parameter y , using Fisher analysis (see Sect. 2.3.5).

We compute the statistical uncertainties in M_{Lz} and y in the lensing parameter space spanning $\log_{10} M_{Lz} \in (0, 5)M_{\odot}$ and $y \in (0.01, 3)$. We introduce microlensing effects to a GW150914-like system with no spins and adjust the luminosity distance to maintain an optimal network SNR of 50 across the Hanford, Livingston, and Virgo detector network, using projected O4 PSDs (Abbott et al. 2018). To compute the covariance matrix, we utilize the publicly available package GWBENCH (Borhanian 2021). To ensure a well-conditioned Fisher matrix, we only vary the parameters $\Theta = \{\mathcal{M}, \eta, a_1, a_2, \log_{10} M_{Lz}, \ln y\}$. We employ the IMRPhenomXPHM WF approximant with lower and upper frequency cutoffs set at 20Hz and 1024 Hz, respectively, with a bin size of 2^{-4} Hz, which is adequate for the signal's duration in this context.

The results are shown in Fig. 3.14, where we plot the statistical relative uncertain-

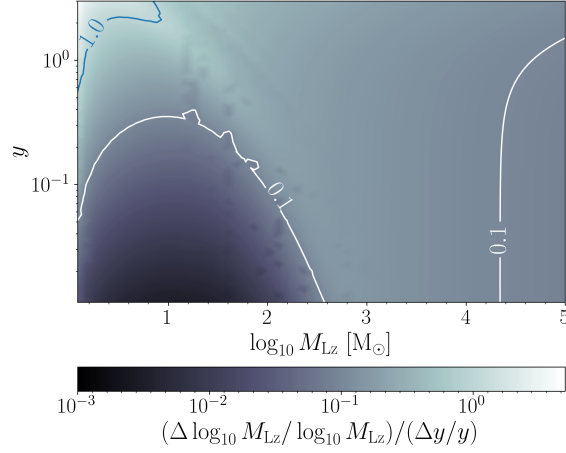


Figure 3.15: Comparison of the relative $1\text{-}\sigma$ uncertainties in the (log) redshifted lens mass $\log_{10} M_{Lz}$ and y . The relative uncertainties in the measurement of $\log_{10} M_{Lz}$ are almost always less than that in y .

ties in the measurement of the redshifted lens mass $\Delta M_{Lz}/M_{Lz}$ (top panel) and impact parameter $\Delta y/y$ (bottom panel) in the (M_{Lz}, y) plane for a point lens. The white and blue lines correspond to 10% and 100% relative errors, respectively. The relative errors in the white regions are larger than 100%.

Firstly, if we focus on the geometrical-optics regime in Fig. 3.14 (top-right corner; see Fig. 2.2 for reference), we observe mostly similar trends between $\Delta M_{Lz}/M_{Lz}$ and $\Delta y/y$. Notably, in the top-right corner of both panels, we observe that the relative uncertainties become independent of variation in the lens mass, i.e., they become constant for a given y value (see, for example, the white contour lines in the top-right corner). Similarly, we observe that as we decrease y below ~ 0.5 keeping $\log_{10} M_{Lz}$ to be high $\gtrsim 3$, the uncertainties increase drastically and can even exceed 100% for low $y < 0.1$. This is because in the geometrical-optics regime, the uncertainties in both the parameters depend only on y and the SNR of the signal. As we go away from $y = 1$, the uncertainties increase. For $y \gg 1$, they are proportional to, roughly, $\sim \sqrt{y}$, while for low $y \ll 1$, they increase as, roughly, $\sqrt{1/y}$. Since we have kept the SNR fixed, the uncertainties become roughly constant for a given y value when lens mass is high $\log_{10} M_{Lz} \gtrsim 3$. These results are consistent with [Takahashi & Nakamura \(2003\)](#), where a thorough investigation of relative uncertainties in the geometrical-optics regime is illustrated. We note that although the region in the bottom-right corner is not where geometrical optics is a good approximation, the divergence in the uncertainties is still well-captured by the expression obtained for that regime ([Takahashi & Nakamura 2003](#)).

In the long-wavelength regime (mainly bottom-left region; see Fig. 2.2 for reference), where the microlensing effects are weak, we notice that the uncertainties in y are much

larger than those in M_{Lz} . This is explained by the fact that in this regime, the modulations are proportional to the dimensionless frequency $\omega = 8\pi GM_{Lz}f/c^3$ in the leading order (Tambalo et al. 2023). Hence, the estimation of M_{Lz} is better than that of y , which leads to the fact that for a given M_{Lz} in this regime, y is only poorly constrained leading to high relative errors.

Lastly, in Fig. 3.15, we plot the ratio of relative uncertainties in the measurement of $\log_{10} M_{Lz}$ and y for comparison. We notice that in the parameter space of interest, $\log_{10} M_{Lz}$ is almost always better measured than y , owing to the majority of region having a value less than unity.

3.7 Discussion and Conclusion

In this chapter, we primarily examine the impact of microlensing caused by isolated microlenses on GW signals. We begin by illustrating how the time delay between microimages divides the microlens parameter space into three distinct regions. Next, we investigate how microlensing can significantly influence the observed SNR, match, and FF values. Subsequently, we analyze the microlensing-induced bias in the observed GW source parameters. Furthermore, we explore the statistical properties of microlensed GW signals and estimate the fraction of missed GW signals if we employ unlensed templates in the search. The distribution of Bayes factors for the population reveals certain regions in the microlensing parameter space that are more likely to be correctly identified as microlensed signals. Finally, we examine more complex and realistic scenarios involving the interaction of strongly lensed GW signals with a population of microlenses residing within lensing galaxies and study their effect on posterior overlap analysis.

Based on our analysis, the results are as follows:

1. Employing unlensed WFs to search for microlensed GW signals can significantly decrease the FF, reaching as low as $\sim 70\%$. The FF values decrease as we increase (decrease) the value of M_{Lz} (y). Consequently, the observed SNR also decreases. However, microlensing itself amplifies the signal and can significantly increase the SNR, with values exceeding 10 times higher in extreme cases. This behaviour overall increases the detector horizon and can even allow us to detect GW signals from high redshifts $z \gtrsim 2$, beyond the peak of the star-formation rate.
2. The correlation study reveals a strong correlation between the microlens parameters and the luminosity distance. Specifically, the parameter y exhibits a significant anti-correlation with the distance, reaching values exceeding 90% in certain cases. More-

over, we observe that the correlations between the microlens parameters and GW signal parameters are generally opposite in nature. For instance, a positive correlation of M_{Lz} with a GW signal parameter often implies an anti-correlation of y with the same parameter. Recovering microlensed GW signals using an unlensed WF model introduces strong degeneracies among the source parameters, particularly when the microlensing effects are significant and slowly varying, such as in the bottom-right corner of the long-wavelength regime (Fig. 2.2). These degeneracies exhibit a highly nonlinear relationship with variations in the microlens parameters. In other words, our analysis indicates that microlensing can lead to a rotation of the correlation among different pairs of parameters.

3. Recovering microlensed GW signals with unlensed GW signals can lead to significant bias in the estimated parameter values, particularly when the microlenses belong to the wave-dominated zone, where $f\tau_d \sim 1$. Among intrinsic parameters, the in-plane spin components, particularly the precession effective spin χ_p , are most affected, suggesting a degeneracy between the effects of microlensing and the modulations arising from spin-induced precession. The errors typically increase with longer signal durations (i.e., for lighter binaries) and can even exceed 90% for $(M_{Lz}, y) = (10^2 M_\odot, 1)$, which is a modest representative of microlensing through an intermediate-mass-black-hole (IMBH). This suggests that any signal showing signs of precession must also be analysed for the presence of microlensing signatures to avoid any erroneous claims regarding the presence of precession. However, vice-versa may not be true, i.e., it is unlikely that the presence of precession can bias microlensing searches. This is because the parameter space of unlensed signals always falls within the subset of the microlensed parameter space. Hence, unless significant WF systematics are involved in inferring the precession of a signal, such biasing is not expected. In addition, other intrinsic parameters related to binary component masses, chirp mass and mass ratio, can also be significantly affected. Although their relative errors is mostly within 10%, it can even exceed 50% when microlensing effects are strong. Moreover, KS-statistics show higher sensitivity of the posterior distribution to microlensing effects compared to the recovered best-fit values.
4. Among extrinsic parameters, the recoveries of luminosity distance are affected the most. In contrast, the trigger time and the sky-position parameters, RA and Dec (α and δ), are the best-recovered source parameters. This is expected since the localization of GW sources is mainly based on the observed time delays between each pair of interferometers and microlensing does not significantly affect them.
5. A population study of microlensed signals reveals that the fraction of potentially identifiable microlensed signals missed due to the use of usual unlensed templates during

the search is around $\epsilon_{\text{UL}}^{\text{ML}} \in (20\%, 30\%)$. Hence, neglecting the loss of microlensed signals during the search process (e.g., [Basak et al. 2022](#)) may impose an over-constraint on the fraction of compact dark matter based on the non-detection of microlensed GW signals. Furthermore, investigating the impact of selection bias on the distribution of microlens parameters in the observed signals reveals a significant deviation of the PDF of the impact parameter, $p(y)$, at low values of $y \lesssim 0.1$. Therefore, in contrast to the commonly used lower limit of 0.1 in microlensing searches of real data (e.g., [Abbott, R. and others 2021](#); [The LIGO Scientific Collaboration et al. 2023a](#)), a value of $y = 0.01$ is not as insignificant as previously thought. On the other hand, we only observe a mild preference for lower $M_{\text{Lz}} (< 10^3 M_{\odot})$ compared to larger ones, which primarily arises from the use of unlensed WFs in recovering microlensed signals.

6. A model comparison study highlights the challenges in confidently identifying microlensing by $\lesssim 100 M_{\odot}$ microlenses, especially with average SNR values of ~ 12 ([Schutz 2011](#)), unless the impact parameter y is very low (i.e., $y < 0.1$). However, for high SNR (~ 50) events, even microlenses with masses $M_{\text{Lz}} \gtrsim 20 M_{\odot}$ can be detected (assuming a characteristic value of $y = 1$). On the other hand, microlensing signatures for an event with $(M_{\text{Lz}}, y) = (10^2 M_{\odot}, 1)$ is not detectable up to an SNR value of around 25.
7. The Bayes factor analysis of our population of microlensed signals indicates certain region in $M_{\text{Lz}} - y$ parameter space have a higher probability of being detected and accurately identified as microlensed. The analysis reveals that events identified as only positively¹⁰ indicating microlensing would typically fall within the parameter space $(\log_{10} M_{\text{Lz}}, y) = (3.35_{-0.93}^{+1.13}, 1.21_{-0.51}^{+0.68})$. On the other hand, events that are expected to favour the microlensing hypothesis strongly would typically lie within the parameter space $(\log_{10} M_{\text{Lz}}, y) = (3.76_{-0.88}^{+0.86}, 0.58_{-0.37}^{+0.70})$.
8. In the GWTC-3 catalog ([Abbott et al. 2023](#)), the most compelling candidate in the microlensing search thus far is the event GW200208_130117, which exhibited the highest Bayes factor of $\log_{10} \mathcal{B}_{\text{UL}}^{\text{ML}} \sim 0.9$ ([The LIGO Scientific Collaboration et al. 2023a](#); [Janquart et al. 2023](#)). The recovered values of the microlens parameters for this event, including median values and 1-sigma errors, are $(\log_{10} M_{\text{Lz}}, y) = (3.15_{-0.21}^{+0.18}, 1.07_{-0.32}^{+0.61})$. Interestingly, we note that this recovered value is remarkably close to our predicted value of $(\log_{10} M_{\text{Lz}}, y) = (3.35_{-0.93}^{+1.13}, 1.21_{-0.51}^{+0.68})$ (see Fig. 3.13) for events that would only positively support the microlensing hypothesis. Hence, based on our population study, there is suggestive evidence in favour of the microlensing hypothesis for the

¹⁰We use the terms "positive" and "strong" to characterise the strength of evidence, in accordance with the terminology used in Jeffreys' or Kass-Raftery's scale for interpreting Bayes Factor values ([Deutsch 1999](#); [Kass & Raftery 1995](#)).

CHAPTER 3. EFFECT ON INFERRED PARAMETERS

event GW200208_130117. However, it is important to acknowledge that further work is required to confirm lensing with certainty, and the true nature of this event remains inconclusive.

In summary, this extensive investigation across various sections sheds light on the diverse effects of microlensing on GW signals. The findings contribute to our understanding of the detectability, parameter estimation biases, and population characteristics associated with microlensed signals.

In future research, it is crucial to distinguish the effects of microlensing from other physical effects, such as eccentricity, precession, tidal heating, etc., as microlensing has the potential to alter the morphology of signals. Furthermore, it is important to investigate whether these effects can lead to false triggers in various tests of general relativity (GR). Additionally, there is a need to delve deeper into the impact of microlensing on strongly lensed GWs and explore their implications for future searches.

Chapter 4

Beyond isolated point lens model: Complex configurations of microlensing

Although an isolated point mass lens model offers many insights into the nature of microlensing and is helpful for pedagogical reasons, it may not be astrophysically viable. It is highly unlikely that isolated compact objects would be roaming around freely in the universe. However, a more realistic scenario is that of a compact object, or a population of them, residing in a macro-potential (strong lens potential), such as lensing galaxies, clusters, etc., which we now study in this chapter.

This chapter is mainly based on our understanding from the papers [Mishra et al. \(2021\)](#), [Meena et al. \(2022\)](#), and (Mishra, A., in prep.).

4.1 Numerical Computation of the Amplification Factor

In a realistic scenario of strong lensing, the possibility of a GW signal encountering a massive isolated point lens is much less relative to it encountering a microlens population. Typically, microlensing of strongly lensed images happens due to the population of point mass lenses instead of a single point mass lens. As a result, the time delay factor, t_d , in Eq. 2.3 is modified and includes a contribution from the macromodel in terms of the convergence and shear at the image position, and the population of microlenses near the macroimage. The resultant potential then becomes $\psi \rightarrow \psi_{\text{total}} = \psi_{\text{SL}} + \psi_{\text{ML}}$, where ψ_{SL} is the macromodel potential and ψ_{ML} is the lens potential due to the microlensing population embedded in the macromodel. These contributions are given by ([Suyu et al. 2024](#); [Saha &](#)

(Williams 2011)

$$\begin{aligned}\psi_{\text{ML}}(\mathbf{x}) &= \sum_k \frac{m_k}{M_0} \ln |\mathbf{x} - \mathbf{x}_k|, \\ \psi_{\text{SL}}(\mathbf{x}) &= \frac{\kappa}{2} (x_1^2 + x_2^2) + \frac{\gamma_1}{2} (x_1^2 - x_2^2) + \gamma_2 x_1 x_2,\end{aligned}\tag{4.1}$$

where m_k and \mathbf{x}_k denote, respectively, the mass and position of the k -th point mass lens in the population; M_0 is an arbitrary mass value as defined in Eq. 2.4; κ and (γ_1, γ_2) represent, respectively, the dimensionless surface mass density of the mass sheet of the lens plane (or convergence) and the components of shear due to the presence of the macrolens. Here, we assume constant κ and γ values since they are usually slowly varying functions of the galactic plane coordinates¹ The diffraction integral, Eq. 2.5, with the above lens potential, containing population of microlenses, cannot be solved analytically, in which case one has to use numerical methods (e.g., Ulmer & Goodman 1995; Diego et al. 2019), to obtain an approximate solution.

Except for the most trivial lens models, like that of an isolated point mass, the Fermat potential $\psi(\mathbf{x})$ takes a complicated form, in which case no analytical form can be derived straightforwardly. Furthermore, it is highly inefficient to numerically integrate the diffraction integral, Eq. 2.5, because of the oscillatory nature of the integrand and the fact that the direct calculation of $F(f)$ is a three-dimensional problem in x_1 , x_2 and f . Hence, one needs to use a numerical method that is more efficient and resolves the problems mentioned above. Such numerical methods have been described in UG95 and D19. In the current work, we follow the method of UG95 to calculate the magnification factor that is described below in Sect. 4.1.1. Subsequently, we also demonstrate the validity of our code for both minima and saddle points macroimages. In Sects. 4.1.2 and 4.1.3, we consider microlensing for two elementary cases, namely, an isolated point mass lens and a point lens situated near a minima-type macroimage in the presence of an external shear. Generally, simulating amplification curves for saddle points is nontrivial, and we discuss the issue separately in Sect. 4.1.4. We also describe our methodology to deal with saddle points macroimages and perform numerical tests to verify our results for simple lensing configurations.

4.1.1 Formalism

By using the methods of contour integration and Fourier transformation (\mathcal{F}), UG95 splits the problem of calculating $F(f)$ into two parts and reduces it into two dimensions as

¹However, we note that the validity of this assumption near highly-magnified macroimages might break down.

described below. Firstly, we define $\Upsilon(\nu) \equiv iF(\nu)/\nu$, assuming \mathbf{y} to be fixed. Then, we have

$$\begin{aligned}\mathcal{F}[\Upsilon(\nu)] &\equiv \tilde{F}(\tau') = \int d^2\mathbf{x} \int d\nu \exp(i2\pi\nu[\tau_d(\mathbf{x}) - \tau']) \\ &\Rightarrow \tilde{F}(\tau') = \int d^2\mathbf{x} \delta[\tau_d(\mathbf{x}) - \tau'],\end{aligned}\tag{4.2}$$

where $\tau' \equiv t/T_s$. Now, using $\nu = T_s f$ and the fact that $\mathcal{F}^{-1}[\tilde{F}(\tau')] = \Upsilon(\nu)$, we get

$$F(f) = \frac{f}{i} \int dt \exp(i2\pi ft) \tilde{F}(t),\tag{4.3}$$

where t represents the time delay value relative to an arbitrary reference time. For a minima-type macroimage, it is usually measured relative to the global minimum of the time delay surface, which marks the arrival of the first microimage. Whereas for macroimages at saddle points, we measure t relative to the arrival of the dominant saddle image (discussed in Sect. 4.1.4). Also, since we will have a finite range of $\tilde{F}(t)$ values in actual computation, we would need to further use an apodization function in Eq. 4.3 that removes the erroneous contribution from the edges. Otherwise, the computed values for both $|F|$ and θ_F would be significantly inaccurate and will show oscillatory behaviour at lower frequencies. In our analysis, we have used a cosine window function (e.g., see D19) that removes these irregularities and produces an excellent output, as discussed in the next subsections.

Equation 4.3 can then be evaluated as a contour integral. The area between the curves defined by $\tau_d(\mathbf{x}, \mathbf{y}) = \tau'$ and $\tau_d(\mathbf{x}, \mathbf{y}) = \tau' + d\tau'$ is $A = \tilde{F}(\tau')d\tau'$ up to first order. This area can also be evaluated as an integral $A = \oint ds dl$, where ds is the infinitesimal length along the contour and $dl = d\tau'/|\nabla_{\mathbf{x}}\tau_d|$ is the orthogonal distance between the two contours at the point of evaluation. Moreover, there can be more than one such contour, in general. Thus, by comparison of the areas evaluated using these two methods, we finally get

$$\tilde{F}(\tau') = \sum_k \oint_{C_k} \frac{ds}{|\nabla_{\mathbf{x}}\tau_d|}.\tag{4.4}$$

The summation is over all the contours, C_k , where $\tau_d(\mathbf{x}, \mathbf{y}) = \tau'$. Thus, for a given time-delay function (or lensing potential), we first compute $\tilde{F}(t)$ using Eq. 4.4 and then inverse Fourier transform it back to get the required $F(f)$, as in Eq. 4.3. Also, from Eq. 4.4, one can see that $\tilde{F}(t)$ is a smooth function except at critical time t_i where the images form, i.e., where $|\nabla_{\mathbf{x}}\tau_d| = 0$.²

²The reader is referred to the appendix of UG95 for further details.

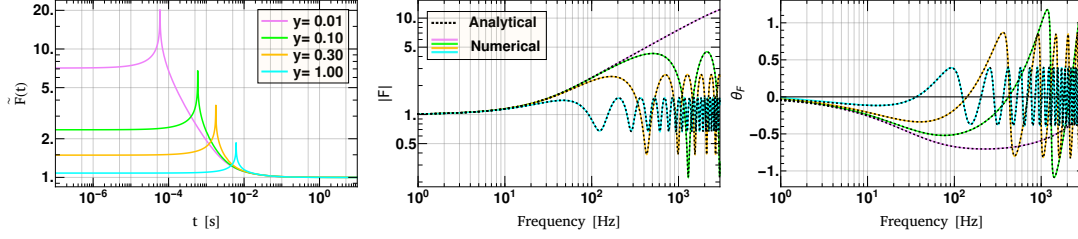


Figure 4.1: Test of numerical code shown for an isolated point lens of $100 M_{\odot}$ at $z_d = 0.5$ for a source at $z_s = 2$. The analysis is done for four different values of the impact parameter $y = \beta/\theta_0 = \{0.01, 0.1, 0.3, 1.0\}$. *Left:* The curves show numerically computed $\tilde{F}(t)$ normalised by a factor of 2π so that its value approaches unity in the no-lens limit (large time delays). *Middle and Right:* The curves show the comparison between the analytical and the numerically computed frequency-dependent amplification factor $F(f) = |F|e^{i\theta_F}$. The solid coloured curves have been numerically obtained from the $\tilde{F}(t)$ curves using Eq. 4.3, whereas the dotted black curves denote analytical results (see Eq. 2.8).

4.1.2 Testing Numerical Code: Isolated Point lens

Since we have the analytic form of $F(f)$ for an isolated point mass lens, Eq. 2.8, it can be used as an initial testing ground for our numerical code based on the above formalism. Hence, in this subsection, we compare $F(f)$ generated via two independent methods: analytical and numerical. We consider a $100 M_{\odot}$ point mass lens placed at a lens redshift $z_d = 0.5$, and a GW source placed at $z_s = 2$. The analysis has been done for four different non-zero source positions: $y = \beta/\theta_0 \in \{0.01, 0.1, 0.3, 1.0\}$. In the case of a point mass lens, two images of opposite parities are always formed, where positive and negative parities correspond to the minimum and the saddle point of the time-delay surface, respectively. The magnification of each image and the (dimensionless) time delay between them is given by

$$\mu_{\pm} = \frac{1}{2} \pm \frac{y^2 + 2}{2y\sqrt{y^2 + 4}}, \quad \Delta\tau_d = \frac{y\sqrt{y^2 + 4}}{2} + \ln \left(\frac{\sqrt{y^2 + 4} + y}{\sqrt{y^2 + 4} - y} \right). \quad (4.5)$$

In the left panel of Fig. 4.1, we show the normalised $\tilde{F}(t)$ curves, computed using Eq. 4.4, for different source positions. The x-axis represents the time delay measured with respect to the global minimum (situated at $t = 0$). Since we are interested in the LIGO frequency range of $10 - 10^4$ Hz, we need to compute $\tilde{F}(t)$ within the range $\sim 10^{-6} - 1$ sec such that we cover the region where $ft_d \lesssim 1$. So, we generate $\tilde{F}(t)$ values for a sufficient number of time-points within this interval and interpolate between them using the Hermite interpolation method to obtain a continuous function $\tilde{F}(t)$, which can be easily

inverse Fourier transformed to obtain $F(f)$ using Eq. 4.3. The $\tilde{F}(t)$ curves shown are normalised such that their value approaches one in the no-lens limit (large time delays). Since the time delay surface approaches a paraboloid at large values, this normalization is done by dividing the obtained curves by 2π (since Eq. 4.4 yields 2π in the no-lens limit, i.e., for circular contours). In this way, the curves start from a value corresponding to the amplification of the image formed at the minimum, i.e., $\sqrt{\mu_+}$, and eventually approach unity at large time delay values. Between these two expected behaviours, it encounters a logarithmic divergence corresponding to the saddle point (image with negative parity). The time delay at the point of this divergence is the time delay between the two images (since the first image occurs at $t = 0$). As expected, we can see that this time delay between the images decreases as we move towards the lens (eventually becoming zero when $y = 0$) while the amplitude of the logarithmic pulse increases, increasing the magnification of the saddle point image.

In the middle and right panels of Fig. 4.1, we show the comparison between the analytical results (obtained using Eq. 2.8) and the numerical results for the computation of the amplification factor $F(f) = |F| \exp(i\theta_F)$. The black-dotted lines represent the $|F(f)|$ and θ_F calculated using the analytical formula given by Eq. 2.8, respectively. The different solid-coloured lines represent the $|F(f)|$ and θ_F values, which have been computed numerically using our code. For the numerical computation, we first generate $\tilde{F}(t)$ values using Eq. 4.4 and substitute it in Eq. 4.3 along with a cosine window function (because of the finite range of $\tilde{F}(t)$). As previously mentioned, without this anodization, the computed $F(f)$ values will show oscillatory behaviour, especially below 100 Hz.

As one can see from Fig. 4.1, the agreement between analytical and numerical values is excellent. In all cases, the factor $|F|$ approaches unity and the phase factor θ_F approaches zero as we go lower in the frequency ($f \ll t^{-1}$), which means that the lens is invisible for signals with large wavelengths compared to the Schwarzschild radius of the lens ($\lambda \gg R_{s0}$). The wave effects start to appear when $\lambda \sim R_{s0}$ ($ft \sim 1$), which causes modulation in the amplification factor. As the frequency increases ($\lambda \ll R_{s0}$), wave optics approaches ray optics, i.e., $F(f)$ oscillates rapidly about its geometric optics limit and the average magnification over a frequency range becomes independent of the frequency (as in strong lensing). In the frequency range shown in the figure, only the blue curve ($y = 1.0$) has been able to approach the ray optics limit approximately. In general, for a point lens, the average values of $|F|$ and θ_F at high frequencies approach $\sqrt{\mu_+}$ and zero, respectively, in accordance with 2.7. We notice that our numerical code recovers all the features mentioned for $\tilde{F}(t)$ and $F(f)$ very well.

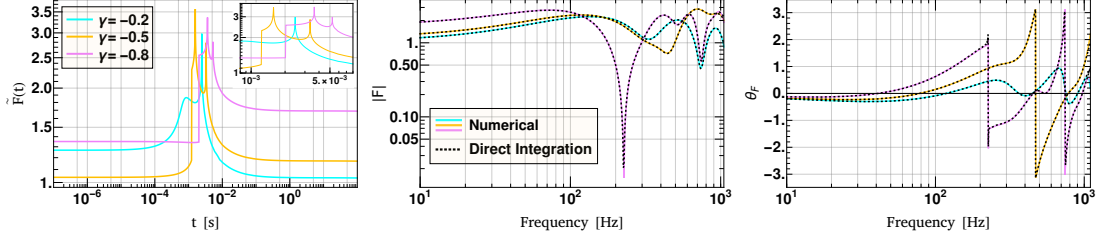


Figure 4.2: Test of numerical code shown for a point mass microlens of $100 M_{\odot}$ at $z_d = 0.5$ in the presence of shear. The source is kept at $z_s = 2$ and the source position is fixed to $(y_1, y_2) = 0.4(\cos(\pi/8), \sin(\pi/8))$. The analysis is done for three different values of the shear $\gamma = \{-0.2, -0.5, -0.8\}$. *Left:* The curves show numerically computed $\tilde{F}(t)$ (using Eq. 4.4) normalised by a factor of 2π , which ensures that they approach their non-microlens (strong lensing) limit, $\sqrt{\mu} = (1 - \gamma^2)^{-1/2}$, at large time-delay values. *Middle and Right:* The curves show the comparison between the numerical and the direct evaluation methods for computing the frequency-dependent amplification factor $F(f) = |F|e^{i\theta_F}$. The solid coloured curves have been numerically obtained from the $\tilde{F}(t)$ curves using Eq. 4.3, while the dotted black curves are obtained via direct (numerical) integration of Eq. 2.5.

4.1.3 Testing Numerical Code: Type-I (Minima) Macroimages

In this subsection, we test our code for a slightly complicated case where we place a point lens of $100M_{\odot}$ close to a minima-type macroimage of a source in the presence of an external shear (γ) with no convergence ($\kappa = 0$). Without loss of generality, one can always choose the principle direction of the shear to be horizontally aligned, in which case $\gamma_2 = 0$, $|\gamma| = \sqrt{\gamma_1^2 + \gamma_2^2} = |\gamma_1|$. Also, we place the macroimage at the origin of the source plane coordinates, i.e., at $\mathbf{y} = (0, 0)$. Unless stated otherwise, we adopt this reference frame throughout our analysis. Now, in this case, the effective lens potential in Eq. 2.3 can be written as

$$\psi_{\text{total}} = \ln \left(\sqrt{x_1^2 + x_2^2} \right) + \frac{\gamma}{2} (x_1^2 - x_2^2). \quad (4.6)$$

For the potential written above, we do not have an analytic solution for the diffraction integral, unlike in the case of a point mass lens. Therefore, to perform the numerical test for this case, we directly evaluate the double integral in Eq. 2.5 numerically and compare it with the one obtained via our code. However, the direct evaluation is slow and does not work well for higher frequencies where the integrand becomes too oscillatory.

For the computation of the amplification factor, the comparison between the direct numerical evaluation (dotted-black lines) and the one obtained via our code (solid-

coloured lines) is shown in the middle and right panel of Fig. 4.2. The analysis has been done for three different values of shear, $\gamma = \{-0.2, -0.5, -0.8\}$, keeping the source position fixed at $(y_1, y_2) = 0.4(\cos(\pi/8), \sin(\pi/8))$. Again, we observe that there is excellent agreement between direct numerical integration and the adopted numerical method of UG95. Also, the amplification curves approach the strong lensing amplification value for low-frequency values (no-microlensing limit) and the phase shift curves approach zero, as expected.

The corresponding calculations of $\tilde{F}(t)$ are shown in the left panel of Fig. 4.2. We have again normalised the plots by dividing the originally obtained ones by a factor of 2π . This normalization ensures that the curves approach to value $\sqrt{\mu} = (1 - \gamma^2)^{-1/2}$ in their no-microlensing (strong lensing) limit at large time delays. The time delay function, in this case, includes four stationary points, at least two of which are always real. In the $\tilde{F}(t)$ plots in Fig. 4.2, we observe that two microimages form in the case of $\gamma = -0.2$ (blue curve). One of these corresponds to the global minima (discontinuity at $t = 0$), and the other is for the saddle point (logarithmic peak at $t \sim 2.5$ ms). The other two values of the shear lead to a four-microimage geometry (orange and magenta curves). These microimages correspond to the two minima at a low time delay (two discontinuities) and the two saddle points at a higher time delay (two logarithmic peaks).

The direct evaluation of the diffraction integral (Eq. 2.5), adopted here for comparison with our code, cannot be used in the case of a microlens population (or for any nontrivial potential), as it becomes highly inefficient and does not perform well at higher frequencies because of the oscillatory integrand. Hence, this method can not be used further, and we solely rely on the method by UG95 to compute the amplification factor $F(f)$, using our code, throughout our analysis in the paper.

4.1.4 Testing Numerical Code: Type-II (Saddle) Macroimages

In this subsection, we describe the numerical scheme that is used to compute the amplification factor for a saddle point image. Unlike in the case of minima, here, the time delay contours neither close locally nor have a global minimum, as they are hyperbolic in nature rather than elliptical. However, if one chooses a sufficiently large region, the contribution from the neighbourhood of a saddle point is given by

$$\tilde{F}(t) = -2\sqrt{|\mu_-|} \log |t - t_i| + \text{non-singular part} + \text{constant} \quad (4.7)$$

where t_i and μ_- denote the time delay and magnification value corresponding to the saddle point, respectively, and the constant depends on the size of the region. By sufficiently large, we mean the size of the region should be such that $|u^{-2}\mu_-|^{-1/2} \gg 1$ near the

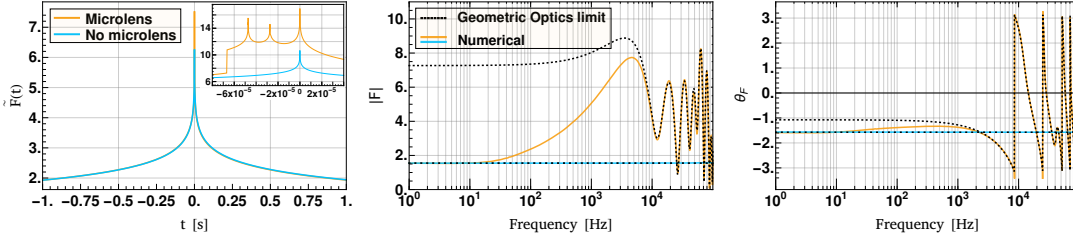


Figure 4.3: Test of our numerical code for the case of microlensing of a saddle point macroimage of a source at $z_s = 2$. The analysis is shown for two cases, with and without the presence of a $100 M_\odot$ microlens at $z_d = 0.5$. *Left:* The curves show numerically computed $\tilde{F}(t)$ obtained using Eq. 4.4. The presence of microlens, in this case, leads to a four-microimage configuration (see orange curve in the inset of the leftmost panel). *Middle and Right:* The curves show the comparison between the numerical and the analytical computation of $F(f) = |F|e^{i\theta_F}$ in the geometrical optics limit ($ft_d \gg 1$). The solid coloured curves have been numerically obtained from the $\tilde{F}(t)$ curves using Eq. 4.3, while the dotted black curves are obtained using Eq. 2.7. For the no microlens case, the geometrical optics limit is equivalent to the strong lens limit ($ft_d \ll 1$), while in general, the geometrical optics limit is reached at high frequencies $\gtrsim 10^4$ Hz where the $F(f)$ and $F(f)|_{\text{geo}}$ match (see dotted black and orange curves).

boundary, where u denotes the arc parameter of the contour (the reader is referred to Appendix B of UG95 for further details). The presence of a constant does not affect the computation of $F(f)$, especially when the integration range is chosen carefully, such that $\text{Re}\{\int dt e^{i2\pi ft}\} = 0$, and at higher frequencies where $\text{Im}\{\int dt e^{i2\pi ft}\} \ll 1$.

When a saddle point macroimage splits into microimages, there will always be a dominant saddle microimage which will dominate $\tilde{F}(t)$ and $F(f)$. In our simulation, we first find this image and measure the time delay values relative to this image, i.e., we fix the arrival time of the dominant saddle image at $t = 0$ (this arbitrary value is chosen for simplicity). Given a time delay function corresponding to a saddle point macroimage, one can find the location of the dominant saddle image numerically by iteratively computing the minima along the coordinate direction with increasing curvature and maxima along the coordinate direction with decreasing curvature. We then compute $\tilde{F}(t)$ values symmetrically about $t = 0$ and inverse Fourier transform it to get the required amplification factor values $F(f)$. A time range of $\mathcal{O}(2)$ s is sufficient for most cases since only the region closer to the divergence would mainly contribute. This is due to the fact that the contribution of the nearly flat part of $\tilde{F}(t)$ in the inverse Fourier transform will mostly be averaged out.

We test our numerical recipe for two cases, namely, in the absence of microlens and

in the presence of a $100 M_{\odot}$ microlens leading to a four–microimage configuration. For both cases, we fix our macro-magnification value to $\mu = -2.4$. In the case of no microlens, one expects to recover strong lensing values for the amplification factor, i.e., $|F| = \sqrt{|\mu|}$ and $\theta_F = -\pi/2$, since there will be no interference in the absence of microlenses. We indeed recover these values as shown in the middle and right panel of Fig. 4.3, where $|F| = \sqrt{2.4}$ and $\theta_F = -\pi/2$ (the Morse phase shift of saddle-type macroimages). The dotted black curve represents the geometrical optics limit, which, in this case, is equivalent to the strong lensing value, while the blue curve represents the $F(f)$ values as obtained through the code numerically.

In the presence of a $100 M_{\odot}$ microlens, we keep the source inside the caustic to get a four–microimage geometry. The time delay and magnification of these microimages are $(\frac{t}{10^{-5}\text{s}}, \mu) \in \{(-6.68, 11.98), (-4.73, -3.76), (2.73, -2.63), (0., -8.00)\}$. These microimages correspond to the discontinuity and spikes in the $\tilde{F}(t)$ as shown in the left panel of Fig. 4.3. Using Eq. 2.7, one can then find the $F(f)$ in the geometrical optics limit ($ft_d \gg 1$) and then compare it with the computed $F(f)$ at high frequencies. The comparison is shown in the middle and right panel of Fig. 4.3, where the dotted black curve represents the geometrical optics limit of $F(f)$ obtained using Eq. 2.7 and the solid orange curve shows the numerically computed $F(f)$ using the $\tilde{F}(t)$ curve as shown in Fig. 4.3.

As we can see, for both cases, the numerically computed $F(f)$ and the expected geometrical optics limit values are in excellent agreement. Furthermore, in Fig. 4.3, the $\tilde{F}(t)$ curves in both cases contain a dominant logarithmic divergence at $t = 0$ (the arrival time of the dominant saddle image) and is roughly symmetric around it, as expected. The difference in $F(f)$ below $\lesssim 10^4$ Hz is mainly due to the diffraction effects and clearly demonstrates why one needs to incorporate wave optics in such cases.

4.2 Single Microlens Embedded in a Macrolens

In this section, we will focus on some realistic configurations of microlensing where a point mass lens is embedded in a macrolens. As we discussed in the previous section, microlensing due to an isolated point mass lens entails interference patterns of two (micro-)images. However, when they are embedded in macrolens, it can even lead up to four images, or the microimages can be amplified because of macro-magnification. Therefore, the interference effects in the presence of macrolens can be severely affected. We will mainly focus on the impact of the macrolens on the microlensing effects.

As we saw in Sect. 2.2.1, the amplification factor in the case of an isolated point mass

CHAPTER 4. BEYOND ISOLATED POINT LENS MODEL: COMPLEX CONFIGURATIONS OF MICROLENSING

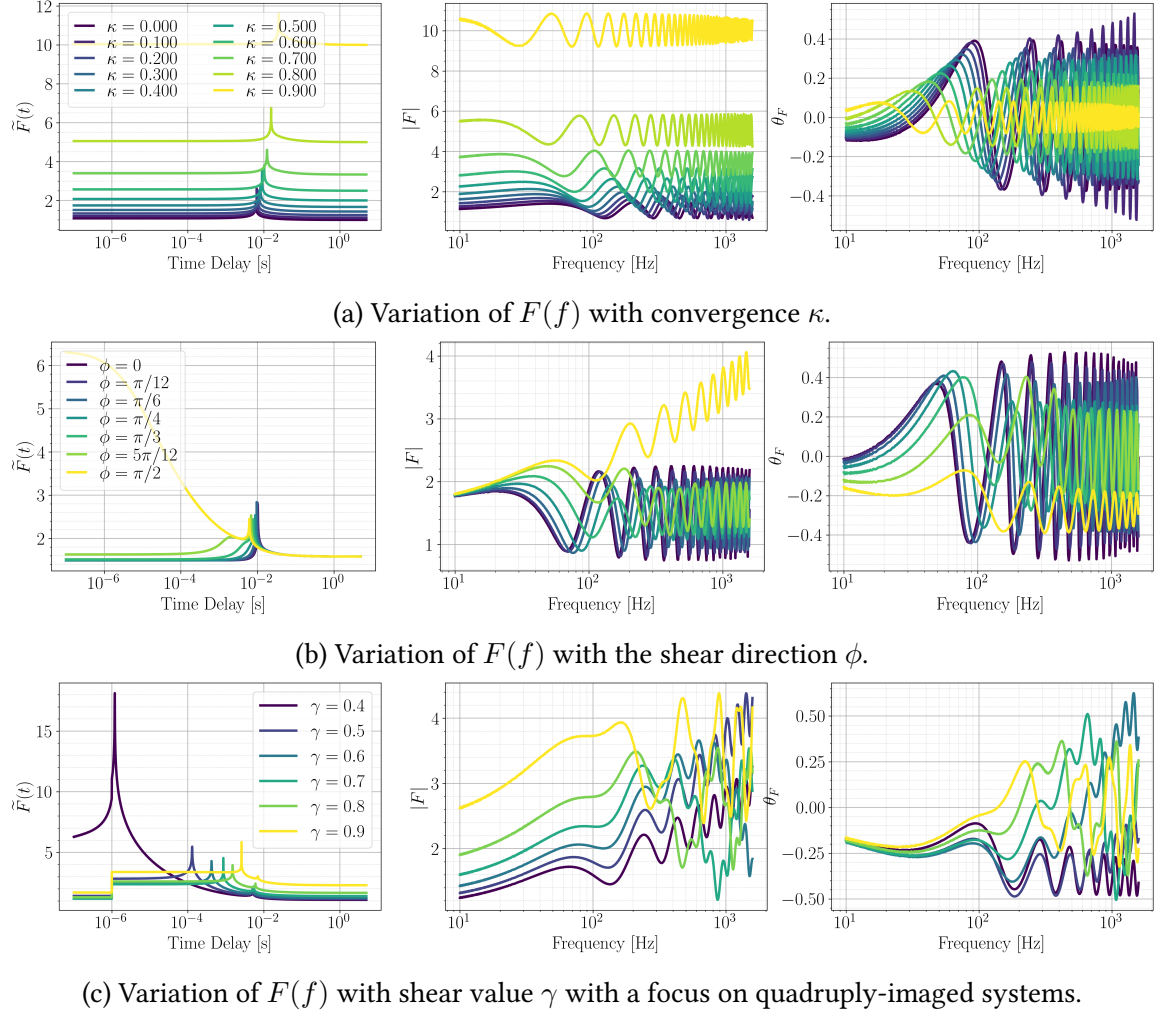


Figure 4.4: Illustration of how microlensing can vary with varying convergence (κ), shear (γ), and the direction of shear (ϕ) by numerically computing the amplification factor $F(f)$ for the time-delay function given in Eq. 4.8. We fix the parameters $\{M_{Lz} = 150 M_{\odot}, y = 1\}$, where we set the redshifts as $\{z_d = 0.5, z_s = 2.0\}$, for all the three cases, and vary the rest three in the three subplots. *Top panel:* variation of $F(f)$ with κ , where we fix the other two parameters as $\{\gamma = 0, \phi = \pi/2\}$, and vary $\kappa \in \{0.0, 0.1, 0.2, 0.3, 0.4, 0.5, 0.6, 0.7, 0.8, 0.9\}$. *Middle panel:* variation of $F(f)$ with the angle ϕ between the shear direction and the source relative to the lens. Here, we fix $\{\kappa = \gamma = 0.3\}$. *Bottom panel:* variation of $F(f)$ with shear value γ with a focus on quadruply-imaged systems. Here, we set $\kappa = 0$ and set $\phi = \pi/2$.

lens depends only on two parameters: the redshifted lens mass M_{Lz} and the impact parameter y . However, in the presence of a macrolens, it becomes a 5-dimensional problem, depending upon the parameters: $\{M_{Lz}, \mathbf{y}, \kappa, \gamma\}$. The source vector needs to be consid-

ered instead of just the impact parameter because its relative orientation relative to the shear direction (when γ is non-zero) can give different result even for the same y . We can split $\mathbf{y} \equiv \{y_1, y_2\}$ or $\mathbf{y} \equiv y\{\cos \phi, \sin \phi\}$, where ϕ is the angle between the shear direction and the source relative to the lens. The time-delay function in case of a microlens embedded in a macrolens can be written as:

$$\tau(\mathbf{x}, \mathbf{y}) = \frac{2GM_{Lz}}{c^3} [(x_1 - y_1)^2 + (x_2 - y_2)^2 - \kappa(x_1^2 + x_2^2) - \gamma(x_1^2 - x_2^2) - \ln(x_1^2 + x_2^2)], \quad (4.8)$$

where we set our origin on the microlens and assume the shear direction to be along x_2 .

In Fig. 4.4, we show how microlensing can vary with varying convergence, shear, and the direction of shear by numerically computing the amplification factor for the above time-delay function. For this exercise, we permanently fix two of the five parameters with $\{M_{Lz} = 150 M_\odot, y = 1\}$, where we set the redshifts as $\{z_d = 0.5, z_s = 2.0\}$. We study the effect of varying the other three parameters in the three subplots in Fig. 4.4. Particularly, in Fig. 4.4a, we study the variation with the convergence κ . For this, we further fix the other two parameters as $\{\gamma = 0, \phi = \pi/2\}$, and vary $\kappa \in \{0.0, 0.1, 0.2, 0.3, 0.4, 0.5, 0.6, 0.7, 0.8, 0.9\}$. Since amplification, in this case, is $\sqrt{\mu} = (1 - \kappa)^{-1}$, we see that with increasing κ , the $\tilde{F}(t)$ takes higher and higher values at large time delays ($\gtrsim 1$ s) in accordance with the $\sqrt{\mu}$ value (which is equivalent to the values towards which $|F(f)|$ converges to at lower frequencies). More importantly, we notice that with increasing κ , the time delay between the two microimages for a given case also increases (the rightward shift in the logarithmic peaks of $\tilde{F}(t)$). This leads to a relatively earlier onset of modulations. For example, if we observe the trend in the middle and right panel showcasing $F(f)$ values, we notice that the modulations start at lower and lower frequencies as κ increases (e.g., observe the first trough and crest of each curve). Moreover, we notice that the amplification at low time-delay values ($\lesssim 10^{-6}$ s) also increases with increasing κ . Since this amplification is directly related to the amplification of the minima type microimage ($\sqrt{\mu_+}$), we infer that $\sqrt{\mu_+}$ also increases with increasing κ in this case. Thus, the effect of increasing convergence is increasing the effective mass of the microlens in addition to amplifying the microimages themselves, thereby increasing the microlensing effects. However, we note that the effect of microlensing on a given GW signal may not be this monotonic, as it might be dependent on the GW source parameters themselves. So in this section, when we say pronounced microlensing effects, we primarily mean enhanced interference effects. We will quantify the effect of such microlensing scenarios on GWs in the subsequent sections.

Next, in Fig. 4.4b, we vary the angle ϕ between the shear direction and the source relative to the lens. For this study, we fix $\{\kappa = \gamma = 0.3\}$. Since ϕ does not affect the strong lensing magnification, it is fixed to $\mu = 2.5$. Here, $\phi = 0$ means in the direction of shear and $\phi = \pi/2$ orthogonal to it. We mainly focus on the first quadrant and vary ϕ

between 0 and $\pi/2$ to take values $\phi \in \{0, \pi/12, \pi/6, \pi/4, \pi/3, 5\pi/12, \pi/2\}$. We notice that the time delay between the microimages (logarithmic peaks in $\tilde{F}(t)$ curves) decreases as ϕ increases away from 0, with maximum for $\phi = 0$ and the least for $\phi = \pi/2$, by a factor of more than twice. However, observing the low time-delay values of $\tilde{F}(t)$, we notice $\sqrt{\mu_+}$ to be increasing with increasing ϕ . Meanwhile, noticing the logarithmic peaks, we find $\sqrt{\mu_-}$ to be decreasing with increasing ϕ . Since the critical curve divides images with different multiplicity, these behaviours tell us that when the source is placed in the direction of shear, the minima image forms farthest from the critical curve when $\phi = 0$ compared to other values while the saddle-point image forms closest to it. This is reversed as the source is orthogonal to the shear direction.

Lastly, in 4.4c, we focus on some microlensing scenarios involving quadruply-lensed systems. Here, we set $\kappa = 0$ and set $\phi = \pi/2$. It is possible to obtain four images from a single-point lens when significant shear is present. This is because the spherical symmetry of the lens is broken in the presence of shear, unlike in the case when only the convergence is present. Therefore, shear is necessary and sufficient for the formation of four images in the case of a point lens. Of these four images usually come, the first two images that arrive are usually minima type, while the other two are saddle-point type. It can be seen from the structure of $\tilde{F}(t)$ curves, which carry two discontinuities at low time delays followed by the two logarithmic peaks. As we can see, the interference patterns from these four microimages can be more complicated than in the case of interference from two microimages (doubly-lensed systems). For example, in the case of interference from two microimages, we usually see a simple pattern of troughs and crests. However, in the case of four microimages interfering, we see some additional features within a single crest and trough, which depends on the time delay between the microimages and their magnification.

4.3 Effect of microlens population present in lensing galaxies on strongly lensed GWs

4.3.1 Methodology

When a GW signal is strongly lensed by an intervening lensing galaxy or a galaxy cluster, it can interact with the microlenses present in the lens. These microlenses may consist of stars, stellar remnants (white dwarf, neutron star and black hole) and possible compact dark matter objects like primordial black holes (PBH; e.g., Bird et al. 2016). The interaction between GWs and these microlenses can lead to the emergence of wave effects where frequency-dependent modulations can lead to observable signatures in the GW

signal. In this section, we investigate such scenarios of microlensing due to the presence of microlens population in lensing galaxies.

We assume our lens to be an isolated elliptical galaxy and model the smooth matter fraction with a singular isothermal ellipsoid (SIE) density profile. Once we obtain the strong lens systems, the next step is to determine the microlens density at the position of the strongly lensed images. In this work, we assume that all of the dark matter is in the form of a smooth component, leaving only stars and stellar remnants as possible microlenses. That is, we assume the total convergence value (κ or the dimensionless surface mass density of the mass sheet of the lens plane) can be broken into smooth and compact components:

$$\kappa = \kappa_s + \kappa_* \quad (4.9)$$

where κ_* constitutes both stars and stellar remnants. To determine the effect of a microlens population present at the location of a macroimage, we then follow these 4 steps:

- i. Generating a stellar population using an initial mass function (IMF). The process that forms stars out of molecular clouds produces objects over a wide range of masses, with an abundance peak of around $0.2 M_\odot$ (e.g., [Chabrier 2003](#); [Maschberger 2013](#)). Particularly, we use the Chabrier IMF with the mass range $0.01 M_\odot$ to $300 M_\odot$.
- ii. Next, we evolve this stellar population for an assumed time frame (between two redshifts). We consider a time period of ~ 5 Gyr stars. This evolution turns stars with masses $\gtrsim 1.2 M_\odot$ into remnants ([Paxton et al. 2011](#)), and we make use of the initial-final mass relation from the Binary Population And Spectral Synthesis (BPASS, [Eldridge et al. 2017](#)) to infer the final mass of the evolved stars. Meanwhile, we assume the mass profile of the lower mass stars ($< 1.2 M_\odot$) is kept unchanged.
- iii. To estimate the projected stellar surface mass density at the image positions, we use the Sérsic profile (see equation 8 in [Vernardos 2019](#)). The total fraction of the mass in the mass range $m \in (0.01, 0.08) M_\odot$ is around 5%. This mass range predominantly affects the frequencies above the higher end of the LIGO frequency range and the relative error due to the removal of this mass range is about $\sim \mathcal{O}(1)\%$ in the $F(f)$ curve for typical strong lensing amplification values. As a result, for computational efficiency, we remove the microlenses below $0.08 M_\odot$ from our population.
- iv. We then generate the population following the mass profile obtained in the above steps. We consider a patch area that encapsulates the contour corresponding to a time delay of at least $t_d = 1$ s, which ensures our results are correct from 10 Hz onwards. These microlenses are then randomly distributed in the patch, after which amplification factor computation is performed.

In Fig. 4.5, we showcase the typical distribution of microlens density (Σ_\bullet) and the corresponding (unsigned) macro-magnification ($|\mu|$) for a population of strong lens systems obtained from a realistically generated mock sample from [More & More \(2022\)](#). For illustration, we only consider quad systems, where the lens leads to the formation of four images, and the detector sensitivity assumed is that of projected O4 sensitivity. The black, yellow, red, and blue points represent the *image-1,2,3,4* of the quad systems, where the numbering is done based on their order of arrival times, i.e., *image-1* arrives first followed by *image-2* and so on. In a typical quad system, it is expected that the first two images that arrive, i.e., *image-1,2*, are of minima-type (type-I), and the latter two correspond to the saddle-point (type-II). Following the terminology in [Meena et al. \(2022\)](#), we note that the distribution of images in the $|\mu| - \Sigma_\bullet$ plane in Fig. 4.5 leads to a *butterfly* shape. We also note that this shape is not expected to be dependent on the sensitivity of the detectors since it is expected that, in a given quad system, *image-2,3* will be more magnified than *image-1,4* and that *image-4* will be formed where microlens density is high as they typically lie closest to the lens centre, while *image-1* will have the least microlens density as it forms farthest from the lens. Specifically, it is worth noting that the magnification for minima images (*image-1* and *image-2*) always have $|\mu| > 1$ whereas the saddle points in addition can also have $|\mu| < 1$. Apart from that, the microlens densities for *image-1, 2, 3, 4* are in increasing order as the saddle points form closer to the centre of the lens galaxy in regions of high densities as compared to the minima. As we can notice, the typical densities are of the order $\mathcal{O}(10^2) M_\odot/\text{pc}^2$ (e.g., see the 1-sigma region of $p(\Sigma_\bullet)$). This can also be understood from the fact that the typical mass of a galaxy in stars is around $\mathcal{O}(10^{10}) M_\odot$ while the size of a galaxy is of the order $\mathcal{O}(10^4) \text{pc}$. Thus, the average surface density comes out to be $\mathcal{O}(10^2) M_\odot/\text{pc}^2$. Meanwhile, the observed median of the distribution of $|\mu|$ is around $\overline{|\mu|} \approx 4.1$. This is an overestimation of the true median because of the selection bias, i.e., images that are highly magnified are more likely to be detected. Thus, due to these selection biases, $\overline{|\mu|}$ should decrease and tend towards the true median as the sensitivity of the detector increases. For example, the median for a third-generation detector is around $\overline{|\mu|} \approx 2.5$. Also, it is worth noting that because GW sources are point-like sources, they can achieve very high magnifications ($|\mu| > 100$) in principle.

Using Equations 2.3 and 4.1, the time delay function in the case of a population of microlens can be written as ([Suyu et al. 2024](#); [Saha & Williams 2011](#); [Zheng et al. 2022](#); [Shan et al. 2023b](#)):

$$t_d(\mathbf{x}, \mathbf{y} = \mathbb{O}, \boldsymbol{\lambda}_{\text{lens}}) = \frac{2GM_0(1+z_d)}{c^3} \left[\left\{ x_1^2(1-\kappa-\gamma) + x_2^2(1-\kappa+\gamma) \right\} - \left\{ \sum_{i=1}^{N_*} \frac{m_i}{M_0} \ln |\mathbf{x} - \mathbf{x}_i|^2 + \phi_{-\kappa_*} \right\} \right], \quad (4.10)$$

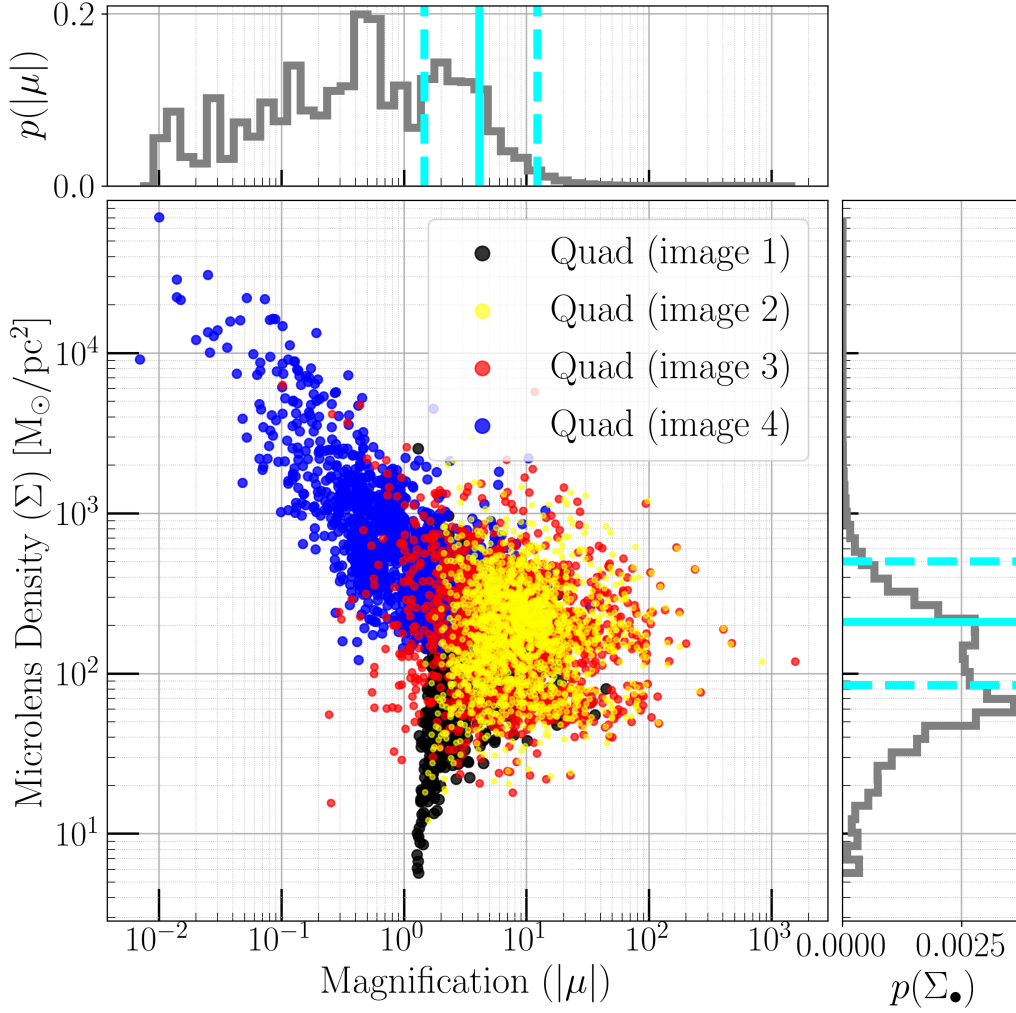


Figure 4.5: Distribution of images formed in quad lens systems in the parameter space of macro-magnification ($|\mu|$) and microlens density (Σ). The black, yellow, red, and blue points represent the image-1 (minima), image-2 (minima), image-3 (saddle points) and image-4 (saddle points), which are ordered according to their time delay values relative to the image-1. The histograms at the top and on the right represent probability density functions for the magnifications $p(|\mu|)$ and microlens density $p(\Sigma_\bullet)$, respectively, for all four images combined. The quad-lensed systems are obtained from a realistically generated mock sample from [More & More \(2022\)](#) assuming projected O4 detector sensitivity.

where λ_{lens} denotes the lens parameters given by $\lambda_{\text{lens}} \in \{\kappa, \gamma, \mathbf{x}_i, m_i\}$ and the coordinate origin \odot has been set at the macro image point (i.e., $y = 0$). The term within the first

set of curly brackets represents the combined effect from strong lensing due to the local convergence (κ), originating from both compact and smooth mass, and the shear (γ). The term within the second set of curly brackets quantifies the contribution from the N_* individual microlenses, whose mean surface mass density is Σ_* . Since microlenses are added on top of total convergence, we add a negative mass sheet $\phi_{-\kappa_*}$ that contains only the smooth matter with the same κ_* to cancel out the "extra mass". This term $\phi_{-\kappa_*}$ depends also on the shape of the patch. We always take a rectangular patch in this work as it is computationally more efficient and avoids incorporating unnecessary microlenses (Zheng et al. 2022). The expression within the second set of curly brackets can be regarded as the perturbation caused by compact objects, i.e., the effect of the microlens population that we wish to study.

4.3.2 Studying effect of microlens population on type-I and type-II macroimages

To demonstrate the effect of microlens population present in lensing galaxies on GWs, we consider an SIE lens kept at a redshift $z_d=0.5$ with a velocity dispersion (σ_{vd}) of 230 km s^{-1} (taken as a rough mean σ_{vd} from lens sample of Sonnenfeld et al. 2013). Since minima and saddle points are the most common types of lensed images seen in galaxy-scale lenses, we consider the microlensing effects for these two images in our analyses. For an SIE lens, the values of κ and γ due to the macrolens at the position of lensed images are equal to each other, i.e., $|\kappa| = |\gamma|$ (e.g., Vernardos 2019). For illustration, we consider a sufficiently wide range of $(\sqrt{\mu}, \Sigma_\bullet)_i$, where $i \in (\text{I}, \text{II})$ in the subscript denotes the image type. For minima (saddle points), we consider five (two) different cases of $(\sqrt{\mu}, \Sigma_\bullet)_i$, which are listed in the Table 4.1. We then compute amplification factors for these systems for 30 different realizations of microlens populations and their distribution around the macroimage. The results are plotted in Figs. 4.6 and 4.7.

In Fig. 4.6, we showcase the results for minima macroimages. Different rows correspond to different cases of macro-amplification $\sqrt{\mu}$ and microlens-density Σ_\bullet values, as labelled in the first column of each row. Furthermore, each row has four columns where the leftmost column shows the $\tilde{F}(t)$ curves. The second and third columns display the absolute part ($|F|$) and the phase part (θ_F), respectively, of the amplification factor resulting from the combined effects of strong lensing and microlensing. The fourth column illustrates the mismatch (see footnote 6) between the strongly lensed WF (h_{SL}) and the one with additional microlensing due to intervening microlens population ($h_{\text{SL+ML}}$) for various equal-mass binary systems where each line corresponds to a specific realisation as shown in the second and third columns. To save space, the labels for the y-axis are placed at the top of each column. Focusing on the leftmost column, $\tilde{F}(t)$ curves, we

Table 4.1: Lens parameter values for minima and saddle points used in simulations. The (κ, γ) are the local convergence and shear values due to the (smooth) macrolens mass distribution. The κ_* is the local convergence due to the mass in compact objects. The μ represents macro-magnification, and Σ_\bullet represents the surface microlens density.

κ	γ	κ_*	$\sqrt{\mu}$	Σ_\bullet ($M_\odot \text{ pc}^{-2}$)
Minima (Type-I)				
0.276	0.276	0.013	1.49	27
0.354	0.354	0.024	1.85	50
0.413	0.413	0.035	2.40	72
0.467	0.467	0.046	3.87	95
0.495	0.495	0.052	10.01	108
Saddle points (Type-II)				
0.548	0.548	0.065	3.21	135
0.722	0.722	0.115	1.50	239

can see the appearance of many microimages in the form of discontinuities and logarithmic divergences. Consequently, the interference of these microimages leads to complicated modulations, as can be seen in the $F(f) = |F|e^{i\theta_F}$ plots in the second and third columns. As discussed in Sect. 4.1, at low frequencies³, we expect the amplification factor to tend towards the macro-amplification ($\sqrt{|\mu|}$) limit, i.e., $|F| \approx \sqrt{|\mu|}$ and $\theta_F \approx 0$ for a macro-minima image. If we focus on the second column, we notice that for low magnification values (first three rows where $\sqrt{|\mu|} < 2.5$), we indeed observe $|F|$ approaching $\sqrt{|\mu|}$ at low frequencies. However, for the rest two higher magnification cases where $|\mu| \in \sim \{15, 100\}$, we notice that $|F| > \sqrt{|\mu|}$ at lower frequencies. For example, for $\sqrt{|\mu|} = 3.87$ case, we notice $|F| \sim 4.5 > 3.87$ while for $\sqrt{|\mu|} = 10.01$ case, it is $|F| \sim 17 > 10$. Thus, we notice that with increasing macro-magnification values for type-I macro-images, the presence of microlens further amplifies the signal. Moreover, in the last column, we notice that the mismatch between h_{SL} and $h_{\text{SL+ML}}$ also increases with increasing μ . For example, the mismatch values in the first row (where $\sqrt{|\mu|} = 1.49$) is $\mathcal{O}(10^{-5})$ while in the last row (where $\sqrt{|\mu|} = 10.01$) the mismatch values are $\mathcal{O}(10^{-2})$. It is worth noting that, for low magnification cases ($\sqrt{|\mu|} < 2.5$), we notice mismatch values to be $\lesssim 10^{-3}$. *This ensures that for low magnification systems, the systematic biases due to intervening microlens population will not be more pronounced than the statistical uncertainties until very high SNR values ($\gtrsim 10^2$).*

The effect of microlens population on type-II macro-images is plotted in Fig. 4.7.

³By low, we usually mean that the wavelength of the signal is much longer than the Schwarzschild radius of the lens but much shorter than the Schwarzschild radius of the lensing galaxy.

CHAPTER 4. BEYOND ISOLATED POINT LENS MODEL: COMPLEX CONFIGURATIONS OF MICROLENSING

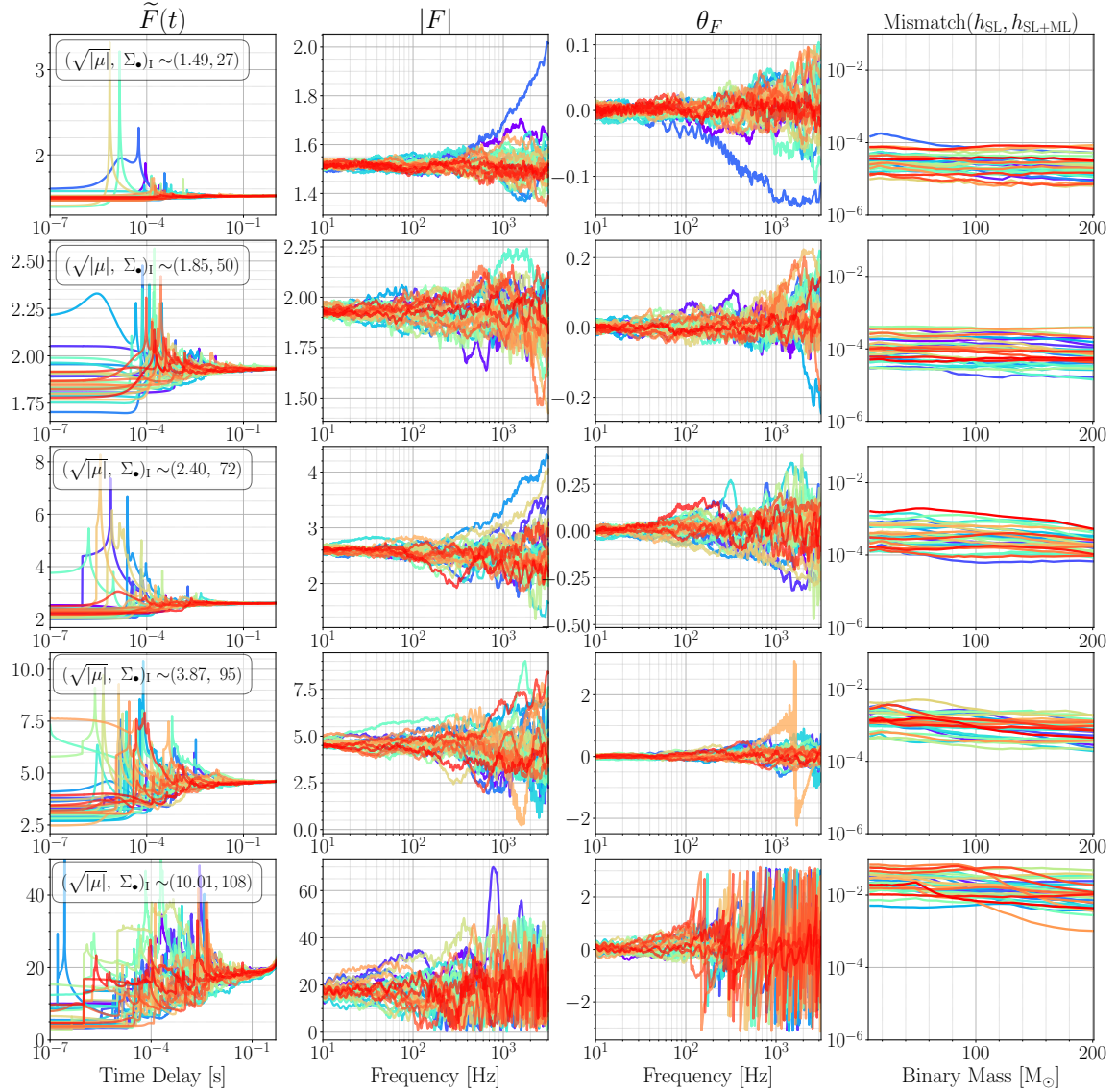


Figure 4.6: Effect of microlens population on the minima type macroimages. The analysis is done for five pairs of the macro amplification and the surface microlens density values as denoted by $(\sqrt{\mu}, \Sigma_{\bullet})_m$ in the left-most panels. These values are drawn from our SIE model (see Table 4.1). *Left:* Normalised $\tilde{F}(t)$ curves, computed numerically using Eq. 4.4. *Middle and Right:* The corresponding amplification factor $F(f) = |F|e^{i\theta_F}$. Each row shows the analysis for all 36 realisations (coloured differently).

The figure is similar in construction to Fig. 4.6. Here, we only consider two cases of $(\sqrt{\mu}, \Sigma_{\bullet})$ because of computational reasons. Moreover, we apply a low-pass filter to our realisations of amplification factor to mitigate numerical errors. A similar investigation as above reveals two insights: (i) We notice that $|F|$ is de-amplified relative to

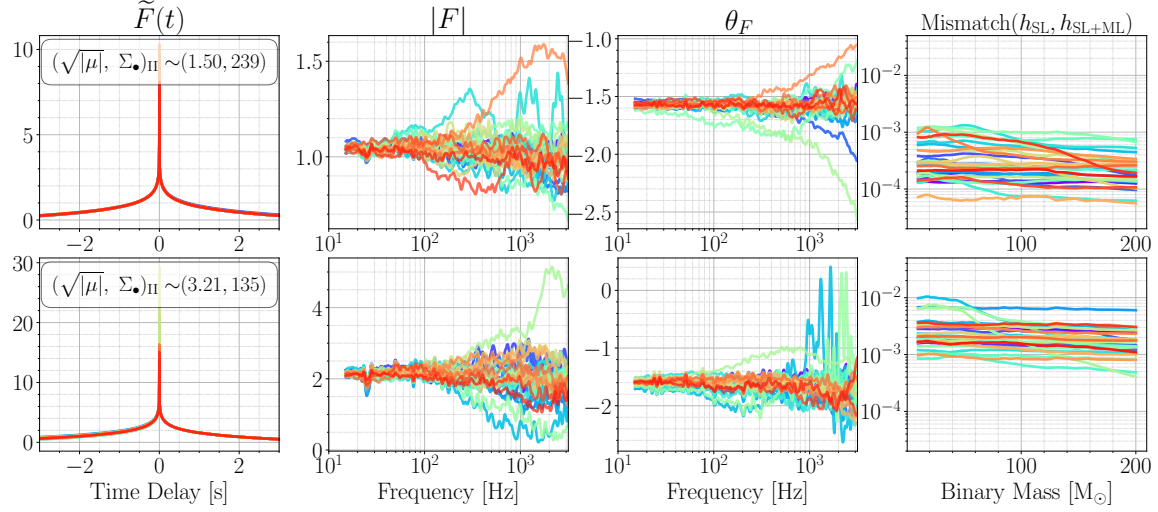


Figure 4.7: Same as Fig. 4.6 but for the saddle point macroimages. The analysis is done for two pairs of the macro amplification and the surface microlens density values as denoted by $(\sqrt{\mu}, \Sigma_{\bullet})_s$ in the left-most panels. These values are drawn from our SIE model (see Table 4.1).

Table 4.2: Lens system information, with the lens and source redshifts denoted by z_L and z_S , respectively, are listed here. The macro (μ_{macro}) and smooth (μ_{smooth}) magnifications, the microlens density (Σ_{\odot}), and the network optimal SNR for both the SL-only case, $\rho_{\text{opt}}^{\text{net}}(h_{\text{SL}})$, and the SL+ML case, $\rho_{\text{opt}}^{\text{net}}(h_{\text{SL+ML}})$, of our chosen GW150914-like source are also tabulated.

system	z_L	z_S	image	μ_{macro}	μ_{smooth}	$\Sigma_{\odot} [\text{M}_{\odot}/\text{pc}^2]$	$\rho_{\text{opt}}^{\text{net}}(h_{\text{SL}})$	$\rho_{\text{opt}}^{\text{net}}(h_{\text{SL+ML}})$	match($h_{\text{SL}}, h_{\text{SL+ML}}$) [%]
1	0.50	0.56	I	4.75	3.27	1030.5	23.7	24.6	99.92
			II	10.85	4.66	1419.5	34.9	38.5	99.21
			III	-11.22	+13.52	2121.6	35.4	34.8	99.96
			IV	-1.56	-2.57	4905.8	11.5	11.4	99.93
2	0.28	0.50	I	6.92	4.41	304.7	32.3	35.2	99.80
			II	11.14	5.54	351.1	50.5	56.5	99.97
			III	-12.64	+25.99	513.31	55.1	50.5	99.89
			IV	-2.59	-4.33	864.94	24.9	23.9	99.97

the macro-amplification value as opposed to further amplification we observed in the case of type-I images. For example, for both cases, we can see that the $|F|$ value at, say, 20 Hz is lower than $\sqrt{\mu}$ values. This behaviour is expected because in the case of type-II macroimages, the probability of the source lying in the region of low magnification becomes significantly higher due to the presence of a microlens population (e.g., [Diego et al. 2018](#); see figures 5 and 10 in [Diego et al. 2019](#)). The fact that minima-images tend to be further amplified while saddle-point images tend to get relatively deamplified relative to the macro-amplification ($|\sqrt{\mu}|$) values, on average, due to an intervening microlens

population is consistent with microlensing studies in the EM domain (e.g., [Schechter & Wambsganss 2002](#)). Moreover, we observe that the mismatch values are also higher in the case of type-II macroimages as compared to type-I macroimages for similar magnifications. For example, compare the first row here (where $\sqrt{|\mu|} = 1.50$), with mismatch values $\mathcal{O}(10^{-5})$, with that of the first row of Fig. 4.6 (where $\sqrt{|\mu|} = 1.49$), with mismatch values $\mathcal{O}(10^{-4})$.

4.3.3 High density systems

In the above discussion, we primarily talked about how macro-amplification can enhance microlensing effects. However, one may ask what happens at extreme microlens densities. In principle, the second saddle-point image in a quadruply lensed system, *image-4*, can form in the lens plane where the microlens densities can even exceed $10^3 M_{\odot}/\text{pc}^2$. So in this subsection, we study the microlensing effects in *image-4* with $\Sigma_{\bullet} > 10^3 M_{\odot}/\text{pc}^2$. We select four individual cases of *image-4* from quad-lensed systems obtained from a realistically generated mock sample from [More & More \(2022\)](#) (see Fig. 1 of [Meena et al. \(2022\)](#)) with microlens densities in the range $(10^3, 10^4) M_{\odot}/\text{pc}^2$. The corresponding macro-magnifications ($|\mu|$) lie in the range $(0.1, 0.6)$. For each of the four images, we simulate 50 realizations with a patch size of $2 \text{ pc} \times 2 \text{ pc}$.

The resulting absolute amplification ($|F|$) curves as a function of GW frequencies are shown in Figure 4.8. For all four cases, we see two different kinds of features: (i) random oscillations unique to each realization with increasing amplitude as we go from low to high frequencies. (ii) coherent oscillations across all realizations of four cases at low frequencies (~ 20 Hz). The random oscillations are genuine features arising due to the presence of microlens population and unique in each realization as the microlenses are randomly distributed. The coherent oscillations at low frequencies are artifacts and arise due to the finite patch size. Increasing the microlens density while keeping the patch size fixed can lead to the formation of micro-images near the edge or outside the patch due to the combined effect of all microlenses inside the patch (e.g., [Wambsganss 1999](#)). As these micro-images are at a large time delay (> 0.1 seconds) with respect to the global minimum or saddle-point, they introduce oscillatory features at low frequencies. If we increase the patch size, the micro-images near the edge or outside the patch will disappear (hence the name spurious images). But, simulating a large patch implies an increase in the number of microlenses, leading to increase in the computational times. Apart from that, the $|F|$ curves only show variation of $\sim 0.2 - 0.3$ over the mean magnification, which tends to be less than one and thus, the amplitude of these oscillations is not significant across LIGO--Virgo frequencies (10 Hz to 10^3 Hz) resulting in negligible effects in the mismatch as well as the parameter estimation. Considering these factors, we choose not to simulate bigger

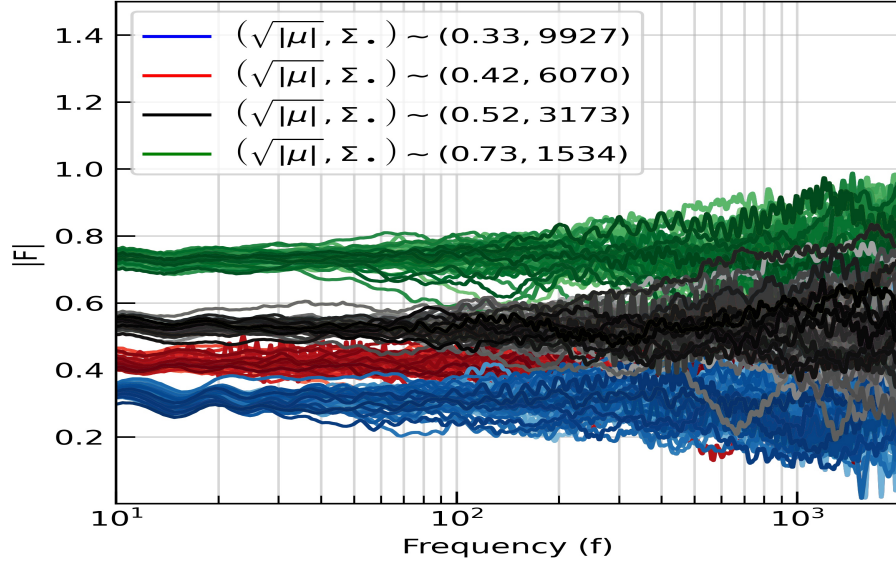


Figure 4.8: Microlensing effects observed in the saddle points of image-4 in high-density regions. The absolute part of the amplification factor $F(f)$ is shown as a function of frequency for four different combinations of $\{|\mu|, \Sigma\}$ (corresponding to maroon stars in Figure 1 of Meena et al. (2022)). There are 50 realizations for each of the four cases, and their respective macro-magnifications and microlens densities are given in the legend. The amplitude of the distortions due to microlensing is negligible despite the high microlens densities owing to the low macro-magnification of these images.

patches in the lens plane as it is expected not to affect our conclusion. We conclude that the microlensing-driven frequency-dependent effects (due to stellar mass population) are negligible in de-magnified lensed GW signals located in high microlens density regions within the lens galaxy.

4.4 Effect of microlens population on the signatures of strong lensing

In this section, we study the effect of microlensing from a population of microlenses on the search for strongly lensed GW signals. The intervening galaxy or galaxy cluster acting as a macrolens contains substructures in the form of microlens population that can further perturb the signal due to microlensing effects (e.g., Diego et al. 2019; Mishra et al. 2021; Meena et al. 2022). We simulate such signals and investigate their effects on strong lensing searches, particularly on the interpretation of *posterior overlap* analysis (Haris et al. 2018). To accomplish this, we perform a set of parameter estimation runs. The strongly

lensed signal, which is taken to further undergo microlensing (to produce an "SL+ML" signal), is generated after computing the amplification factor for such systems using the methodology described in [Mishra et al. \(2021\)](#) and (Mishra, A., in prep.).

Posterior overlap analysis is a fast and robust method for identifying potential strongly lensed pairs of GW signals. The method relies on two primary observations: (i) strongly lensed images should originate from the same patch of the sky, and (ii) the gravitational lensing does not affect the GW phasing, which means that the parameter estimation for the intrinsic parameters should remain unaffected. Consequently, the sky and the intrinsic parameters should exhibit similarity between the two images of a strongly lensed system. So, for any two GW signals, one can compute the overlap between the posteriors for the aforementioned parameters and develop a statistic to assess its significance. Given the posteriors of two events d_1 and d_2 , the Bayes factor for the (strongly-) lensed hypothesis over the unlensed hypothesis can be defined as ([Haris et al. 2018](#))

$$\mathcal{B}_U^L = \int d\boldsymbol{\theta} \frac{P(\boldsymbol{\theta}|d_1)P(\boldsymbol{\theta}|d_2)}{P(\boldsymbol{\theta})}, \quad (4.11)$$

where $\boldsymbol{\theta}$ is the set of parameters over which we compute the overlap. As mentioned above, $\boldsymbol{\theta}$ is at most a 9D quantity, i.e., $\boldsymbol{\theta} = \{\mathcal{M}, q, a_1, a_2, \theta_1, \theta_2, \theta_{\text{JN}}, \alpha, \delta\}$, where the symbols have their usual meaning as described in [Sec. 2.3](#).

For the lensing systems, we selected two (quadruply) lensed systems from the catalog described in [More & More \(2022\)](#). We specifically chose systems where the source redshift was relatively lower to ensure high SNR events and where the brightest image had a (macro-)magnification of $\gtrsim 10$. As mentioned in [Sect. 3.3](#), we used a GW150914-like event as the source, including its spins. The properties of both systems are provided in [Table 4.2](#). As expected, our choice of lens systems with low source redshifts led to a smaller Einstein angle (0.03" and 0.54" for system-1 and system-2, respectively) compared to typical lens systems in EM observations where Einstein angle is $\sim 1''$. However, as we specifically focus on high SNR systems for our introductory analysis, we proceed with these systems in our current work and leave a more detailed analysis for future work.

The results of the posterior overlap analysis are shown in [Fig. 4.9](#). This figure compares the Bayes factors in favour of lensing obtained from the posterior overlap analysis for both the strongly lensed macroimages (black solid circles) and the macroimages that further undergo microlensing (red solid stars). The middle and right panels of the figure also display the corresponding (micro-)lensing amplification factors $F(f)$ for the four macroimages. The small-scale fluctuations observed in the $F(f)$ curves are numerical artifacts that are mitigated by applying a high-pass filter before their utilization. Firstly, for system 1 (top row), we note that the Bayes factor values can significantly reduce in extreme cases of microlensing in the path of a strongly lensed signal. For example, in

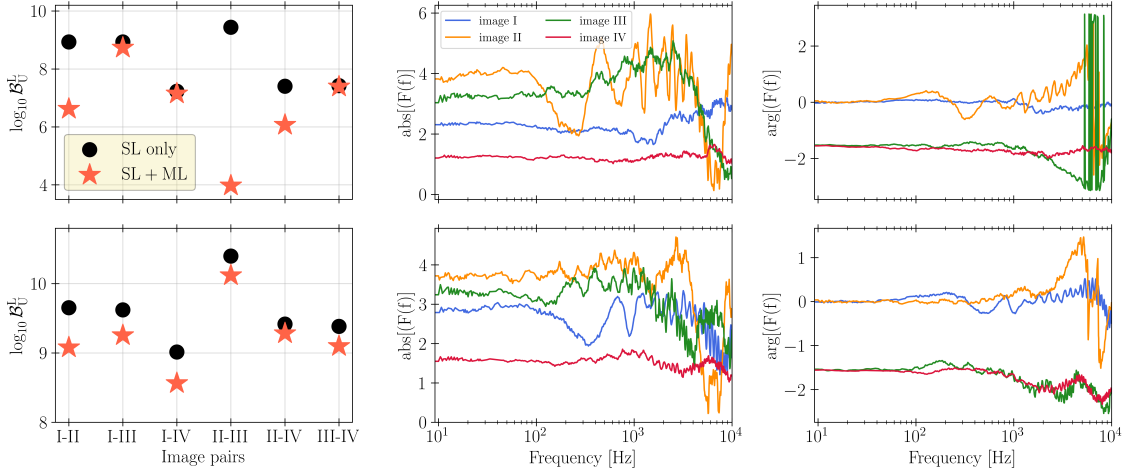


Figure 4.9: Effect of microlensing on strongly lensed GW signals due to a population of microlenses. *Left panel:* The comparison between the Bayes factors in favour of lensing using the posterior overlap analysis is shown for two quadruple-lensed systems (*top* and *bottom* rows), indicating both the strongly lensed systems ("SL only"; represented using black circled markers) and the systems further undergoing microlensing ("SL+ML"; represented using star-shaped red markers). *Middle and Right panels:* A realisation of the (micro-)lensing amplification factor $F(f)$ is displayed for the four macroimages, resulting due to the presence of microlens population in the vicinity of the macroimages.

the top-left panel, we see orders of magnitude drop in the \mathcal{B}_U^L for image pairs I-II, II-III and II-IV, i.e., all image pairs with the second image. This behaviour can be explained if we note that the corresponding amplification factor, $F(f)$, curves in the middle and right panels of the first row. Even though the $F(f)$ curves for the third and fourth images show large modulations, they do so only at high frequencies ($> 10^3$ Hz). On the other hand, one can clearly notice from visual inspection that only the $F(f)$ curves for image II (orange-coloured curve) show significant modulations at low frequencies, where most of the power of the GW is contained. For system 2 (bottom row), we still see Bayes factor values drop for all image pairs but relatively less than that for system 1. In this case, $F(f)$ curves for images I and III showed significant modulation at lower frequencies compared to other images. One can see this from the phase plots in the lower-right panel, where blue and green curves start deviating from orange and red curves at around ~ 100 Hz.

One can further ask which of the parameters incorporated for the computation of the posterior overlap is responsible for such a drop in the Bayes factor values for some of the microlensing cases. To that end, in Fig. 4.10, we show 1D marginalised posteriors corresponding to the parameters used for computing the overlap. For ease of representation, we denote spin components using $\{\chi_{\text{eff}}, \chi_p\}$ instead of $\{a_1, a_2, \theta_1, \theta_2\}$. The differently

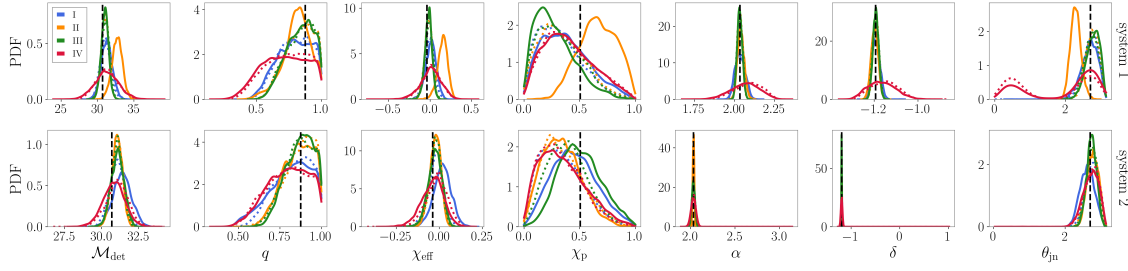


Figure 4.10: Effect of microlensing due to a population of microlenses on strongly lensed GW signals. The panels display 1D marginalised posterior distributions for a set of parameters, as labelled on the x -axis, for two systems (along the row). These parameters were utilised to compute the posterior overlap, with the exception that we have condensed the spin parameters to $\{\chi_{\text{eff}}, \chi_{\text{p}}\}$ instead of $\{a_1, a_2, \theta_1, \theta_2\}$ for the ease of representation here. The differently coloured curves correspond to posteriors associated with different images, as shown in Figure 4.9. The dotted curves represent cases with only strong lensing, while the solid curves depict recoveries for signals that undergo both strong lensing and microlensing. The dashed black vertical lines represent the injected values.

coloured curves correspond to posteriors associated with different images, as shown in Fig. 4.9. The dotted curves represent cases with only strong lensing (SL only), while the solid curves depict recoveries for signals that undergo both strong lensing and microlensing (SL+ML). The dashed black vertical lines depict the injected values. We notice that the posteriors for most of the parameters are well recovered around the true injected value for both cases (SL only and SL+ML). However, in system 1, the posteriors representing the recoveries for the second image of SL+ML case show the maximum deviation from the injected value among different parameters (solid orange-coloured curves). In the case of system 2, although the deviation between the recovered parameters for the SL and SL+ML scenarios is largely similar, the posterior distributions for parameters in the SL+ML case exhibit slightly greater variability, which can be attributed to the variability in $F(f)$ values for different images.

Among all the parameters considered here, the sky-position parameters, i.e., RA and Dec (α and δ), are the best-recovered parameters, as their posteriors are sharply peaked around the injected value for both systems. Therefore, the sky-position parameters contribute the most to the posterior overlap values. The drop in the Bayes factor values is then mostly coming from the biased recoveries of parameters like $\{\mathcal{M}_{\text{det}}, \chi_{\text{eff}}, \chi_{\text{p}}, \theta_{\text{JN}}\}$ for SL+ML case.

We note that in this section, we studied only a few scenarios of microlensing due to a population of microlenses affecting strongly lensed GWs. Due to our selection of systems with high SNR values, even small deviations (high match values in Table 4.2; also

see Fig. 4.10) led to a significant decrease in the Bayes factor. However, it is important to conduct a more comprehensive statistical study to generalise the effects of microlensing on strong lensing searches. We leave this to future investigations.

4.5 Conclusions

In this chapter, we investigated the effects of microlensing in the LIGO/Virgo frequency band when a microlens, or a population of them, is embedded in a macro-potential. We first developed methodologies for simulating amplification factor curves for both types of macroimages, minima (type-I) and saddle points (type-II). We studied how macrolens parameters, such as local convergence, shear and orientation of microlens relative to shear, etc., affect microlensing. Additionally, we calculated the microlensing effects for various combinations of surface microlens density and macro-magnification, typically found at the location of macroimages in galaxy-scale lenses.

Our main conclusions from these investigations are as follows.

1. The most important factor for microlensing to be significant is the strong lensing amplification value ($\sqrt{\mu}$) regardless of other parameters, such as the stellar density, type of images or IMF. This happens due to the fact that the image plane gets compressed by a factor of μ in the source plane, leading to the high density of overlapping micro-caustics. Moreover, higher μ allows relatively larger time delays between sufficiently amplified microimages, which causes modulation even at lower frequencies (e.g., [Diego 2019](#); [Diego, Jose M. 2020](#)). From our analyses, we observed that microlensing effects are not significant at low macro-magnifications ($\mu \lesssim 15$). However, the likelihood of finding realisations that may affect GWs significantly increases at high macromagnification values ($\mu \gtrsim 100$).
2. On average, the microlensing population tends to introduce further amplification (de-amplification) for minima (saddle points). Similar behaviour is also seen in the lensing of EM waves (e.g., [Schechter & Wambsganss 2002](#); [Foxley-Marrable et al. 2018](#)).
3. With increasing surface microlens density, we find an overall rise in scatter in $F(f)$. This is because of the presence of many microimages, which interfere, leading to more complex interference patterns.
4. In extreme cases of macro-magnification ($\gtrsim 100$), we notice that the mismatch values are high and can even exceed $\sim 5\%$. Such high magnification for GW sources is possible as they are point-like sources. When they lie very close to macro-caustics, their

magnifications can indeed be very high $\mu \sim \mathcal{O}(10^2 - 10^3)$ and hence, such possibilities cannot be ignored.

5. Finally, to study the effect of microlensing on the search of strongly lensed GW signals, specifically the posterior overlap analysis, we focused our attention on a much more complex scenario of microlensing when a strongly lensed GW signal encounters a population of $\mathcal{O}(10^4)$ microlenses present in the lensing galaxy. We find that, in general, the presence of microlens population decreases the measured Bayes factor in favour of strong lensing (see Fig. 4.9). However, the exact amount of drop is sensitive to the magnitude of microlensing effects in the signal, which in turn depends primarily on the strong lensing magnification and properties of the microlens population. This suggests that, in extreme cases, the presence of microlensing may pose challenges in accurately identifying and characterizing strongly lensed GW signals. However, a more detailed study is required to generalise the above inferences.

Chapter 5

Unveiling Microlensing Biases in Testing General Relativity with Gravitational Waves

GW from chirping BBHs provide unique opportunities to test GR in the strong-field regime. However, testing GR can be challenging when incomplete physical modeling of the expected signal gives rise to systematic biases. In this chapter, we investigate the potential influence of wave-optics effects in GL (which we refer to as microlensing) on tests of GR using GWs for the first time. We utilize an isolated point-lens model for microlensing with the lens mass ranging from $10 - 10^5 M_\odot$ and base our conclusions on an astrophysically motivated population of BBHs in the LIGO-Virgo detector network. Our analysis centers on two theory-agnostic tests of gravity: the inspiral-merger-ringdown consistency test (IMRCT) and the parameterized tests, providing insights into deviations from GR across different evolutionary phases of GW signals: inspiral, intermediate, and merger-ringdown. Our findings reveal two key insights: First, microlensing can significantly bias GR tests, with a confidence level exceeding 5σ . Notably, substantial deviations from GR ($\sigma > 3$) tend to align with a strong preference for microlensing over an unlensed signal, underscoring the need for microlensing analysis before claiming any erroneous GR deviations. Nonetheless, we do encounter scenarios where deviations from GR remain significant ($1 < \sigma < 3$), yet the Bayes factor lacks the strength to confidently assert microlensing. Second, deviations from GR correlate with pronounced interference effects, which appear when the GW frequency (f_{GW}) aligns with the inverse time delay between microlens-induced images (t_d). These false deviations peak in the wave-dominated region and fade where $f_{\text{GW}} \cdot t_d$ significantly deviates from unity. Particularly, in the geometrical optics regime ($f_{\text{GW}} \cdot t_d \gg 1$), biases remain minimal despite instances of strong microlensing effects. Our findings apply broadly to any microlensing scenario, extending beyond specific models and parameter spaces, as we relate the observed biases to the fundamental characteristics of lensing.

5.1 Introduction

GR has withstood numerous strong field gravity tests and remains the most successful theory of gravity to date. These tests encompass a wide range of phenomena, from precise solar system measurements (Will 2006) to the observation of binary pulsars (Wex 2014), and most notably, the direct detection of GWs by the LIGO (Aasi et al. 2015) and Virgo (Acernese et al. 2015) detectors. The groundbreaking observations from the first three observing runs of Advanced LIGO and Advanced Virgo (Abbott et al. 2019b, 2021a; The LIGO Scientific Collaboration et al. 2024; Abbott et al. 2023) have provided a unique opportunity to explore the characteristics of gravity within the highly nonlinear and dynamic regime (Abbott, B. P. and others 2016; Abbott et al. 2019c,a, 2021d,b), thus subjecting Einstein's theory of gravity to novel scrutiny. The remarkable agreement between these observations and the predictions of GR has consistently reaffirmed the theory's robustness and validity.

The LIGO-Virgo-KAGRA (LVK) collaboration has been instrumental in conducting rigorous tests of GR using GWs. These tests primarily rely on GR to identify potential deviations from its predictions, as no reliable modified gravity WF models are currently available which can describe the complete inspiral-merger-ringdown dynamics of a compact binary system. It involves comparing the data collected by GW detectors with theoretical WF models. While such tests have effectively probed GR in various aspects, they also exhibit sensitivity to unaccounted-for physical phenomena, including eccentricity and the presence of exotic compact objects, in addition to potential beyond-GR physics. Hence, it is imperative that these models incorporate all relevant physics to avoid any potential false biases in the tests.

One particularly intriguing source of bias in tests of GR arises from the propagation effect of lensing of GWs when they traverse the vicinity of massive objects. The observed alterations encompass a spectrum of manifestations, including repeated events, phase shifts, variations in amplitude, the emergence of beating patterns, and distortions. From probing the relative speeds of GWs with respect to light (Collett & Bacon 2017; Fan et al. 2017), modified velocity dispersion (Yang et al. 2019; Chung & Li 2021) and propagation (Mukherjee et al. 2020; Mukherjee, Suvodip et al. 2020; Finke et al. 2021; Iacovelli et al. 2022), to understanding the nature of GW polarization in alternate theories of gravity with additional degrees of freedom (Goyal et al. 2021; Magaña Hernandez 2022) leading to birefringence (Goyal et al. 2023), lensing can be a useful tool for GR tests.

In this chapter, we will focus on the lensing scenario where a GW signal traverses the spacetime near an isolated compact object (microlens) such that the (micro-)images produced by the microlens are not resolved temporally, leading to either interference effects

or superposition of images. This phenomenon, which we refer to as *microlensing*¹, may lead to significant frequency-dependent effects if the frequency of the signal is comparable to the inverse time delay between microimages (Deguchi & Watson 1986; Nakamura 1998; Baraldo et al. 1999; Nakamura & Deguchi 1999; Bulashenko & Ubach 2022; Leung et al. 2023; Mishra et al. 2023b). These microlenses can be in the form of stars, stellar remnants, or even compact dark matter, etc., in the mass-range $\sim 1 - 10^5 M_{\odot}$. This mass range is particularly pertinent for ground-based detectors searching for microlensing signatures and aligns with the parameter space used by the LVK collaboration (Abbott, R. and others 2021; The LIGO Scientific Collaboration et al. 2023a). We explore the underlying physics of these lensing phenomena and investigate how they can affect the observed GW signals and their potential to introduce biases in the tests of GR. We note that the search for such microlensing signatures can shed light on the fraction of compact dark matter objects in this mass range (Jung & Shin 2019; Basak et al. 2022; Diego, Jose M. 2020). In this chapter, we restrict ourselves to isolated point lenses and do not consider complex scenarios of microlensing, such as microlenses embedded in a strong lens potential (Diego et al. 2019; Diego, Jose M. 2020; Seo et al. 2022; Mishra et al. 2021; Meena et al. 2022; Meena 2023). We also restrict ourselves to ground-based detectors. However, wave-optics effects in the context of space-based detectors can also affect the inferred parameters (Çalışkan et al. 2023c,a) and might lead to biases in the tests of GR. We also note that we do not consider lensing scenarios where the images are completely separated out, i.e., the time delay between the images is larger than the duration of the signal (strong-lensing cases).

We focus on two fundamental types of tests: consistency tests and parameterized tests, each designed to scrutinize GR in distinct ways. Consistency tests, as the name suggests, focus on evaluating the adherence of observed GW signals to the expected behavior prescribed by GR, without invoking specific parameterizations of deviations from the theory. These tests serve as a measure of the self-consistency of the signal or its overall consistency with the available data. In this chapter, we use the inspiral-merger-ringdown consistency test (IMRCT) (Ghosh et al. 2016, 2018). The IMRCT seeks to ascertain the consistency between the low-frequency and high-frequency components of the GW signal, shedding light on potential departures from GR (Abbott, B. P. and others 2016; Abbott et al. 2019a, 2021d,b). In contrast to consistency tests, parameterized tests are tailored to invoke specific parametrizations that are particularly suited to uncover deviations from GR rooted in distinct physical effects. For instance, here we deploy the parameterized

¹Some authors specifically differentiate the phenomenon where multiple images overlap from interference effects, referring to it as *millilensing* (e.g., Liu et al. 2023). Millilensing can also result in a modulated signal (see Fig. 1 in Janquart et al. 2023). In our study, while we primarily focus on the lensing parameter space relevant for inducing wave effects, we use the term "geometric optics regime" within our microlensing parameter space for cases where signals can be assumed to overlap as a result of lensing.

tests of post-Newtonian (PN) coefficients which are designed to be sensitive to physical effects manifesting at different PN orders (Arun et al. 2006b,a; Yunes & Pretorius 2009; Li et al. 2012; Yunes et al. 2016).

In this chapter, we explore the possibility of microlensing-induced biases in tests of GR. We first analyze simulated GW150914-like microlensed signals, which serve as our initial motivation for the exploration of these biases and enable us to search for any possible patterns in the distortions. We find that the biases are pronounced where the wave effects are dominated but do not correlate with the detection statistic that the LVK collaboration uses for microlensing searches. We further validate our findings for a population of simulated GW signals. Through a rigorous examination of this lensing scenario, we contribute to the ongoing effort to ensure the accuracy and robustness of GR tests conducted in the strong gravitational field regime. To our knowledge, this is the first such study that looks into the biases in tests of GR due to frequency-dependent modulations coming from wave-optics effects. However, we do note that some previous studies have explicitly looked into the effect of Morse phase shift in type-II strong lensing scenarios, which is also a consequence of the wave-optics effect capable of biasing inferred parameters (Ezquiaga et al. 2022; Janquart, Justin and Seo, Eungwang and Hannuksela, Otto A. and Li, Tjonnje G. F. and Broeck, Chris Van Den 2021; Vijaykumar et al. 2023). These phase shifts can introduce distortions that may be degenerate with GW propagation involving a modified dispersion relation, potentially leading to biases in tests of GR (Ezquiaga et al. 2022).

This chapter is mainly based on the paper Mishra et al. (2023a), and is organized as follows: In Sect. 5.2, we discuss the basics of microlensing and the two tests of GR that we adopt for our study. We also give details of our computational setup. In Sect. 5.3, we discuss the results from our analysis and conclude in Sect. 5.4. We consistently report all mass related quantities, such as M_{Lz} , in units of the solar mass (M_{\odot}).

5.2 Basics

5.2.1 Tests of General Relativity (TGR)

Inspiral-Merger-Ringdown Consistency Test (IMRCT)

The IMRCT is one of the standard consistency tests of GR that is performed on real GW events. The test relies on checking the consistency between the measurements of mass and spin of the remnant BH inferred independently from the inspiral and post-inspiral parts of the GW signal. The demarcation between the inspiral and the post-inspiral regime

is typically done by employing a cutoff frequency f_c^{IMR} in the frequency domain, which is the dominant mode GW frequency f_{ISCO} of the innermost stable circular orbit (ISCO) of the remnant Kerr BH with mass M_f and dimensionless spin χ_f . In this work, the ISCO frequency of the final Kerr black hole is measured using the median values of the 1D-marginalized posteriors of the final mass and spin inferred from the full IMR WF² (Ghosh et al. 2016, 2018). To calculate the final mass and spin, we use the NR-calibrated fits as detailed in Ref. (Abbott et al. 2017b, 2021d; Johnson-McDaniel et al. 2016) where the method extends the final spin fit of aligned-spin binaries to a precessing case (see Eqn. 1 of Ref. (Johnson-McDaniel et al. 2016) for details).

To elaborate, we independently infer the posterior distributions of M_f and χ_f from both the inspiral and the post-inspiral parts of the signal by using the augmented NR calibrated final state fits (Hofmann et al. 2016; Jiménez-ForTEza et al. 2017; Healy & Lousto 2017). To constrain possible deviations from GR, a set of fractional deviation parameters $\Delta M_f/\overline{M}_f$ and $\Delta\chi_f/\overline{\chi}_f$ are defined, where

$$\frac{\Delta M_f}{\overline{M}_f} \equiv 2 \frac{M_f^{\text{insp}} - M_f^{\text{post-insp}}}{M_f^{\text{insp}} + M_f^{\text{post-insp}}} \quad (5.1)$$

and

$$\frac{\Delta\chi_f}{\overline{\chi}_f} \equiv 2 \frac{\chi_f^{\text{insp}} - \chi_f^{\text{post-insp}}}{\chi_f^{\text{insp}} + \chi_f^{\text{post-insp}}}, \quad (5.2)$$

where \overline{M}_f and $\overline{\chi}_f$ denote the mean values and the superscripts denote the inspiral (insp) and the post-inspiral (postinsp) portions of the signal. If a given GW signal is consistent with GR, the fractional deviations $\Delta M_f/\overline{M}_f$ and $\Delta\chi_f/\overline{\chi}_f$ should vanish in the ideal situation. We estimate the posteriors on these fractional deviation parameters and check the consistency with GR.

To check the consistency of inspiral and post-inspiral measurements statistically, we use the GR quantile Q_{GR} . In this case, the GR quantile for the 2-D distribution of final mass and spin parameters measures the fraction of the posterior samples that contain the GR value. Specifically, we utilize the `summarytgr` executable within `PESummary` (Hoy & Raymond 2021) to calculate the GR deviations. Notice that a smaller value denotes better agreement with GR, meaning that a large fraction of samples are contained in a small iso-probability contour. We use `IMRPhenomXPHM` (Pratten et al. 2021) as our WF approximant for both injection and recovery of the IMRCT analysis throughout.

²We note that the LVK analyses use a more complicated method to compute f_{ISCO} from the posteriors obtained from IMR, see, e.g., (Abbott et al. 2019a, 2021b).

Parameterized test

The dynamics of a BBH system can be described in three regimes: the inspiral, the merger and the ringdown. In the inspiral, the post-Newtonian formalism accurately describes the evolution, which is an expansion in the velocity parameter $v/c \ll 1$, where c is the velocity of light (Blanchet 2006). In contrast, one needs numerical relativity techniques to model the dynamics towards the merger regime (Pretorius 2007; Duez & Zlochower 2019), where the strong-field dynamics play a critical role. In the post-merger phase, BH perturbation theory provides a good description (Berti et al. 2006).

Parameterized tests of post-Newtonian (PPN) theory are among the multiple ways of performing theory-agnostic tests of GR. Even though the PPN tests were restricted to the inspiral regime (Arun et al. 2006b,a; Agathos et al. 2014), later on, they were also extended to the post-inspiral regime by employing the phenomenological WF models (Abbott et al. 2019a, 2021d; Meidam et al. 2018; Abbott, B. P. and others 2016; Abbott et al. 2019c,a, 2021d). The PPN tests introduce a novel way of looking for deviations in the inspiral-merger-ringdown coefficients from the GR model by appropriately incorporating parameterized deviation coefficients in the model. We denote the inspiral coefficients as $\{\chi_i\}$ ³, and the post-inspiral coefficients as $\{\alpha_i, \beta_i\}$, where $\{\beta_i\}$ accounts for deviations mainly in the intermediate phase while $\{\alpha_i\}$ in the merger-ringdown phase. The parameterized deviations to these coefficients are of the form, $\chi_i \rightarrow (1 + \delta\hat{\chi}_i)\chi_i$, $\alpha_i \rightarrow (1 + \delta\hat{\alpha}_i)\alpha_i$ and $\beta_i \rightarrow (1 + \delta\hat{\beta}_i)\beta_i$, where $\delta\hat{\chi}_i$, $\delta\hat{\alpha}_i$ and $\delta\hat{\beta}_i$ are the fractional deviations from the GR coefficient. In the case of phenomenological WF models, the post-Newtonian inspiral coefficients are extended further by fitting to numerical relativity coefficients (Ajith et al. 2008, 2011; Santamaria et al. 2010; Husa et al. 2016; Khan et al. 2016; García-Quirós et al. 2020; Pratten et al. 2020). Besides the inspiral, the parameters $\delta\hat{\beta}_i$ explicitly capture deformations in the NR calibrated coefficients β_i in the intermediate regime, whereas the parameters $\delta\hat{\alpha}_i$ describe deformations of the merger-ringdown coefficients α_i obtained by calibration to NR (Meidam et al. 2018; Abbott et al. 2019a). The data provide constraints on these parameterized deviations from GR and can be used to test the consistency of GR. That means we obtain posterior probability distributions on each of the parameterized deviation coefficients. If the data is consistent with GR, the distribution will peak at zero, the GR value. Any deviation from GR can hint at the presence of an alternative theory model or missing physics in our models, such as various systematic effects. To quantify such a possible deviation from GR, we use σ_{GR} , defined as, $\sigma_{\text{GR}} = (\mu - \mu_{\text{GR}})/\sigma$. Here μ is the mean of the distribution, μ_{GR} is the GR value, and σ is the standard deviation of the posterior distribution. Since $\mu_{\text{GR}} = 0$, we simply get $\sigma_{\text{GR}} = \mu/\sigma$.

³Not to be confused with the spin parameter.

In this study, we restrict to two inspiral coefficients, $\delta\hat{\chi}_0$ (0PN) and $\delta\hat{\chi}_4$ (2PN), respectively, which appear in the Newtonian and the second post-Newtonian order in the inspiral phase of the WF. Moreover, we consider two coefficients in the post-inspiral regime: $\delta\hat{\beta}_2$ from the intermediate phase and $\delta\hat{\alpha}_2$ from the merger-ringdown phase. We employ IMRPhenomPv2⁴ WF model for this study, which is a dominant-mode model for precessing BBHs where the inspiral coefficients are obtained from PN theory and calibration to NR WFs, and the post-inspiral coefficients by fitting to NR-simulations (Hannam et al. 2014; Husa et al. 2016; Khan et al. 2016; Alejandro et al. 2016). Consequently, the inspiral phase is defined up to a cutoff frequency $f_{\text{cut}} = f_c^{\text{PAR}} = 0.018/M$, where M is the total mass of the binary (Husa et al. 2016; Khan et al. 2016).

5.2.2 GW data analysis and Parameter Estimation Setup

Building on the discussion in Section 2.3, we discuss some general setups commonly utilized throughout this chapter.

Injections

Firstly, in Sect. 5.3.1, we consider a set of 30 zero-noise microlensed BBH injections, consisting of GW150914-like non-spinning signals with added microlensing effects. The component masses and the extrinsic parameters of the signals are kept similar to those of GW150914⁵, except for the luminosity distance, which is tuned to fix the network optimal SNR to 50 for each injection in the detector network of advanced LIGO at Hanford, Livingston and, Virgo. In addition, the spin components are kept zero to avoid possible systematic errors in the inference of the deviation parameters from GR and make sure any biases arise predominantly from microlensing effects. This is because one needs to have even higher SNR values of $\gtrsim 10^2$ to reliably estimate both the spin components (Pürrer et al. 2016). The microlens parameters used for generating the injections correspond to $\log_{10} M_{\text{Lz}} \in \{1, 2, 3, 4, 5\}$ and $y \in \{0.01, 0.05, 0.1, 0.5, 1.0, 3.0\}$, making 30 injections in total.

⁴Though there are recent phenomenological models with more accurate spin-precession description (Pratten et al. 2021, 2020) and sub-dominant modes (García-Quirós et al. 2020), we stick to IMRPhenomPv2 WF model for our analysis.

⁵The posterior samples can be found at <https://zenodo.org/records/6513631>. Specifically, we used the median values of 1D-marginalized posteriors from the 'C01:Mixed' channel in 'IGWN-GWTC2p1-v2-GW150914_095045_PEDataRelease_mixed_cosmo.h5'.

In Sect. 5.3.2, to robustly analyze the effect of microlensing on tests of GR, we consider a population of simulated microlensed signals. We generate a mock GW data set of $\sim 2.5 \times 10^4$ microlensed BBH signals, where the mass and spin priors are derived from the inferred population model of GWTC-3 data (Abbott et al. 2023): the source-frame component masses are sampled from the Power Law + Peak distribution and spin parameters are drawn from a Gaussian isotropic distribution. We assume the Madau-Dickison profile for the merger rate density in the universe (Madau 1997; Fishbach et al. 2018), with the source redshift range set to $z_S \in (0.001, 10)$. The upper limit of $z_S = 10$ is set because isolated point lenses tend to amplify the signals, increasing their optimal SNR and, consequently, their detection horizon (Mishra et al. (2023b)). To sample microlens parameters, we assume a log-uniform prior in M_{Lz} and a linear power-law prior for y , where:

$$\begin{aligned} p(\log_{10} M_{Lz}) &\propto \text{Uniform}(1, 5), \\ p(y) &\propto y, \quad y \in (0.01, 3.00). \end{aligned} \tag{5.3}$$

The motivation to use $p(y) \propto y$ comes from geometry and isotropy (Lai et al. 2018). The other parameters were sampled from the usual prior distributions: isotropic sky location and orientation, and uniform polarization angle. We put an observed network SNR, ρ_{opt}^N , threshold of 8 when using the unlensed templates for recovery in the LIGO-Virgo detector network. We further impose an additional requirement that $\text{SNR} > 6$ in both the inspiral and post-inspiral parts of the signal. This requirement ensures that we have an adequate amount of information for our analyses in both signal regimes. The demarcation between these two regimes is done via a cutoff frequency f_{cut} in the frequency domain. We define $f_{\text{cut}} = f_{\text{ISCO}}$ for IMRCT and $f_{\text{cut}} = f_{\text{C}}^{\text{PAR}}$ for the parameterized test, as explained in Sect. 5.2.1. For performing IMRCT, these SNR thresholds are consistent with the previous analyses (Abbott et al. 2021b,d). However, we note that for parameterized tests, our SNR thresholds are stricter. For example, to study the deviations in the coefficients corresponding to the inspiral regime, such as $\delta\hat{\chi}_0$ and $\delta\hat{\chi}_4$ considered here, one only needs to have the inspiral $\text{SNR} > 6$. A stricter condition of $\text{SNR} > 6$ in both the inspiral and post-inspiral regimes is employed so that each injection can be analyzed for all four testing GR parameters.

Parameter Estimation

Throughout this chapter, we use the publicly available Bayesian inference library Bilby (Ash-ton et al. (2019)) for performing parameter estimation runs. Specifically, we use the dynesty (Spea-gle (2020)) nested sampler with the ‘acceptance-walk’ method for the Markov-Chain Monte-Carlo (MCMC) evolution as implemented in Bilby, along with the sampler settings of `nlive= 1024`, `n-accept= 60` and `n-parallel= 2` per injection. The lower frequency limit of the likelihood evaluation is set to $f_{\text{low}} = 20$ Hz, which is also the reference frequency.

Furthermore, in order to compute microlensing effects, whether for generating microlensed injections or inferring microlens parameters, we employ a custom frequency domain source model, which incorporates the two microlensing parameters M_{Lz} and y in addition to the standard 15 BBH parameters and is made publicly available via Python/Cython package GWMAT (Mishra, A., in prep.).

While inferring microlens parameters in our simulated microlensed signals with injected $M_{Lz} \equiv M_{Lz}^{\text{true}}$ and $y \equiv y^{\text{true}}$, we assume a log-uniform prior in M_{Lz} and a linear power-law prior for y , where:

$$p(\log_{10} M_{Lz}) \propto \begin{cases} \text{Uniform}(-1, 5), & \text{if } \log_{10} M_{Lz}^{\text{true}} < 3 \\ \text{Uniform}(-1, 7), & \text{otherwise} \end{cases} \quad (5.4)$$

$$p(y) \propto y, \text{ where } \begin{cases} y \in (0.001, 3.00), & \text{when } y^{\text{true}} < 1 \\ y \in (0.001, 5.00), & \text{otherwise.} \end{cases} \quad (5.5)$$

We also use these priors while generating a population of microlensed signals.

For the parameterized test of GR, we independently vary each of the four deviation parameters instead of simultaneously varying them, aligning with the methodology employed in the LVK catalog analyses (Abbott et al. 2021d,b) and similar studies (Narayan et al. 2023). However, we do note that in an alternative theory of gravity, one would anticipate modifications to all post-Newtonian (PN) coefficients beyond a certain order. This choice of varying only one parameter at a time is made to avoid uninformative results, as observed in cases where multiple parameters are allowed to vary simultaneously, as illustrated for GW150914 in (Abbott, B. P. and others 2016). Nevertheless, earlier studies (Meidam et al. 2018; Johnson-McDaniel et al. 2022) have demonstrated that even when varying a single testing parameter, it is still possible to detect deviations from GR that modify multiple PN coefficients (even when this testing parameter is itself not modified).

5.2.3 Comparative Analysis of Fitting Factor and Time-Delay Trends in the Microlensing Parameter Space

In Fig. 5.1, in addition to showing the trend of f_{ML} , we also illustrate the trend of variation of FF in the $M_{Lz} - y$ parameter space. For each microlensed signal, the binary parameters are kept fixed to a non-spinning equal mass binary having $60 M_{\odot}$ ⁶, and the FF value is

⁶We note that the general trend of the variation of the FF values in the $M_{Lz} - y$ parameter space should not depend on the source properties because the FF depends only weakly on the binary parameters relative to the lensing parameters (see Fig. 2 in Mishra et al. 2023b).

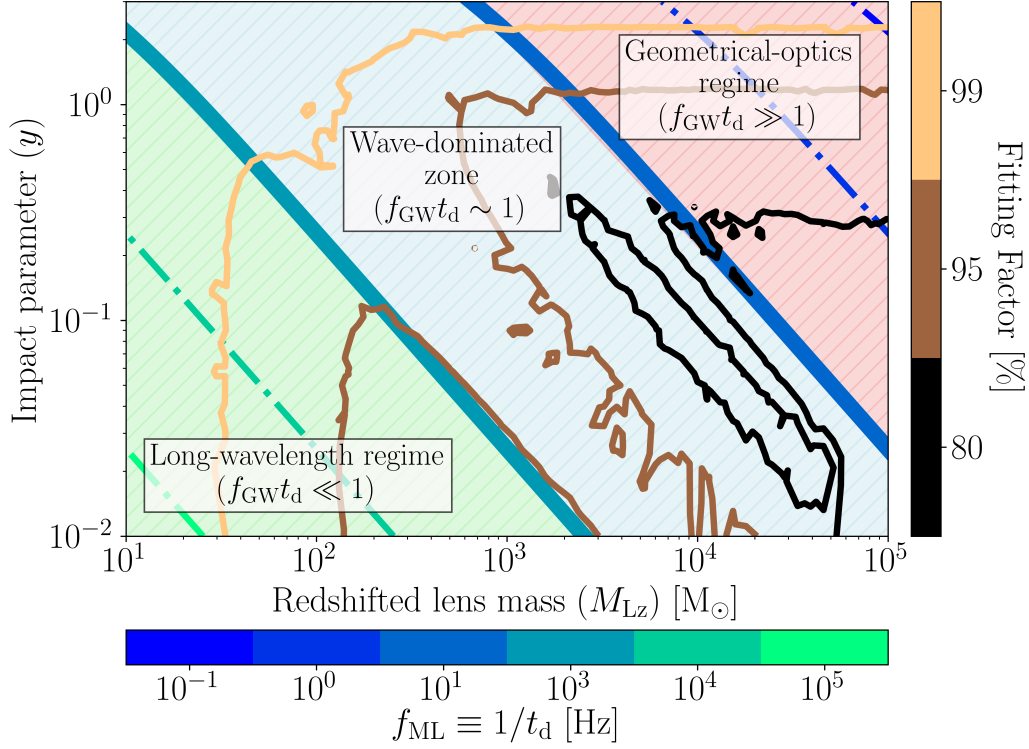


Figure 5.1: Similar to Fig. 2.2 but with added FF contours, illustrating the contrast in trends between the variations of f_{ML} and the FF values when microlensed signals are recovered using unlensed templates. f_{ML} indicates the onset of significant microlensing effects (see Eq. 2.12), whereas FF is related to the Bayes Factor in favour of microlensing against the unlensed hypothesis (see Eq. 2.33). The analysis is conducted within the parameter space relevant to isolated point lenses, focusing on the current-generation ground-based detectors. The f_{ML} values are shown in *Blue - Green colorbar*. Contours at 10 and 1000 Hz denote the rough transition regions, dividing the parameter space into three zones. (i) Long-Wavelength Regime where the GW frequency (f_{GW}) is significantly lower than f_{ML} , meaning $f_{GW} \ll f_{ML}$, resulting in minimal interaction between GWs and the microlens, as seen from the light green colored region of the figure. (ii) Wave Dominated Zone: This is the region where $f_{GW} \sim f_{ML}$, leading to substantial interference effects on GWs, depicted with light blue color. (iii) Geometrical-Optics Regime: The right-most region in the figure is shown with light coral colour where $f_{GW} \gg f_{ML}$. This region is inclusive of milli-lensing and strong-lensing scenarios. *Blue - Green colorbar* represent FF contours where the parameters of the source binary are kept fixed to a non-spinning equal mass binary having $60 M_{\odot}$. For each microlensed WF, the FF values are computed by maximizing its match with the unlensed WFs within the parameter space of component masses and aligned spins.

obtained by maximizing the match between the microlensed WF and the 4-dimensional aligned-spin template WFs, modelled by the two component masses and their aligned spins. The match is maximized using the Nelder-Mead algorithm as implemented in the 'optimization' module of the Scipy library (Virtanen et al. 2020). As we can see, the trend of variation of FF is different from that of the variation of f_{ML} . Notably, the FF values roughly increase as we move towards the bottom-right corner of the parameter space, with increasing M_{Lz} and $1/y$ values. Conversely, the f_{ML} values increase as we move from the top-right corner of the $M_{\text{Lz}} - y$ parameter space towards the bottom-left corner. It is important to note that the region where wave effects dominate differs from the area associated with low match values (high Bayes factor values in favour of microlensing). This observation plays a crucial role in the interpretation of our results.

It is important to note that the region where wave-optics effects dominate differs from the area associated with low match values (high Bayes factor values in favour of microlensing). This observation plays a crucial role in the interpretation of our results.

5.3 Results and Discussions

5.3.1 GW150914-like Microlensed Injections

As described in Sect. 5.2.2, here we consider zero-noise GW150914-like non-spinning injections with added microlensing effects. The microlens parameters used for generating the injections correspond to $\log_{10} M_{\text{Lz}} \in \{1, 2, 3, 4, 5\}$ and $y \in \{0.01, 0.05, 0.1, 0.5, 1.0, 3.0\}$, making 30 injections in total. These ideal microlensed BBH injections serve as our initial motivation for the exploration of microlensing-induced biases in tests of GR and enable us to search for patterns in the distortions, helping us identify the intriguing microlensing parameter space where deviations become more prominent.

IMRCT

We conduct six sets of parameter estimation runs for all the 30 microlensed injections. In the case of IMRCT, each set includes runs for the inspiral part, post-inspiral part, and the full IMR signal, for both unlensed and microlensed hypotheses. The inspiral and post-inspiral regions of our injections are demarcated by the cutoff frequency of $f_c^{\text{IMR}} = f_{\text{ISCO}} = 128 \text{ Hz}$.⁷

⁷We note that in the ideal case, one may determine this cutoff frequency from the mass and spin estimates of the binary considering the full-IMR analysis. However, even when computed using un-lensed

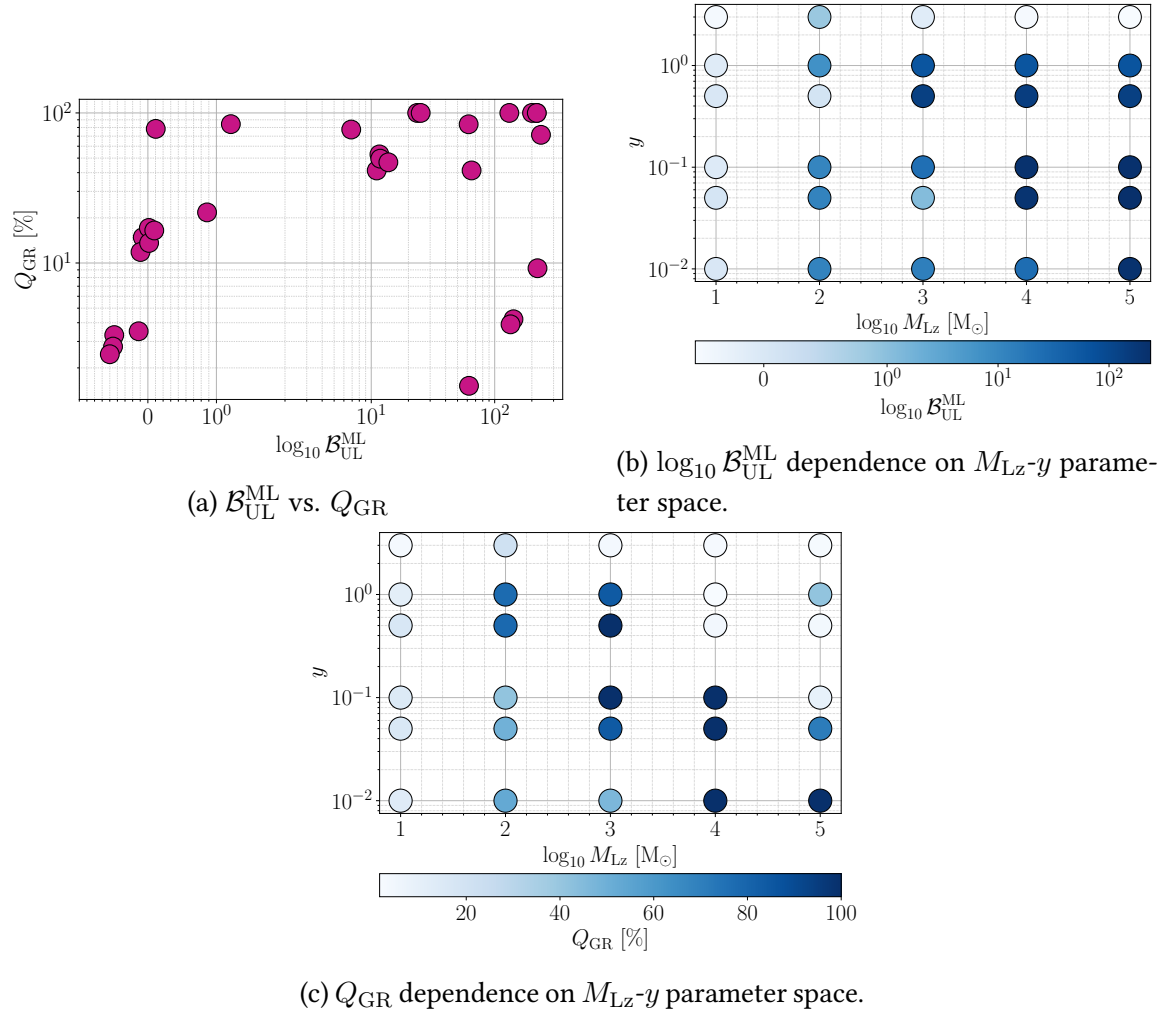


Figure 5.2: IMR consistency test results for GW150914-like microlensed injections, highlighting deviations from GR (Q_{GR}), alongside the microlensing Bayes factor ($\log_{10} \mathcal{B}_{\text{UL}}^{\text{ML}}$) for reference.

In Figure 5.2, we present the results of the IMR consistency test for GW150914-like microlensed injections. We focus on identifying deviations from GR using the GR quantile value, denoted as Q_{GR} . We also illustrate the logarithmic Bayes factor $\log_{10} \mathcal{B}_{\text{UL}}^{\text{ML}}$ in favour of the microlensed hypothesis over the unlensed hypothesis for the full IMR signal, for reference. Firstly, in Figure 5.2a, we depict the relationship between Q_{GR} and $\log_{10} \mathcal{B}_{\text{UL}}^{\text{ML}}$. We immediately observe that microlensing effects can introduce bias in the IMR consistency test, resulting in high Q_{GR} values that surpass 90% in some cases. However, despite noting several occurrences of high Q_{GR} values ($> 70\%$) when $\log_{10} \mathcal{B}_{\text{UL}}^{\text{ML}}$ is also high (> 1), we do not discern any significant correlation between the two quantities. In other words, there are instances where $\log_{10} \mathcal{B}_{\text{UL}}^{\text{ML}}$ is low (< 1), yet Q_{GR} is high ($> 70\%$), and vice versa, where Q_{GR} is low ($< 10\%$), even when $\log_{10} \mathcal{B}_{\text{UL}}^{\text{ML}}$ is high (> 1).

Upon closer inspection, we find that the dependence of Q_{GR} and $\log_{10} \mathcal{B}_{\text{UL}}^{\text{ML}}$ values on the $M_{\text{Lz}} - y$ parameter space shows a characteristic trend that is notably different between the two (see Figs. 5.2b and 5.2c). Specifically, $\log_{10} \mathcal{B}_{\text{UL}}^{\text{ML}}$ adheres to the expected behaviour, monotonically increasing as we increase the lens mass while reducing the impact parameter. For instance, in Fig. 5.2c, the $\log_{10} \mathcal{B}_{\text{UL}}^{\text{ML}}$ is negative where the microlensing effects are weak (for injections having either $\log_{10} M_{\text{Lz}} = 1$ or $y = 3$) and increases as we move towards the bottom-right region in the $\log_{10} M_{\text{Lz}} - y$ plane, where it reach values $\mathcal{O}(10^2)$, indicating strong preference for microlensing. In contrast, the variation in the Q_{GR} values does not mirror the trend as exhibited by $\log_{10} \mathcal{B}_{\text{UL}}^{\text{ML}}$, as significant Q_{GR} values (exceeding 50%) are primarily confined within a diagonal region spanning from the top-left to the bottom-right corner. Within the diagonal region, the Q_{GR} values are high for high lens mass and low impact parameters (bottom-right region of the diagonal) and decrease as we move up in the diagonal towards the top-left direction.

As shown in Figure 2.2 and elaborated upon in Sect. 2.2.1, the diagonal region in the $\log_{10} M_{\text{Lz}} - y$ parameter space corresponds to the range where wave effects dominate within the sensitivity band of ground-based detectors. In practical terms, the microlens parameters lying in this diagonal region would lead to interference patterns for signals in the frequency range of roughly 10-1000 Hz. We observe that Q_{GR} is significant primarily within the 'wave-dominated zone' and decreases as it moves toward the 'long-wavelength regime'. Conversely, in the 'geometric-optics regime' (the parameter space where the

IMR recoveries, the value of f_{ISCO} for our injections typically remains close to ~ 130 Hz, except for a few exceptional cases where it varies between, roughly, 115 Hz and 160 Hz. It is important to note that the choice of the cutoff frequency itself serves as an arbitrary threshold for distinguishing the inspiral phase from the post-inspiral phase. Previous studies have demonstrated that small variations in the cutoff frequency do not have a significant impact on the IMRCT results (Ghosh et al. 2016). Therefore, we believe that these variations in f_{ISCO} do not substantially affect our findings. Moreover, our choice of a high SNR of 50 ensures that there is sufficient information content in both the inspiral and post-inspiral phases for accurately inferring the final mass and spin.

geometric-optics approximation tends to hold), we often encounter cases where deviations from GR are minimal ($Q_{\text{GR}} < 10\%$) albeit the lensing effects being very high $\log_{10} \mathcal{B}_{\text{UL}}^{\text{ML}} \sim \mathcal{O}(10)$.

Therefore, from Fig. 5.2c, it is evident that deviations from GR appear to occur primarily when interference effects are pronounced. We will further validate this claim using a parameterized test as well as by studying a simulated population similar to GWTC-3 in the following sections.

Parameterized test of GR

To further investigate the apparent deviation from GR due to microlensing effects in the inspiral, intermediate, and merger-ringdown phases of the signal, we perform the parameterized test of GR on our microlensed injection set. As discussed in Sect. 5.2.1, we utilize four parameterization variables: $\delta\hat{\chi}_0$, $\delta\hat{\chi}_4$, $\delta\hat{\beta}_2$, and $\delta\hat{\alpha}_2$.

In Fig. 5.3, we show the results of the parameterized test conducted on our microlensed injection set. Each of the four panels displays the Gaussian sigma values at which GR is excluded (σ_{GR} ; see Sect. 5.2.1) in one of the four parameterized parameters, as indicated in the colorbar, within the $\log_{10} M_{\text{Lz}} - y$ parameter space. The larger the magnitude of σ_{GR} , the greater the significance of deviations from GR. For better visualization, we mark the cases with significant deviations ($\sigma_{\text{GR}} > 1$) using a diamond marker instead of the circular markers. For all four parameters, we observe that the deviations are primarily significant within the wave-dominated zone and gradually decay as we move further into the long-wavelength regime. Meanwhile, the geometrical optics regime doesn't give any significant deviations. This pattern resembles our observation of the Q_{GR} value in Fig. 5.2c.

To robustly illustrate the relationship between the deviations from GR and the characteristic frequency f_{ML} at which wave effects caused by a microlens are expected to become more pronounced, we suppress the two-dimensional parameter space of $M_{\text{Lz}} - y$, shown in Fig. 5.3, into a one-dimensional representation using f_{ML} . We then represent the sigma deviation values in Fig. 5.4, explicitly emphasizing three distinct regions: the long-wavelength regime, the wave-dominated zone, and the geometrical-optics regime. Moreover, we also depict the $\log_{10} \mathcal{B}_{\text{UL}}^{\text{ML}}$ values for each injection using a colormap for comparison between the deviations from GR with the overall strength of microlensing. The transparent markers that are not colored and only contain a black edge (unfilled circles) are cases where $\log_{10} \mathcal{B}_{\text{UL}}^{\text{ML}} < 0$ are cases where $\log_{10} \mathcal{B}_{\text{UL}}^{\text{ML}} < 0$. We also mark the 1σ and the 3σ deviations with dotted-red lines for better visualization.

For all four parameters, we clearly observe that the deviations from GR primarily

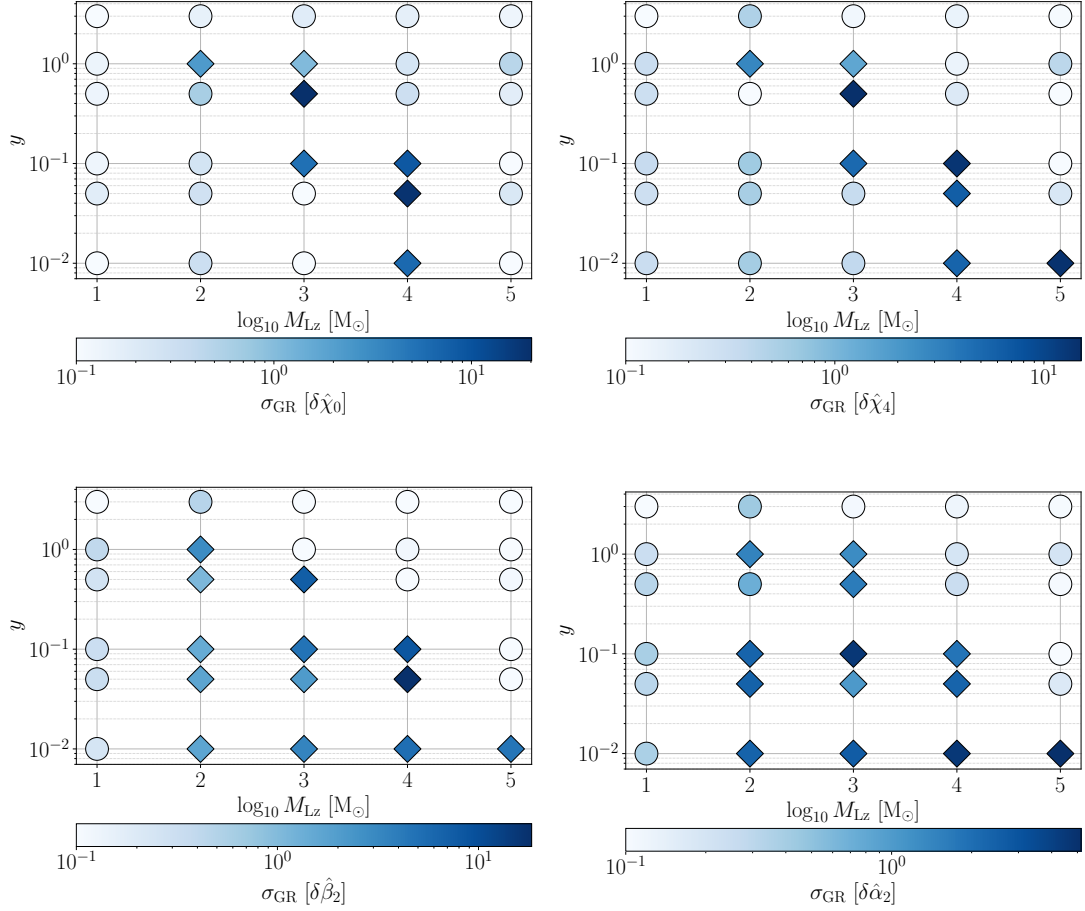


Figure 5.3: Bias in the parametrised test of GR in GW150914-like microlensed injections for four deviation parameters $\{\delta\chi_0, \delta\chi_4, \delta\alpha_2, \delta\beta_2\}$. Each of the four panels displays the Gaussian sigma values at which GR is excluded (σ_{GR}) in one of the four parametrized parameters, as indicated in the colorbar, within the $\log_{10} M_{Lz} - y$ parameter space. The larger the magnitude of σ_{GR} , the greater the significance of deviations from GR. For better visualization, we mark the cases with significant deviations ($\sigma_{GR} > 1$) using a diamond marker instead of the circular markers.

increase in the wave-dominated zone (blue shaded region in the middle of each panel), including several cases with $\sigma_{GR} \gtrsim 5^8$ for all the parameters. Similarly, within the long-wavelength regime, we only observe significant deviations ($\sigma_{GR} > 1$) for parameters that measure deviations in the post-inspiral regime, i.e., $\delta\hat{\alpha}_2$ and $\delta\hat{\beta}_2$, where we also observed slight deviations around the intersection of the wave-dominated zone and the

⁸We note that based on $\mathcal{O}(10^4)$ sample points in our posterior distributions, a value greater than 3 Gaussian sigma cannot be stated with certainty (Narayan et al. 2023). Nonetheless, we still quote the actual Gaussian sigma values derived from our distributions, along with this cautionary note.

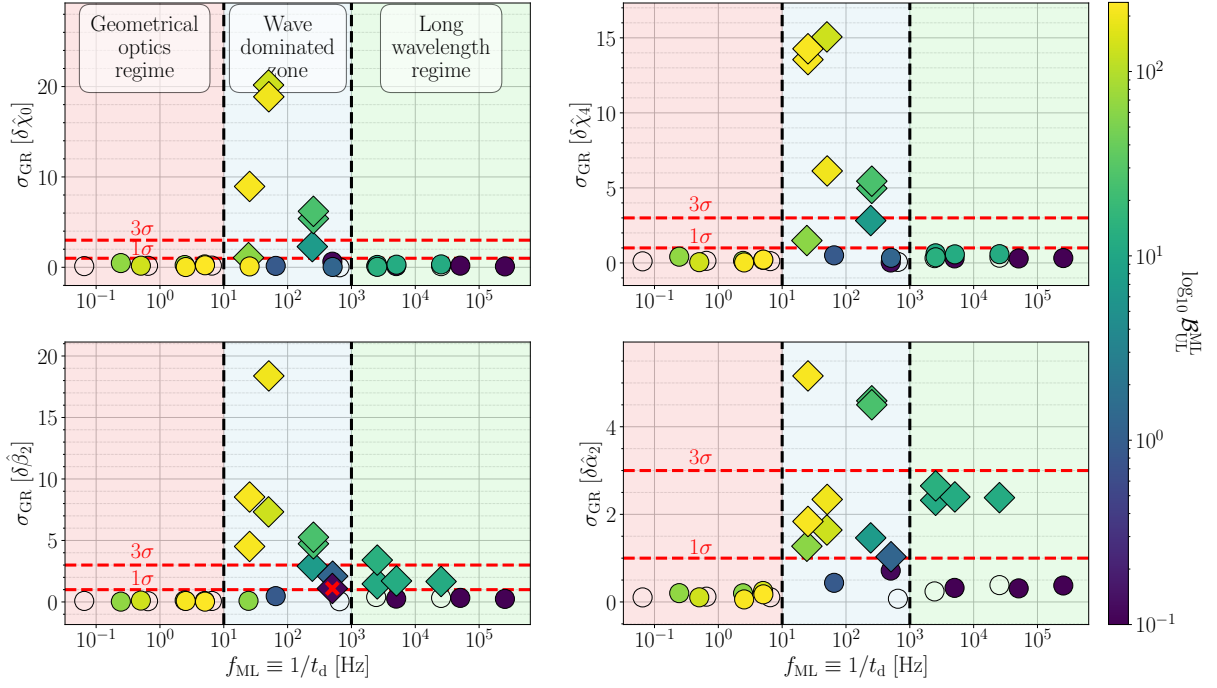


Figure 5.4: Similar to Fig. 5.3, but with $M_{Lz} - y$ parameter space suppressed into a one-dimensional representation using f_{ML} (see Eq. 2.12). The figure highlights three scenarios: the long-wavelength regime, the wave-dominated zone, and the geometrical optics regime. The colormap represents $\log_{10} \mathcal{B}_{\text{UL}}^{\text{ML}}$ values for each injection. Transparent markers with black edges indicate cases where $\log_{10} \mathcal{B}_{\text{UL}}^{\text{ML}} < 0$. Dotted-red lines indicate the 1σ and 3σ significance of deviations. Diamond markers indicate significant deviations ($\sigma_{\text{GR}} > 1$), and cases meeting $\log_{10} \mathcal{B}_{\text{UL}}^{\text{ML}} < 1$ (indicating stealth bias) have an added red cross.

long-wavelength regime (also see Sect. 5.3.4). Within the geometrical-optics regime, we do not notice any significant deviations for any parameter despite encountering several cases with high values of $\log_{10} \mathcal{B}_{\text{UL}}^{\text{ML}}$, including values $\mathcal{O}(10^2)$.

It's also worth noting that in all cases where high biases are observed ($\sigma_{\text{GR}} > 3$), we consistently find a high Bayes factor ($\log_{10} \mathcal{B}_{\text{UL}}^{\text{ML}} > 1$) in favour of microlensing. Conversely, there is only a single instance (marked with a red cross in the bottom-left panel) where significant biases are present ($1 < \sigma_{\text{GR}} < 3$), but the Bayes factor remains notably low ($\log_{10} \mathcal{B}_{\text{UL}}^{\text{ML}} < 0.5$). *This suggests that events showing high deviations ($\sigma_{\text{GR}} > 3$) from GR must also be analyzed for the presence of microlensing features before claiming any (erroneous) GR deviations.* However, to establish this conclusion more firmly, we conduct a more robust study using a population of microlensed signals, as detailed in Section 5.3.2.

5.3.2 Population of Microlensed Injections

To robustly analyze the effect of microlensing on tests of GR, we consider a population of simulated microlensed signals (see Sect. 5.2.2 for details).

IMRCT

For the study of IMRCT on our microlensed signals, we only consider a subset of those having total mass in the range $50 - 100 M_{\odot}$, to which our detectors are sensitive from inspiral to ringdown phase of the coalescence (also called "golden" binaries). This leaves us with a total of $\sim 1.5 \times 10^4$ signals.

Unlike our strategy in Sect 5.3.1, we do not perform parameter estimation for this study. We save the computational expense of performing parameter estimation runs by instead studying a quantity that closely resembles the deviation parameter Q_{GR} in IMRCT. We realize from our study of GW150914-like injections in Sect. 5.3.1 that, for IMRCT, the Q_{GR} value shows a positive correlation with the difference in the match between the microlensed and unlensed WFs in the inspiral and post-inspiral phases, respectively. In quantitative terms, we observe that the quantity:

$$\Delta \mathfrak{M}_{\text{MR}}^{\text{I}} = |\mathfrak{M}(h_{\text{UL}}^{\text{I}}, h_{\text{ML}}^{\text{I}}) - \mathfrak{M}(h_{\text{UL}}^{\text{MR}}, h_{\text{ML}}^{\text{MR}})|, \quad (5.6)$$

where \mathfrak{M} represents match as defined in Eq. 2.20, shows a positive Pearson correlation value of around $\sim 57\%$ with Q_{GR} (see Fig. 5.5). Hence, we compute this quantity for our population as a computationally more cost-effective alternative for estimating the trend of the Q_{GR} value in IMRCT.

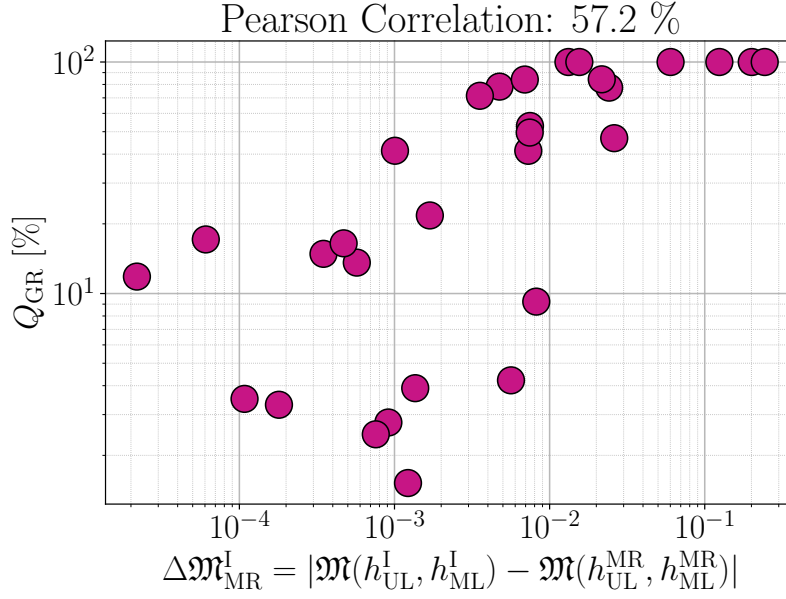


Figure 5.5: Illustration of correlation between Q_{GR} and $\Delta\mathcal{M}_{\text{MR}}^{\text{I}}$.

The results are shown in Fig. 5.6. In the top panel, we depict the quantity $\Delta\mathcal{M}_{\text{MR}}^{\text{I}}$ in the parameter space of $\log_{10} M_{\text{Lz}}$ and y . Both colour and size of the markers are proportional to the strength of $\Delta\mathcal{M}_{\text{MR}}^{\text{I}}$. In other words, markers with dark red colour and relatively larger size represent regions where we expect IMRCT to be biased due to microlensing. We again observe that deviations from GR are prominent mainly in the wave-dominated zone. This is more explicitly shown in bottom panel, where we plot the deviation parameter $\Delta\mathcal{M}_{\text{MR}}^{\text{I}}$ as a function of f_{ML} . We also colour the markers based on their Bayes factor values $\log_{10} \mathcal{B}_{\text{UL}}^{\text{ML}}$, estimated using Eq. 2.33. We clearly see deviations to increase sharply in the wave-dominated zone. In the geometrical-optics regime and the transition region from the wave-dominated to geometrical-optics regime, we again notice several cases having high $\log_{10} \mathcal{B}_{\text{UL}}^{\text{ML}}$ values but with no significant $\Delta\mathcal{M}_{\text{MR}}^{\text{I}}$ value. These results are consistent with our observations in the previous sections.

Parameterized test of GR

To get a population-wide behavior of deviations in the parameterized test of GR, we choose 100 injections from our population of microlensed signals. To ensure a significant number of events strongly favours microlensing, we restrict the injected impact parameter value to be less than unity (i.e., $y < 1$). Furthermore, the selection employs Eq. 2.33 to determine $\log_{10} \mathcal{B}_{\text{UL}}^{\text{ML}}$. Since this estimation is not reliable at lower SNRs, we keep the threshold on $\log_{10} \mathcal{B}_{\text{UL}}^{\text{ML}} > 9$ for the majority of events ($\sim 50\%$) (Mishra et al. 2023b). The

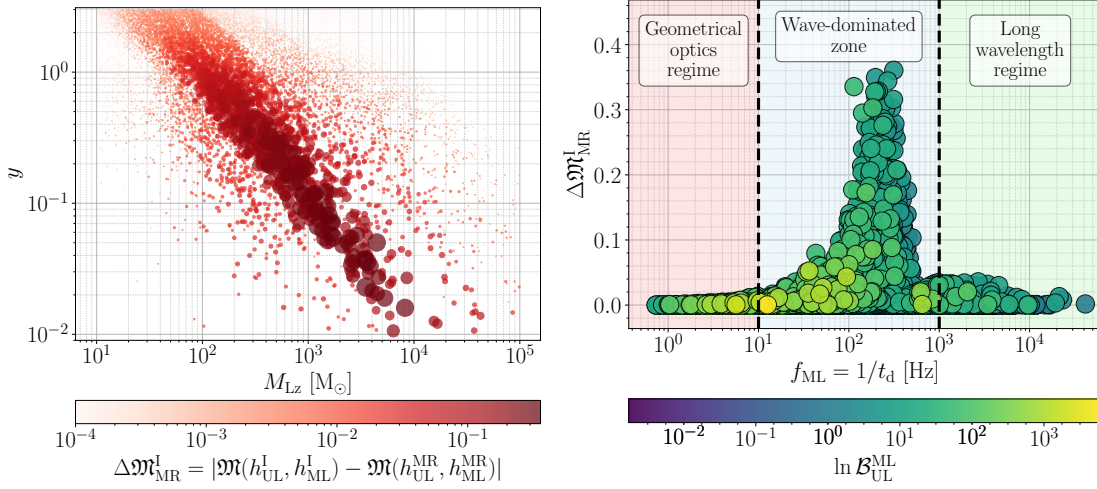


Figure 5.6: IMRCT results for a population of simulated microlensed signals using $\Delta\mathfrak{M}_{MR}^I$ (Eq. 5.6) as a proxy to quantify deviations in IMRCT. *Top panel:* Depicts $\Delta\mathfrak{M}_{MR}^I$ in the $\log_{10} M_{Lz} - y$ parameter space. Marker colour and size represent the strength of $\Delta\mathfrak{M}_{MR}^I$. *Bottom panel:* Depicts $\Delta\mathfrak{M}_{MR}^I$ as a function of f_{ML} . The colorbar represents Bayes factor values $\ln \mathcal{B}_{UL}^{ML}$ estimated using Eq. 2.33.

rest of the population corresponds to cases where microlensing is too weak to be correctly identified in the model selection process. Such a population of weakly microlensed signals help us in investigating the possibility of *stealth bias* (Cornish et al. 2011; Vallisneri, Michele 2012; Vitale & Del Pozzo 2014) in the context of microlensing - cases where microlensing itself is not large enough to be detectable but the systematic errors due to it remain significant (i.e., larger than the statistical uncertainties in parameter estimation), appearing as deviations from GR⁹.

As discussed in 5.2.1, we study the deviations in each of the four deviation parameters ($\delta\hat{\chi}_0$, $\delta\hat{\chi}_4$, $\delta\hat{\alpha}_2$, $\delta\hat{\beta}_2$) separately. The results are plotted in Fig. 5.7 and Fig. 5.8, in a similar fashion as in Sect. 5.3.1. Particularly, in Fig. 5.7, we plot the Gaussian sigma deviations in the parameter space of $M_{Lz} - y$. We again show the cases having $\sigma_{GR} > 1$ with a diamond marker for better visualization. As we can see, there are several cases that give significant deviation from GR ($\sigma_{GR} > 1$). These include cases that lie in the modest regime in our parameter space, i.e., having the characteristic impact parameter value of $y \approx 1$ and the

⁹The term ‘stealth-bias’ was coined by Cornish et al. (2011) in the context that GR templates can be significantly biased even when there is no significant evidence for adopting an alternative theory of gravity. In our work, we use this term to mean when microlensing effects lead to biases in tests of GR without being detectable themselves.

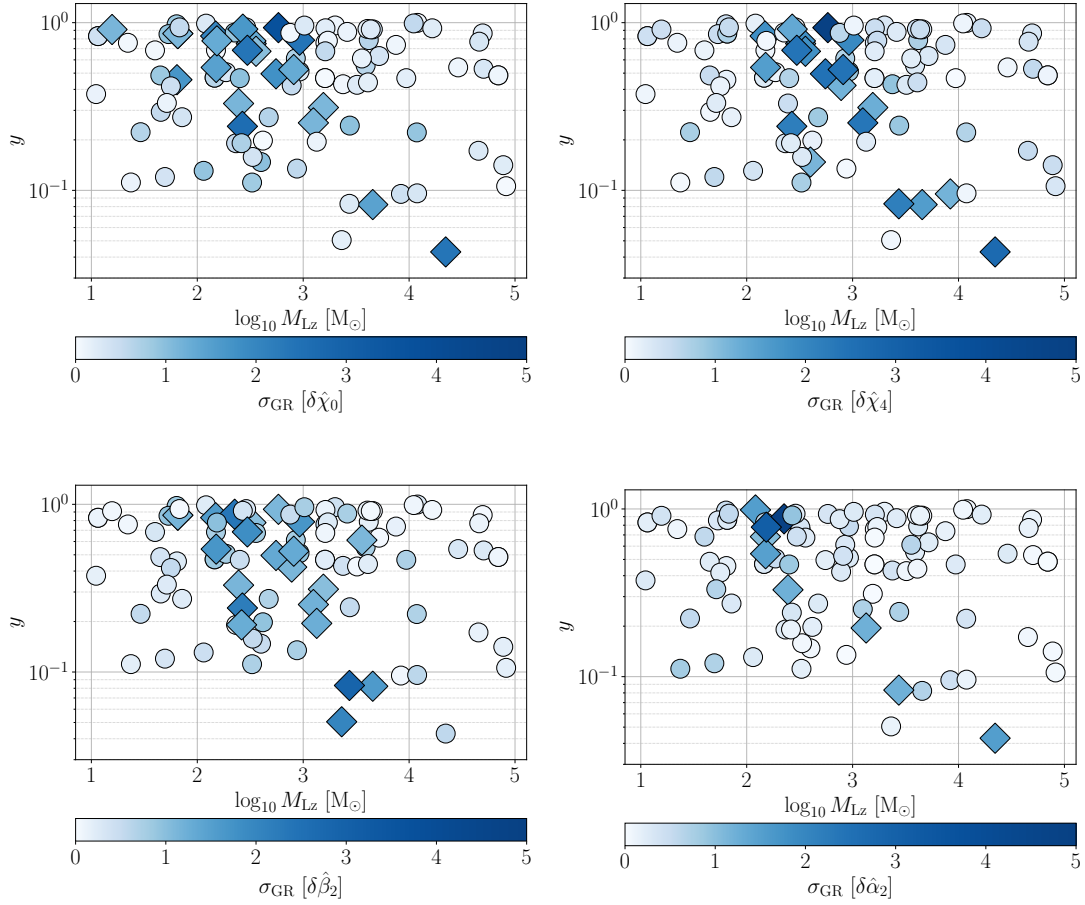


Figure 5.7: Same as Fig. 5.3, but for a population of microlensed injections as studied in Sect. 5.3.2.

lens mass $M_{Lz} < 100 M_{\odot}$.

Meanwhile, in Fig. 5.8, we plot it against the f_{ML} with colors representing the Bayes factor $\log_{10} \mathcal{B}_{UL}^{ML}$ values obtained via nested sampling. We also put an upper cap of 10 on the colorbar to get a better visibility of Bayes factors around unity. We observed several instances where $\sigma_{GR} > 1$ for all the parameters, including cases where it is even beyond $3\sigma_{GR}$. However, we only saw two cases having $\sigma_{GR} > 5$, one for $\delta\hat{\chi}_4$ and the other for $\delta\hat{\alpha}_2$. We clearly see that deviations increase pre-dominantly in the wave-dominated zone and fall off as we go further into the long-wavelength regime. We do not see any deviation from GR in the geometrical optics regime. These results are consistent with all our previous observations.

To investigate the possibility of *stealth bias*, we specifically identify cases with significant deviations from GR ($\sigma_{GR} > 1$) but without a strong preference for the microlensing model ($\log_{10} \mathcal{B}_{UL}^{ML} < 1$), marking them with a red cross. It is worth noting that although

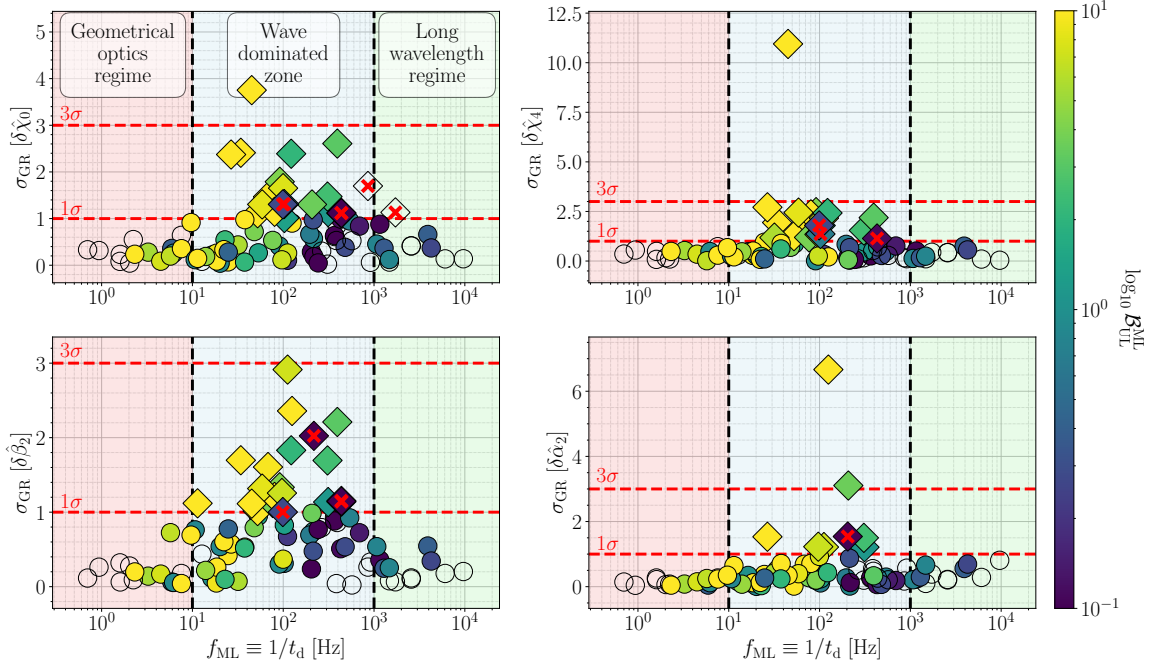


Figure 5.8: Same as Fig. 5.4, but for a population of microlensed injections as studied in Sect. 5.3.2.

several such cases are found, none reach the 'evidence'-level significance ($\sigma_{\text{GR}} > 3$). This is because all cases with $\sigma_{\text{GR}} > 3$ also exhibit a strong preference for the microlensing hypothesis over the null hypothesis ($\log_{10} \mathcal{B}_{\text{UL}}^{\text{ML}} > 1$).

5.3.3 Normality Test of Posterior Samples

In Sections 5.3.1 and 5.3.2, we conducted parameterized test analysis using Gaussian sigma values to quantify deviations from General Relativity (GR). However, this approach implicitly assumes that the posterior distributions are Gaussian. To assess the validity of this assumption, we performed the Shapiro-Wilk test of normality [Shapiro & Wilk \(1965\)](#) on our posterior samples of the deviation parameters, namely, $\delta\hat{\chi}_0$, $\delta\hat{\chi}_4$, $\delta\hat{\alpha}_2$, $\delta\hat{\beta}_2$. The Shapiro-Wilk test is known to be one of the most powerful normality tests ([Mendes & Pala 2003](#); [Keskin 2006](#); [Razali et al. 2011](#)). The test statistic, denoted as \mathcal{SW} , tends to be higher as the samples more closely resemble a Gaussian distribution and should approach 100% for a true Gaussian distribution.

In Fig. 5.9, we present the results of the Shapiro-Wilk test. The corresponding SNR values of the events are displayed in the colorbar. The samples obtained for GW150914-like injections in Sect. 5.3.1 exhibit a high degree of confidence in being Gaussian distributions. With the exception of two cases, all other cases yield a statistic value above 95%

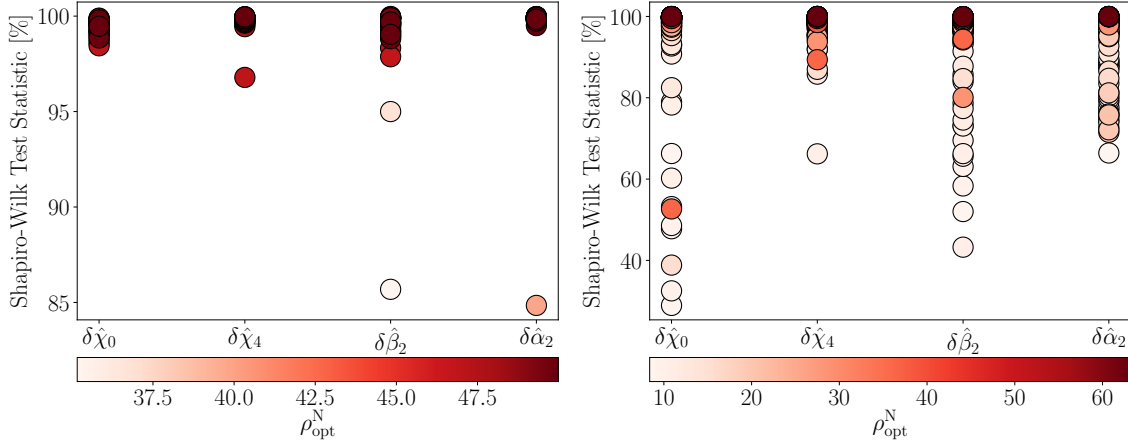


Figure 5.9: Shapiro-Wilk normality test for the posterior samples of $\{\delta\hat{\chi}_0, \delta\hat{\chi}_4, \delta\hat{\alpha}_2, \delta\hat{\beta}_2\}$ in our injections. The colorbar shows the corresponding SNR of the events. *Left-panel:* Shapiro-Wilk test statistic for samples obtained for GW150914-like injections in Sect. 5.3.1 (see also Figs. 5.3 and 5.4). *Right-panel:* Shapiro-Wilk test statistic for the samples obtained for the study of the microlensed population in Sect. 5.3.2 (see also Figs. 5.7 and 5.8).

(i.e., $SW > 95\%$ for the majority of cases).

Building on this observation, we introduce a new metric *p-index*, denoted as \mathcal{P} , to quantify the nature of these distributions more robustly. It is defined as the value such that $\mathcal{P}\%$ of the samples in the distribution have values above $\mathcal{P}\%$. In mathematical terms, for a distribution $\mathbb{D} = \{d_i\}$ of percentages, it can be expressed as:

$$\mathcal{P} = \arg \min_{x \in (0,100)} \left| \frac{\text{count}(\{d_i : d_i > x\})}{\text{count}(\{d_i\})} - \frac{x}{100} \right|, \quad (5.7)$$

where x denotes the possible percentage values, and 'count' represents the number of elements in the set inside the parentheses. This additional metric further reinforces our confidence in the Gaussian nature of the data. Specifically, the Shapiro-Wilk test statistic values for our deviation parameters, including $\delta\hat{\chi}_0$, $\delta\hat{\chi}_4$, $\delta\hat{\alpha}_2$, and $\delta\hat{\beta}_2$, yield \mathcal{P} values of 98.5%, 96.8%, 95.0%, and 96.7%, respectively. For instance, this means that the statistic values for the posterior distribution of $\delta\hat{\chi}_0$ are above 98.5% for approximately 98.5% of the cases, and so on.

In a similar fashion, the *right-panel* of Fig. 5.9 displays the test statistic results for the samples obtained during the study of the microlensed population in Sect. 5.3.2. Here, \mathcal{P} values for our deviation parameters, $\delta\hat{\chi}_0$, $\delta\hat{\chi}_4$, $\delta\hat{\alpha}_2$, and $\delta\hat{\beta}_2$ are 88.0%, 93.8%, 84.7%, and 82.7%, respectively.

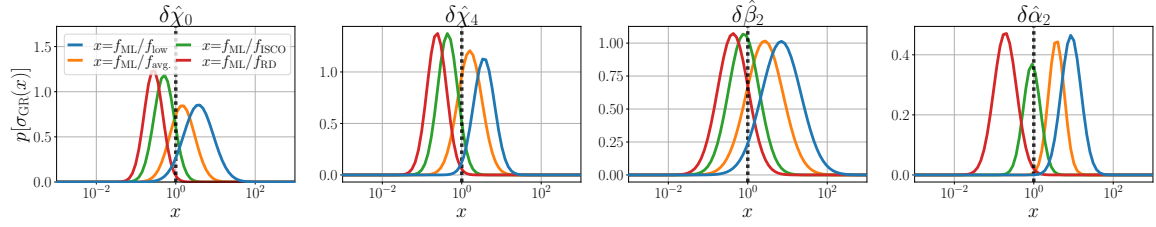


Figure 5.10: Gaussian fits to the distribution of σ_{GR} for the microlensed population injections plotted against the variable $x \in \{f_{\text{ML}}/f_{\text{low}}, f_{\text{ML}}/f_{\text{avg.}}, f_{\text{ML}}/f_{\text{ISCO}}, f_{\text{ML}}/f_{\text{RD}}\}$ for all the deviation parameters $\{\delta\hat{\chi}_0, \delta\hat{\chi}_4, \delta\hat{\alpha}_2, \delta\hat{\beta}_2\}$ (indicated on top of each panel). A dashed-black line is included at $x = 1$ for reference, representing the characteristic frequency of GW f_{GW}^c which when comparable to f_{ML} gives rise to wave effects.

In conclusion, the assumption of Gaussianity holds well in our case, especially for high SNR events. For GW150914-like injections, approximately 95% of the cases yielded a statistic value exceeding 95%, while in the case of the population study, approximately 85% of the cases yielded a statistic value above 85%.

5.3.4 Investigating the correspondence between f_{ML} and f_{GW} : A closer perspective

As discussed in Section 2.2, the condition for wave effects is that $f_{\text{ML}} \sim f_{\text{GW}}$. In the sections leading up to this point, we assumed that $f_{\text{GW}} \in (10, 1000)$ Hz, based on the sensitivity of ground-based detectors. However, we can be more precise in defining the characteristic frequency of GW, denoted as f_{GW}^c , which when comparable to f_{ML} gives rise to wave effects. This approach is possible because, for a given GW signal, we can explicitly determine the frequency range where it exhibits significant power in the detectors. Therefore, in this section, we leverage this knowledge to establish a closer correspondence between f_{ML} and f_{GW} .

The lower frequency cutoff typically used for GW data analysis is $f_{\text{low}} = 20$ Hz, below which the noise dramatically increases, especially due to seismic and thermal noise sources (Abbott et al. 2016; Valdes et al. 2022). Next, the inspiral and post-inspiral sections are typically demarcated using the frequency at the inner-most stable circular orbit f_{ISCO} (Hanna et al. 2009; Abbott et al. 2021b), which is the same cutoff frequency we used for IMRCT (see Sect. 5.2.1). We note that this demarcation is not the same as the demarcation used for the parameterized test. Moreover, a rough estimate of the upper frequency of a GW signal can be determined based on the ringdown frequency, f_{RD} , associated with the dominant quasi-normal mode ($l = 2, m = 2, n = 0$) (Hanna et al. 2009; Berti et al.

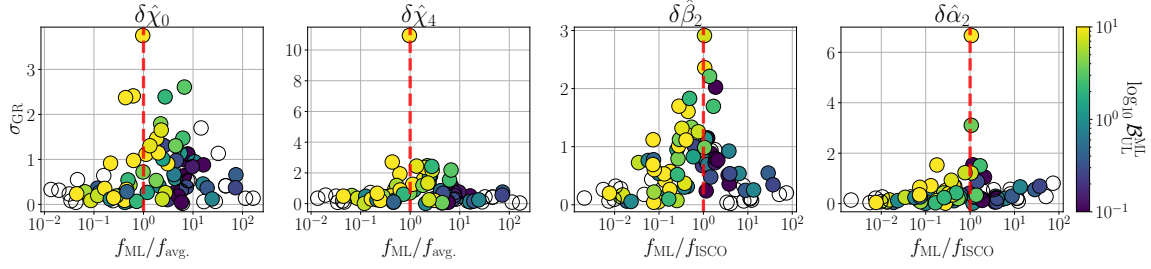


Figure 5.11: The distribution of σ_{GR} is analyzed in the context of some selected values of x for different deviation parameters. *Leftmost two panels:* $x = f_{\text{ML}}/f_{\text{avg.}}$ is considered with deviation parameters $\{\delta\hat{\chi}_0, \delta\hat{\chi}_4\}$. *Rightmost two panels:* For parameters $\{\delta\hat{\alpha}_2, \delta\hat{\beta}_2\}$, we choose $x = f_{\text{ML}}/f_{\text{ISCO}}$. A dashed-red line at $x = 1$ is included for reference.

2006). Additionally, one can define a signal's power-weighted average frequency, denoted as $f_{\text{avg.}}$, using the following equation:

$$f_{\text{avg.}} = \frac{\int_{-\infty}^{\infty} f \cdot |\tilde{h}(f)|^2 df}{\int_{-\infty}^{\infty} |\tilde{h}(f)|^2 df}. \quad (5.8)$$

This power-weighted average frequency reflects where most of the signal power is concentrated. In the case of GW signals, the inspiral phase typically contributes the most power. Consequently, we usually expect $f_{\text{avg.}} < f_{\text{ISCO}}$. Thus, a signal that spans a sufficient number of cycles in the inspiral phase within the current detectors can be effectively divided into different phases of its evolution using these frequency markers: $f_{\text{low}} < f_{\text{avg.}} < f_{\text{ISCO}} < f_{\text{RD}}$.

We consider posterior distributions of the deviation parameters, namely, $\delta\hat{\chi}_0$, $\delta\hat{\chi}_4$, $\delta\hat{\alpha}_2$, and $\delta\hat{\beta}_2$, for the different injections studied in 5.3.2. Since the characteristic frequencies mentioned above differ for each injection, we study the ratio of f_{ML} with these frequencies, i.e., we examine the quantity: $x : x \in \{f_{\text{ML}}/f_{\text{low}}, f_{\text{ML}}/f_{\text{avg.}}, f_{\text{ML}}/f_{\text{ISCO}}, f_{\text{ML}}/f_{\text{RD}}\}$. Given that the condition for pronounced wave effects is $f_{\text{ML}} \sim f_{\text{GW}}^c$, we analyze the distribution of σ_{GR} as a function of x to determine which ratio results in a peak near 1.

In Fig. 5.10, we present the distribution of σ_{GR} for the microlensed population injections against the variable x for all the deviation parameters (indicated on top of each panel). To enhance clarity, we employ Gaussian fits to combine all four $\sigma_{\text{GR}} - x$ distributions of a given deviation parameter into a single panel. An example illustrating the actual $\sigma_{\text{GR}} - x$ distribution is provided in Fig. 5.11 for specific cases. We also include a dashed-black reference line at $x = 1$, representing the frequency where $f_{\text{ML}} \sim f_{\text{GW}}^c$. Given that, for our injections, $1/f_{\text{RD}} < 1/f_{\text{ISCO}} < 1/f_{\text{avg.}} < 1/f_{\text{low}}$, the Gaussian curves follow a consistent trend. Specifically, the $\sigma_{\text{GR}} - x$ distribution for $x = f_{\text{ML}}/f_{\text{RD}}$ occupies the leftmost position with its peak significantly below 1 (indicated by the red curves), while for

$x = f_{\text{ML}}/f_{\text{low}}$, it occupies the rightmost position in all panels with the peak significantly above 1 (indicated by the blue curves). In other words, assuming $f_{\text{GW}}^c = f_{\text{low}}$ would result in an underestimation, whereas assuming $f_{\text{GW}}^c = f_{\text{RD}}$ would lead to an overestimation. Therefore, the fact that the curves of these ratios lie on different sides of unity implies that the condition for microlensing in the case of a given GW signal can be more precisely defined as when $f_{\text{ML}} \in (f_{\text{low}}, f_{\text{RD}})$, as opposed to the generic range of (10, 1000)Hz we used earlier.

We also note that for the deviation parameters $\delta\hat{\chi}_0$ and $\delta\hat{\chi}_4$, the peak corresponding to $x = f_{\text{ML}}/f_{\text{avg.}}$ is closest to unity. This implies that these deviation parameters exhibit the highest bias when $f_{\text{ML}} \sim f_{\text{GW}}^c \sim f_{\text{avg.}}$. This outcome is expected because these parameters primarily measure deviations from GR during the inspiral phase of the signal. In Fig. 5.11, we explicitly depict the distribution of σ_{GR} for the $x = f_{\text{ML}}/f_{\text{avg.}}$ ratio for these two parameters in the leftmost two columns, where we observe an increase in deviations around $x \sim 1$. In contrast, for the deviation parameters $\delta\hat{\alpha}_2$ and $\delta\hat{\beta}_2$, the peak corresponding to $x = f_{\text{ML}}/f_{\text{ISCO}}$ is closest to unity, indicating that these deviation parameters exhibit the highest bias when $f_{\text{ML}} \sim f_{\text{GW}}^c \sim f_{\text{ISCO}}$. This can be explained by the fact that these parameters primarily measure deviations from GR during the post-inspiral phase of the signal. In Fig. 5.11, we explicitly display the distribution of σ_{GR} for the $x = f_{\text{ML}}/f_{\text{ISCO}}$ ratio for these two parameters in the rightmost two columns, where, once again, we notice an increase in deviations around $x \sim 1$.

In conclusion, we find that the condition for microlensing in the case of a given GW signal can be more precisely defined as when $f_{\text{ML}} \in (f_{\text{low}}, f_{\text{RD}})$, as opposed to the generic range of (10, 1000) Hz we used earlier. We went further and tried to find even specific conditions. For example, for parameters that measure deviations in the inspiral regime, such as $\delta\hat{\chi}_0$ and $\delta\hat{\chi}_4$, the deviations increase when $f_{\text{ML}} \sim f_{\text{avg.}}$. While for parameters that measure deviations in the post-inspiral regime, such as $\delta\hat{\alpha}_2$ and $\delta\hat{\beta}_2$, the deviations increase when $f_{\text{ML}} \sim f_{\text{ISCO}}$.

5.4 Conclusion

In this study, we examined the potential impact of microlensing effects on tests of GR. We adopted an isolated point-lens model for our study, covering a parameter space typically relevant for the ground-based detectors, i.e., $M_{\text{Lz}} \in (1, 10^5) M_{\odot}$ and $y \in (0.01, 3)$. However, it is important to note that our findings and conclusions are expected to apply broadly to any microlensing scenario, regardless of the specific parameter space, as we relate the biases observed to the fundamental characteristic of gravitational lensing. Our investigation centered on two theory-agnostic tests of GR: the inspiral-merger-ringdown

consistency test (IMRCT) and the parameterized tests of GR. These tests allowed us to explore deviations from GR across different evolutionary phases of a GW signal: inspiral, intermediate, and merger-ringdown. We consider both high-SNR GW150914-like systems and a population of microlensed signals similar to GWTC-3 with added microlensing effects.

Our findings lead to the following conclusions:

1. Microlensing can significantly bias tests of GR, with confidence levels even exceeding 5σ . Fortunately, whenever there is a strong deviation from GR ($\sigma > 3$), there is also a strong preference for microlensing over the null hypothesis that the signal is unlensed. In other words, we consistently observe $\log_{10} \mathcal{B}_{\text{UL}}^{\text{ML}} > 1$ in cases where $\sigma_{\text{GR}} > 3$, preventing us from falsely claiming deviations from GR. However, it is important to note that we do encounter scenarios in which deviations from GR are still significant $\sigma_{\text{GR}} \in (1, 3)$, but the Bayes factor isn't strong enough to confidently assert microlensing ($\log_{10} \mathcal{B}_{\text{UL}}^{\text{ML}} < 1$). We refer to these situations as the *stealth bias* of microlensing in tests of GR.
2. In general, we do not find any correlation between the deviations from GR and the Bayes factor $\log_{10} \mathcal{B}_{\text{UL}}^{\text{ML}}$. Upon closer inspection, we demonstrate that the deviations from GR occur primarily when interference effects are pronounced, i.e., when $f_{\text{GW}} \sim 1/t_{\text{d}} \equiv f_{\text{ML}}$. These deviations intensify within the wave-dominated region of the $M_{\text{Lz}} - y$ parameter space, where $f_{\text{ML}} \in (10, 10^3)$ Hz, and diminish as we move further into the long-wavelength regime ($f_{\text{ML}} > 10^3$ Hz). In geometrical optics regime ($f_{\text{ML}} < 10$ Hz), where we can consider the resultant signal to be a trivial superposition of two signals which differ only by a constant amplitude, a phase shift of $\pi/2$, and a time-delay value smaller than the chirp time of the signal, we saw the least bias despite noting several instances where the lensing Bayes factor strongly supported microlensing ($\log_{10} \mathcal{B}_{\text{UL}}^{\text{ML}} > 1$).
3. We further refine the microlensing condition for a given GW signal, suggesting that it is more precisely defined as when $f_{\text{ML}} \in \sim (f_{\text{low}}, f_{\text{RD}})$, rather than the generic (10, 1000) Hz range used in our study. Upon closer inspection, we observe that parameters quantifying deviations in the inspiral phase, such as $\delta\hat{\chi}_0$ and $\delta\hat{\chi}_4$, exhibit increasing deviations when $f_{\text{ML}} \sim f_{\text{avg}}$ (power-weighted average frequency). Conversely, for parameters assessing deviations in the post-inspiral phase, such as $\delta\hat{\alpha}_2$ and $\delta\hat{\beta}_2$, the deviations tend to increase when $f_{\text{ML}} \sim f_{\text{ISCO}}$ (frequency corresponding to the innermost stable circular orbit).

Since the rate of expected microlensing events is significantly lower in comparison to unlensed signals, the potential for microlensed signals to bias tests of GR at a population

level is highly improbable. Nonetheless, as our study demonstrates, there is a possibility that certain individual events in the future could exhibit notable deviations from GR due to microlensing effects. This would necessitate conducting dedicated microlensing analyses, alongside investigations into other potential effects, before making any erroneous claims of deviations from GR. Notably, these deviations in a few events could serve as indicators, helping to prioritize them as potential microlensing candidates, as microlensing searches are computationally expensive.

While our current study primarily focuses on demonstrating how microlensing effects can introduce deviations from GR, future research has the potential to explore additional aspects. For example, one could investigate potential biases in microlensing searches resulting from non-GR effects, addressing the possible degeneracy between non-GR effects and microlensing. Furthermore, future studies might investigate the impact of microlensed signals on population-level tests of GR, considering various compact dark matter fractions and detector sensitivities. Lastly, a crucial avenue for future research involves a detailed examination of cases leading to stealth biases of microlensing on tests of GR.

Chapter 6

Unraveling the Connection: Eccentric Binary Black Holes and Microlensed Signals

We investigate the potential biases in GW microlensing searches when the source is an eccentric BBH system for the first time. Microlensing searches help us constrain compact dark matter, whereas studying the eccentric population can shed light on the formation mechanisms of BBHs. Despite the differences in their astrophysical origin, our research demonstrates that microlensed templates outperform quasi-circular unlensed templates in recovering eccentric WFs, where we utilize an isolated point-mass lens model for microlensing throughout our analysis. Using reliable eccentric WFs derived from numerical relativity simulations, we first demonstrate how eccentric signals can significantly bias microlensing hypotheses over unlensed scenarios. Our investigation involves comprehensive analyses, including population-wide assessments and injection studies employing the `TEOBResumS` WF model. Both the FF and Bayesian analyses, which encompass parameter estimation and Bayesian model selection, indicate that the preference for microlensing recoveries increases with higher eccentricities, longer WFs, and higher SNR values. Population-wide studies consistently favor microlensing templates over unlensed templates, particularly for eccentricities exceeding 0.2. Bayesian analysis shows that the Bayes factor in evidence of microlensing over unlensed hypothesis can even exceed 10^5 for low mass binaries ($< 30 M_{\odot}$) at eccentricity of ~ 0.3 . Lastly, by conducting eccentric injections and recoveries using `TEOBResumS`, we demonstrate the potential to break the degeneracy and resolve biases when eccentricity is considered as a free parameter in the recovery process. This underscores the importance of eccentricity analysis before claiming any erroneous microlensing effects. These findings carry significant implications for the future of GW detectors, including third-generation instruments like CE and ET, as well as space-based detectors like DECIGO.

6.1 Introduction

In this chapter, we demonstrate, for the first time, how the presence of eccentricity can bias the search for microlensing signatures in the GW signals. We focus on the GW signals expected to be detected by the Advanced LIGO (Aasi et al. 2015) and Virgo detectors (Acernese et al. 2015) at the current detector sensitivities. The search for microlensing in the ground-based sensitivity band is particularly important as it provides an unparalleled opportunity to constrain the compact dark matter fraction in the mass range $\sim 10 - 10^5 M_\odot$ (e.g., Basak et al. 2022). This region is currently not well constrained¹.

The observations made by the LVK collaboration during the first three observation runs have revealed a diverse population of BBHs, BNSs, and NS-BH systems. These detections have provided invaluable data for studying the astrophysical processes involved in the formation, evolution, and ultimate merger of these compact object binaries, paving the way for further advancements in our understanding of the Universe (The LIGO Scientific Collaboration et al. 2023b). All these signals are mostly well modeled by quasi-circular templates (Abbott et al. 2019d), though four events have been reported to show support for non-zero eccentricity (Romero-Shaw et al. 2022). This indicates that these systems likely underwent sufficient circularization by the time their GWs entered the sensitivity band of the ground-based detectors (Peters 1964). While negligible eccentricities are expected in binaries formed through isolated channels (Mapelli 2021), there are alternative formation mechanisms that can result in significant eccentricities ($e \gtrsim 0.5$ at 10 Hz) at small binary separations (Zevin et al. 2019). Examples include binary formation from primordial black holes (Cholis et al. 2016), dynamical interactions in dense stellar environments (Wen 2003), and the evolution of isolated triple systems (Antonini et al. 2014).

The effects arising from non-zero eccentricity will become increasingly significant as we probe the early stages of binary evolution or enhance the sensitivity of detectors. This leads us to anticipate the detection of eccentric GW signals with future detectors such as Cosmic Explorer (CE) (Reitze et al. 2019), Einstein Telescope (ET) (Maggiore et al. 2020), and deci-Hertz observatories (Kawamura et al. 2008; Luo et al. 2016). Although the true rate of microlensed events is still unknown, we find a striking resemblance between eccentric and microlensed GW signals, despite the differences in their astrophysical origin. Consequently, it becomes important to understand if the current microlensing searches by the LVK collaboration can be biased due to the presence of eccentricity in the signal. Understanding and disentangling these effects is crucial for accurate astrophysical

¹We note that GWs also put an indirect constraint on compact dark matter fraction using the observed merger rate density.

interpretations and for distinguishing genuine microlensed events from eccentric binary sources. Our findings shed light on the challenges associated with identifying microlensing events and underscore the importance of careful analysis when interpreting GW observations. Furthermore, we employ Bayesian analysis to investigate eccentric injections and conduct a population-wide analysis for a comprehensive understanding. As a result, this study enables us to make valuable predictions, including the parameter space region where the degeneracy between the two effects is most pronounced.

Throughout this chapter, we use the publicly available Bayesian inference library Bilby (Ashton et al. 2019, 2020) for performing parameter estimation runs. Specifically, we use Dynesty (Speagle 2020) nested sampler with the ‘acceptance-walk’ method for the Markov-Chain Monte-Carlo (MCMC) evolution as implemented in Bilby, along with the sampler settings of $n_{\text{live}} = 1024$, $n_{\text{accept}} = 60$ and $n_{\text{parallel}} = 2$ per injection. Unless otherwise noted, we use the WF approximant IMRPhenomXPHM for quasi-circular recoveries with the likelihood evaluation set to $f_{\text{low}} = 20$ Hz, which is also the reference frequency.

6.2 Results

6.2.1 Numerical Relativity Injections

In this subsection, we examine the potential bias in microlensing searches due to the presence of a non-zero eccentricity in BBH GW signals. We perform a model comparison study between the unlensed and the microlensed hypotheses for some ideal test cases by considering three pairs of quasi-circular and eccentric WFs generated using numerical

Table 6.1: Model comparison analysis between the unlensed (UL) and the microlensed (ML) hypotheses for numerical relativity injections corresponding to quasi-circular (or non-eccentric) and eccentric signals. The source binary considered is a non-spinning BBH with a total mass of $M_{\text{tot}} = 80 M_{\odot}$ and mass ratio $q \in \{1, 2, 3\}$.

q	Orbit type	$\log_{10} \mathcal{B}_{\text{noise}}^{\text{ML}}$	$\log_{10} \mathcal{B}_{\text{noise}}^{\text{UL}}$	$\log_{10} \mathcal{B}_{\text{QCUL}}^{\text{QCML}}$	Interpretation ¹	$\log_{10} M_{Lz}$	$\text{JS}(M_{Lz})^2$	y	$\text{JS}(y)^2$
1	Quasi-circular	3501.18	3501.78	-0.6	Negative	$-0.17^{+0.85}_{-0.71}$	0.57	$3.78^{+1.1}_{-2.34}$	0.07
	Eccentric	3442.59	3437.88	4.7	Very strong / Decisive	$2.19^{+0.09}_{-0.12}$	0.76	$4.38^{+0.83}_{-0.54}$	0.55
2	Quasi-circular	2759.26	2759.73	-0.5	Negative	$-0.23^{+1.06}_{-0.67}$	0.56	$3.78^{+1.09}_{-2.35}$	0.08
	Eccentric	2702.71	2697.11	5.6	Very strong / Decisive	$2.0^{+0.09}_{-0.13}$	0.76	$3.97^{+0.76}_{-0.49}$	0.59
3	Quasi-circular	1990.65	1991.07	-0.4	Negative	$-0.13^{+1.08}_{-0.76}$	0.54	$3.8^{+1.08}_{-2.42}$	0.07
	Eccentric	1934.17	1932.79	1.4	Strong	$1.93^{+0.26}_{-0.34}$	0.70	$4.51^{+0.97}_{-0.74}$	0.50

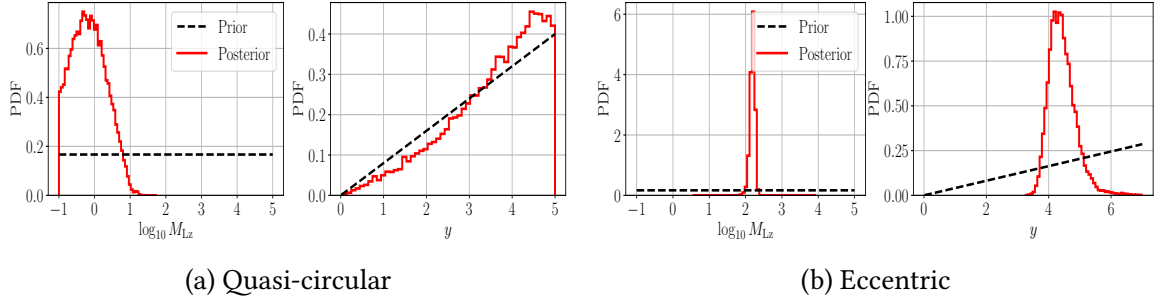


Figure 6.1: Recovered 1D marginalized posterior densities for the microlens parameters M_{Lz} and y for NR injections corresponding to (a) quasi-circular and (b) eccentric signals. The source binary considered is a non-spinning BBH with $\{M_{\text{tot}}/M_{\odot}, q\} = \{80, 1\}$ (see Table 6.1).

relativity (NR) simulations and obtained from the Simulating eXtreme Spacetimes (SXS) catalogue Boyle et al. (2019). The NR injections studied are non-spinning, having a (red-shifted) total mass of $80 M_{\odot}$, with mass ratios $q = \{1, 2, 3\}$. The binaries are observed face-on at a luminosity distance of 400 Mpc, having signal-to-noise ratios $\gtrsim 100$ (Narayan et al. 2023). The eccentric WFs have eccentricities $e \sim 0.1$ at 17 Hz for the total mass of $80 M_{\odot}$. However, we note that in subsequent sections, we adopt a different reference frequency for defining the eccentricity.

The results of our model comparison study are summarized in Table 6.1. Notably, the recovered Bayes factor $\log_{10} \mathcal{B}_{\text{UL}}^{\text{ML}}$ for all eccentric injections are consistently above unity, strongly supporting the microlensing hypothesis. In contrast, for all quasi-circular cases, we observe $\log_{10} \mathcal{B}_{\text{UL}}^{\text{ML}} < 0$, decisively rejecting the microlens hypothesis, as expected. Furthermore, the 1D marginalized posteriors of the recovered microlens parameters for eccentric cases are well recovered, exhibiting unimodal distributions with small standard deviations and peaks at $\log_{10} M_{Lz} \approx 2 M_{\odot}$ and $y \approx 4$. This observation is corroborated by a comparison between the prior distributions and the recovered posterior distributions, both via visual inspection (Fig. 6.1) and by evaluating the Jensen-Shannon (JS) divergence values (Lin (1991); check columns eight and ten in Table 6.1). For example, see the recovered median values with 1-sigma uncertainty for the microlens parameters in Table 6.1. Additionally, Fig. 6.1 proves a visual illustration of the 1D marginalized posteriors of the recovered microlens parameters for both quasi-circular and eccentric cases for $q = 1$ case. In the quasi-circular case (left panel), the posterior for the impact parameter follows the prior (dashed black lines), while the lens mass favors a value towards the lower bound set by the prior. Conversely, for the eccentric case (right panel), we clearly see sharp peaks for both $\log_{10} M_{Lz}$ and y around values 2.2 and 4.4, respectively. Moreover, the JS divergence values for the recoveries of y in the case of eccentric injections are consistently greater than 0.5, indicating substantial information gain. In contrast, for quasi-circular

WFs, the JS values for y consistently remain below 0.1, indicating that the posteriors are uninformative and closely resemble our prior distribution, as mentioned earlier. This behavior aligns with expectations for typical unlensed BBH signals. Similarly, the JS values for $\log_{10} M_{Lz}$ are consistently higher in the case of eccentric injections compared to the quasi-circular cases by a margin of ~ 0.2 .

In the case of eccentric injections, we observe that the evidence for microlensing, $\log_{10} \mathcal{B}_{\text{QCUL}}^{\text{QCML}}$, does not exhibit a consistent trend with changes in the mass ratio q . For instance, it initially increases from 4.7 for $q = 1$ to 5.6 for $q = 2$. However, there is a notable and significant drop to 1.4 for the $q = 3$ case. This behavior can be attributed to the fact that the $q = 3$ case had the lowest SNR among all cases since SNR decreases monotonically with increasing asymmetry in component masses (high mass ratios) when the distance and the binary mass are held fixed. Consequently, the Bayes factors supporting the presence of a signal against noise, i.e., $\log_{10} \mathcal{B}_{\text{noise}}^{\text{UL}}$ and $\log_{10} \mathcal{B}_{\text{noise}}^{\text{ML}}$, individually decrease as the mass ratio increases (e.g., see the third and fourth columns in Table 6.1). This reduction can subsequently lead to a decrease in $\log_{10} \mathcal{B}_{\text{QCUL}}^{\text{QCML}}$ (observed in Eq. 2.33).

The findings in this section highlight the presence of degeneracies between the microlensing and eccentric effects, emphasizing the need for a more comprehensive investigation, which are presented in the subsequent sections.

6.2.2 Population Study

To understand the broader impact of eccentricity on microlensing searches, we study a population of eccentric signals. We generate mock GW data of around $\sim 2 \times 10^4$ non-spinning eccentric BBH signals using TEOBResumS (Nagar et al. 2018, 2023) WF model, where BBH parameters are derived from the population model constructed using the GWTC-3 catalogue (The LIGO Scientific Collaboration et al. 2023b). We put an observed network SNR threshold of 8 when using the eccentric templates for recovery in the joint network of LIGO–Virgo detectors. The detector noise PSDs used correspond to the target O4 sensitivities. The population model provides a fit to the distribution of observed parameters, particularly masses, spin magnitudes, spin tilts, and the redshift distribution of the BBH mergers. All other BBH parameters are sampled uniformly from their respective domains. The eccentricity of the signals is defined at the same point in the evolution of a binary by fixing the dimensionless frequency to ~ 0.003 at apastron, equivalent to 10 Hz for a $60 M_{\odot}$ binary. We use a log-uniform prior in eccentricity, $e \in (0.01, 0.5)$. Furthermore, we assume the Madau-Dickison profile for the merger rate density in the universe, giving the source-redshift density model as given in (Madau 1997; Fishbach et al. 2018).

We aim to study the comparison between the unlensed and the microlens WF models

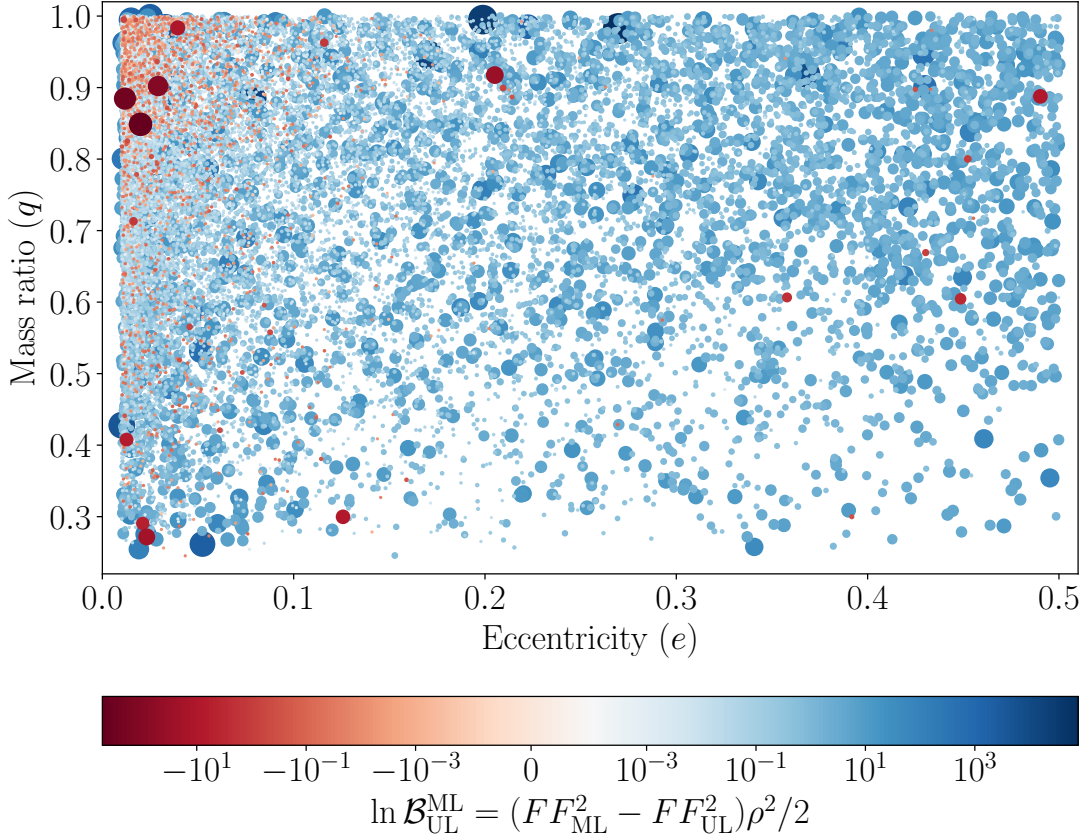


Figure 6.2: Illustration of the preference for microlensed templates over unlensed templates in the recovery of a population of eccentric signals (Sect. 6.2.2). The Bayes factors of microlensed vs. unlensed hypotheses, $\ln \mathcal{B}_{\text{UL}}^{\text{ML}}$, are shown in the parameter space of eccentricity and mass ratio. These values have been computed using Eq. 2.33, as indicated in the colorbar label. Both color and size of the markers are associated with the deviation of Bayes factors from zero, with red indicating a preference for unlensed templates over microlensed templates, while blue signifies the opposite preference.

for the recoveries of our simulated eccentric signals. Since computing Bayes factor values (e.g., using nested sampling algorithm) is usually computationally expensive, we utilize Eq. 2.33 to compare the two hypotheses, unlensed and microlensed, for our simulated eccentric signals. Specifically, we compare $\ln \mathcal{B}_{\text{Ecc}}^{\text{ML}}$ and $\ln \mathcal{B}_{\text{Ecc}}^{\text{UL}}$, which compares the two models against the true eccentric WF model. One can write,

$$\ln \mathcal{B}_{\text{UL}}^{\text{ML}} = \ln \mathcal{B}_{\text{Ecc}}^{\text{ML}} - \ln \mathcal{B}_{\text{Ecc}}^{\text{UL}} = \frac{1}{2}(FF_{\text{ML}}^2 - FF_{\text{UL}}^2)\rho_{\text{Ecc}}^2, \quad (6.1)$$

where FF_{UL} (FF_{ML}) are the FF values when the recovery model is unlensed (microlensed), and ρ_{Ecc} depicts the true optimal SNR of the eccentric signal. A positive value of $\ln \mathcal{B}_{\text{UL}}^{\text{ML}}$ suggests the microlens model is preferred over the unlensed hypothesis.

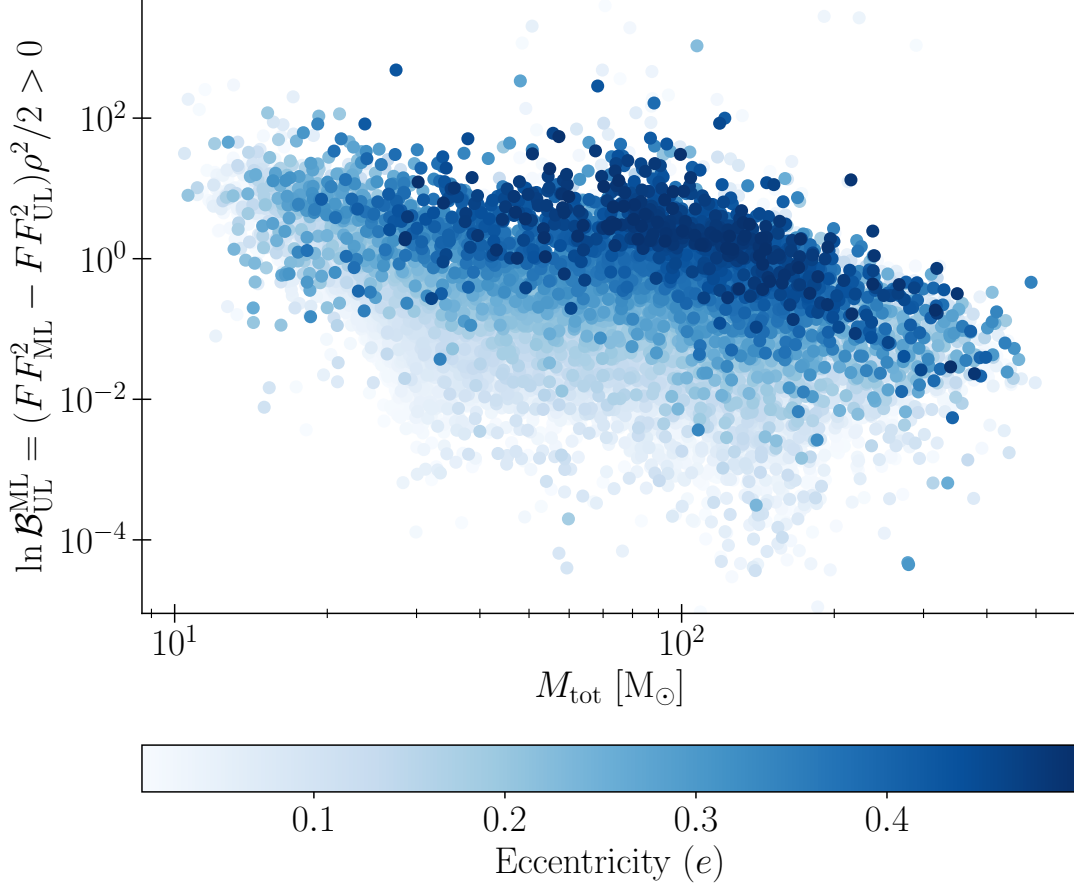


Figure 6.3: Variation in the Bayes factors of microlensed vs. unlensed hypotheses, $\ln \mathcal{B}_{\text{UL}}^{\text{ML}}$, with the binary mass, M_{tot} , for our population of eccentric signals (Sect. 6.2.2). The colorbar represents eccentricity.

In Fig. 6.2, we plot the quantity $\ln \mathcal{B}_{\text{UL}}^{\text{ML}}$ for our simulated eccentric signals. We illustrate the population in the parameter space of eccentricity and mass-ratio, while the colorbar shows the $\ln \mathcal{B}_{\text{UL}}^{\text{ML}}$ values. A blue marker implies the preference for the microlens model over the unlensed model in recovering the eccentric signal (red colored markers depict the opposite scenario). Moreover, the size of the circular markers is proportional to the absolute value of $\ln \mathcal{B}_{\text{UL}}^{\text{ML}}$, so that the dark-colored markers (either blue or red) are also larger in size, showing a clear distinction between the interesting cases of both the models. The markers are plotted in such a manner that red markers are always on top so that they are not missed visually due to their low values (light color and size). One can clearly see that in most of the parameter space, especially when eccentricities are significant ($e \gtrsim 0.1$), the microlensed templates fit better than the unlensed templates (blue-colored markers). In fact, for larger eccentricities, say $e \gtrsim 0.2$, the microlens model is almost always preferred over the unlensed model.

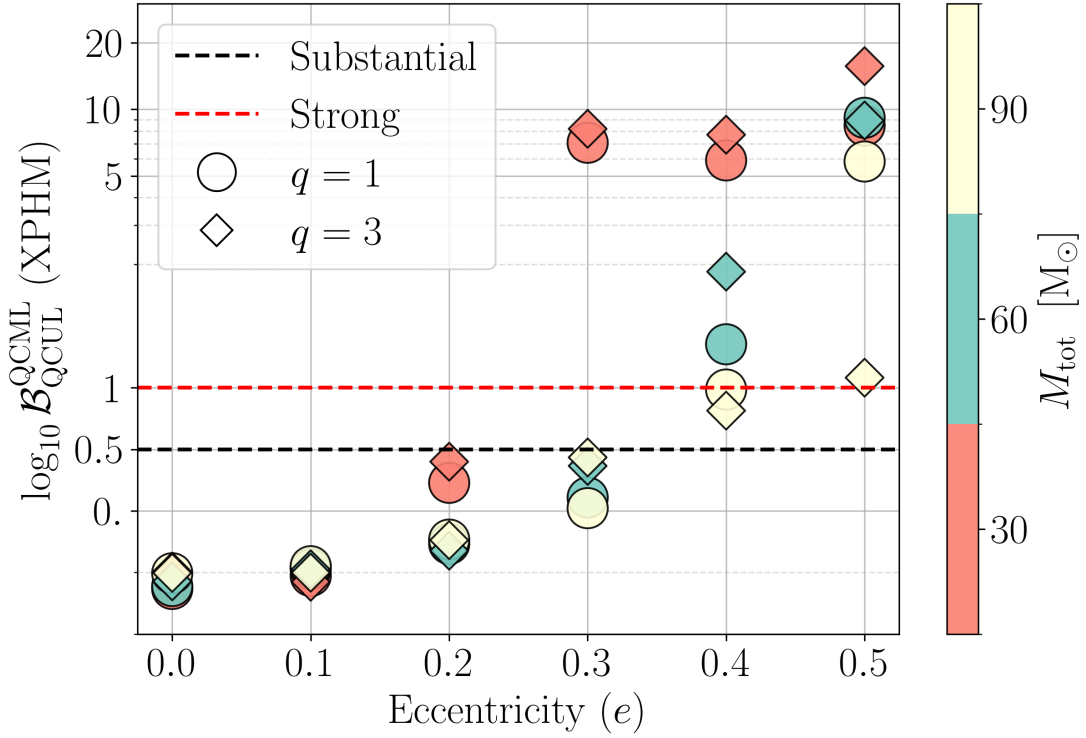


Figure 6.4: Bias in microlensing searches due to the presence of eccentricity. The variation in the Bayes factors of (quasi-circular, or QC) microlensed vs. QC unlensed hypotheses, $\ln \mathcal{B}^{\text{QCML}}_{\text{QCUL}}$, is shown a function of eccentricity (e), binary mass (M_{tot}), and mass-ratio (q). The Bayes factors are computed using the WF approximant IMRPhenomXPHM, which is a fully processing WF model utilizing all 15 parameters in the model for a typical quasi-circular BBH system.

This observation can be further understood from the fact that the microlens model has two additional parameters as discussed in Sect. 2.2.1. Consequently, a better fit is expected. However, it is important to understand that in many cases, we find $\ln \mathcal{B}^{\text{ML}}_{\text{UL}} > 1$, implying that fit may be good enough to overcome Occam’s penalty in order to be significantly favored over unlensed model during microlensing searches.

Furthermore, upon studying the distribution of population parameters, we do not find any significant correlation between $\ln \mathcal{B}^{\text{ML}}_{\text{UL}}$ with either the inclination or the mass-ratios. However, we do see a slight anti-correlation of $\ln \mathcal{B}^{\text{ML}}_{\text{UL}}$ with the total binary mass, for instances where the microlens model is preferred over the unlensed model ($\ln \mathcal{B}^{\text{ML}}_{\text{UL}} > 0$). This is illustrated in Fig. 6.3, where we show $\ln \mathcal{B}^{\text{ML}}_{\text{UL}}$ against the binary mass for cases where $\ln \mathcal{B}^{\text{ML}}_{\text{UL}} > 0$. This suggests that, for a given eccentricity, the microlensing signatures are able to mimic modulations in eccentric WFs better with increasing duration of the signal. This further suggests that the two effects, eccentricity and microlensing, are

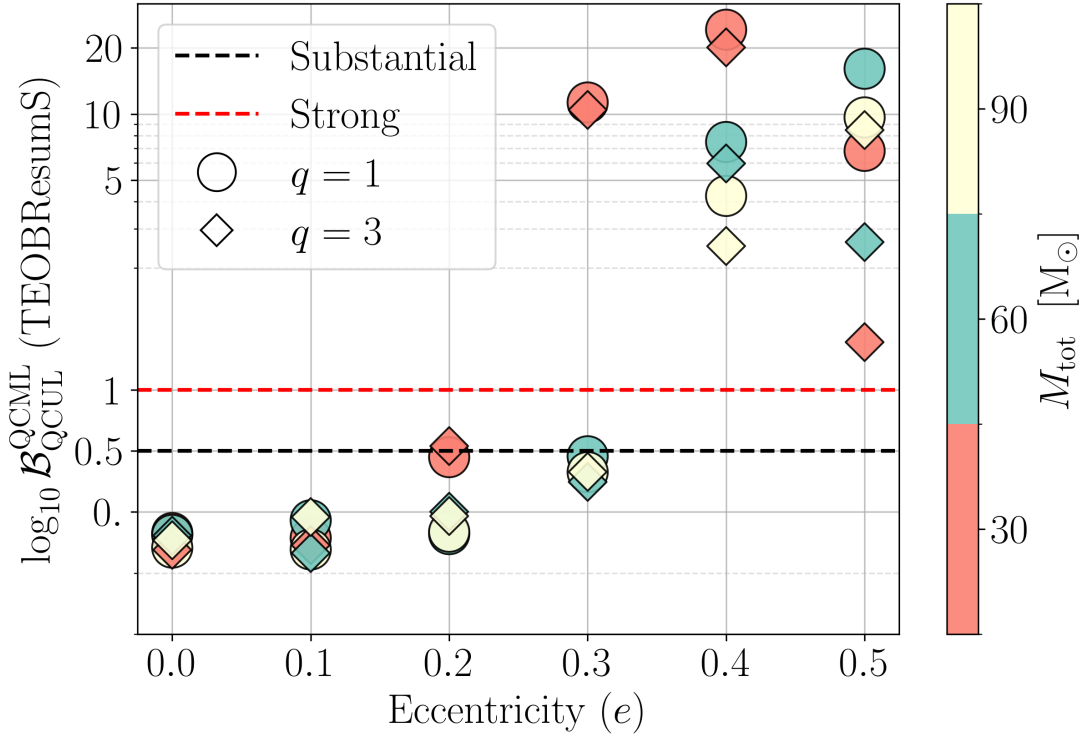


Figure 6.5: Same as Fig. 6.4, but utilizing the WF approximant TEOBResumS, where we keep eccentricity at zero in the recovery. This makes it an 11D model for a quasi-circular aligned-spin BBH system.

not orthogonal as they share some overlapping features.

6.2.3 Eccentric BBH Injection Study using TEOBResumS

Gravitational microlensing searches using Quasi-Circular WF models: IMRPhenomXPHM and TEOBResumS with zero eccentricity

We resort back to the nested sampling algorithm to estimate Bayes factors and parameters. Similar to the setup used in Sect. 6.2.2, we use TEOBResumS (Nagar et al. 2018, 2023) WF model for generating non-spinning eccentric BBH signals. Specifically, we select three distinct binary mass values $M_{\text{tot}} \in \{30, 60, 90\} M_{\odot}$, two mass ratio values $q \in \{1, 3\}$, and six values for eccentricity $e \in \{0, 0.1, 0.2, 0.3, 0.4, 0.5\}$, with zero eccentricity injections chosen for reference. Eccentricity is defined at a dimensionless frequency of ~ 0.003 at apastron, as in the previous section. Our choice of extrinsic parameters closely matches those of GW150914, except for the luminosity distance, which is adjusted to achieve an optimal network SNR of 30 when these eccentric signals are injected into the joint LIGO-

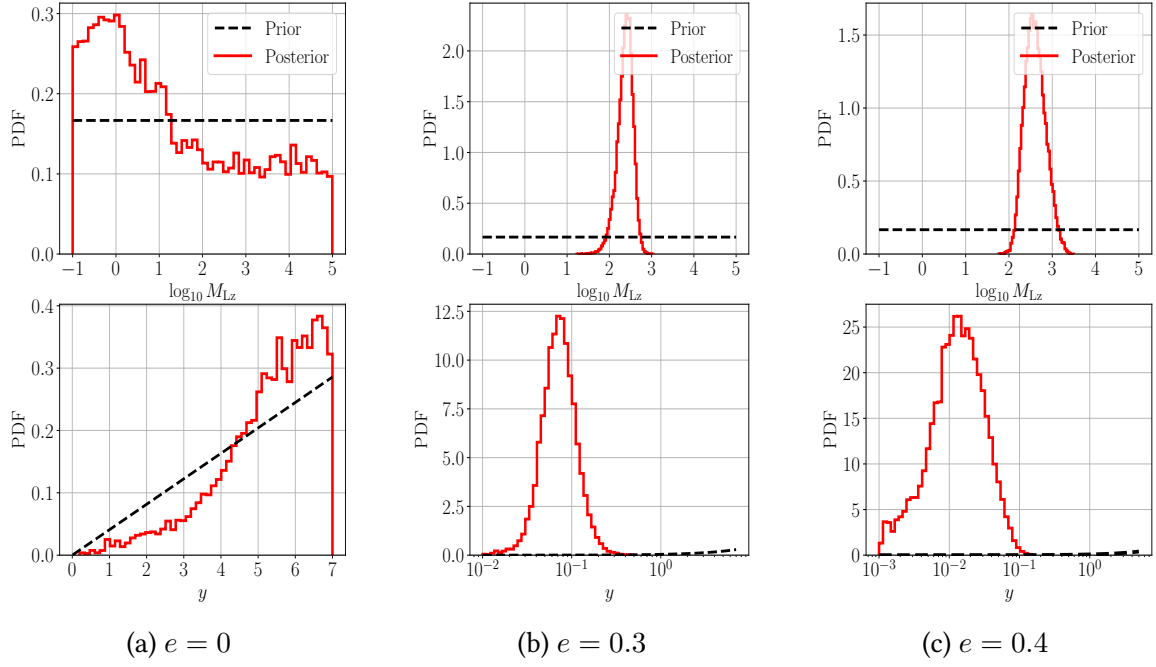


Figure 6.6: Recovered 1D marginalized posterior densities for the microlens parameters M_{Lz} and y for TEOBResumS injections corresponding to a non-spinning equal mass BBH of $30 M_{\odot}$ for (a) $e = 0$, (b) $e = 0.3$, and (c) $e = 0.4$.

Virgo network. This assumes the target O4 sensitivities as our model for the PSD. For the recovery process, motivated by real microlensing searches, we only employ quasi-circular (QC) WF models. We initially use IMRPhenomXPHM, a precessing model that uses all 15 parameters to model a typical QC BBH signal. The injected signals and the recovery analysis employ the same mode contents of $(l, |m|) = \{(2, 2), (2, 1), (3, 2), (3, 3), (4, 4)\}$, representing all available modes in IMRPhenomXPHM. However, to explicitly account for possible WF systematics between TEOBResumS and IMRPhenomXPHM, we later also analyze the bias in microlensing searches using the aligned-spin TEOBResumS WF model while keeping the eccentricity to zero. Moreover, we set the lower frequency limit for likelihood evaluation to $f_{\text{low}} = 20$ Hz for the $30 M_{\odot}$ binary mass case and 15 Hz for the other two heavier binary mass cases. This adjustment aims to increase the signal duration and generate more cycles, particularly for cases with higher eccentricity where signal duration decreases drastically.

We recover the signals using unlensed and microlensed hypotheses, \mathcal{H}_{UL} and \mathcal{H}_{ML} , and compare the two models using Bayes factor values. The results are plotted in Fig. 6.4, where we show $\log_{10} \mathcal{B}_{\text{QCUL}}^{\text{QCML}}$ against the injected eccentricity values, for different binary masses and mass-ratio considered. The circular markers represent the case where $q = 1$, while diamond-shaped markers depict $q = 3$ cases. The dashed black and red lines il-

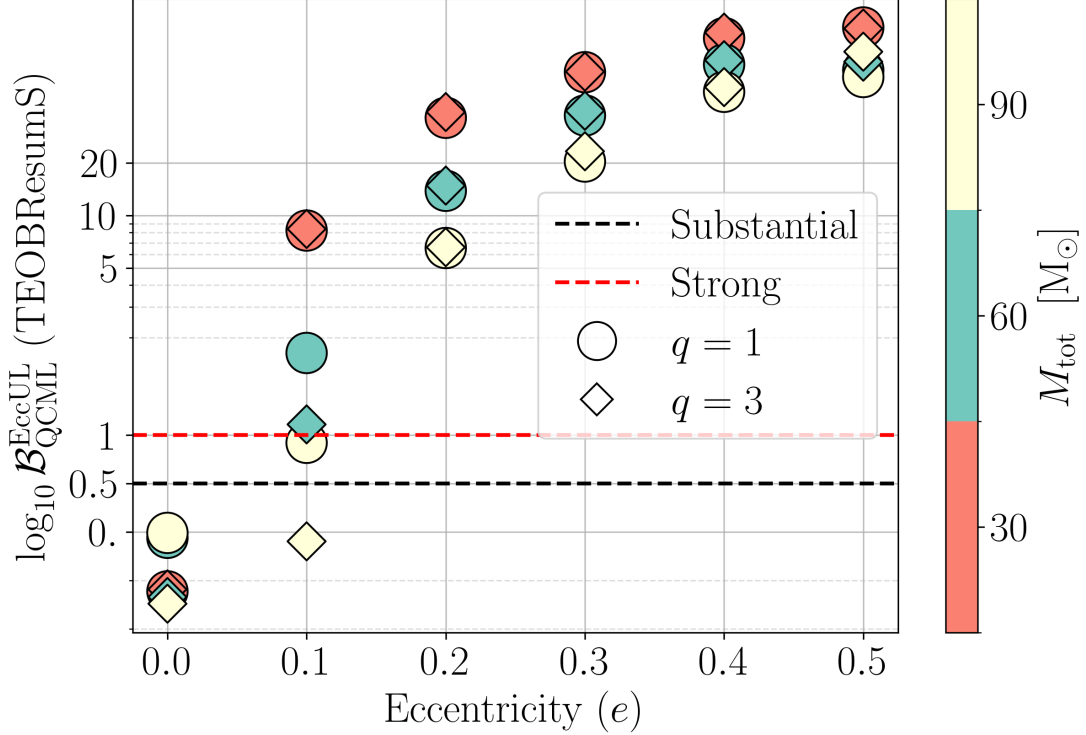


Figure 6.7: Breaking the degeneracy between eccentricity and microlensing and resolving bias in microlensing searches by incorporating eccentricity as a parameter in the recovery process using TEOBResumS WF model. The Bayes factor $\log_{10} \mathcal{B}_{\text{QCML}}^{\text{EccUL}}$ represents the evidence in favor of eccentricity vs. microlensing.

illustrate the threshold for substantial and strong evidence according to the Jefferey's scale (Deutsch 1999). It is evident from the plot that the evidence in favor of the microlens hypothesis over the unlens hypothesis increases almost monotonically as eccentricity increases while keeping other parameters fixed. For $M_{\text{tot}} = 30 M_{\odot}$ case, the evidence in favour of microlensing becomes strong from $e = 0.3$ onwards, while for the other two cases of binary masses (60 and 90), the evidence becomes strong from $e = 0.4$ onwards. Furthermore, for a given eccentricity, when $\log_{10} \mathcal{B}_{\text{QCML}}^{\text{EccUL}}$ is significant, it is always more for smaller mass binary relative to the heavier binaries. However, similar to our observation in sub-sections 6.2.1 and 6.2.2, we find that the effect of mass-ratio is non-linear and does not show any coherent trend. For high eccentricities (> 0.3) and low binary mass ($\lesssim 30 M_{\odot}$), we find that $\log_{10} \mathcal{B}_{\text{QCML}}^{\text{EccUL}}$ values can even exceed 5, which is huge. We also note a peculiar trend shown by the $30 M_{\odot}$ binary between eccentricity values of 0.2 and 0.4, which is the only case where we see the non-monotonic behavior of $\log_{10} \mathcal{B}_{\text{QCML}}^{\text{EccUL}}$ with eccentricity. We see a sudden spike of $\log_{10} \mathcal{B}_{\text{QCML}}^{\text{EccUL}}$ for $e = 0.3$, which is slightly more than the value at $e = 0.4$. We did various tests to confirm this peculiar behavior is indeed

a physical effect and not an artefact. We changed the prior ranges and their densities, but the observation was similar. We suspect this non-monotonic behavior of $\log_{10} \mathcal{B}_{\text{QCUL}}^{\text{QCML}}$ in a few cases, and the non-linearity of $\log_{10} \mathcal{B}_{\text{QCUL}}^{\text{QCML}}$ with the mass-ratios can be dependent in a non-linear fashion with the source considered. We leave further investigation to future studies.

In Fig. 6.6, we show the recoveries of the 1D marginalized posteriors for the microlens parameters for a few cases (solid red colored lines). Specifically, we consider the $\{M_{\text{tot}}, q\} = \{30, 1\}$ case for three eccentricity values $e \in \{0, 0.3, 0.4\}$. Similar to Fig. 6.1, we find no interesting signatures of microlensing for the non-eccentric case, which is expected. However, for the other two eccentric cases, we see the well-converged recoveries for M_{Lz} and y , strongly deviating from the prior density (dashed black colored lines). We also notice that in most cases studied in this subsection, the recoveries of y prefer a lower value as the eccentricity increases (compare, for example, recoveries of y in Figures 6.6b and 6.6c). We can see that the tail of PDF of (y) can go as low as 10^{-3} , which is orders of magnitude lower than the current lower limit used in the search for microlensing in the LIGO Scientific collaboration (Abbott, R. and others 2021; The LIGO Scientific Collaboration et al. 2023a).

In Fig. 6.5, we replicate the computations performed in Fig. 6.4, but this time by employing aligned-spin TEOBResumS WFs for the recovery, while keeping eccentricity zero. The parameter estimation runs using TEOBResumS follow a methodology similar to that described in O'Shea & Kumar (2023) but employ a different implementation provided by GWEAT². This analysis serves to confirm whether biases in microlensing searches, as depicted in Figure 6.5, result from WF systematics or are attributed to eccentricity. Our observations mostly align with those in Figure 6.5. We note that for the case with a binary total mass of $30 M_{\odot}$, the evidence in favor of microlensing becomes strong from $e = 0.3$ onwards. Conversely, for the other two cases with binary masses (60 and 90), the evidence becomes strong from $e = 0.4$ onwards. However, it's important to mention that the Bayes factor values differ between the two figures due to their different parameter spaces. While IMRPhenomXPHM is a precessing model, TEOBResumS is an aligned spin model. The trend remains consistent with the previous plot up to $e = 0.4$, where we observe a consistent increase in the preference for the microlensed hypothesis for any given mass and mass ratio. However, the sudden drop in $\log_{10} \mathcal{B}_{\text{QCUL}}^{\text{QCML}}$ for the case with $e = 0.5$ compared to $e = 0.4$ for most cases is not well understood, and further investigation is needed to determine the physical causes leading to such behavior.

²Gravitational Wave Eccentricity Analysis Tools, a Python package developed by the author of this thesis.

Breaking the degeneracy: Eccentric recoveries using TEOBResumS WF model

In the preceding sections, we illustrated how the presence of eccentricity in the data can bias microlensing searches. Now, we will demonstrate how to overcome these biases by performing eccentric recoveries. This involves incorporating the eccentricity parameter into the parameter estimation process as well, which is achieved by utilizing the TEOBResumS WF model as implemented in GWEAT.

In Fig. 6.7, we directly compare the eccentric and microlensed models by plotting the Bayes factor values $\log_{10} \mathcal{B}_{\text{QCML}}^{\text{EccUL}}$, representing the Bayes factor for the preference of the Eccentric unlensed hypothesis over the microlensing hypothesis. We observe that the degeneracy is effectively resolved when performing eccentric recoveries. Specifically, starting from $e = 0.1$, strong evidence in favor of eccentricity is evident in all cases except for the $M_{\text{tot}} = 90 M_{\odot}$ case, where it becomes strong from $e = 0.2$. From Figs. 6.4 and 6.5, we observe that biases in our microlensing searches emerge when eccentricity reaches $e = 0.3$ for the lowest mass and $e = 0.4$ for the two heavier masses. In these scenarios, $\log_{10} \mathcal{B}_{\text{QCML}}^{\text{EccUL}}$ consistently exceeds 10 for all cases with $e \geq 0.3$. Thus, we can confidently assert that employing an eccentricity analysis effectively eliminates the degeneracy, preventing erroneous claims of microlensing. However, future studies should conduct a more comprehensive analysis considering the effects of SNR and noise. It is also important to note that currently, no WF model incorporates both eccentricity and precession. Thus, future studies can investigate possible biases in microlensing searches when the true signal originates from a precessing eccentric BBH system. In such cases, the possibility for the preference of a model with precession and microlensing may improve over a model with only aligned spin and eccentricity.

6.3 Conclusion

In this chapter, we investigated how eccentricity can affect microlensing searches. Starting with the most reliable eccentric WFs from numerical relativity simulations, we showed in 6.2.1 how the eccentric signals can strongly favor the microlens hypothesis over the unlensed hypothesis. We later employed population-wide investigation and several injection studies in sections 6.2.2 and 6.2.3 using TEOBResumS WF model to have a more comprehensive understanding of the biases in microlensing searches. Lastly, we also showed how the biases can be resolved by breaking the degeneracy between eccentricity and microlensing by including eccentricity in the recovery process, where we employed the TEOBResumS WF model as implemented in GWEAT.

Based on our study, we arrive at the following conclusion:

1. Our study suggests that there is a significant degeneracy between eccentricity and microlensing, enough to falsely classify an event as a microlensed event if eccentricity is not accounted for. The Bayes factor $\log_{10} \mathcal{B}_{\text{UL}}^{\text{ML}}$ in favor of the microlensed hypothesis compared to the unlensed hypothesis can be high by several orders of magnitude. For example, $\log_{10} \mathcal{B}_{\text{UL}}^{\text{ML}}$ can even exceed a value of 5 for low mass binaries ($< 30 M_{\odot}$) at eccentricity of ~ 0.3 .
2. Both the FF and Bayesian analyses, encompassing parameter estimation and Bayesian model selection, show that the preference for microlensing recoveries over the unlensed recoveries intensifies as the strength of eccentric features increases in the data, which correlates with: (i) higher eccentricities, (ii) longer WFs, and (iii) high SNR values.
3. Population study shows that microlensing templates are almost always preferred over unlensed templates, especially for $e \gtrsim 0.2$.
4. Interestingly, the PDF of the recovered impact parameter y can even take values outside the current priors used in the microlensing searches, which is $y \in (0.1, 3)$. This prior is often employed because a low value $y < 0.1$ is improbable from a geometric point of view, while a large value $y > 3$ leads to very small microlensing effects. However, we noticed that when eccentricities are large enough, the tail of the PDF of y can have significant values in the range $y \in (0.001, 0.1)$. Meanwhile, when SNR values are high, the tail of the recovered densities can even go as high as $y \sim 7$.
5. Lastly, we demonstrated that the bias in the microlensing search due to the presence of eccentricity can be resolved by conducting an eccentricity analysis to confidently eliminate the degeneracy. This underscores the need for such analyses before making any claims of microlensing. We find that the Bayes factors in favour of eccentricity are significantly higher than those of microlensing for almost all the eccentricity values considered in our analyses. However, future studies should conduct a more comprehensive analysis by considering the effects of SNR and noise. Additionally, it is important to note that currently, there are no faithful WF model incorporating both eccentricity and precession. Thus, future studies can investigate possible biases in microlensing searches when the true signal originates from a precessing eccentric BBH system. In such cases, the possibility for the preference of a model with precession and microlensing may improve over a model with only aligned spin and eccentricity.

Our study strongly suggests that any event showing strong evidence of microlensing should also be analysed using an eccentric WF model in order to break the degeneracy. Since the effects due to a non-zero eccentricity will become important as we probe the early stages of a binary evolution or as the sensitivities of detectors increase, our study

CHAPTER 6. ECCENTRICITY VS MICROLENSING

holds great significance for future detectors such as 3G detectors like CE and ET or space-based detectors like DECIGO.

Chapter 7

Concluding Remarks and Future Directions

We live on an island surrounded by a sea of ignorance. As our island of knowledge grows, so does the shore of our ignorance.

John Archibald Wheeler

In this thesis, we investigated the impact of wave-optics effects (microlensing) in gravitational lensing (GL) of gravitational waves (GWs) originating from binary black hole mergers. We addressed several key questions, including: When do frequency-dependent modulations due to microlensing become noticeable? Which source parameters are susceptible to these modulations? How do microlenses behave when present within a strong lens? What impact do they have on the information extracted from GW signals? Can they introduce biases in other GW analyses, such as tests of general relativity (GR)? We also explored the prospects for detecting microlensing effects and examined the challenges associated with model comparison studies. Some of these questions were explored for the first time in the existing literature.

In the first couple of chapters, we laid out the foundation for the subsequent chapters by covering the basics of GL, including wave-optics effects, and GW data analysis relevant to our work. In the third chapter, we employed an isolated point-mass lens model of microlensing to study the impact of frequency-dependent modulations on the detection and parameter estimation of GWs, explore the feasibility of confidently detecting these lensing features, and investigate the population characteristics of such microlensed signals.

CHAPTER 7. CONCLUSION AND FUTURE DIRECTIONS

Chapter 4 extended our exploration to more realistic scenarios of microlensing where a microlens, or a population of stellar-mass microlenses, embedded within lensing galaxies can affect strongly lensed GWs. In Chapter 5, we delved into the critical implications of neglecting microlensing in GW data analysis, particularly in the context of its potential to bias tests of GR. Finally, Chapter 6 ventured into the intriguing possibility that other atypical physical effects, such as eccentric binaries, could introduce biases in microlensing searches. This chapter sheds light on the challenges associated with model comparison studies.

Our research has laid the groundwork for further analysis in several areas. In Chapter 3, we mainly focused on zero-noise non-spinning microlensed systems to study the biases in inferring BBH parameters. A logical extension would involve studying biases in the presence of Gaussian or real noise, or exploring biases for precessing microlensed signals. Moreover, while studying a population of microlensed signals and predicted regions in the lensing parameter space that are more likely to be detected as well as correctly identified as microlensed, one could incorporate the Occam's factor term using Fisher-Information matrix formalism, which we omitted for simplicity. Chapter 4 highlighted the need for more robust exploration of high macro-magnification cases, particularly due to the observed potential for high mismatch values exceeding 5%. There's also room for refinement and increased efficiency in the methodology for computing amplification factors, especially for saddle-point images. This extends to exploring more efficient methods for computing amplification factors for both minima and saddle-point images. Additionally, a more statistical and robust examination of the effect of microlensing on strong lensing searches is recommended, as discussed in Chapter 5. This would provide a more accurate assessment of the implications. In the context of Chapter 5, there are opportunities to study deviations in general relativity due to microlensing effects, accounting for Gaussian or real noise. Furthermore, exploring the possibilities of non-GR effects affecting microlensing and assessing their likelihood, considering the high accuracy of GR tests, is a valuable avenue for further research. In alignment with Chapter 6, researchers may consider investigating how other unconventional physical effects, such as those originating from overlapping signals, waveform systematics (e.g., due to lack of faithful precessing eccentric waveforms), and precession, could potentially introduce biases in microlensing searches. Furthermore, the role of noise systematics, especially the non-Gaussianity present in real noise, should be further explored in the context of microlensing searches.

Traditionally, microlensing searches have predominantly relied on isolated point mass lens models, primarily because analytical solutions are available for simple lens systems. However, our work emphasizes the need for developing waveform models that can accommodate more realistic scenarios where microlenses are embedded within a macrolens. This presents a challenging problem, as the typical generation time for ampli-

fication factors in such scenarios is $\mathcal{O}(10\text{ s})$, whereas for practical parameter estimation or evidence computation, an evaluation time of $\mathcal{O}(10^{-3}\text{ s})$ is usually needed to complete the analysis within the reasonable time frame, such as a single day.

In conclusion, this thesis establishes the importance of microlensing in GW data analysis and keeps it alongside other astrophysical viable atypical physical effects, such as eccentricity and precession. Our research has revealed that neglecting microlensing can introduce significant biases in parameter inferences, potentially undermine fundamental tests such as those assessing the validity of general relativity. As we move forward, it is imperative to develop advanced waveform models capable of handling realistic microlensing scenarios, a challenge that holds the key to a better understanding of the nature of dark matter and, hence, the universe. By addressing these challenges, we can advance our understanding of the cosmos and refine the precision of GW astronomy.

References

- Aasi, J., et al. 2015, *Class. Quant. Grav.*, 32, 074001, doi: [10.1088/0264-9381/32/7/074001](https://doi.org/10.1088/0264-9381/32/7/074001)
- Abbott, B., Abbott, R., Abbott, T., et al. 2019a, *Phys. Rev. D*, 100, 104036, doi: [10.1103/PhysRevD.100.104036](https://doi.org/10.1103/PhysRevD.100.104036)
- Abbott, B. P., Abbott, R., Abbott, T., et al. 2016, *Phys. Rev. D*, 93, 112004, doi: [10.1103/PhysRevD.93.112004](https://doi.org/10.1103/PhysRevD.93.112004)
- Abbott, B. P., et al. 2017a, *Astrophys. J. Lett.*, 848, L13, doi: [10.3847/2041-8213/aa920c](https://doi.org/10.3847/2041-8213/aa920c)
- Abbott, B. P., Abbott, R., Abbott, T., et al. 2017b, *Phys. Rev. Lett.*, 118, 221101, doi: [10.1103/PhysRevLett.118.221101](https://doi.org/10.1103/PhysRevLett.118.221101)
- Abbott, B. P., et al. 2018, *Living Rev. Rel.*, 21, 3, doi: [10.1007/s41114-020-00026-9](https://doi.org/10.1007/s41114-020-00026-9)
- Abbott, B. P., Abbott, R., Abbott, T., et al. 2019b, *Phys. Rev. X*, 9, 031040, doi: [10.1103/PhysRevX.9.031040](https://doi.org/10.1103/PhysRevX.9.031040)
- Abbott, B. P., et al. 2019c, *Phys. Rev. Lett.*, 123, 011102, doi: [10.1103/PhysRevLett.123.011102](https://doi.org/10.1103/PhysRevLett.123.011102)
- Abbott, B. P., Abbott, R., Abbott, T. D., et al. 2019d, *Astrophys. J.*, 883, 149, doi: [10.3847/1538-4357/ab3c2d](https://doi.org/10.3847/1538-4357/ab3c2d)
- Abbott, R., Abbott, T., Acernese, F., et al. 2023, *Phys. Rev. X*, 13, 041039, doi: [10.1103/PhysRevX.13.041039](https://doi.org/10.1103/PhysRevX.13.041039)
- Abbott, R., Abbott, T., et al. 2021a, *Phys. Rev. X*, 11, 021053, doi: [10.1103/PhysRevX.11.021053](https://doi.org/10.1103/PhysRevX.11.021053)
- Abbott, R., et al. 2021b. <https://arxiv.org/abs/2112.06861>

REFERENCES

- Abbott, R., Abbott, T., Abraham, S., et al. 2021c, *Astrophys. J. Lett.*, 913, L7, doi: [10.3847/2041-8213/abe949](https://doi.org/10.3847/2041-8213/abe949)
- Abbott, R., et al. 2021d, *Phys. Rev. D*, 103, 122002, doi: [10.1103/PhysRevD.103.122002](https://doi.org/10.1103/PhysRevD.103.122002)
- Abbott, B. P. and others. 2016, *Phys. Rev. Lett.*, 116, 221101, doi: [10.1103/PhysRevLett.116.221101](https://doi.org/10.1103/PhysRevLett.116.221101)
- Abbott, R. and others. 2021, *Astrophys. J.*, 923, 14, doi: [10.3847/1538-4357/ac23db](https://doi.org/10.3847/1538-4357/ac23db)
- Acernese, F., et al. 2015, *Class. Quant. Grav.*, 32, 024001, doi: [10.1088/0264-9381/32/2/024001](https://doi.org/10.1088/0264-9381/32/2/024001)
- Agathos, M., Del Pozzo, W., Li, T. G., et al. 2014, *Physical Review D*, 89, 082001
- Ajith, P., Fotopoulos, N., Privitera, S., Neunzert, A., & Weinstein, A. J. 2014, *Phys. Rev. D*, 89, 084041, doi: [10.1103/PhysRevD.89.084041](https://doi.org/10.1103/PhysRevD.89.084041)
- Ajith, P., et al. 2008, *Phys. Rev. D*, 77, 104017, doi: [10.1103/PhysRevD.77.104017](https://doi.org/10.1103/PhysRevD.77.104017)
- Ajith, P., Hannam, M., Husa, S., et al. 2011, *Phys. Rev. Lett.*, 106, 241101, doi: [10.1103/PhysRevLett.106.241101](https://doi.org/10.1103/PhysRevLett.106.241101)
- Alejandro, B., et al. 2016, PhenomPv2 -- technical notes for the LAL implementation. <https://dcc.ligo.org/LIGO-T1500602/public>
- Allen, B., Anderson, W. G., Brady, P. R., Brown, D. A., & Creighton, J. D. E. 2012, *Phys. Rev. D*, 85, 122006, doi: [10.1103/PhysRevD.85.122006](https://doi.org/10.1103/PhysRevD.85.122006)
- Antonelli, A., Burke, O., & Gair, J. R. 2021, *Mon. Not. Roy. Astron. Soc.*, 507, 5069, doi: [10.1093/mnras/stab2358](https://doi.org/10.1093/mnras/stab2358)
- Antonini, F., Murray, N., & Mikkola, S. 2014, *The Astrophysical Journal*, 781, 45
- Arun, K., Iyer, B. R., Qusailah, M., & Sathyaprakash, B. S. 2006a, *Phys. Rev. D*, 74, 024006, doi: [10.1103/PhysRevD.74.024006](https://doi.org/10.1103/PhysRevD.74.024006)
- Arun, K., Iyer, B. R., Sathyaprakash, B. S., & Sundararajan, P. A. 2005, *Physical Review D*, 71, 084008
- Arun, K. G., Iyer, B. R., Qusailah, M. S. S., & Sathyaprakash, B. S. 2006b, *Class. Quant. Grav.*, 23, L37, doi: [10.1088/0264-9381/23/9/L01](https://doi.org/10.1088/0264-9381/23/9/L01)
- Ashton, G., Romero-Shaw, I., Talbot, C., Hoy, C., & Galaudage, S. 2020, *Bilby Pipe: 1.0*.

REFERENCES

- Ashton, G., et al. 2019, *Astrophys. J. Suppl.*, 241, 27, doi: [10.3847/1538-4365/ab06fc](https://doi.org/10.3847/1538-4365/ab06fc)
- Asmodelle, E. 2017, Bachelor thesis, Central Lancashire U. <https://arxiv.org/abs/1705.04397>
- Baraldo, C., Hosoya, A., & Nakamura, T. T. 1999, *Phys. Rev. D*, 59, 083001, doi: [10.1103/PhysRevD.59.083001](https://doi.org/10.1103/PhysRevD.59.083001)
- Barausse, E., et al. 2020, *Gen. Rel. Grav.*, 52, 81, doi: [10.1007/s10714-020-02691-1](https://doi.org/10.1007/s10714-020-02691-1)
- Basak, S., Ganguly, A., Haris, K., et al. 2022, *Astrophys. J.*, 926, L28, doi: [10.3847/2041-8213/ac4dfa](https://doi.org/10.3847/2041-8213/ac4dfa)
- Bernardeau, F. 1999. <https://arxiv.org/abs/astro-ph/9901117>
- Berti, E., Cardoso, V., & Will, C. M. 2006, *Phys. Rev. D*, 73, 064030, doi: [10.1103/PhysRevD.73.064030](https://doi.org/10.1103/PhysRevD.73.064030)
- Bhat, S. A., Saini, P., Favata, M., & Arun, K. G. 2023, *Phys. Rev. D*, 107, 024009, doi: [10.1103/PhysRevD.107.024009](https://doi.org/10.1103/PhysRevD.107.024009)
- Bird, S., Cholis, I., Muñoz, J. B., et al. 2016, *Phys. Rev. Lett.*, 116, 201301, doi: [10.1103/PhysRevLett.116.201301](https://doi.org/10.1103/PhysRevLett.116.201301)
- Blanchet, L. 2006, *Living Rev. Rel.*, 9, 4
- Bondarescu, R., Ubach, H., Bulashenko, O., & Lundgren, A. P. 2023, *Phys. Rev. D*, 108, 084033, doi: [10.1103/PhysRevD.108.084033](https://doi.org/10.1103/PhysRevD.108.084033)
- Borhanian, S. 2021, *Class. Quant. Grav.*, 38, 175014, doi: [10.1088/1361-6382/ac1618](https://doi.org/10.1088/1361-6382/ac1618)
- Boyle, M., et al. 2019, *Class. Quant. Grav.*, 36, 195006, doi: [10.1088/1361-6382/ab34e2](https://doi.org/10.1088/1361-6382/ab34e2)
- Broadhurst, T., Diego, J. M., & Smoot, G. 2018. <https://arxiv.org/abs/1802.05273>
- Broadhurst, T., Diego, J. M., & Smoot, G. F. 2019. <https://arxiv.org/abs/1901.03190>
- Broadhurst, T., Diego, J. M., & Smoot, G. F. 2020, arXiv e-prints, arXiv:2006.13219. <https://arxiv.org/abs/2006.13219>
- Broadhurst, Tom, Diego, Jose M, & Smoot, George F. 2020. <https://arxiv.org/abs/2002.08821>

REFERENCES

- Bulashenko, O., & Ubach, H. 2022, JCAP, 07, 022, doi: [10.1088/1475-7516/2022/07/022](https://doi.org/10.1088/1475-7516/2022/07/022)
- Canton, T. D., & Harry, I. W. 2017, arXiv preprint arXiv:1705.01845
- Cao, Z., Li, L.-F., & Wang, Y. 2014, Phys. Rev. D, 90, 062003, doi: [10.1103/PhysRevD.90.062003](https://doi.org/10.1103/PhysRevD.90.062003)
- Çalışkan, M., Anil Kumar, N., Ji, L., et al. 2023a, Phys. Rev. D, 108, 123543, doi: [10.1103/PhysRevD.108.123543](https://doi.org/10.1103/PhysRevD.108.123543)
- Çalışkan, M., Ezquiaga, J. M., Hannuksela, O. A., & Holz, D. E. 2023b, Phys. Rev. D, 107, 063023, doi: [10.1103/PhysRevD.107.063023](https://doi.org/10.1103/PhysRevD.107.063023)
- Çalışkan, M., Ji, L., Cotesta, R., et al. 2023c, Phys. Rev. D, 107, 043029, doi: [10.1103/PhysRevD.107.043029](https://doi.org/10.1103/PhysRevD.107.043029)
- Chabrier, G. 2003, Publ. Astron. Soc. Pac., 115, 763, doi: [10.1086/376392](https://doi.org/10.1086/376392)
- Cholis, I., Kovetz, E. D., Ali-Haïmoud, Y., et al. 2016, Phys. Rev. D, 94, 084013, doi: [10.1103/PhysRevD.94.084013](https://doi.org/10.1103/PhysRevD.94.084013)
- Christensen, N., & Meyer, R. 2022, Rev. Mod. Phys., 94, 025001, doi: [10.1103/RevModPhys.94.025001](https://doi.org/10.1103/RevModPhys.94.025001)
- Christian, P., Vitale, S., & Loeb, A. 2018, Phys. Rev. D, 98, 103022, doi: [10.1103/PhysRevD.98.103022](https://doi.org/10.1103/PhysRevD.98.103022)
- Chung, A. K.-W., & Li, T. G. F. 2021, Phys. Rev. D, 104, 124060, doi: [10.1103/PhysRevD.104.124060](https://doi.org/10.1103/PhysRevD.104.124060)
- Collett, T. E., & Bacon, D. 2017, Phys. Rev. Lett., 118, 091101, doi: [10.1103/PhysRevLett.118.091101](https://doi.org/10.1103/PhysRevLett.118.091101)
- Cornish, N., Sampson, L., Yunes, N., & Pretorius, F. 2011, Phys. Rev. D, 84, 062003, doi: [10.1103/PhysRevD.84.062003](https://doi.org/10.1103/PhysRevD.84.062003)
- Creighton, J. D. E., & Anderson, W. G. 2011, Gravitational-wave physics and astronomy: An introduction to theory, experiment and data analysis
- Cremonese, P., Ezquiaga, J. M., & Salzano, V. 2021, Phys. Rev. D, 104, 023503, doi: [10.1103/PhysRevD.104.023503](https://doi.org/10.1103/PhysRevD.104.023503)
- Cremonese, P., Mota, D. F., & Salzano, V. 2023, Annalen Phys., 535, 2300040, doi: [10.1002/andp.202300040](https://doi.org/10.1002/andp.202300040)

REFERENCES

- Cutler, C., & Flanagan, E. E. 1994, Physical Review D, 49, 2658
- Dai, L., & Venumadhav, T. 2017. <https://arxiv.org/abs/1702.04724>
- Dai, L., Zackay, B., Venumadhav, T., Roulet, J., & Zaldarriaga, M. 2020. <https://arxiv.org/abs/2007.12709>
- Dalang, C., Cusin, G., & Lagos, M. 2022, Phys. Rev. D, 105, 024005, doi: [10.1103/PhysRevD.105.024005](https://doi.org/10.1103/PhysRevD.105.024005)
- Deguchi, S., & Watson, W. D. 1986, ApJ, 307, 30, doi: [10.1086/164389](https://doi.org/10.1086/164389)
- Deutsch, D. 1999, Proc. Roy. Soc. Lond. A, 455, 3129, doi: [10.1098/rspa.1999.0443](https://doi.org/10.1098/rspa.1999.0443)
- Diego, J. M. 2019, Astron. Astrophys., 625, A84, doi: [10.1051/0004-6361/201833670](https://doi.org/10.1051/0004-6361/201833670)
- Diego, J. M., Broadhurst, T., & Smoot, G. 2021, Phys. Rev. D, 104, 103529, doi: [10.1103/PhysRevD.104.103529](https://doi.org/10.1103/PhysRevD.104.103529)
- Diego, J. M., Hannuksela, O. A., Kelly, P. L., et al. 2019, Astron. Astrophys., 627, A130, doi: [10.1051/0004-6361/201935490](https://doi.org/10.1051/0004-6361/201935490)
- Diego, J. M., et al. 2018, Astrophys. J., 857, 25, doi: [10.3847/1538-4357/aab617](https://doi.org/10.3847/1538-4357/aab617)
- Diego, Jose M. 2020, Phys. Rev. D, 101, 123512, doi: [10.1103/PhysRevD.101.123512](https://doi.org/10.1103/PhysRevD.101.123512)
- Droz, S. 1999, Phys. Rev. D, 59, 064030, doi: [10.1103/PhysRevD.59.064030](https://doi.org/10.1103/PhysRevD.59.064030)
- Duez, M. D., & Zlochower, Y. 2019, Rept. Prog. Phys., 82, 016902, doi: [10.1088/1361-6633/aadb16](https://doi.org/10.1088/1361-6633/aadb16)
- Einstein, A. 1916, Annalen Phys., 49, 769, doi: [10.1002/andp.19163540702](https://doi.org/10.1002/andp.19163540702)
- Einstein, Albert. 1936, Science, 84, 506, doi: [10.1126/science.84.2188.506](https://doi.org/10.1126/science.84.2188.506)
- Eldridge, J. J., Stanway, E. R., Xiao, L., et al. 2017, Publ. Astron. Soc. Austral., 34, e058, doi: [10.1017/pasa.2017.51](https://doi.org/10.1017/pasa.2017.51)
- Evans, M., et al. 2021. <https://arxiv.org/abs/2109.09882>
- Ezquiaga, J. M., Holz, D. E., Hu, W., Lagos, M., & Wald, R. M. 2021, Phys. Rev. D, 103, 064047, doi: [10.1103/PhysRevD.103.064047](https://doi.org/10.1103/PhysRevD.103.064047)
- Ezquiaga, J. M., Hu, W., Lagos, M., Lin, M.-X., & Xu, F. 2022, JCAP, 08, 016, doi: [10.1088/1475-7516/2022/08/016](https://doi.org/10.1088/1475-7516/2022/08/016)

REFERENCES

- Fairhurst, S., Green, R., Hoy, C., Hannam, M., & Muir, A. 2020, Phys. Rev. D, 102, 024055, doi: [10.1103/PhysRevD.102.024055](https://doi.org/10.1103/PhysRevD.102.024055)
- Fan, X.-L., Liao, K., Biesiada, M., Piorkowska-Kurpas, A., & Zhu, Z.-H. 2017, Phys. Rev. Lett., 118, 091102, doi: [10.1103/PhysRevLett.118.091102](https://doi.org/10.1103/PhysRevLett.118.091102)
- Finke, A., Foffa, S., Iacovelli, F., Maggiore, M., & Mancarella, M. 2021, Phys. Rev. D, 104, 084057, doi: [10.1103/PhysRevD.104.084057](https://doi.org/10.1103/PhysRevD.104.084057)
- Finn, L. S. 1992, Phys. Rev. D, 46, 5236, doi: [10.1103/PhysRevD.46.5236](https://doi.org/10.1103/PhysRevD.46.5236)
- Fishbach, M., Holz, D. E., & Farr, W. M. 2018, Astrophys. J. Lett., 863, L41, doi: [10.3847/2041-8213/aad800](https://doi.org/10.3847/2041-8213/aad800)
- Foxley-Marrable, M., Collett, T. E., Vernardos, G., Goldstein, D. A., & Bacon, D. 2018, Mon. Not. Roy. Astron. Soc., 478, 5081, doi: [10.1093/mnras/sty1346](https://doi.org/10.1093/mnras/sty1346)
- García-Quirós, C., Colleoni, M., Husa, S., et al. 2020, Phys. Rev. D, 102, 064002, doi: [10.1103/PhysRevD.102.064002](https://doi.org/10.1103/PhysRevD.102.064002)
- Gerosa, D., Mould, M., Gangardt, D., et al. 2021, Physical Review D, 103, 064067
- Ghosh, A., et al. 2016, Phys. Rev. D, 94, 021101, doi: [10.1103/PhysRevD.94.021101](https://doi.org/10.1103/PhysRevD.94.021101)
- Ghosh, A., Johnson-Mcdaniel, N. K., Ghosh, A., et al. 2018, Class. Quant. Grav., 35, 014002, doi: [10.1088/1361-6382/aa972e](https://doi.org/10.1088/1361-6382/aa972e)
- Goodman, J. W. 2005, Introduction to Fourier optics (Roberts and Company Publishers)
- Goyal, S., Haris, K., Mehta, A. K., & Ajith, P. 2021, Phys. Rev. D, 103, 024038, doi: [10.1103/PhysRevD.103.024038](https://doi.org/10.1103/PhysRevD.103.024038)
- Goyal, S., Vijaykumar, A., Ezquiaga, J. M., & Zumalacarregui, M. 2023, Phys. Rev. D, 108, 024052, doi: [10.1103/PhysRevD.108.024052](https://doi.org/10.1103/PhysRevD.108.024052)
- Hanna, C., Megevand, M., Ochsner, E., & Palenzuela, C. 2009, Class. Quant. Grav., 26, 015009, doi: [10.1088/0264-9381/26/1/015009](https://doi.org/10.1088/0264-9381/26/1/015009)
- Hannam, M., Schmidt, P., Bohé, A., et al. 2014, Phys. Rev. Lett., 113, 151101, doi: [10.1103/PhysRevLett.113.151101](https://doi.org/10.1103/PhysRevLett.113.151101)
- Hannuksela, O. A., Collett, T. E., Çalışkan, M., & Li, T. G. F. 2020, Mon. Not. Roy. Astron. Soc., 498, 3395, doi: [10.1093/mnras/staa2577](https://doi.org/10.1093/mnras/staa2577)
- Hannuksela, O. A., Haris, K., Ng, K. K. Y., et al. 2019, Astrophys. J. Lett., 874, L2, doi: [10.3847/2041-8213/ab0c0f](https://doi.org/10.3847/2041-8213/ab0c0f)

REFERENCES

- Haris, K., Mehta, A. K., Kumar, S., Venumadhav, T., & Ajith, P. 2018. <https://arxiv.org/abs/1807.07062>
- Healy, J., & Lousto, C. O. 2017, Phys. Rev. D, 95, 024037, doi: [10.1103/PhysRevD.95.024037](https://doi.org/10.1103/PhysRevD.95.024037)
- Hofmann, F., Barausse, E., & Rezzolla, L. 2016, Astrophys. J. Lett., 825, L19, doi: [10.3847/2041-8205/825/2/L19](https://doi.org/10.3847/2041-8205/825/2/L19)
- Hossenfelder, S. 2006, Phys. Lett. B, 636, 119, doi: [10.1016/j.physletb.2006.03.038](https://doi.org/10.1016/j.physletb.2006.03.038)
- Hoy, C., & Raymond, V. 2021, SoftwareX, 15, 100765, doi: [10.1016/j.softx.2021.100765](https://doi.org/10.1016/j.softx.2021.100765)
- Hu, Q., & Veitch, J. 2023, Astrophys. J., 945, 103, doi: [10.3847/1538-4357/acbc18](https://doi.org/10.3847/1538-4357/acbc18)
- Hughes, S. A., & Menou, K. 2005, The Astrophysical Journal, 623, 689
- Hulse, R. A., & Taylor, J. H. 1975, Astrophys. J. Lett., 195, L51, doi: [10.1086/181708](https://doi.org/10.1086/181708)
- Husa, S. 2009, Gen. Rel. Grav., 41, 1667, doi: [10.1007/s10714-009-0762-5](https://doi.org/10.1007/s10714-009-0762-5)
- Husa, S., Khan, S., Hannam, M., et al. 2016, Phys. Rev. D, 93, 044006, doi: [10.1103/PhysRevD.93.044006](https://doi.org/10.1103/PhysRevD.93.044006)
- Iacovelli, F., Finke, A., Foffa, S., Maggiore, M., & Mancarella, M. 2022, in 56th Rencontres de Moriond on Gravitation. <https://arxiv.org/abs/2203.09237>
- Isoyama, S., Sturani, R., & Nakano, H. 2020, doi: [10.1007/978-981-15-4702-7_31-1](https://doi.org/10.1007/978-981-15-4702-7_31-1)
- Jana, S., Kapadia, S. J., Venumadhav, T., & Ajith, P. 2023, Phys. Rev. Lett., 130, 261401, doi: [10.1103/PhysRevLett.130.261401](https://doi.org/10.1103/PhysRevLett.130.261401)
- Janquart, J., et al. 2023, Mon. Not. Roy. Astron. Soc., 526, 3832, doi: [10.1093/mnras/stad2909](https://doi.org/10.1093/mnras/stad2909)
- Janquart, Justin and Seo, Eungwang and Hannuksela, Otto A. and Li, Tjonnie G. F. and Broeck, Chris Van Den. 2021, Astrophys. J. Lett., 923, L1, doi: [10.3847/2041-8213/ac3bcf](https://doi.org/10.3847/2041-8213/ac3bcf)
- Jiménez-Forteza, X., Keitel, D., Husa, S., et al. 2017, Phys. Rev. D, 95, 064024, doi: [10.1103/PhysRevD.95.064024](https://doi.org/10.1103/PhysRevD.95.064024)
- Johnson-McDaniel, N. K., Ghosh, A., Ghonge, S., et al. 2022, Phys. Rev. D, 105, 044020, doi: [10.1103/PhysRevD.105.044020](https://doi.org/10.1103/PhysRevD.105.044020)

REFERENCES

- Johnson-McDaniel, N. K., et al. 2016, Determining the final spin of a binary black hole system including in-plane spins: Method and checks of accuracy. https://dcc.ligo.org/public/0126/T1600168/006/Final_mass_and_spin_public.pdf
- Jung, S., & Shin, C. S. 2019, Phys. Rev. Lett., 122, 041103, doi: [10.1103/PhysRevLett.122.041103](https://doi.org/10.1103/PhysRevLett.122.041103)
- Kass, R. E., & Raftery, A. E. 1995, J. Am. Statist. Assoc., 90, 773, doi: [10.1080/01621459.1995.10476572](https://doi.org/10.1080/01621459.1995.10476572)
- Kawamura, S., et al. 2008, J. Phys. Conf. Ser., 122, 012006, doi: [10.1088/1742-6596/122/1/012006](https://doi.org/10.1088/1742-6596/122/1/012006)
- Kawamura, Seiji, et al. 2021, PTEP, 2021, 05A105, doi: [10.1093/ptep/ptab019](https://doi.org/10.1093/ptep/ptab019)
- Keskin, S. 2006, Journal of Applied Science Research, 2, 296
- Khan, S., Chatziioannou, K., Hannam, M., & Ohme, F. 2019, Phys. Rev. D, 100, 024059, doi: [10.1103/PhysRevD.100.024059](https://doi.org/10.1103/PhysRevD.100.024059)
- Khan, S., Husa, S., Hannam, M., et al. 2016, Phys. Rev. D, 93, 044007, doi: [10.1103/PhysRevD.93.044007](https://doi.org/10.1103/PhysRevD.93.044007)
- Kim, K., & Liu, A. 2023. <https://arxiv.org/abs/2301.07253>
- Lai, K.-H., Hannuksela, O. A., Herrera-Martín, A., et al. 2018, Phys. Rev. D, 98, 083005, doi: [10.1103/PhysRevD.98.083005](https://doi.org/10.1103/PhysRevD.98.083005)
- Lawrence, J. K. 1971, Nuovo Cimento B Serie, 6B, 225, doi: [10.1007/BF02735388](https://doi.org/10.1007/BF02735388)
- Leung, C., Jow, D., Saha, P., et al. 2023. <https://arxiv.org/abs/2304.01202>
- Li, S.-S., Mao, S., Zhao, Y., & Lu, Y. 2018, Mon. Not. Roy. Astron. Soc., 476, 2220, doi: [10.1093/mnras/sty411](https://doi.org/10.1093/mnras/sty411)
- Li, T. G. F., Del Pozzo, W., Vitale, S., et al. 2012, Phys. Rev. D, 85, 082003, doi: [10.1103/PhysRevD.85.082003](https://doi.org/10.1103/PhysRevD.85.082003)
- Liao, K., Fan, X.-L., Ding, X.-H., Biesiada, M., & Zhu, Z.-H. 2017, Nature Commun., 8, 1148, doi: [10.1038/s41467-017-01152-9](https://doi.org/10.1038/s41467-017-01152-9)
- Lin, J. 1991, IEEE Trans. Info. Theor., 37, 145, doi: [10.1109/18.61115](https://doi.org/10.1109/18.61115)
- Liu, A., Wong, I. C. F., Leong, S. H. W., et al. 2023, Mon. Not. Roy. Astron. Soc., 525, 4149, doi: [10.1093/mnras/stad1302](https://doi.org/10.1093/mnras/stad1302)

REFERENCES

- Liu, X., Magana Hernandez, I., & Creighton, J. 2021, *Astrophys. J.*, 908, 97, doi: [10.3847/1538-4357/abd7eb](https://doi.org/10.3847/1538-4357/abd7eb)
- London, L., Khan, S., Fauchon-Jones, E., et al. 2018, *Phys. Rev. Lett.*, 120, 161102, doi: [10.1103/PhysRevLett.120.161102](https://doi.org/10.1103/PhysRevLett.120.161102)
- Luo, J., et al. 2016, *Class. Quant. Grav.*, 33, 035010, doi: [10.1088/0264-9381/33/3/035010](https://doi.org/10.1088/0264-9381/33/3/035010)
- Madau, P. 1997, *AIP Conf. Proc.*, 393, 481, doi: [10.1063/1.52821](https://doi.org/10.1063/1.52821)
- Magaña Hernandez, I. 2022. <https://arxiv.org/abs/2211.01272>
- Maggiore, M., et al. 2020, *JCAP*, 03, 050, doi: [10.1088/1475-7516/2020/03/050](https://doi.org/10.1088/1475-7516/2020/03/050)
- Mapelli, M. 2021, *Formation Channels of Single and Binary Stellar-Mass Black Holes*, doi: [10.1007/978-981-15-4702-7_16-1](https://doi.org/10.1007/978-981-15-4702-7_16-1)
- Margutti, R., & Chornock, R. 2021, *Ann. Rev. Astron. Astrophys.*, 59, 155, doi: [10.1146/annurev-astro-112420-030742](https://doi.org/10.1146/annurev-astro-112420-030742)
- Maschberger, T. 2013, *Mon. Not. Roy. Astron. Soc.*, 429, 1725, doi: [10.1093/mnras/sts479](https://doi.org/10.1093/mnras/sts479)
- Meena, A. K. 2023. <https://arxiv.org/abs/2305.02880>
- Meena, A. K., & Bagla, J. S. 2020, *Mon. Not. Roy. Astron. Soc.*, 492, 1127, doi: [10.1093/mnras/stz3509](https://doi.org/10.1093/mnras/stz3509)
- Meena, A. K., Mishra, A., More, A., Bose, S., & Bagla, J. S. 2022, *Mon. Not. Roy. Astron. Soc.*, 517, 872, doi: [10.1093/mnras/stac2721](https://doi.org/10.1093/mnras/stac2721)
- Meidam, J., et al. 2018, *Phys. Rev. D*, 97, 044033, doi: [10.1103/PhysRevD.97.044033](https://doi.org/10.1103/PhysRevD.97.044033)
- Mendes, M., & Pala, A. 2003, *Pakistan Journal of Information and Technology*, 2, 135
- Mishra, A., Krishnendu, N. V., & Ganguly, A. 2023a. <https://arxiv.org/abs/2311.08446>
- Mishra, A., Meena, A. K., More, A., & Bose, S. 2023b, doi: [10.1093/mnras/stae836](https://doi.org/10.1093/mnras/stae836)
- Mishra, A., Meena, A. K., More, A., Bose, S., & Bagla, J. S. 2021, *Mon. Not. Roy. Astron. Soc.*, 508, 4869, doi: [10.1093/mnras/stab2875](https://doi.org/10.1093/mnras/stab2875)
- More, A., & More, S. 2022, *Mon. Not. Roy. Astron. Soc.*, 515, 1044, doi: [10.1093/mnras/stac1704](https://doi.org/10.1093/mnras/stac1704)

REFERENCES

- Mukherjee, S., Broadhurst, T., Diego, J. M., Silk, J., & Smoot, G. F. 2021, *Mon. Not. Roy. Astron. Soc.*, 506, 3751, doi: [10.1093/mnras/stab1980](https://doi.org/10.1093/mnras/stab1980)
- Mukherjee, S., Datta, S., Tiwari, S., Phukon, K. S., & Bose, S. 2022, *Phys. Rev. D*, 106, 104032, doi: [10.1103/PhysRevD.106.104032](https://doi.org/10.1103/PhysRevD.106.104032)
- Mukherjee, S., Wandelt, B. D., & Silk, J. 2020, *Mon. Not. Roy. Astron. Soc.*, 494, 1956, doi: [10.1093/mnras/staa827](https://doi.org/10.1093/mnras/staa827)
- Mukherjee, Suvodip, Wandelt, Benjamin D, & Silk, Joseph. 2020, *Phys. Rev. D*, 101, 103509, doi: [10.1103/PhysRevD.101.103509](https://doi.org/10.1103/PhysRevD.101.103509)
- Nagar, A., Rettegno, P., Gamba, R., et al. 2023, *Phys. Rev. D*, 108, 124018, doi: [10.1103/PhysRevD.108.124018](https://doi.org/10.1103/PhysRevD.108.124018)
- Nagar, A., et al. 2018, *Phys. Rev. D*, 98, 104052, doi: [10.1103/PhysRevD.98.104052](https://doi.org/10.1103/PhysRevD.98.104052)
- Nakamura, T. T. 1998, *Phys. Rev. Lett.*, 80, 1138, doi: [10.1103/PhysRevLett.80.1138](https://doi.org/10.1103/PhysRevLett.80.1138)
- Nakamura, T. T., & Deguchi, S. 1999, *Prog. Theor. Phys. Suppl.*, 133, 137, doi: [10.1143/ptps.133.137](https://doi.org/10.1143/ptps.133.137)
- Nakano, H., Tanaka, T., & Nakamura, T. 2015, *Phys. Rev. D*, 92, 064003, doi: [10.1103/PhysRevD.92.064003](https://doi.org/10.1103/PhysRevD.92.064003)
- Narayan, P., Johnson-McDaniel, N. K., & Gupta, A. 2023, *Phys. Rev. D*, 108, 064003, doi: [10.1103/PhysRevD.108.064003](https://doi.org/10.1103/PhysRevD.108.064003)
- Ng, K. K. Y., Vitale, S., Zimmerman, A., et al. 2018, *Phys. Rev. D*, 98, 083007, doi: [10.1103/PhysRevD.98.083007](https://doi.org/10.1103/PhysRevD.98.083007)
- Nitz, A., Harry, I., Brown, D., et al. 2020, *gwastro/pycbc: PyCBC Release 1.17.0, v1.17.0*, Zenodo, doi: [10.5281/zenodo.4355793](https://doi.org/10.5281/zenodo.4355793)
- Oguri, M. 2018, *Mon. Not. Roy. Astron. Soc.*, 480, 3842, doi: [10.1093/mnras/sty2145](https://doi.org/10.1093/mnras/sty2145)
- Ohanian, H. C. 1974, *Int. J. Theor. Phys.*, 9, 425, doi: [10.1007/BF01810927](https://doi.org/10.1007/BF01810927)
- O'Shea, E., & Kumar, P. 2023, *Phys. Rev. D*, 108, 104018, doi: [10.1103/PhysRevD.108.104018](https://doi.org/10.1103/PhysRevD.108.104018)
- Pagano, G., Hannuksela, O. A., & Li, T. G. F. 2020, *Astron. Astrophys.*, 643, A167, doi: [10.1051/0004-6361/202038730](https://doi.org/10.1051/0004-6361/202038730)
- Paxton, B., Bildsten, L., Dotter, A., et al. 2011, *Astrophys. J. Suppl.*, 192, 3, doi: [10.1088/0067-0049/192/1/3](https://doi.org/10.1088/0067-0049/192/1/3)

REFERENCES

- Perlick, V. 2010. <https://arxiv.org/abs/1010.3416>
- Peters, P. C. 1964, PhD thesis, Caltech
- Poggiani, R. 2019, PoS, FRAPWS2018, 013, doi: [10.22323/1.331.0013](https://doi.org/10.22323/1.331.0013)
- Pratten, G., Husa, S., Garcia-Quiros, C., et al. 2020, Phys. Rev. D, 102, 064001, doi: [10.1103/PhysRevD.102.064001](https://doi.org/10.1103/PhysRevD.102.064001)
- Pratten, G., et al. 2021, Phys. Rev. D, 103, 104056, doi: [10.1103/PhysRevD.103.104056](https://doi.org/10.1103/PhysRevD.103.104056)
- Pretorius, F. 2007. <https://arxiv.org/abs/0710.1338>
- Pürrer, M., Hannam, M., & Ohme, F. 2016, Phys. Rev. D, 93, 084042, doi: [10.1103/PhysRevD.93.084042](https://doi.org/10.1103/PhysRevD.93.084042)
- Racine, E. 2008, Phys. Rev. D, 78, 044021, doi: [10.1103/PhysRevD.78.044021](https://doi.org/10.1103/PhysRevD.78.044021)
- Razali, N. M., Wah, Y. B., et al. 2011, Journal of statistical modeling and analytics, 2, 21
- Reitze, D., Adhikari, R. X., Ballmer, S., et al. 2019, arXiv preprint arXiv:1907.04833
- Romero-Shaw, I. M., Lasky, P. D., & Thrane, E. 2022, Astrophys. J., 940, 171, doi: [10.3847/1538-4357/ac9798](https://doi.org/10.3847/1538-4357/ac9798)
- Romero-Shaw, I. M., et al. 2020, Mon. Not. Roy. Astron. Soc., 499, 3295, doi: [10.1093/mnras/staa2850](https://doi.org/10.1093/mnras/staa2850)
- Saha, P., & Williams, L. L. R. 2011, Mon. Not. Roy. Astron. Soc., 411, 1671, doi: [10.1111/j.1365-2966.2010.17797.x](https://doi.org/10.1111/j.1365-2966.2010.17797.x)
- Saini, P., Favata, M., & Arun, K. G. 2022, Phys. Rev. D, 106, 084031, doi: [10.1103/PhysRevD.106.084031](https://doi.org/10.1103/PhysRevD.106.084031)
- Saleem, M., et al. 2022, Class. Quant. Grav., 39, 025004, doi: [10.1088/1361-6382/ac3b99](https://doi.org/10.1088/1361-6382/ac3b99)
- Santamaria, L., et al. 2010, Phys. Rev. D, 82, 064016, doi: [10.1103/PhysRevD.82.064016](https://doi.org/10.1103/PhysRevD.82.064016)
- Sathyaprakash, B. S., & Dhurandhar, S. V. 1991, Phys. Rev. D, 44, 3819, doi: [10.1103/PhysRevD.44.3819](https://doi.org/10.1103/PhysRevD.44.3819)
- Schechter, P. L., & Wambsganss, J. 2002, Astrophys. J., 580, 685, doi: [10.1086/343856](https://doi.org/10.1086/343856)
- Schmidt, P., Ohme, F., & Hannam, M. 2015, Phys. Rev. D, 91, 024043, doi: [10.1103/PhysRevD.91.024043](https://doi.org/10.1103/PhysRevD.91.024043)

REFERENCES

- Schneider, P., & Weiss, A. 1986, *Astronomy and Astrophysics*, 164, 237
- Schutz, B. F. 2011, *Class. Quant. Grav.*, 28, 125023, doi: [10.1088/0264-9381/28/12/125023](https://doi.org/10.1088/0264-9381/28/12/125023)
- Seo, E., Hannuksela, O. A., & Li, T. G. F. 2022, *Astrophys. J.*, 932, 50, doi: [10.3847/1538-4357/ac6dea](https://doi.org/10.3847/1538-4357/ac6dea)
- Shan, X., Chen, X., Hu, B., & Cai, R.-G. 2023a. <https://arxiv.org/abs/2301.06117>
- Shan, X., Li, G., Chen, X., Zheng, W., & Zhao, W. 2023b, *Sci. China Phys. Mech. Astron.*, 66, 239511, doi: [10.1007/s11433-022-1985-3](https://doi.org/10.1007/s11433-022-1985-3)
- Shan, X., Wei, C., & Hu, B. 2021, *Mon. Not. Roy. Astron. Soc.*, 508, 1253, doi: [10.1093/mnras/stab2567](https://doi.org/10.1093/mnras/stab2567)
- Shapiro, S. S., & Wilk, M. B. 1965, *Biometrika*, 52, 591
- Sharma, V. K., Harikumar, S., Grespan, M., Biesiada, M., & Verma, M. M. 2023. <https://arxiv.org/abs/2310.10346>
- Skilling, J. 2006, *Bayesian Analysis*, 1, 833, doi: [10.1214/06-BA127](https://doi.org/10.1214/06-BA127)
- Smith, G. P., et al. 2017, *IAU Symp.*, 338, 98, doi: [10.1017/S1743921318003757](https://doi.org/10.1017/S1743921318003757)
- Smith, G. P., Bianconi, M., Jauzac, M., et al. 2019, *Mon. Not. Roy. Astron. Soc.*, 485, 5180, doi: [10.1093/mnras/stz675](https://doi.org/10.1093/mnras/stz675)
- Somiya, K. 2012, *Class. Quant. Grav.*, 29, 124007, doi: [10.1088/0264-9381/29/12/124007](https://doi.org/10.1088/0264-9381/29/12/124007)
- Sonnenfeld, A., Treu, T., Gavazzi, R., et al. 2013, *Astrophys. J.*, 777, 98, doi: [10.1088/0004-637X/777/2/98](https://doi.org/10.1088/0004-637X/777/2/98)
- Soucail, G., Mellier, Y., Fort, B., Mathez, G., & Cailloux, M. 1988, *A&A*, 191, L19
- Speagle, J. S. 2020, *Mon. Not. Roy. Astron. Soc.*, 493, 3132, doi: [10.1093/mnras/staa278](https://doi.org/10.1093/mnras/staa278)
- Suyu, S. H., Goobar, A., Collett, T., More, A., & Vernardos, G. 2024, *Space Sci. Rev.*, 220, 13, doi: [10.1007/s11214-024-01044-7](https://doi.org/10.1007/s11214-024-01044-7)
- Takahashi, R. 2017, *Astrophys. J.*, 835, 103, doi: [10.3847/1538-4357/835/1/103](https://doi.org/10.3847/1538-4357/835/1/103)
- Takahashi, R., & Nakamura, T. 2003, *Astrophys. J.*, 595, 1039, doi: [10.1086/377430](https://doi.org/10.1086/377430)

REFERENCES

- Tambalo, G., Zumalacárregui, M., Dai, L., & Cheung, M. H.-Y. 2023, Phys. Rev. D, 108, 043527, doi: [10.1103/PhysRevD.108.043527](https://doi.org/10.1103/PhysRevD.108.043527)
- The LIGO Scientific Collaboration, the Virgo Collaboration, the KAGRA Collaboration, et al. 2023a. <https://arxiv.org/abs/2304.08393>
- The LIGO Scientific Collaboration, the Virgo Collaboration, the KAGRA Collaboration, Abbott, R., et al. 2023b, Phys. Rev. X, 13, 011048, doi: [10.1103/PhysRevX.13.011048](https://doi.org/10.1103/PhysRevX.13.011048)
- The LIGO Scientific Collaboration, the Virgo Collaboration, Abbott, R., et al. 2024, Phys. Rev. D, 109, 022001, doi: [10.1103/PhysRevD.109.022001](https://doi.org/10.1103/PhysRevD.109.022001)
- Thrane, E., & Talbot, C. 2019, Publ. Astron. Soc. Austral., 36, e010, doi: [10.1017/pasa.2019.2](https://doi.org/10.1017/pasa.2019.2)
- Ulmer, A., & Goodman, J. 1995, Astrophys. J., 442, 67, doi: [10.1086/175422](https://doi.org/10.1086/175422)
- Urrutia, J., & Vaskonen, V. 2021, Mon. Not. Roy. Astron. Soc., 509, 1358, doi: [10.1093/mnras/stab3118](https://doi.org/10.1093/mnras/stab3118)
- Usman, S. A., et al. 2016, Class. Quant. Grav., 33, 215004, doi: [10.1088/0264-9381/33/21/215004](https://doi.org/10.1088/0264-9381/33/21/215004)
- Valdes, G., Hines, A., Nelson, A., Zhang, Y., & Guzman, F. 2022, Appl. Phys. Lett., 121, 234102, doi: [10.1063/5.0122495](https://doi.org/10.1063/5.0122495)
- Vallisneri, M. 2008, Phys. Rev. D, 77, 042001, doi: [10.1103/PhysRevD.77.042001](https://doi.org/10.1103/PhysRevD.77.042001)
- Vallisneri, Michele. 2012, Phys. Rev. D, 86, 082001, doi: [10.1103/PhysRevD.86.082001](https://doi.org/10.1103/PhysRevD.86.082001)
- Vernardos, G. 2019, Monthly Notices of the Royal Astronomical Society, 483, 5583, doi: [10.1093/mnras/sty3486](https://doi.org/10.1093/mnras/sty3486)
- Vijaykumar, A., Mehta, A. K., & Ganguly, A. 2023, Phys. Rev. D, 108, 043036, doi: [10.1103/PhysRevD.108.043036](https://doi.org/10.1103/PhysRevD.108.043036)
- Virtanen, P., et al. 2020, Nature Meth., 17, 261, doi: [10.1038/s41592-019-0686-2](https://doi.org/10.1038/s41592-019-0686-2)
- Vitale, S., & Del Pozzo, W. 2014, Phys. Rev. D, 89, 022002, doi: [10.1103/PhysRevD.89.022002](https://doi.org/10.1103/PhysRevD.89.022002)
- Walsh, D., Carswell, R. F., & Weymann, R. J. 1979, Nature, 279, 381, doi: [10.1038/279381a0](https://doi.org/10.1038/279381a0)
- Wambsganss, J. 1999, Journal of Computational and Applied Mathematics, 109, 353

REFERENCES

- Weisberg, J. M., Taylor, J. H., & Fowler, L. A. 1981, *Sci. Am.*, 245, 66, doi: [10.1038/scientificamerican1081-74](https://doi.org/10.1038/scientificamerican1081-74)
- Wen, L. 2003, *Astrophys. J.*, 598, 419, doi: [10.1086/378794](https://doi.org/10.1086/378794)
- Wex, N. 2014. <https://arxiv.org/abs/1402.5594>
- Will, C. M. 2006, *Living Rev. Rel.*, 9, 3, doi: [10.12942/lrr-2006-3](https://doi.org/10.12942/lrr-2006-3)
- Wu, J., Ho, C.-M., & Boyanovsky, D. 2009, *Phys. Rev. D*, 80, 103511, doi: [10.1103/PhysRevD.80.103511](https://doi.org/10.1103/PhysRevD.80.103511)
- Yang, T., Hu, B., Cai, R.-G., & Wang, B. 2019, *Astrophys. J.*, 880, 50, doi: [10.3847/1538-4357/ab271e](https://doi.org/10.3847/1538-4357/ab271e)
- Yunes, N., & Pretorius, F. 2009, *Phys. Rev. D*, 80, 122003, doi: [10.1103/PhysRevD.80.122003](https://doi.org/10.1103/PhysRevD.80.122003)
- Yunes, N., Yagi, K., & Pretorius, F. 2016, *Phys. Rev. D*, 94, 084002, doi: [10.1103/PhysRevD.94.084002](https://doi.org/10.1103/PhysRevD.94.084002)
- Zevin, M., Samsing, J., Rodriguez, C., Haster, C.-J., & Ramirez-Ruiz, E. 2019, *Astrophys. J.*, 871, 91, doi: [10.3847/1538-4357/aaf6ec](https://doi.org/10.3847/1538-4357/aaf6ec)
- Zheng, W., Chen, X., Li, G., & Chen, H.-z. 2022, *Astrophys. J.*, 931, 114, doi: [10.3847/1538-4357/ac68ea](https://doi.org/10.3847/1538-4357/ac68ea)
- Zwicky, F. 1937, *Phys. Rev.*, 51, 290, doi: [10.1103/PhysRev.51.290](https://doi.org/10.1103/PhysRev.51.290)

Appendix A

Wave-optics effects in Gravitational Lensing of Gravitational Waves: Technical derivations and assumptions

A.1 Lensing Amplification Factor derivation

A.1.1 Basic Equations

We consider GWs propagating under the gravitational potential of a lens object. The background metric is given by¹ (Hossenfelder 2006; Takahashi & Nakamura 2003),

$$ds^2 = -(1 - 2U)dt^2 + (1 - 2U)d\mathbf{r}^2 \equiv g_{\mu\nu}^{(B)} dx^\mu dx^\nu, \quad (\text{A.1})$$

where $U(r)$ is the gravitational potential of the lens object, satisfying $|U(r)| \ll 1$ (weak field regime). Let us consider linear perturbations $h_{\mu\nu}$ to the background metric $g_{\mu\nu}^{(B)}$ as

$$g_{\mu\nu} = g_{\mu\nu}^{(B)} + h_{\mu\nu}. \quad (\text{A.2})$$

Adopting the transverse traceless Lorentz gauge condition of $h_{\mu;\nu}^\nu = 0$ and $h_{\mu}^{\mu} = 0$ (where semicolon represents the covariant derivative), and assuming that the wavelength of the propagating GW is much smaller than the typical radius of the background curvature (which holds well in the weak-field regime and for the sensitivity band of ground-based detectors), we arrive at

$$\square h_{\mu\nu} = 0. \quad (\text{A.3})$$

¹we work in natural units, unless otherwise noted.

Using the eikonal approximation, the GW signal can be expressed as

$$h_{\mu\nu} = \phi e_{\mu\nu}, \quad (\text{A.4})$$

where ϕ is the scalar amplitude and $e_{\mu\nu}$ is the polarisation tensor satisfying the conditions $e_{\mu}^{\mu} = 0$ and $e_{\mu\nu}e^{\mu\nu} = 2$. Since e_{μ}^{μ} is parallel-transported along the null-geodesic, the effect on e_{μ}^{μ} due to lensing is of the order $U(\ll 1)$ ². Thus, we treat the scalar wave ϕ , instead of the GW $h_{\mu\nu}$, propagating through the curved space-time, described by the equation:

$$\partial_{\mu} \left(\sqrt{-g_{\mu\nu}^{(B)}} g^{(B)\mu\nu} \partial_{\nu} \phi \right) = 0. \quad (\text{A.5})$$

For the scalar wave in the frequency domain $\tilde{\phi}(\omega, \mathbf{r})$, the above equation A.5 can be expressed as,

$$(\nabla^2 + \omega^2)\tilde{\phi} = 4\omega^2 U\tilde{\phi}, \quad (\text{A.6})$$

where we made use of the metric in Eq. A.1.

A.1.2 Kirchhoff's Diffraction Integral

The complex disturbance $\tilde{\phi}$ at an observation point in space can be calculated using Green's theorem, which states (Goodman 2005):

Let $\tilde{\phi}(P)$ and $G(P)$ be two complex-valued functions of position, and let S be a closed surface surrounding a volume V . If $\tilde{\phi}(P)$, $G(P)$, and their first and second partial derivatives are single-valued and continuous within and on S , then we have

$$\iiint_V (\tilde{\phi} \nabla^2 G - G \nabla^2 \tilde{\phi}) dV = \iint_S \left(\tilde{\phi} \frac{\partial G}{\partial n} - G \frac{\partial \tilde{\phi}}{\partial n} \right) dS, \quad (\text{A.7})$$

where dV and dS are differential volume and surface elements, respectively, and $\partial/\partial n$ signifies a partial derivative in the outward normal direction at each point on S .

While this theorem forms the foundation of scalar diffraction theory, its application to the diffraction problem requires a prudent choice of an auxiliary function G and a closed surface S . Next, we discuss Kirchhoff's choice of the auxiliary function and the consequent integral theorem that follows.

Kirchhoff's formulation of the diffraction problem is based on an integral theorem that expresses the solution of the homogeneous wave equation at an arbitrary point in

²While we currently disregard the influence of lensing on the polarization tensor, it's worth noting that some investigations have explored its potential impact (e.g., Dalang et al. 2022; Sharma et al. 2023)

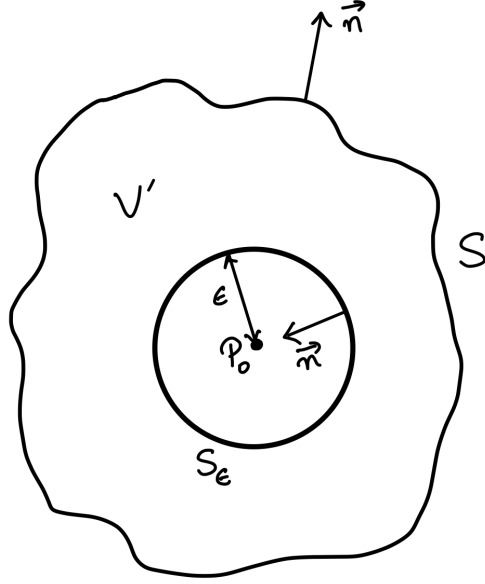


Figure A.1: A depiction of the surface of integration.

terms of the solution and its first derivative on an arbitrary closed surface surrounding that point. Let P_0 denote the point of observation and let S be an arbitrary closed surface surrounding P_0 (see Fig. A.1). If there are no sources inside S , then Eq. A.6 becomes a homogeneous wave equation:

$$(\nabla^2 + \omega^2)\tilde{\phi} = 0. \quad (\text{A.8})$$

We aim to express the disturbance at the point P_0 in terms of its values on S . Choosing the auxiliary function G to be the Green's function for the homogeneous Maxwell's equation, i.e., a unit-amplitude spherical wave expanding about P_0 , then the value of G at an arbitrary point P_1 is given by:

$$G(P_1) = \frac{e^{i\omega r_{01}}}{r_{01}}, \quad (\text{A.9})$$

where $r_{01} = |r_{P_0} - r_{P_1}|$. This ensures that:

$$(\nabla^2 + \omega^2)G = 0. \quad (\text{A.10})$$

We then utilize Green's theorem for functions $\tilde{\phi}$ and G . However, since G is not defined at P_0 , a small surface S_ϵ having radius ϵ is inserted around P_0 . Green's theorem is then applied to region V' lying between S and S_ϵ as shown in Fig. A.1, yielding (Goodman

2005):

$$\begin{aligned} \iiint_{V'} (\tilde{\phi} \nabla^2 G - G \nabla^2 \tilde{\phi}) dV &= 0 = \iint_{S+S_\epsilon} \left(\tilde{\phi} \frac{\partial G}{\partial n} - G \frac{\partial \tilde{\phi}}{\partial n} \right) dS, \\ \Rightarrow \iint_{S_\epsilon} \left(\tilde{\phi} \frac{\partial G}{\partial n} - G \frac{\partial \tilde{\phi}}{\partial n} \right) dS &= - \iint_S \left(\tilde{\phi} \frac{\partial G}{\partial n} - G \frac{\partial \tilde{\phi}}{\partial n} \right) dS. \end{aligned} \quad (\text{A.11})$$

On S_ϵ , we have:

$$G(\epsilon) = \frac{e^{i\omega|\epsilon|}}{|\epsilon|}. \quad (\text{A.12})$$

Thus, the partial derivative of $G(\epsilon)$ with respect to the outward normal direction at P_0 becomes:

$$\frac{\partial G(\epsilon)}{\partial n} = \frac{e^{i\omega|\epsilon|}}{|\epsilon|} \left(i\omega - \frac{1}{|\epsilon|} \right) \frac{\partial(\vec{\epsilon})}{\partial n}. \quad (\text{A.13})$$

Since $\frac{\partial(\vec{\epsilon})}{\partial n} = -1$, we get

$$\frac{\partial G(\epsilon)}{\partial n} = \frac{e^{i\omega|\epsilon|}}{|\epsilon|} \left(\frac{1}{|\epsilon|} - i\omega \right). \quad (\text{A.14})$$

Taking the limit $\epsilon \rightarrow 0$, we obtain:

$$\begin{aligned} \lim_{\epsilon \rightarrow 0} \iint_{S_\epsilon} \left(\tilde{\phi} \frac{\partial G}{\partial n} - G \frac{\partial \tilde{\phi}}{\partial n} \right) dS &= 4\pi\epsilon^2 \lim_{\epsilon \rightarrow 0} \left[\tilde{\phi}(P_0) \frac{e^{i\omega|\epsilon|}}{|\epsilon|} \left(\frac{1}{|\epsilon|} - i\omega \right) - \frac{\partial \tilde{\phi}(P_0)}{\partial n} \frac{e^{i\omega|\epsilon|}}{|\epsilon|} \right] \\ &= 4\pi \tilde{\phi}(P_0). \end{aligned} \quad (\text{A.15})$$

By combining equations A.11 and A.15, we arrive at the integral theorem of Helmholtz and Kirchhoff (Goodman 2005):

$$\tilde{\phi}(P_0) = \frac{1}{4\pi} \iint_S \left[\left(\frac{e^{i\omega r_{01}}}{r_{01}} \right) \frac{\partial \tilde{\phi}}{\partial n} - \tilde{\phi} \frac{\partial}{\partial n} \left(\frac{e^{i\omega r_{01}}}{r_{01}} \right) \right] dS, \quad (\text{A.16})$$

which plays a crucial role in the scalar diffraction theory by expressing the field at any point P_0 in terms of the "boundary values" of the wave on any arbitrary closed surface surrounding that point.

A.1.3 Diffraction by a microlensing compact object

Now, we delve into the specific problem relevant to this thesis: diffraction caused by an intervening microlensing compact object. Figure A.2 illustrates the lensing geometry involving the source, the lens, and the observer, akin to the setup depicted in Figure 2.1. D_L , D_S , D_{LS} represent the separations from the observer to the lens, from the observer

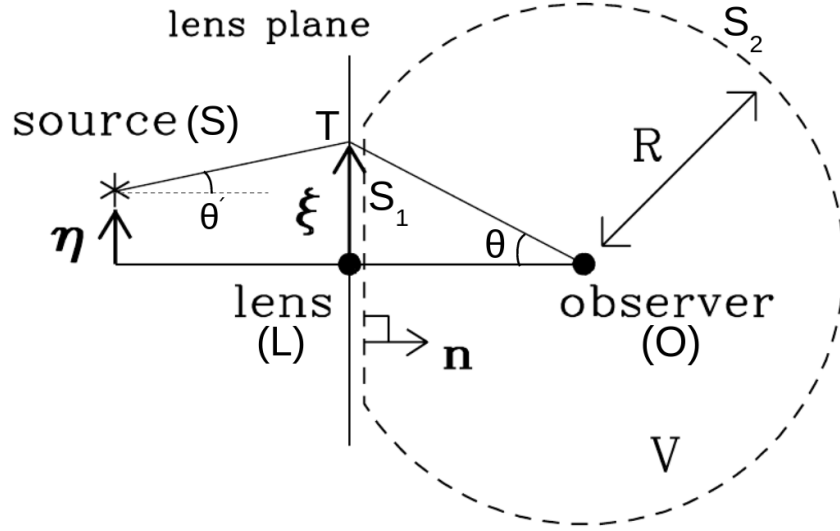


Figure A.2: Illustration of the volume V inside the dashed line. The boundary of this region consists of two parts: S_1 lies close to the lens plane but excludes it, while S_2 constitutes the surface of a sphere with a radius R , centered at the observer. \mathbf{n} is the normal vector to the lens plane. [Figure adapted from [Takahashi & Nakamura \(2003\)](#)].

to the source, and from the lens to the source, respectively. $\boldsymbol{\eta}$ is a position vector of the source in the source plane, while $\boldsymbol{\xi}$ is the impact parameter in the lens plane. We use the thin lens approximation in which the lens is characterized by the surface mass density $\Sigma(\boldsymbol{\xi})$, and the GWs are scattered only at the thin lens plane. This approximation holds well in typical lensing scenarios where D_S is much larger than the typical size of the lens.

We define a volume V within [Figure A.2](#), enclosed by the dashed line. The boundary of this region consists of two parts: S_1 lies close to the lens plane but excludes it, while S_2 constitutes the surface of a sphere with a radius R , centering at the observer. As per the thin lens approximation, $U = 0$ within V , thereby reducing [Equation A.6](#) to the Helmholtz equation, as in [Equation A.8](#), within V . Utilizing the integral theorem of Helmholtz and Kirchhoff, [Eq. A.16](#), we express ([Goodman 2005](#)):

$$\tilde{\phi}(P_0) = \frac{1}{4\pi} \iint_{S=S_1+S_2} \left[\tilde{\phi} \frac{\partial}{\partial n} \left(\frac{e^{i\omega R}}{R} \right) - \left(\frac{e^{i\omega R}}{R} \right) \frac{\partial \tilde{\phi}}{\partial n} \right] dS, \quad (\text{A.17})$$

where a negative sign has been absorbed due to the inward direction of \mathbf{n} . We first focus on the integral over the surface S_2 . Since both $\tilde{\phi}$ and $G = e^{i\omega R}/R$ fall off as $1/R$, they will be vanishingly small at the surface. But since S_2 's area will also increase as R^2 , we do not know whether the integral will have non-zero contributions. Interestingly, if we consider the fact that waves travel with finite speed, they would not have had time to reach S_2 , and so the integral over S_2 will vanish identically. However, this argument falls

APPENDIX A. WAVE-OPTICS EFFECTS IN GRAVITATIONAL LENSING OF GRAVITATIONAL WAVES: TECHNICAL DERIVATIONS AND ASSUMPTIONS

short because of our assumption of monochromatic disturbances, which (by definition) have existed for all time. Thus, it needs a more careful investigation which we do next. Upon setting $R \rightarrow \infty$, we can write

$$\iint_{S_2} \left[\tilde{\phi} \frac{\partial}{\partial n} \left(\frac{e^{i\omega R}}{R} \right) - \left(\frac{e^{i\omega R}}{R} \right) \frac{\partial \tilde{\phi}}{\partial n} \right] dS = \iint_{S_2} \left(\frac{e^{i\omega R}}{R} \right) \left(i\omega \tilde{\phi} - \frac{\partial \tilde{\phi}}{\partial n} \right) R^2 d\Omega, \quad (\text{A.18})$$

where Ω is the solid angle subtended by S_2 at P_0 . Since $|e^{i\omega R}|$ is uniformly bounded on S_2 , the integral vanishes uniformly over Ω when:

$$\lim_{R \rightarrow \infty} R \left(i\omega \tilde{\phi} - \frac{\partial \tilde{\phi}}{\partial n} \right) = 0, \quad (\text{A.19})$$

which holds true when $\tilde{\phi}$ vanishes at least as fast as the diverging spherical wave. Consequently, the integral over S_2 indeed vanishes, yielding (Goodman 2005):

$$\tilde{\phi}(P_0) = \frac{1}{4\pi} \iint_{S_1} \left[\tilde{\phi} \frac{\partial}{\partial n} \left(\frac{e^{i\omega R}}{R} \right) - \left(\frac{e^{i\omega R}}{R} \right) \frac{\partial \tilde{\phi}}{\partial n} \right] dS. \quad (\text{A.20})$$

Now, we will use eikonal approximation to determine $\tilde{\phi}$ and $\partial \tilde{\phi} / \partial n$ on the boundary S_1 . We assume $\tilde{\phi}$ has the form (Takahashi & Nakamura 2003):

$$\tilde{\phi} = A e^{i\omega S} \equiv A e^{i s_p}, \quad (\text{A.21})$$

where the eikonal approximation captures the high-frequency limit of a wave solution,, i.e., assuming $\omega \gg 1$. This assumption implies that A represents a slowly varying amplitude, while s_p constitutes a rapidly varying phase. Mathematically, this translates to: $|\nabla A / A| \ll |\nabla S_p / S_p|$ and $|\nabla^2 S_p| \ll |\nabla S_p|^2$. Upon substituting this into the wave equation $\partial^\mu \partial_\mu \tilde{\phi} = 0$ and expanding in powers of ω , at leading order, we obtain the *eikonal equation* (Bernardeau 1999):

$$g^{\mu\nu} S_{,\mu} S_{,\nu} = 0, \quad (\text{A.22})$$

where $g^{\mu\nu}$ is the (inverse) metric. Applying this to Eq. A.6, we get

$$\begin{aligned} \omega^2 [1 - (\nabla S)^2] \tilde{\phi} &= 4\omega^2 U \tilde{\phi}, \\ \Rightarrow (\nabla S) &\approx (1 - 2U), \\ \text{or, } S &= \int dl (1 - 2U), \end{aligned} \quad (\text{A.23})$$

where dl represents the measure of the integral along the path of the GW. Now, the phase at T , the intersection point between the GW and the lens plane (see Fig. A.2), will be (Takahashi & Nakamura 2003)

$$S_p = \omega \int_S^T dl (1 - 2U) = \omega \left[\int_S^O dl - \int_T^O dl \right] (1 - 2U). \quad (\text{A.24})$$

APPENDIX A. WAVE-OPTICS EFFECTS IN GRAVITATIONAL LENSING OF GRAVITATIONAL WAVES: TECHNICAL DERIVATIONS AND ASSUMPTIONS

Utilizing the fact the GW propagates along a null geodesic, we can write

$$dt = dl(1 - 2U), \quad (\text{A.25})$$

for the metric in Eq. A.1. Consequently, the first term in Eq. A.24 represents the arrival time t_L of the GW from S to O , while the second term is just the distance r between T and O , i.e.,

$$S_p = \omega(t_L - r). \quad (\text{A.26})$$

Thus, we have:

$$\tilde{\phi} = Ae^{i\omega(t_L - r)}; \quad \frac{\partial \tilde{\phi}}{\partial n} = i\omega \tilde{\phi} \cos \theta'. \quad (\text{A.27})$$

$$G = \frac{e^{i\omega r}}{r}; \quad \frac{\partial G}{\partial n} = -\cos \theta \frac{e^{i\omega r}}{r} \left(i\omega - \frac{1}{r} \right). \quad (\text{A.28})$$

Under realistic scenarios, the small angle approximation holds well, i.e., $|\theta| \ll 1$ and $|\theta'| \ll 1$. Therefore, the lensed field at the observer $\tilde{\phi}_{\text{obs}}^L$ in Eq. A.20 is given by (Bernardeau 1999; Takahashi & Nakamura 2003):

$$\tilde{\phi}_{\text{obs}}^L(\omega, \boldsymbol{\eta}) = \frac{\omega A}{2\pi i D_L} \int d^2\xi \exp[i\omega t_L(\boldsymbol{\xi}, \boldsymbol{\eta})]. \quad (\text{A.29})$$

A.1.4 Lensing Amplification Factor

The lensing amplification factor $F : \mathbb{R} \rightarrow \mathbb{C}$ quantifies the impact of GL on GW signals. It's defined as (Takahashi & Nakamura 2003):

$$F(\omega, \boldsymbol{\eta}) = \frac{\tilde{\phi}_{\text{obs}}^L(\omega, \boldsymbol{\eta})}{\tilde{\phi}_{\text{obs}}(\omega, \boldsymbol{\eta})}, \quad (\text{A.30})$$

where $\tilde{\phi}_{\text{obs}}^L(\omega, \boldsymbol{\eta})$ and $\tilde{\phi}_{\text{obs}}(\omega, \boldsymbol{\eta})$ represent the GW amplitudes with and without lensing, respectively. In the absence of lensing ($U = 0$), $\tilde{\phi}_{\text{obs}}(\omega, \boldsymbol{\eta})$ is given by:

$$\tilde{\phi}_{\text{obs}}(\omega, \boldsymbol{\eta}) = A' e^{i\omega t_{\text{UL}}(\boldsymbol{\eta})}, \quad (\text{A.31})$$

where t_{UL} denotes the arrival time in the absence of lensing. Using the fact that the amplitude falls linearly with the distance, we can express A' in terms of A as:

$$A' = \left(\frac{D_{\text{LS}}}{D_{\text{S}}} \right) A. \quad (\text{A.32})$$

Therefore, the amplification factor is given by (Bernardeau 1999; Takahashi & Nakamura 2003):

$$F(\omega, \boldsymbol{\eta}) = \frac{D_{\text{S}}}{D_{\text{L}} D_{\text{LS}}} \frac{\omega}{2\pi i} \int d^2\xi \exp[i\omega t_{\text{d}}(\boldsymbol{\xi}, \boldsymbol{\eta})], \quad (\text{A.33})$$

where $t_d(\boldsymbol{\xi}, \boldsymbol{\eta})$ signifies the time delay between the arrival times of lensed and unlensed signals:

$$t_d(\boldsymbol{\xi}, \boldsymbol{\eta}) = t_L(\boldsymbol{\xi}, \boldsymbol{\eta}) - t_{UL}(\boldsymbol{\eta}) + \phi_m(\boldsymbol{\eta}) . \quad (\text{A.34})$$

Here, $\phi_m(\boldsymbol{\eta})$ represents an arbitrary constant independent of the lens properties, typically chosen to ensure $\min_{\{\boldsymbol{\xi}, \boldsymbol{\eta}\}} [t_d(\boldsymbol{\xi}, \boldsymbol{\eta})] = 0$. Employing dimensionless units and considering signal traverses cosmological distances (wherein ω transforms as $\omega \rightarrow (1 + z_L)\omega$) we can express the amplification factor given in Eq. A.33 into its dimensionless form, as given in Eq. 2.5. Note that the phase of the lensing amplification factor is determined by the factor ωt_d , which sets the threshold for the significance of wave-optics effects. When $\omega t_d \sim 1$, wave-optics effects become dominant, resulting in frequency-dependent modulations in $F(\omega)$. Conversely, in the geometric optics limit where $\omega t_d \gg 1$, the phase becomes highly oscillatory, and only the stationary points of t_d contribute to the integral, leading to the expression in Equation 2.7.

A.2 Lensing Time Delay Derivation

The time delay function t_d plays a pivotal role in GL, serving as a measure of the delay relative to the straight, undeflected path of light rays. This function encapsulates essential information about the lensing system, encompassing its physical properties and enabling the derivation of fundamental equations such as the lens equation. Moreover, as illustrated in the preceding section, t_d also plays a crucial role in determining the lensing amplification factor. In this section, we delve into the explicit formulation of the time delay function arising from the presence of an intervening lens.

The total time delay, denoted as t_d , consists of two primary components: the geometric time delay Δt_{geom} and the gravitational time delay Δt_{grav} , expressed as follows (Suyu et al. 2024):

$$t_d = \Delta t_{\text{geom}} + \Delta t_{\text{grav}} . \quad (\text{A.35})$$

The geometric time delay originates from the disparity in the paths traversed by the lensed and unlensed light signals. Conversely, the gravitational time delay, also referred to as the Shapiro delay, arises solely due to the gravitational influence of the lens on the spacetime metric. In the subsequent discussion, we derive each of these temporal delays individually.

A.2.1 Geometric Time Delay

Consider Figure 1, where we depict a lensing scenario comprising a source (S), observer (O), and a lens (L). The line segment SO denotes the path that a GW signal would

traverse if unaffected by lensing. In the presence of the lens, the signal deviates from this path and follows STO . Our objective is to quantify the time delay resulting from the differences in the lengths of these paths. Throughout this derivation, we adopt the small-angle approximation.

In Fig. A.3, it is apparent that (Suyu et al. 2024)

$$\Delta t_{\text{geom}} = t_{\text{geom}}^{\text{L}} - t_{\text{geom}}^{\text{UL}} = D_{\text{L}}(\theta - \beta) \cdot \delta. \quad (\text{A.36})$$

Moreover, δ can be determined in terms of α using basic trigonometric relations, as noted below:

$$p + \delta + q = \pi, \quad (\text{A.37})$$

$$\delta + (\pi - p) + (\pi - \alpha) + (\pi - q) = 2\pi. \quad (\text{A.38})$$

Using these two equations, we get

$$\delta = \alpha/2. \quad (\text{A.39})$$

Furthermore, we utilize the lens equation (which can also be obtained purely from geometric arguments),

$$\theta - \beta = \frac{D_{\text{LS}}}{D_{\text{S}}}\alpha \quad (\text{A.40})$$

Thus, using equations A.36, A.39 and A.40, we can write the general form of the geometric time delay as (Suyu et al. 2024):

$$\Delta t_{\text{geom}} = \frac{D_{\text{L}}D_{\text{S}}}{2D_{\text{LS}}}(\theta - \beta)^2. \quad (\text{A.41})$$

We can further transform this function from coordinates $(\theta, \beta) \rightarrow (\mathbf{x}, \mathbf{y})$ using the relations between the two as given below Eq. 2.1, to yield (Takahashi & Nakamura 2003):

$$\Delta t_{\text{geom}} = \frac{2GM}{c^3}|\mathbf{x} - \mathbf{y}|^2, \quad (\text{A.42})$$

where we reintroduced c for clarity. In this equation, M represents the lens mass, and we choose the arbitrary scaling length ξ_0 corresponding to the Einstein radius of mass M . This formulation constitutes the desired form of the geometric time delay employed throughout this thesis.

A.2.2 Gravitational Time Delay (Shapiro Delay)

The gravitational time delay Δt_{grav} (or the Shapiro delay) occurs due to the fact that the spacetime is affected due to the presence of the deflector. In realistic scenarios of GL, the

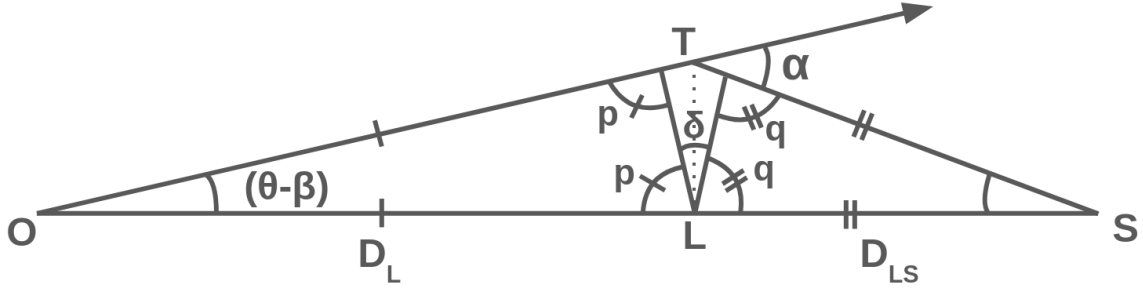


Figure A.3: Excess path length giving rise to the geometric time delay. The line segment SO denotes the path that a GW signal would traverse if unaffected by lensing. In the presence of the lens, the signal deviates from this path and follows STO .

weak field limit holds well, where the spacetime metric induced by the lens approximates the weak field limit of the Schwarzschild metric. In Cartesian coordinates, this metric can be expressed as (Suyu et al. 2024):

$$ds^2 = -(1 + 2\phi)dt^2 + (1 - 2\phi)(dx^2 + dy^2 + dz^2), \quad (\text{A.43})$$

where ϕ is the Newtonian gravitational potential. Considering the propagation of GW ($ds = 0$) between two points A and B , with the coordinate system oriented such that the z -axis aligns with the GW trajectory along the line joining A to B , we obtain:

$$t_{\text{grav}}^L = t_B - t_A = \int_{z_A}^{z_B} dz \sqrt{\frac{(1 - 2\phi)}{(1 + 2\phi)}} \approx \int_{z_A}^{z_B} dz (1 - 2\phi). \quad (\text{A.44})$$

Similarly, in the absence of any lens, we simply have

$$t_{\text{grav}}^{\text{UL}} = t_B - t_A = \int_{z_A}^{z_B} dz \quad (\text{A.45})$$

Thus, the gravitational time delay Δt_{grav} can be expressed as

$$\Delta t_{\text{grav}} = t_{\text{grav}}^L - t_{\text{grav}}^{\text{UL}} = -\frac{2}{c^3} \int_{z_A}^{z_B} dz \phi(z). \quad (\text{A.46})$$

Operating under the thin-lens approximation, it is meaningful to define the total potential in terms of the reduced projected gravitational potential as

$$\psi'(\boldsymbol{\xi}) \equiv \int dz \phi(\boldsymbol{\xi}, z), \quad (\text{A.47})$$

which, using Poisson's equation, can be related to the surface mass density distribution $\Sigma(\boldsymbol{\xi})$ through

$$\nabla_{\boldsymbol{\xi}}^2 \psi'(\boldsymbol{\xi}) = 4\pi G \Sigma(\boldsymbol{\xi}). \quad (\text{A.48})$$

Using equations A.46-A.48, we get (Suyu et al. 2024):

$$\Delta t_{\text{grav}} = -\frac{2}{c^3}\psi'(\boldsymbol{\xi}), \quad (\text{A.49})$$

where we reintroduced the constants for clarity.

A.2.3 Total lensing time delay

Using equations A.34, A.35, A.42, and A.49, we can express the total lensing time delay t_d in terms of the dimensionless coordinates $\{\mathbf{x}, \mathbf{y}\}$ as (Takahashi & Nakamura 2003):

$$t_d(\mathbf{x}, \mathbf{y}) = (1 + z_L) \frac{4GM}{c^3} \left[\frac{1}{2} |\mathbf{x} - \mathbf{y}|^2 - \psi(\mathbf{x}) + \phi_m(\mathbf{y}) \right], \quad (\text{A.50})$$

where $\psi(\mathbf{x}) = \frac{\psi'(\mathbf{x})}{4GM/c^2}$ and, as mentioned below Eq. A.34, $\phi_m(\mathbf{y})$ is an arbitrary constant chosen such that $\min_{\{\mathbf{x}, \mathbf{y}\}} [t_d(\mathbf{x}, \mathbf{y})] = 0$. The term $(1 + z_L)$ is introduced to account for the expansion of the Universe during the GW's travel from the lens to the observer.

As an example, let's determine the projected potential $\psi(\mathbf{x})$ for a point-mass lens and derive the total time delay for such a case. By considering the general form of the deflection $\boldsymbol{\alpha}'(\boldsymbol{\xi})$ as the superposition of the deflections produced by the individual mass differentials, we have (Suyu et al. 2024):

$$\boldsymbol{\alpha}'(\boldsymbol{\xi}) = \frac{4G}{c^2} \int d^2\xi' \Sigma(\boldsymbol{\xi}') \frac{\boldsymbol{\xi} - \boldsymbol{\xi}'}{|\boldsymbol{\xi} - \boldsymbol{\xi}'|^2}. \quad (\text{A.51})$$

Utilizing equations A.48 and A.51, along with the Green's function for the 2D Laplacian (satisfying $\nabla_{\boldsymbol{\xi}}^2 \mathcal{G}(\boldsymbol{\xi}, \boldsymbol{\xi}') = 2\pi\delta^2(\boldsymbol{\xi} - \boldsymbol{\xi}')$) as $\mathcal{G}(\boldsymbol{\xi}, \boldsymbol{\xi}') = \ln |\boldsymbol{\xi} - \boldsymbol{\xi}'|$, we can write

$$\psi(\boldsymbol{\xi}) = 2G \int d^2\xi' \Sigma(\boldsymbol{\xi}') \ln |\boldsymbol{\xi} - \boldsymbol{\xi}'|, \quad (\text{A.52})$$

$$\boldsymbol{\alpha}'(\boldsymbol{\xi}) = \frac{2}{c^2} \nabla_{\boldsymbol{\xi}}^2 \psi(\boldsymbol{\xi}). \quad (\text{A.53})$$

Using equations A.51-A.53, it is now straightforward to show that for a point-mass lens, $\psi(\mathbf{x}) = \ln |\mathbf{x}|$, leading to (Takahashi & Nakamura 2003; Suyu et al. 2024):

$$t_d^{\text{point}}(\mathbf{x}, \mathbf{y}) = (1 + z_L) \frac{4GM}{c^3} \left[\frac{1}{2} |\mathbf{x} - \mathbf{y}|^2 - \ln |\mathbf{x}| + \phi_m(\mathbf{y}) \right]. \quad (\text{A.54})$$